



UNIVERSITÀ DEGLI STUDI DI TRIESTE
e
UNIVERSITÀ CA' FOSCARI DI VENEZIA

XXXI CICLO DEL DOTTORATO DI RICERCA IN CHIMICA

**Derivatization of Metal Oxide with Bis-phosphonic Acids: A
Straightforward Approach for Tailoring the Superficial
Properties of the Nanoparticles for Drug Delivery Purposes**

SSD :CHIM/02

Ph.D Thesis of KHOHINUR HOSSAIN
Student Number: 989081
Year of Discussion: 2020

COORDINATOR
PROF. BARBARA MILANI

Handwritten signature of Barbara Milani in blue ink.

SUPERVISOR
PROF. PATRIZIA CANTON

Handwritten signature of Patrizia Canton in blue ink.

ACADEMIC YEAR 2018/2019

Abstract

The development of new hybrid organic-inorganic nanosystems is a cutting-edge field of research specifically for high potential biomedical applications. Specifically, the interaction between the organic ligands and the inorganic nanoparticles need to be specifically investigated and tailored in order to achieve stability and to impart specific properties to the nano-assemblies. Zirconia is a very interesting material for nano-technological applications, in particular for biomedical purposes due to its biocompatibility derived by a large inertness and high thermal, mechanical and chemical stability except at very high pH conditions. Similarly to silica NPs, ZrNPs are subjected to extensive study and functionalization to modify the surface properties of these materials. The surface chemistry on zirconia is not comparable to that of silica in particular due to the decreased chemical stability of the silane bond from Zr–O–Si–R with respect to Si–O–Si–R. In fact, the organosilane chemistry for the functionalization of zirconia provides limited applications in this case. Because of this, one of the most common methods employed for zirconia functionalization is based on the deposition of a silica-coating layer to which it is possible a further silane application to tailor the surface properties of the NPs. It is worth to notice that the use of silane derivatives implies a condensation reaction with often release of alcohol or halides as by products. It is well known that zirconia, thanks to its surface structure, can efficiently interact with phosphate and phosphonate-based ligands, as evidenced also by the application of zirconia to remove phosphates from water.

Bisphosphonic acids (BPs) are a well-known class of organic molecules that represents the typical scaffold present in the most common drugs to contrast osteoporosis and bone diseases. BPs can be prepared with a series of synthetic approaches involving. We considered the reaction of vinylidenebisphosphonate ester with nucleophiles through Michael or hetero-Michael as a versatile reaction enabling the preparation from a common scaffold of a wide range of possible BPs products starting from diethyl phosphite via formation of methylenebisphosphonate ester. In the present contribution we introduce a versatile approach for the modification of the surface properties of ZrNPs and to some extent also other metal oxide NPs, based on the employment of a family of BPs as derivatizing species. The latter organic molecules can be endowed with specific functional groups in the side chain such as amino, carboxylic acid, alcohol, alkene and

many others and their interaction with ZrNPs turned out to be very efficient, with high grafting density. The functionalization was obtained by simple mixing in aqueous solution the zirconia with the desired BPs under buffered conditions leading to a wide range of surface modified NPs with enhanced colloidal stability due to the presence of negative charges on the surface over a wide range of pH, as demonstrated by ζ -potential measurements. The modified nanoparticles were characterized by IR, TGA, XPS to investigate the grafting density and the loading of the bisphosphonic acid, TEM and SEM to investigate the size and morphologies of the nanoparticles and ^{31}P and ^1H Solid State NMR to investigate the coordination motif of the phosphonate units on the surface. All these analytical techniques demonstrated the strong affinity of the bisphosphonic moiety for the Zr(IV) metal centers. The bisphosphonic acid showed also efficient binding to other metal oxide nanoparticles such as Bi_2O_3 , while interaction with SiO_2 nanoparticles was too weak due to the non-metallic character of the Si centers. The functionalization of metal oxide nanoparticles with bisphosphonic acids represents a straightforward covalent approach for derivatization that is complementary to the typical *tris*-alkoxy-silane or trichloro-silane reagents largely employed for the functionalization of silica and metal oxide nanoparticles.



Student's signature

The woods are lovely, dark and deep,

But I have promises to keep,

And miles to go before I sleep,

And miles to go before I sleep.

By Robert Frost

Acknowledgements

After three years of study and research at University of Ca 'Foscari, the time has come to do a due and deserved thanks to all the people who have contributed in direct and indirect way to prepare doctoral thesis work. My supervisor prof. Patrizia Canton and Prof. Alvise Benedetti and prof. Pietro Riello, giving me the opportunity to carry out the doctoral course in their group research. Specially Prof. Alessandro Scarso, for the welcome and the always alive availability towards the research project and of course the valuable scientific contacts.

The prof. of Institut National de la Recherche Scientifique (Montréal) Fiorenzo Vetrone for his hospitality during mine stay in Montreal and the important help given to the research.

For all the beautiful moments spent inside and above all outside the university; an immense thanks to Gabriele S, Gloria, Andrea, Eleonora, Giulia, Martina, Francesca, Marta, Anna, Michele, Riccardo, Emmanuele, Enrico S, Enrico P, Davide and Titian.

Finally, as always and even more come to this moment, all my family members always present and never too anxious towards me during the latter three years, specially my husband who make me happy.

A sincere thanks to all.

Summary:

1. Introduction	1
1.1 Background.....	1
1.2 Oxide Nanoparticles.....	1
1.2.1 ZrO ₂ Nanoparticles	1
1.2.2 TiO ₂ Nanoparticles.....	2
1.2.3 SiO ₂ Nanoparticles	3
1.2.4 Bi ₂ O ₃ Nanoparticles	3
1.3 Surface modification of Metal Oxides.....	4
1.3.1 Organosilane.....	6
1.3.2 Polymer.....	7
1.3.3 Organophosphate (a) (Phosphonic Acids/ Ester)	9
(b) Bishosphonic Acids/ Ester (BPs).....	10
1.4 Application of Bis-phosphonic Acid (BPs).....	11
1.4.1 Bone Tissue.....	11
1.4.2 Bone Modeling and Remodeling Process	12
1.4.3 Osteoporosis: treatment of bone disease.....	14
1.4.4 Drug targeting: Mechanism of action of Bisphosphonate	15
1.4.5 Systems used for delivery of Bisphosphonates (BPs).....	18
1.5 Nanoparticles in the Biomedical Application.....	20
1.5.1 Zirconium Oxide: a new frontier of Inorganic Biomaterials.....	23
2. Synthesis of the family of Bis-phosphonic (BPs) Acids	24
2. Results and Discussion	24
2.1 Synthesis of BPs Precursors.....	24
2.1.1 Tetraethyl methylenebis(phosphonate) (MBP).....	25
2.1.2 Diethyl (1-(ethoxy(methoxy)phosphoryl)vinyl)phosphonate (VBP).....	26
2.1.3 Tetraethyl ethane-1,1-diylbis(phosphonate) (EBP).....	27
2.2 Synthesis of Sulfur Containing Bisphosphonate Ester.....	31
2.2.1 Tetraethyl (2-(allylthio)ethane-1,1-diyl)bis(phosphonate (BPSAL).....	33

2.2.2 Tetraethyl (2-((3-hydroxypropyl)thio)ethane-1,1-diyl)bis(phosphonate) (BPHPT)..36	
2.2.3 tetraethyl (2-((2-aminoethyl)thio)ethane-1,1-diyl)bis(phosphonate) (AETI).....40	
2.2.4 Benzyl 2-((2,2-bis(diethoxyphosphoryl)ethyl)thio)acetate (BPBTG)49	
2.2.5 Tetraethyl (2-(pentamethylene dimercaptan) ethane-1,1-diyl)bis(phosphonate) (BPPMD)54	
2.2.6 Tetraethyl 2-(octamethylene dimercaptan) ethane-1,1 diyl)bis(hosphonate) (BPOMD)...58	
2.2.7 Tetraethyl (2-(1-hexadecane thiol) ethane-1,1 diyl)bis(phosphonate) (BPHDT).....61	
2.3 Synthesis of Bis-phosphonic Acids.....65	
2.3.1. Methylene Bis-phosphonic Acid (MBP, 1a)66	
2.3.2. Ethan-1,1-diylbis(phosphonic Acid) (EBP, 1b))..... 68	
2.3.3. 2-((3-hydroxypropyl) thiol)ethane-1,1- diyl)bis(phosphonic acid) (BPHPT, 1c)..... 70	
2.3.4. (2-((2-aminoethyl)thio)ethane-1,1-diyl)bis(phosphonic acid) (AETI, 1d).....73	
2.3.5. 2-((2,2-diphosphonoethyl)thio)acetic acid (BPSC,1e)74	
2.3.6. (2-(allylthio)ethane-1,1-diyl)bis(phosphonic acid) (BPSAL, 1f).....76	
2.3.7. (2- (pentamethylene dimercaptan)ethane-1,1- diyl)bis(phosphonic Acid) (BPPMD, 1g).....80	
2.3.8. (2-(octamethylene dimercaptan)ethane-1,1- diyl)bis(phosphonic Acid) (BPOMD, 1h)..... .83	
2.3.9. (2-(1-hexadecane thiol)ethane-1,1- diyl)bis(phosphonic Acid) (BPHDT, 1k).....85	
2.4. Experimental Section.....88	
2.4.1. Tetraethyl methylenebis(phosphonate) (MBP).....89	
2.4.2. Diethyl (1-(ethoxy(methoxy)phosphoryl)vinyl)phosphonate (VBP)).....89	
2.4.3. Tetraethyl ethane-1,1-diylbis(phosphonate) (EBP).....90	
2.4.4. Tetraethyl (2-(allylthio)ethane-1,1-diyl)bis(phosphonate) (BPSAL).....90	
2.4.5. Tetraethyl (2-((3-hydroxypropyl)thio)ethane-1,1-diyl)bis(phosphonate) (BPHPT) 91	
2.4.6a. Synthesis of 2-(Boc-amino) ethanethiol.....91	
2.4.6b. Tert-butyl (2-((2,2-bis(diethoxyphosphoryl)ethyl)thio)ethyl)carbamate (BPBAT)....92	
2.4.6c. Tetraethyl (2-((2-aminoethyl)thio)ethane-1,1-diyl)bis(phosphonate) (BPAET)...92	
2.4.7. Benzyl 2-((2,2-bis(diethoxyphosphoryl)ethyl)thio)acetate (BPBTG)93	
2.4.8. Tetraethyl (2-(pentamethylene dimercaptan) ethane-1,1-diyl)bis(phosphonate) (BPPMD).....93	
2.4.9. Tetraethyl 2-(octamethylene dimercaptan) ethane-1,1 diyl)bis(hosphonate (BPOMD)..94	

2.4.10. Tetraethyl (2-(1-hexadecane thiol) ethane-1,1 diyl)bis(phosphonate) (BPHDT)..	94
2.4.11. Methylene Bisphosphonic Acid (MBP, 1a)	95
2.4.12. Ethan-1,1-diylbis(phosphonic Acid (EBP, 1b)).....	95
2.4.13.2-((3-hydroxypropyl) thiol)ethane-1,1- diyl)bis(phosphonic acid (BPHPT, 1c)	96
2.4.14. (2-((2-aminoethyl)thio)ethane-1,1-diyl)bis(phosphonic acid) (AETI, 1d).....	96
2.4.15. 2-((2,2-diphosphonoethyl)thio)acetic acid (BPSC,1e)	97
2.4.16. (2-(allylthio)ethane-1,1-diyl)bis(phosphonic acid) (BPSAL, 1f).....	97
2.4.17.(2-(pentamethylene dimercaptan)ethane-1,1- diyl)bis(phosphonic Acid) (BPPMD, 1g).....	98
2.4.18. (2-(octamethylene dimercaptan)ethane-1,1- diyl)bis(phosphonic Acid) 1h.....	98
2.4.19. (2-(1-hexadecane thiol)ethane-1,1- diyl)bis(phosphonic Acid) (BPHDT, 1k).....	99
3. Synthesis of Metal Oxide Nanoparticles.....	100
3.1. Synthesis of ZrNPs.....	100
3.2. ZrNPs Characterization.....	100
3.3. Synthesis of TiNPs.....	102
3.4 Characterization of TiNPs.....	102
3.5 Synthesis of FeNPs.....	103
3.7 Characterization of BiNPs.....	103
4. Interaction of bis-phosphonic acid with Metal Oxide.....	104
4. Results and Discussion.....	104
4.1 Analysis and study of the interaction between buffer solutions and inorganic NPs.....	104
4.1.1 Buffer-Zirconia interaction (ZrO ₂).....	105
4.1.2 Silica-buffer interaction (SiO ₂).....	109
4.1.3 Buffer-Bismuth interaction (Bi ₂ O ₃).....	112
4.2 Analysis and study of the interaction between the nanoparticulate supports and the bis- and mono-phosphonic organic molecules under examination.....	112
4.2.1 Methylene Bis-phosphonic acid (MBP, 1a).....	113
4.2.1.1 Zirconium oxide (ZrO ₂).....	114
4.2.1.2 Silicon oxide (SiO ₂).....	120
4.2.1.3 Bismuth oxide (Bi ₂ O ₃).....	123
4.2.1.4 Titanium Oxide (TiO ₂).....	126

4.2.2 Functionalized bis-phosphonic acids.....	127
3.2.2.1 Ethane-1,1-diylbis(phosphonic acid) (EBP, 1b).....	127
4.2.2.2. (2-((2-aminoethyl)thio)ethane-1,1-diyl)bis(phosphonic acid) (AETI, 1d)..	129
4.2.2.3. 2-((2,2-diphosphonoethyl)thio)acetic acid (BPSC).....	130
4.2.2.4 2-(2-propene- 1-thiol) ethane-1,1- diyldiphosphonic acid (BPSAL).....	133
4.2.2.5 Comparison of the affinity between the various BPs and ZrNPs.....	134
4.2.3 Commercial monophosphate acids.....	136
4.2.3. 3-phosphono-1-propanoic acid (AFP).....	137
4.2.3. 2 Acid (2-aminoethyl) phosphonic acid (AEFO).....	138
4.2.3. 3 Comparison of affinity of monophosphonates and bisphosphonates against ZrNPs...	139
4.3 Study and determination of the MBP-NPs interaction in aqueous solution.....	140
4.3.1 Zirconium oxide.....	145
4.3.2 Bismuth oxide.....	147
4.3.3 Silicon oxide.....	148
4.4 Study of the interaction between BPs and MPs with ZrNPs for applications in the biomedical field.....	150
4.4.1 PBS (Phosphate-buffered saline)	152
4.4.2 Plasma.....	154
4.5 Use of plasma components such as DDS.....	156
4.5.1 Methylene bis-phosphonic acid.....	156
4.5.2 Indomethacin and Nitrofurantoin monohydrate.....	157
4.6 Study of the loading and release in aqueous solution of drugs from ZrNPs and SiNPs through quantitative ¹ H NMR analysis.....	159
4.6.1 Indomethacin.....	161
4.6.2 Nitrofurantoin monohydrate.....	168
4.7 Experimental Part.....	171
4.7.1 Instrumentation.....	171
3.7.2 Experimental procedures.....	171
5. Physical Characterization of Metal Oxide Surface Modification.....	173
5. Experimental Section.....	173

5.1. Materials & Methods.....	173
5.2 Surface Modification of Metal Oxides (ZrO ₂ , TiO ₂ , SiO ₂ , Bi ₂ O ₃).....	176
5.3. Result and Discussion.....	176
5.3.1. Characterization of BPs@ZrNPs.....	176
5.3.2. Characterization of MBP@ BiNPs.....	187
5.3.3. Characterization of MBP@ TiNPs.....	187
5.4 Application of thiol bearing BPs as linker of mMZN and AuNPs.....	189
6. Optical properties of Neodymium doped Zirconia NPs.....	191
6.1 Materials and metods.....	191
6.1.2 Synthesis of Nd ³⁺ -doped ZrNPs.....	191
6.1.3 Synthesis of water soluble Nd ³⁺ -doped ZrNPs	192
6.1.4 Characterization techniques.....	192
6.2 Results and discussion.....	192
7. Conclusions.....	194
8. Reference	195

CHAPTER 1

Introduction

1.1 Background

Nanoparticles (NPs) are attracting considerable interest in both research and application fields than the corresponding bulk materials because of their unique mechanical behavior, [1] phase transition temperature, [2] magnetic behavior, [3] electronic [4] or optical properties [5] and along with hydrodynamic properties of NPs suspended in solvents. Advanced functionalized Nanoparticles such as inorganic oxides with excellent properties have opened the door to various innovations in biology, chemistry, and physics, for example the latest developments can be found in chromatography, [6] sensing, [7] drug release, [8,9] and solar cells. [10,11] The surfaces of metal oxides NPs have the tendency to adsorb adventitious organic materials readily to lower the free energy of the interface between the metal oxide and the ambient environment, [12] which have a significant influence on the stability of nanostructures of metal oxides; the organic material can act as a physical or electrostatic barrier against aggregation. In the field of biomedical applications, NPs must be predictable and controllable and deliver the desired result with minimum cytotoxicity. [13] To meet these criteria careful tailoring of the surface properties of NPs to allowing stabilization, specific targeting and recognition of biochemical species is mandatory. In vivo, NPs must avoid non-specific interactions with plasma proteins (opsonization) and either evade or allow uptake by the reticuloendothelial system (RES) depending on the application, to reach their intended target efficiently. They must also maintain colloidal stability under physiological conditions, preferably including a wide range of pH. NPs carrying a payload, such as drug molecules or DNA for gene therapy must avoid premature release. Chemical modification of the NP surface is necessary for specific interactions with biomolecules of interest.

1.2 Oxide Nanoparticles

1.2.1 ZrO₂ Nanoparticles

Zirconium oxide or zirconia (ZrO₂) is an interesting, useful and resourceful metal oxide in many different application fields, thanks to its good mechanical, thermal, functional and sometimes unique properties. [14,15] This great versatility it comes from its different crystal modifications. From structural and crystallographic point of view, zirconia has three well-known polymorphs with stabilization thermal range: monoclinic (*m*) until 1170 °C, tetragonal (*t*) from 1170 °C to 2370 °C and cubic (*c*) from 2370 °C until the melting point at 2680 °C. At very high pressure other less studied phases (especially orthorhombic) could be obtained. Like Ti, Zr is protected by a thin passive layer of ZrO₂ under atmospheric conditions. The oxide layer is virtually inert, it is stable in most acids and basic solutions. The bandgap of ZrO₂ is 5 - 7 eV, [16] which means that the material shows rather insulating properties and light of lower wavelength is necessary for excitation compared to TiO₂. These materials are commonly used as thermal barrier coatings

(TBCs), [17] dental and bone prostheses, [18,19] high resistance laminates,[20] solid oxide fuel cells (SOFCs), [21,22] gas sensors, [23,24] optical devices [25,26] and catalysts.[27]Zirconium oxide could be considered as one of the most fascinating oxide and it could offer some advantages, such as biocompatibility and chemical inertia, [28] interesting properties for in vivo biomedical application and drug loading process.



Figure 1.1: Examples of zirconia engineering applications

1.2.2 TiO_2 Nanoparticles

TiO_2 NPs are the most studied metal oxide nanoparticles. [29] The most common crystal phases are anatase (tetragonal, $a = b = 3.782 \text{ \AA}$, $c = 9.502 \text{ \AA}$), rutile (tetragonal, $a = b = 4.584 \text{ \AA}$, $c = 2.953 \text{ \AA}$) and brookite (orthorhombic, $a = 5.436 \text{ \AA}$, $b = 9.166 \text{ \AA}$, $c = 5.135 \text{ \AA}$). [30]

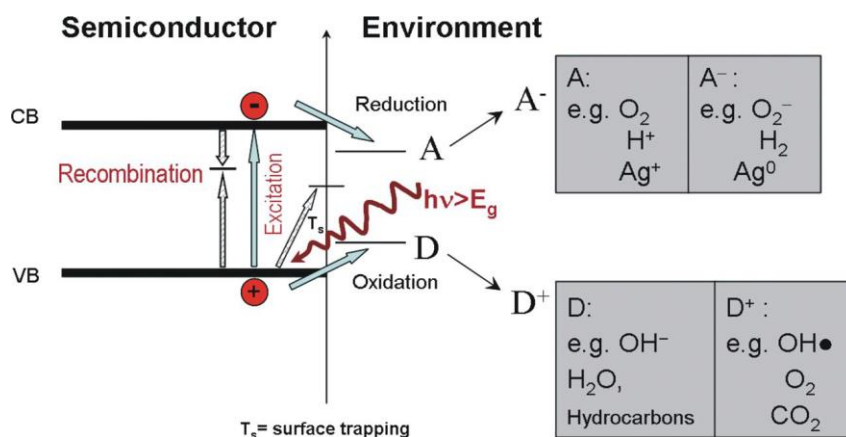


Figure 1.2: Scheme of photo-induced processes at a TiO_2 semiconductor/electrolyte interface. Light ($h\nu$) excites a valence band electron to the conduction band. e^- and h^+ can react with the environment.

Acceptor (A) and donor (D) species are reduced and oxidized (= photocatalytic reactions). Competing with the reaction is recombination and trapping of electrons and holes (= reducing photocatalytic efficiency). The grey boxes give typical reactants and reaction products in photocatalytic reactions on TiO₂

These nanoparticles have a high refractive index (2.5 - 2.6) and widely used as pigments and fillers in paints, coatings, and in the paper industry. Unlike SiO₂, TiO₂ is a n-type semiconductor and has an indirect optical bandgap for anatase of 3.2 eV, for rutile of 3.0 eV, and amorphous material is reported to have a mobility gap of about 3.2–3.5 eV.[31] TiO₂ anatase is used extensively as self-cleaning coatings, catalysis, optical industry, gas sensing.[29, 32] and used in energy conversion, for instance in dye-sensitized solar cells.[33] TiO₂ is applied as photocatalyst, irradiation with UV- light is energetically suited to generate electron-hole pairs in the material. The band diagram of an illuminated semiconductor under irradiation is schematically shown in Figure 1.2

1.2.3 SiO₂ Nanoparticles

Silica NPs are cheap, have a high hardness and good chemical stability. SiO₂ NPs can be synthesized in aggregated powders form by precipitation methods and flame processes. In 1971, Ulrich reported a flame hydrolysis method to obtain SiO₂ nanoparticles by combustion of SiCl₄. [34] This high-temperature method leads to powder of aggregated SiO₂ NPs of approximately 50 nm. Precipitated silica is produced by precipitation from a solution containing silicate salts, for example, by addition of H₂SO₄. In case of colloidal dispersions form, sols of silica spherical NPs are generally synthesized by sol-gel process in basic medium or in reverse micro-emulsions.[35] In 1968, Stöber et al. proposed an innovative synthesis by a sol-gel route based on the hydrolysis and condensation of tetraethoxysilane (TEOS) in ethanol with ammonia as a catalyst.[36] This method leads to the formation of monodisperse and electrostatically stabilized silica particles with diameters ranging from 50 nm to 1 μm. Since the synthesis of the M41S family by templating techniques using surfactant micelles, [37] mesoporous silica has received much attention in diverse areas, such as catalysis, adsorption, separation, and chromatography. Controlling the ordered arrangement and apertures of mesopores has been investigated by changing the templates and preparation conditions. [37-42]

1.2.4 Bi₂O₃ Nanoparticles

Bismuth oxide (Bi₂O₃) is well-known for its optical and electrical properties such as dielectric permittivity, refractive index, large energy band gap, photoconductivity and photoluminescence. [43] The applicability of Bi₂O₃ extends from fireworks to oxygen gas sensors and solid oxide fuel cells [44-49]. Interest in Bi₂O₃ is also increasing because it shows similar properties as lead (II) oxide (PbO); namely, the ability to form transparent glasses with a high refractive index useful in optical telecommunication and processing devices [50,51] and in ecological lead-free glasses for several applications [52,53]. Furthermore, there is a recent great interest in the

properties of Bi_2O_3 at high temperatures and high pressures. Under these conditions phase transitions to various polymorphs, which are metastable at ambient conditions, have been observed and whose properties could be interesting for several applications. [54,55] Bi_2O_3 has five crystallographic polymorphs depending on temperature. At room temperature $\alpha\text{-Bi}_2\text{O}_3$ has a monoclinic crystal structure (a complex structure with layers of oxygen atoms with layers of bismuth atoms between them and a δ -phase (cubic) and an ε - phase (triclinic)).

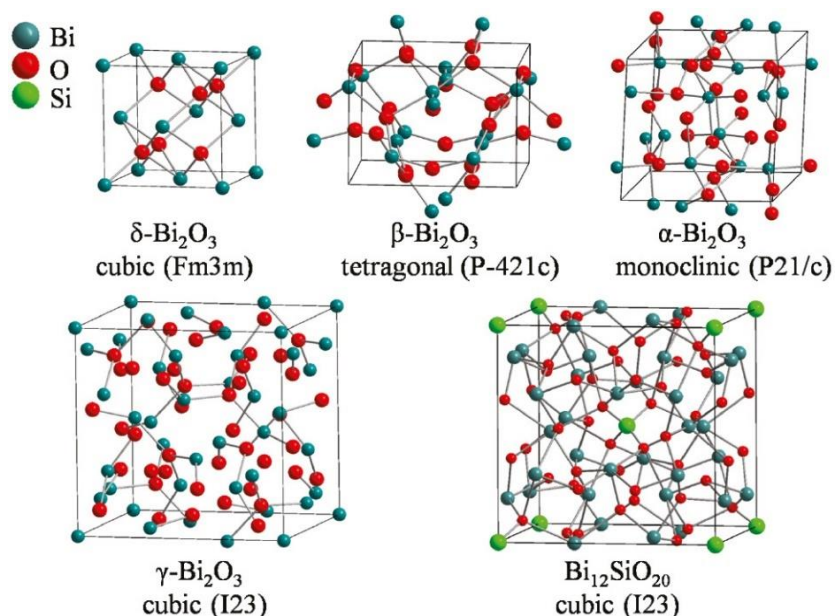


Figure 1.3: Bismuth oxide clusters

$\beta\text{-Bi}_2\text{O}_3$ has a structure related to fluorite [56] whereas $\gamma\text{-Bi}_2\text{O}_3$ has a structure related to that of sillenite ($\text{Bi}_{12}\text{SiO}_{20}$) [57] and $\delta\text{-Bi}_2\text{O}_3$ has a defective fluorite -type crystal structure in which two of the eight oxygen sites in the unit cell are vacant. [58] Among these phases, $\alpha\text{-Bi}_2\text{O}_3$ and $\delta\text{-Bi}_2\text{O}_3$ are the stable phases, while rest other phases are metastable. The $\delta\text{-Bi}_2\text{O}_3$ is known for its high conductivity among all other phases, which make it best material in solid oxide fuel cell. Although its application as oxide ion conductor is limited, because it is only stable in the narrow temperature range. Recently, the stability of $\delta\text{-Bi}_2\text{O}_3$ is reported to be increased by various kind of dopants such as Er_2O_3 and Y_2O_3 etc. Bi_2O_3 NPs can easily synthesize from a solution of bismuth nitrate pentahydrate in ethylene glycol by a hydrolysis solvothermal route at temperature of 120-150°C. Bi_2O_3 is an advanced functional material with potential applications such as electronic material, burning rate catalyst, photocatalytic decomposition material, optical material, medical composite material and anti-radiative material. Bi_2O_3 is used as an additive in paints. Bi_2O_3 also used as a composite in polymers, rubber, fireproofing papers, disinfectant and have applications in medicine and artificial bone imaging.

1.3 Surface modification of Metal Oxides

There are many properties of a substrate that can be changed by modification of the surface with organic monolayers. While the ability to change surface, wetting is the property most widely studied, there are other key properties of inorganic materials that can be modified with organic monolayers, such as chemical functionality, electronic, and optical properties.

There are many accounts in the literature where the surface energies of substrates have been modified by attaching organic monolayers. [59-61] One common theme is the control of hydrophobicity and hydrophilicity of a surface. [62, 63] For nanoparticle modification, organic monolayers can completely change the solubility properties of a given nanoparticle. [64] This can allow for previously water-insoluble particles to become completely soluble in aqueous conditions, (Fig. 4). Or, for larger particles, the ability to suspend them for long periods of time in various media is important for depositing homogeneous, well-dispersed films of these particles or for doing further chemistry.

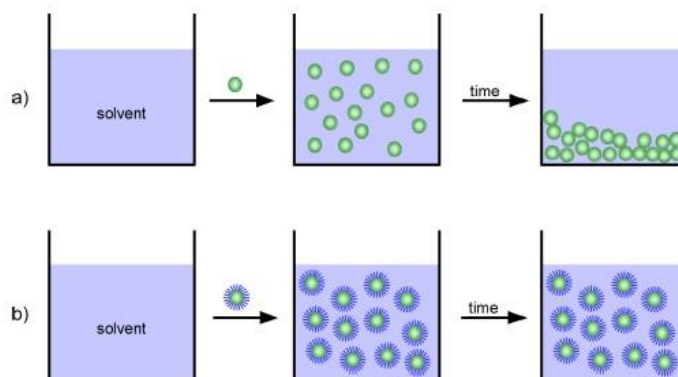


Figure 1.4: Illustration of how monolayers on nanoparticles can affect their compatibility with solvents. a) Loading of bare nanoparticles into a solvent where the nanoparticles settle after a specific period of time, and b) loading of monolayer protected nanoparticles into the same solvent where after the same amount of time the nanoparticles are still well-dispersed in solution.

Moreover, the addition of a monolayer to a material can change that materials' surface chemistry. It may be possible to enable new chemistry which previously would have been impossible by altering the chemistry on a surface. Many organic reactions, such as nucleophilic substitution, oxidation/reduction, and free radical halogenation can be performed on surfaces in a manner like the analogous bulk media. While in principle many different types of reactions can be performed on and off of surfaces, in practice most reactions are performed on monolayers with terminal carboxyl, amino, or hydroxyl groups, and are affected by the following factors: 1 solvent effects (the solvation of the functional groups on the monolayer can differ from that in the bulk), steric effects (the molecules in monolayers tend to have a particular orientation with respect to the surface and/or conformation and this may affect sterically demanding reactions), and electronic effects (close proximity of other functional groups may affect reactivity through field effects or hydrogen bonding). Progress is continually made in the field of monolayer science. Particularly, the use of metal oxides and surface modification, which can often be

inexpensive and nontoxic (though not true of ITO), in a variety of applications is becoming an important area of research and development. For example, the groups of Halik [66, 67] and Marks [68-70] have used monolayers of phosphonic acids and silanes, respectively, to significantly improve the properties, such as operating voltage and flexibility, of organic-based transistors. Schwartz and coworkers, at Princeton, have shown that coating titanium implant materials with monolayers of phosphonic acids can help their adhesion to biological tissue as well as increase bone-growth on their surface. [71, 72]

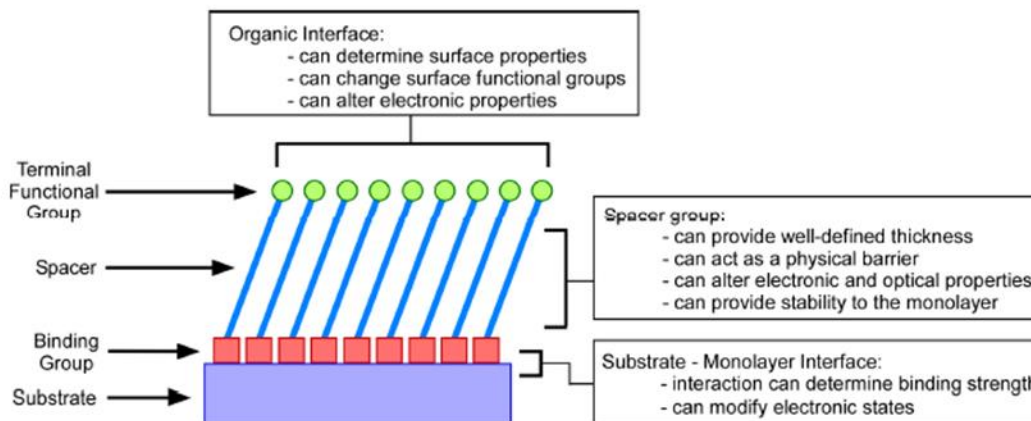


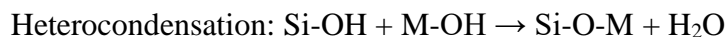
Figure 1.5: Schematic of an organic monolayer attached to a substrate, the various constituents of the monolayer, and the role that each constituent plays. [65]

Monolayers have been used to significantly protect metals, such as iron, from corrosion. [73] Numerous groups have shown an ability to tune the electrodes of organic electronic devices by use of a monolayer, which have the potential to improve their transport properties. [74-77]

1.3.1 Organosilane

The most common approaches for functionalization of metal oxides either are chelation based, including the use of β -diketones, β -ketoesters, and carboxylic acids. [78, 79] A major approach for the surface functionalization of metal oxides use the covalent attachment of organic coupling molecules, which may form monolayers on the surfaces. Over the last few decades, organosilanes are the most widespread grafted molecules. The chemical formula of organosilanes is $R_nSiX_{(4-n)}$ with $n = 1, 2, \text{ or } 3$. R is an organic group linked to Si by a Si-C bond, which is stable toward hydrolysis, and X a hydrolysable organic group, in most cases ethoxy, methoxy, or chloro. These molecules can be grafted onto many oxide surfaces, for example, SiO_2 , Al_2O_3 , and TiO_2 . The organosilanes can react with surface OH groups of the oxides via condensation reactions, resulting in the formation of a covalent bond between the coupling agent and oxide substrate. [80, 81] An example of an important coupling agent is 3-(trimethoxysilyl) propyl methacrylate (γ -MPS), [82] which is used in a variety of applications to promote the adhesion of

polymers to inorganic surfaces such as glass or metal oxide particles. However, the stabilization of R-SiX₃ coupling molecules on metal oxide surfaces (ZrO₂ and TiO₂) is mainly caused by the lateral cross condensation of the silanes, providing Si-O-Si bonds by homocondensation, whereas modification with R₃-SiX (hetercondensation-generation of Ti/Zr-O-Si bonds) results in less-stable layers, [83] due to the sensitivity of the Ti/Zr-O-Si bonds toward hydrolysis.[84]



The competition between these two reactions governs the nature and homogeneity of the grafted layer. It depends on the water content of the medium, the temperature and the nature of the oxide support. [85, 86] In absence of water, only partial monolayers are formed. A small amount of water is required to form a dense monolayer, which may be a polysiloxane layer linked to the surface by Si-O-M bonds. As the water content increases, homocondensation may lead to the formation of 3-dimensional polysiloxane layers, up to tens of nanometer thick. [87, 88].

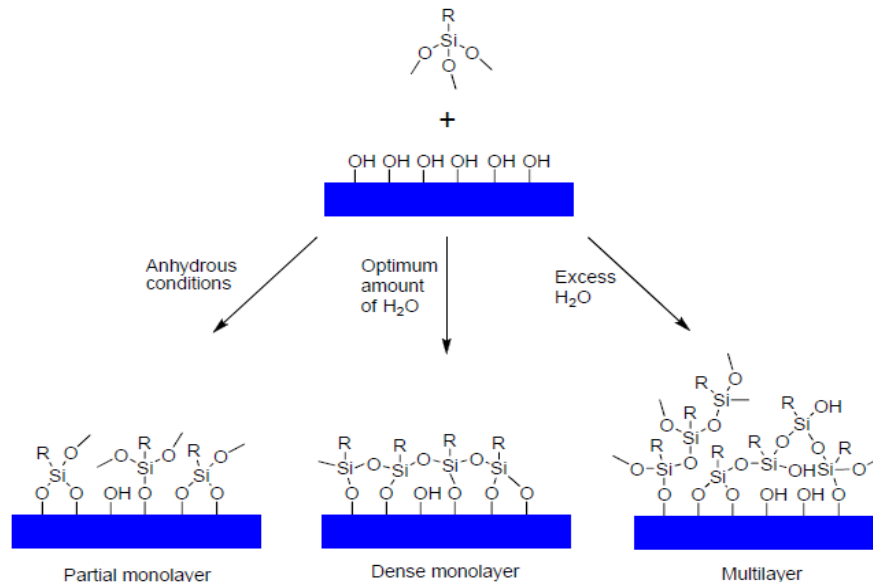


Figure 1.6: Schematic representation of the structure of organotrialkoxysilane layers for different water contents of the grafting medium. [88]

Therefore, grafting is usually performed in organic medium with a strict control of the water content in the solvent and adsorbed onto the surface. In addition, most organosilanes are not water soluble. This, as well as the risk of anarchic homocondensation, makes the grafting of organosilanes in aqueous medium difficult. Because of decreased chemical stability of the silane bond from Si-O-Si-R \geq Zr-O-Si-R > Ti-O-Si-R, the use of organosilanes for the functionalization of transition metal oxide provides limited applicability. [89] It is also important to note that surface modification by chloro- or alkoxy silanes leads to HCl or alcohol byproducts, which can alter the nanoparticle. For example, magnetic ferrite nanoparticles were found to disintegrate immediately because of the liberation of HCl, which is known to dissolve ferrite materials.

Another drawback to silanes is that to ensure their long-term integrity they need to be stored in anhydrous conditions as they may self-condense over time.

1.3.2 Polymer

Even though polymers can be used to improve the biocompatibility of the transition metal surface and to provide a wide range of functionalities for further modification, few publications

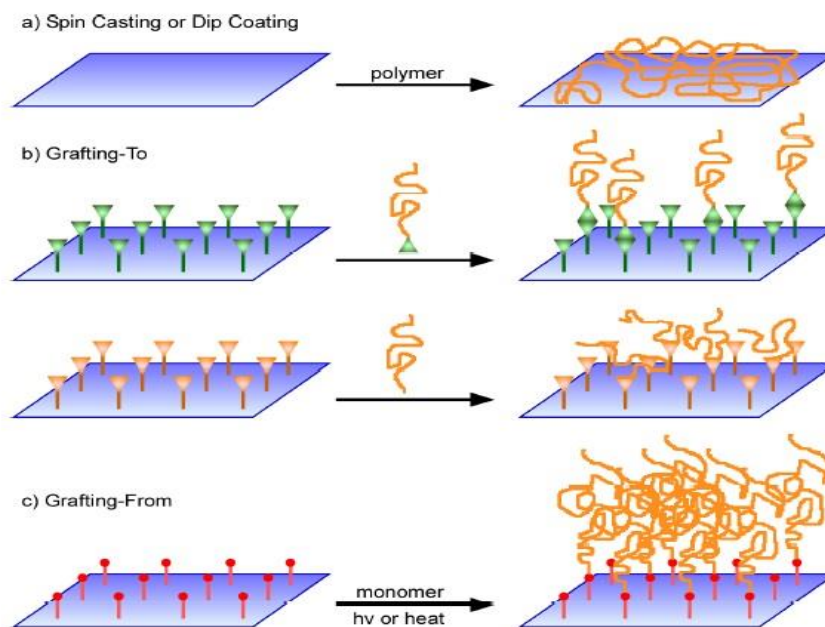


Figure 1.7: Two ways in which polymers can be attached to a surface: b) ‘grafting to’ approach where already formed polymers are attached to the surface via some sort of crosslinking group; c) ‘grafting from’ approach where polymers are initiated at and grown from the surface. In a) the polymer is not chemically bound to the surface. Figure adapted from Dyer.

have been made that report the bonding (physisorption) of a polycationic polymer onto a negatively charged titanium surface. [90] Beside such physical adsorption, there are different methods to covalently bind a polymer to a surface. For example, the “grafting onto” method requires a polymer with a special functionality to react with appropriate surface sites. So, this approach is restricted to tailored polymers. Furthermore, the layer thickness and grafting density are limited. [91] In the “grafting from” method, the polymer is directly grown from an initiator monolayer at the surface by a chain growth mechanism. In literature there are examples of grafting from using free radical, [92] controlled radical, [93] anionic, [94] cationic, [95] or transition metal catalyzed [96] polymerization from the surface. However, the initiator monolayer must be appropriate and requires extensive synthetic efforts. Encapsulation provides another way to obtain polymer-coated NPs. The monomers are adsorbed on the NPs surface, and then the polymerization takes place in the adsorbed layer, to finally form polymer-coated NPs.

However, this method has several drawbacks: depending on the experimental conditions, individual or multiple NPs can be covered by the same shell, and isolated polymer particles can be formed. [97]

1.3.3 Organophosphate

(a) (Phosphonic Acids/ Ester)

Since the late 1970s, organophosphorus acids such as phosphonic acids (PAs) and their derivatives (salts and esters) are widely used to control surface and interface properties, especially to modify metal oxide surfaces.[98] PAs are superior in many cases because homocondensation of P–OH and P–O-bonds does not occur at mild conditions and/or in aqueous conditions but interact exclusively with surface hydroxyls or coordinatively unsaturated surface metal atoms of metal oxides such as TiO₂,[99,100] ZrO₂,[99] Ta₂O₅,[101] Y₂O₃,[102] Fe₃O₄,[103] lanthanide oxides,[104] and perovskites (BaTiO₃) [105] to form P-O-M bonds. The fact that the quality of modification is independent of the amount of water present means that less stringent conditions need to be followed when using phosphonic acids with respect to silanes. The nature of the P-O-M bond can vary from an ionic to covalent character as a function of the nature and oxidation state of the metal ion and therefore influences the stability of the phosphonic acid attachment to the surface. In fact, very strong metal/phosphonate interaction are observed in the case of metal ions of high oxidation state (tetravalent and higher). This explains the increasing interest in surface/ interface modification by PAs, [106–109] which appear to be a valuable alternative to the commonly used organosulfur compounds (thiols, disulfides), [110] organosilicon compounds (e.g. trialkoxy- and trichlorosilanes) [111] or carboxylic acids. [112] Carboxylic acids have been used successfully to bind to different metal oxides, but usually through a variety of binding moieties, including as an uncoordinated anion, a monodentate ligand, a bidentate chelate or a bridging bidentate. [113] Despite the fact that high-coverage monolayers can be prepared utilizing carboxylic acids, the combination of binding modes and their relative weakness means that the monolayers are often not bound strongly to the surface and can be easily removed, sometimes by simple rinsing in solvents. [114] Additionally, the presence of additional polar sites on the carboxylic acid molecules can result in competition for surface sites, thus preventing well-organized, high coverage monolayers. [113]

The hydrolytic stability of phosphonate monolayers is significantly higher than that of carboxylate monolayers, [115, 116] likely reflecting the higher covalent character of interfacial M–O–P bonds compared to M–O–C bonds and the higher denticity of phosphonate groups. The surface modification of titania films with dodecylphosphonate, mercaptosuccinic acid, and thioglycolic acid showed that monophosphonates bind very strongly to the surface, whereas the carboxylic compounds were quickly released upon a pH change. [117] The carbon-phosphorus

bond shows very high chemical stability, higher than silicon-carbon, and furthermore, provides the opportunity for a multitude of organic functionalities due to the versatility of phosphorus chemistry. [118] An example of the extraordinarily high hydrolytic stability (between pH 1 and pH 12) can be found for magnesia zirconia chromatographic separation phases. [119] The superior stability makes this class of materials very interesting for applications under very harsh conditions, for example, highly durable separation media for nuclear fuel reprocessing has recently been suggested. [120] Another reason for the high stability of these phases is the multiple tridentate bonding which was shown by ^{17}O NMR. [121]. The hydrolytic stability of octadecyl PA monolayers on TiO_2 or ZrO_2 particles at pH values ranging from 1 to 10 was also found to be better (particularly at pH 1) than that of octadecylsilane monolayers, despite the numerous Si–O–Si bridges between the silane molecules which help increase the stability of these layers. [122]

(b) Bishosphonic Acids/ Ester (BPs)

Even if, as reported above, phosphonic acids (PAs) have advantage over silanes for surface modification of versatile oxide nanoparticles. there is question as to the surface coverage that can be obtained with phosphonic acids. phosphonic acids (PAs) initially adsorb randomly on surface and consequently formed ordered monolayer with higher surface concentration whereas silanes show an insular growth with cross-linking of neighboring molecules. [123] The maximum surface coverage is limited by the amount of available adsorption sites (OH groups on the nanoparticle surface) i.e., the density of -OH groups determine the maximum number of adsorbates (PAs) since they do not form intramolecular bonds as like siloxanes. [124] Furthermore, a drawback of the use of PAs is the possible dissolution-precipitation of the metal oxide with the phosphonic acid. This reaction leads to the formation of a crystalline phase of metal phosphonate (fig. 8). The competition between surface modification and dissolution-precipitation has been evidenced for high surface area metal oxide substrates (nanoparticles), even for a highly stable oxide such as titania. [125] However, dissolution-precipitation can be in most cases avoided by carefully choosing the reaction conditions. [125, 126]

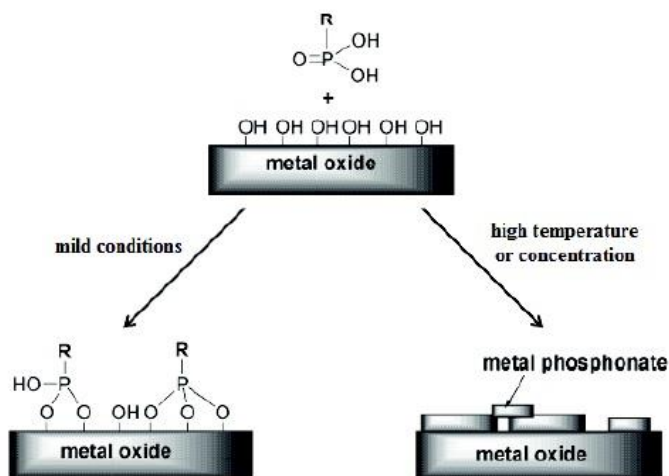


Figure 1.8: Competition between surface modification and dissolution-precipitation of a phosphonic acid with a metal oxide surface depending on the experimental conditions. [88]

The stability of PA monolayer under physiological conditions is a controversial issue. Mani et al. reported that dodecylphosphonic acid monolayer deposited from aqueous solutions and simply rinsed with water (without any thermal annealing) exhibited poor stability in Tris-buffered saline at 37 °C compared to dodecylthiol monolayer on Au or dodecyltrichlorosilane monolayer on Ti. [127] Conversely, Bhure et al. found that octadecylphosphonic acid deposited on Cr–Co alloy from THF solutions at 35 °C were strongly bound to the surface and were not significantly desorbed after 14 days in a phosphate buffered saline (PBS) solution (pH 7.4) at 35 °C. [102] Similarly, Jo et al. [128] praised the robustness of long chain (C11) carboxy-terminated PA on ITO in pure water, under ambient air conditions and in PBS solution.

Based on the above results, to optimize the stability of functionalized nanoparticle in physiological environment we can introduce multiple metal-Oxygen-phosphorus bonds using a bisphosphonic acid that can contribute both phosphonic acid groups results in a durable functionalization. Recent works suggest that the use of gem-bisphosphonate anchors can lead to particularly stable bonding to the surface. [129–132] The surface modification of stainless steel with 1,1-bisphosphonic acid was found to be stable for months in ultrapure water at 50 °C and were not significantly degraded after 3 h in PBS solutions of pH 1–12. [129] The stability of films anchored by bisphosphonate molecules could be ascribed to the formation of multilayers that resisted desorption even in the presence of phosphate ions. [133] Although, gem-bisphosphonic acids (BPs) and phosphonates have similar chemical reactivity but show major differences. The bis-phosphonic group increases the affinity for oxidized surfaces [134,135] compared to mono-phosphonates [136] and increases the polarity of the molecule, probably by increasing aqueous solubility. Mono-phosphonates/ phosphates can form SAMs on titanium but can't form on silicon when dissolved in water. [137] Comparatively, BP allows easy aqueous deposition of monolayers on various materials [138] when mono-phosphonic acid is mostly deposited in an organic medium. [139-141]

1.4 Application of Bis-phosphonic Acid (BPs)

1.4.1 Bone Tissue

Bone is a complex connective tissue that performs many roles in the body such as structural support and movement, protection for vital organs, and mineral storage, and provide the site for blood cell production as bone marrow houses hematopoietic cells generating red blood cells, leukocytes, and platelets. Macroscopically, bone can be divided into two part: an inner part (trabecular, cancellous or spongy bone) and an outer part called cortical or compact bone, which makes about 80% of the total weight of the skeleton. Microscopically, cortical and spongy bone in the adult skeleton are made of well-ordered parallel collagen fibers, organized in a lamellar pattern made of bone structural units (BSUs). [142] In cortical bone called osteons i.e. cylinders

made of concentric lamellae where in the center there is a canal of nutrient blood vessels. Bone tissue is a dynamic tissue as it is continuously remodeled through anabolic and catabolic processes that allow it to adapt during the life of the body. It made up of different type of bone cell such as osteoblasts, osteocytes and osteoclasts. They are dispersed in an extracellular matrix of protein nature composed in turn by a component of organic nature (~ 30% of dry weight of which 90% of collagen and glycoproteins) and a mineral component of impure hydroxyapatite (60% of dry weight).

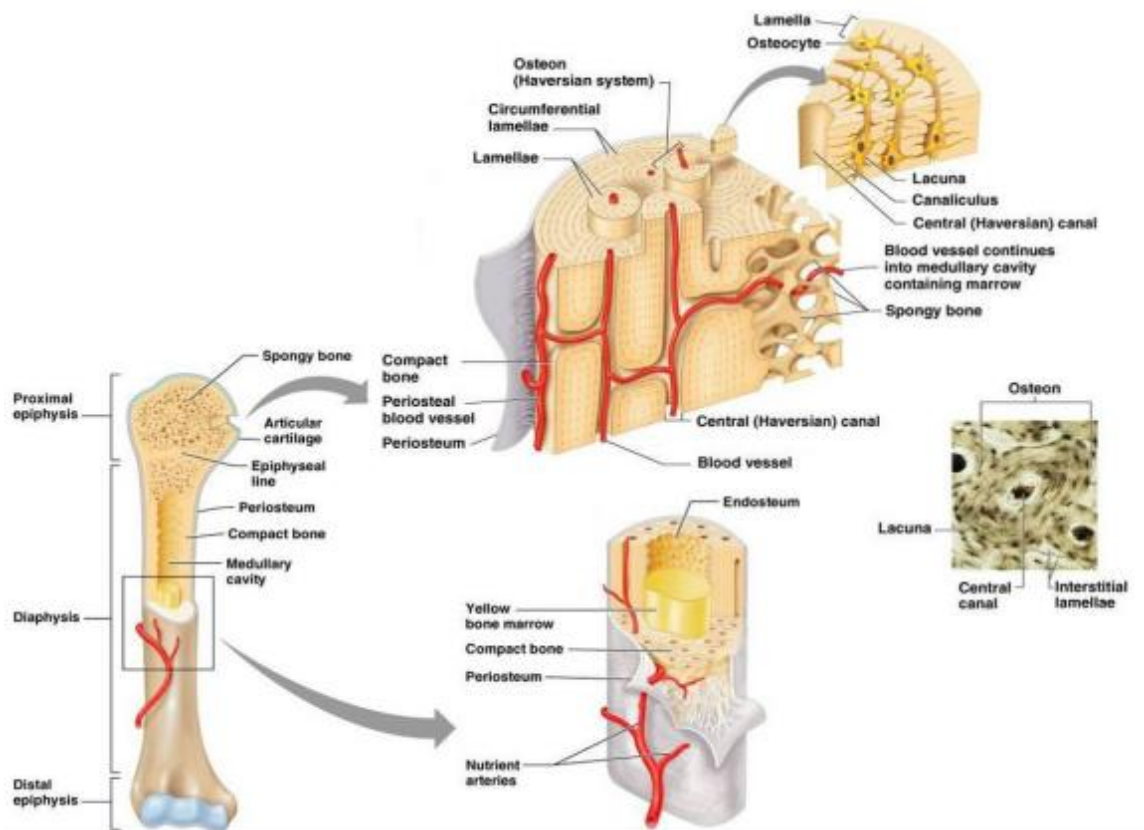


Figure 1.9: Bone Morphology

Bone is not uniformly solid but consist of flexible matrix. The matrix is hardened by the binding of crystal lattice of biological hydroxyapatite (HAP), of formula $\text{Ca}_{10}(\text{PO}_4)_6(\text{OH})_2$, presents many elements different from calcium and the anionic H_2PO_4^- unit, for example magnesium, fluorine, sodium, strontium and carbonate ion. These elements cause a reduction in the crystallinity of the HAP and are present internally to the crystal lattice or externally absorbed on the surface of the crystals [143]. The HAP crystals have the form of thin prisms with a hexagonal section with a thickness of 2-3nm and a variable length from 20 to 50nm (Figure. 1.9).

1.4.2 Bone Modeling and Remodeling Process

Bone remodeling is a highly complex biological process by which old bone is replaced by new bone to repair any microfractures present in the tissue and to ensure optimal adaptation structural structure of the organism. This cyclic process comprised of three phases: (1) initiation of bone resorption by osteoclasts, (2) the transition or reversal period from resorption to new bone formation, and (3) the bone formation by osteoblasts [144, 145]. It occurs due to coordinated actions of osteoclasts, osteoblasts, osteocytes, and bone lining cells which together form the temporary anatomical structure called basic multicellular unit (BMU) [146–148]. This process is controlled by local (e.g., growth factors and cytokines) and systemic (e.g., calcitonin and estrogens) factors that all together contribute for bone homeostasis. The osteoblasts (Figure.11.1, a) are cuboidal cells located along the bone surface comprising 4–6% of the total cells in the tissue. [149] They obtain from the differentiation of mesenchymal stem cells (MSC) consequently to the action of some transcription factors (intracellular proteins) and to the subsequent activation or inhibition of certain genes. The synthesis of bone matrix by osteoblasts derives from deposition of organic matrix which secrete mainly type I collagen proteins and its subsequent mineralization into two phases: vesicular and fibrillar. [150,151] At the end of the tissue remodeling process, some osteoblasts are incorporated into the bone matrix. becoming osteocytes (a structural and morphological change of the cell follows).

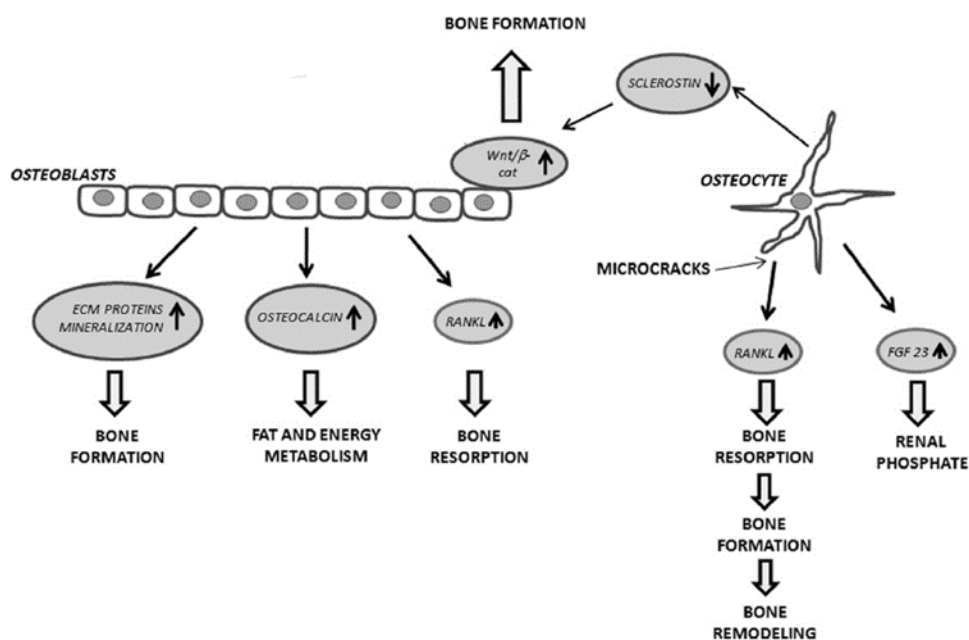


Figure 1.10: Schematic representation of the formation of osteoblasts and osteocytes

The osteocytes (Figure.1.11, b) comprise 90-95% of the total bone cells and derive from the osteoblastic differentiation of the MSC. This type of cell is of major importance in the initiation of the remodeling mechanism: the formation of micro-fractures in the bone tissue determines the osteocytic apoptosis and the subsequent expression of some osteoclastogenesis activators

(development of the osteoclasts) necessary for the resorption of the damaged bone and the consequent formation of the new tissue [152] (Figure. 1.10). Osteoclasts (Figure.1.11, c), are terminally differentiated multinucleated cells originated from hematopoietic stem cells of the myeloid lineage (HSC) under the influence of numerous stimulating factors produced by osteoblasts and osteocytes. The mononuclear progenitor cells, originating from HSC, can differentiate into macrophages, dendritic cells of the immune system or osteoclasts, the latter deriving from their fusion. They are the only cells in nature that can degrade mineralized bone tissue and actively intervene in calcium homeostasis [153]. Moreover, osteocytes produce factors that influence osteoblast and osteoclast activities, whereas osteocyte apoptosis is followed by osteoclastic bone resorption.

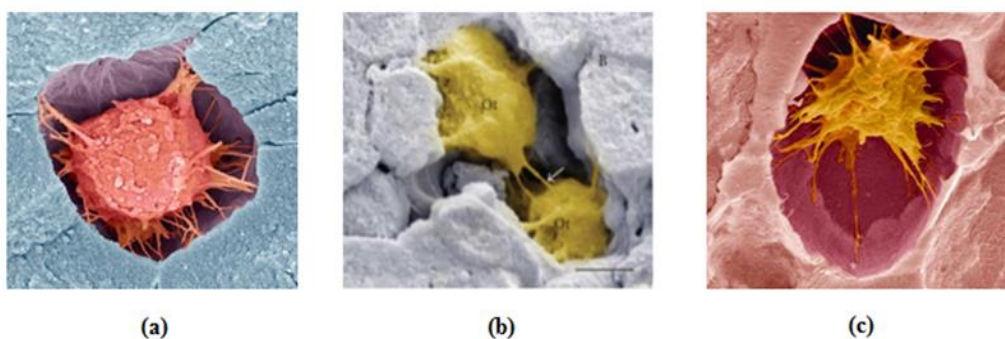


Figure 1.11: Electronic scanning microscopy showing (a) Osteoblasts, (b) Osteocytes, (c) Osteoclasts.

The balance between bone resorption and formation depends on signals from cytokines, hormones, chemokines, and mechanostimulation, and resorption by osteoclasts is essential for maintenance of normal bone density, trabeculae in spongy bone, and release of minerals. An imbalance in these processes results in degenerative bone diseases osteoporosis, which is predicted to affect 61 million men and women by 2020 [154]

1.4.3 Osteoporosis: treatment of bone disease

Osteoporosis is a disease characterized by decreased bone mass with the consequent increase in skeletal fragility. In fact, the loss of bone tissue can alter its architecture leading to a microstructural deterioration and the subsequent risk of fractures. [155] Since bone tissue is subjected to a continuous remodeling process, an imbalance may occur in this mechanism with increasing the age of subject which leading to a greater resorption of the tissue or a minor osteogenesis, causing a sharp bone loss. Annually, osteoporosis is responsible for more than 8.9 million fracture cases, accounting for an osteoporotic fracture every 3 s. There are two kind of osteoporosis: primary and secondary. Primary osteoporosis is due to two separate entities, one is “Type I osteoporosis” to signify a loss of trabecular bone (mainly involves cancellous bone) that related to lack of endogenous estrogen and is a rapid bone loss of variable intensity after the menopause, and other “Type II osteoporosis” to represent a loss of cortical and trabecular bone

in men and women as the result of age-related bone loss. [156] “Type II osteoporosis” reflects the composite influences of long-term remodeling inefficiency, intestinal mineral absorption, renal mineral handling, adequacy of dietary calcium and vitamin D and parathyroid hormone (PTH) secretion. Secondary osteoporosis depends on other diseases such as hypogonadism, malignant diseases, liver diseases or immobilization. Bone mineral density (BMD) is the amount of bone mineral in bone tissue and this index depends on the age, genetic, physical, hormonal and nutritional factors acting alone or in concert to diminish skeletal integrity and is used to check and evaluate the amount of mineral material present in the bones. Through an osteodensitometry (DXA) analysis, if there are T-scores (number of standard deviations above or below the average for a healthy adult of thirty years of the same sex and ethnicity of the patient) above 2, 5, the subject is affected by osteoporosis. If this index is lower than 2.5, osteopathy is diagnosed (reduction of mineral density below normal values) [157] Following

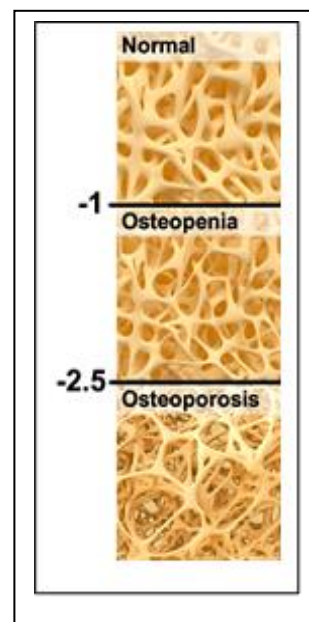


Figure 1.12: T-score scale and relative representation of bone density

numerous studies, together with genetic and biochemical factors, hormones like estrogens and testosterone seem to be the determining characteristics correlating the onset of osteoporotic pathologies in the female gender after the onset of menopause. In fact, estrogens inhibit the apoptosis of osteoblasts and osteocytes by inducing it in osteoclasts [154]. Treatment of osteoporosis favors the use of anti-resorptive agents (includes estrogens, selective estrogen receptor modulators SERMs, denosumab and bisphosphonates.) and osteoanabolic agents (parathyroid hormone PTH. Although, estrogens decrease tissue resorption, is not applied for long-term treatment because it is related to breast cancer side effect. [158] Oestrogens / SERMs that function as hormones / hormone analogs by binding to cell receptors to express their pharmacological functions whereas bisphosphonates are chemically stable molecules with a structure like pyrophosphates with a high affinity towards hydroxyapatite. This characteristic allows bisphosphonates used as most widely administered therapeutic agents with increasing bone resorption associated with osteoclastic activity, as well as osteoporosis, Paget and metastatic bone diseases. [159,160] Bisphosphonates disrupt bone resorption and lead to osteoclasts death, thereby reducing loss of bone mass. [161]

1.4.4 Drug targeting: Mechanism of action of Bisphosphonate

An ideal bone-targeting therapeutic agent will have specific targeting of bone mineral or bone localized cells, stable to systemic exposure during the time prior to bone binding, labile enough to release its drug payloads at times after its bone localization, efficacy at the bone lesion is achieved with very limited systemic exposure, and healthy tissue including bone is not adversely

affected. In this way, the therapeutic efficacy is increased by allowing administrations with lower dosages and a decrease in unwanted side effects. In 1960, following studies on the physiological role of pyrophosphate (inhibit the crystallization of calcium salts) (Figure. 1.13) within the body, a new class of drugs was developed specifically for the treatment of bone dysfunctions: bisphosphonates (BPs).

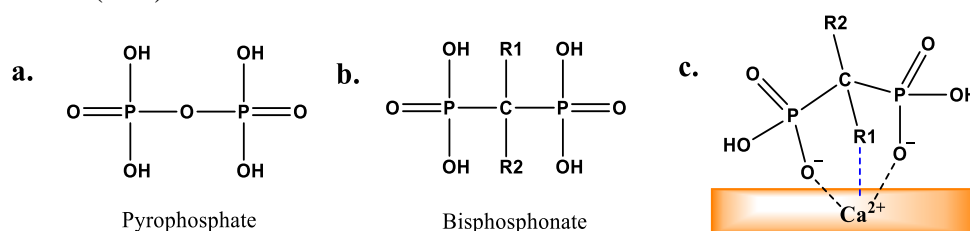


Figure 1.13: Pyrophosphoric acid (a) a generic structure of a bis-phosphonic acid (b) and (c) Bisphosphonates bind bone via chelation of calcium ions.

Inorganic pyrophosphate consists of two phosphate groups linked by an oxygen atom (P-O-P structure), while bisphosphonates distinguished by a P-C-P bond covalently attached two side chains, R₁ and R₂, the central oxygen atom being substituted by a carbon atom [162,163] The P-C-P configuration of bisphosphonates confers a resistance to chemical and enzymatic hydrolysis, resulting in a stable molecule that is absorbable when taken orally and not metabolized. The P-C-P structure allows a great number of possible variations, either by changing the two lateral chains on the carbon atom or by esterifying the phosphate groups. Nine BPs are commercially available and part of these are sold in their bis-phosphonic acid salt form [164]; modifications to one of the phosphonate groups can dramatically reduce the affinity of the BP for bone mineral [165] as well as the biochemical potency. [166] The R₁ and R₂ side-chains attached to the carbon atom are responsible for the large range of activity observed among the BPs.

When the hydroxyl (OH) or amino (NH₂) groups are present as substituents to R₁, they enhance the bone binding properties of bisphosphonates through tridentate binding to calcium, while the major function of R₂ is to influence bisphosphonates' antiresorptive potency [167]. It is worthy to note that though the hydroxyl and phosphate groups are significantly responsible for the bisphosphonates' attraction for the bone matrix, however, the final structural moiety (in the R₂ position) which bounds to the carbon at the center mainly determines the efficacy of BPs to inhibit bone resorption [168]. The relationship between biological activity, the chemical structure of bisphosphonates and their ability to inhibit bone resorption by intervening in bone-related biological mechanisms has only recently been identified.

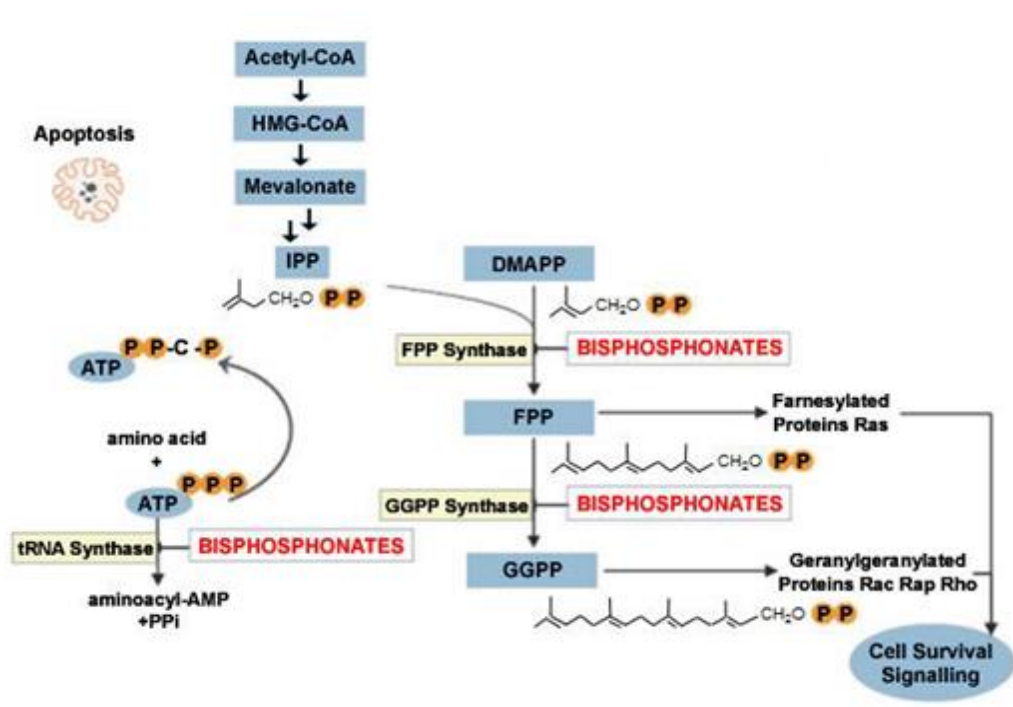


Figure 1.14: Mechanism of inhibition of FPPS and GGPPS due to Bisphosphonates

Functionality $(\text{HO})_2-(\text{O})\text{P}-\text{C}-\text{P}(\text{O})-(\text{OH})_2$ is responsible for the chelation of calcium ions present in the HAP lattice and allows these molecules to express preferential targeting of tissues bone. In addition to the chelating capacity against the Ca^{2+} ions constituting hydroxyapatite, new studies have shown an anti-resorbing effect of bisphosphonates on osteoclasts determined by inhibition of the enzyme Farnesyl Pyrophosphate Synthase (FPPS), a cardinal enzyme in the metabolic pathway of mevalonic acid (they inhibit the synthesis of farnesyl pyrophosphate and isopentenyl pyrophosphate, (Figure.1.14). FPPS allows the formation of terpenic lipids used for the synthesis of sterols and for post-modification translation of the GTP-proteins (protein sub-units bound to the guanosintrifosfate), molecules essential to osteoclasts in carrying out their resorptive function. During bone resorption, osteoclasts, by modifying the pH in contact with the bone, determine the hydrolysis of the inorganic matrix and the dissociation of the BPs from the mineral surface. Due to their ability to acidify the bone surface, only these cells together with macrophages can absorb substantial amounts of BPs. Through exocytosis, the bisphosphonates complexed with Ca^{2+} ions enter the osteoclasts and begin to perform their enzymatic inhibitory function [169].

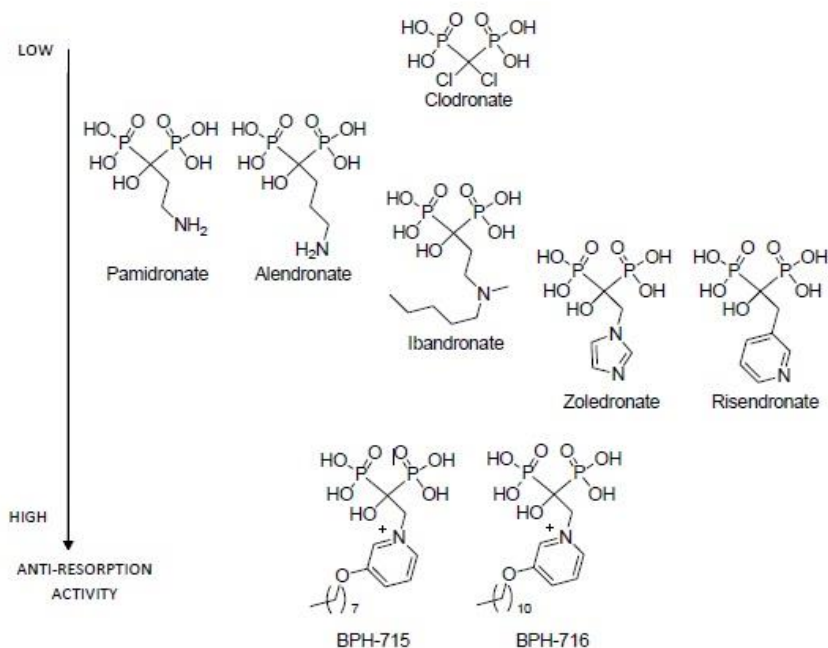


Figure 1.15: structure/activity relationship of BPs that target FPPS and GGPPS.

The overall pharmacological effects of these molecules seem to depend mainly on the two properties mentioned above, namely the affinity for the bone mineral and the inhibitory character on the osteoclasts. The relative contributions of these properties differ from one molecular structure to another allowing their use in the treatment of different diseases related to the skeletal system such as bone tumors, Paget's disease and osteoporosis. [170] BPs act on the osteoclast cells by two different mechanism, depending on the category whether it is nitrogen containing or not. Various types of bisphosphonates have unique antiresorptive potency and binding affinities. BPs containing nitrogen atoms or nitrogen heterocyclic substituents are very potent however intensity of the effect is also dependent on the aliphatic side chain and a three-dimensional structural requirement appears to be involved. It is worth to notice that Zhang et al reported that novel lipophilic pyridinium bisphosphonates (Figure.1.15) are approximately 250 times more effective than any other bisphosphonate drugs. [171]

1.4.5 Systems used for delivery of Bisphosphonates (BPs)

The exceptional affinity of BPs towards hydroxyapatite has been used for the transport of numerous types of drugs in bone tissues, employing BPs as building blocks of numerous specific vectors and for the diagnosis of numerous bone diseases. BPs effectively inhibit bone resorption by osteoclasts [172–175]. As a result, the drugs have found a wide range of medical applications which include their uses in the treatment of Paget's disease, osteoporosis prevention and treatment, hypercalcaemia or non-hypercalcemia related bone metastasis, primary

hyperparathyroidism, multiple myeloma, osteogenesis imperfecta, fibrous dysplasia and other bone conditions characterized by bone frailty [176–178]. The combination of BPs with some anticancer drugs is aimed at concentrating the antineoplastic activity of therapeutic agents in the bones following a systemic administration, avoiding the non-skeletal tissues and the subsequent unwanted side effects (Figure.1.16,1). Molecules such as BP-DTPA (diethylene triamino pentaacetic acid, Figure 1.16,2) also used in anticancer therapies are able to carry radioisotopes such as ^{153}Sm , ^{186}Re and ^{188}Re . The BPs, together with the drugs connected to them, have a direct effect on the cancer cells, causing them to apoptosis and inhibiting their activity. Antibacterial agents conjugated to BPs, such as ciprofloxacin (Figure 1.16,3) are used in the treatment of osteomyelitis. The BPs can also act as resorbing agents by inhibiting the catalytically active sites of some enzymes present in the osteoclasts and transmitting in them molecules with the same effect as the estrogens and the SERMs (Figure 1.16.4).

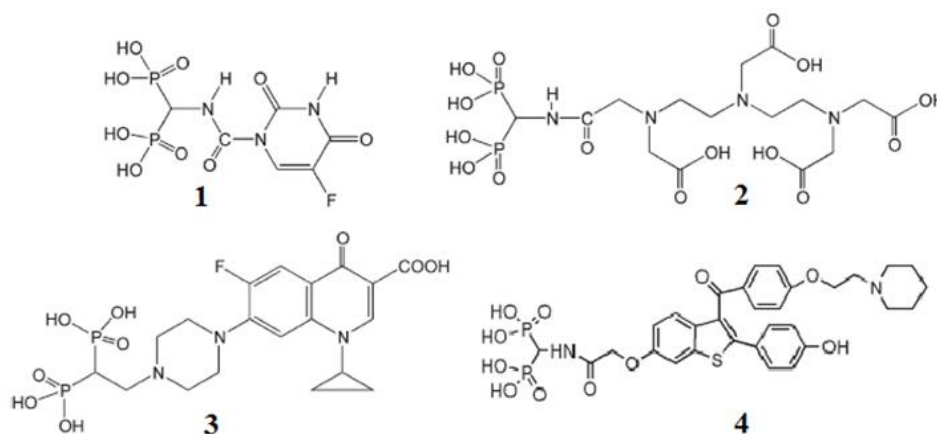


Figure 1.16: Chemical structure of some specific therapeutic agents: (1) 1-aminomethylene 1,1bisphosphonate with 5-fluorouracil; (2) BP-DTPA; (3) BP-ciprofloxacin; (4) BP-raloxifene (SERM).

However, despite their pharmaceutical efficacy, BPs suffer from a few drawbacks which include: poor oral bioavailability (1%–3%) [179–181], side effects of acute gastro-intestinal conditions such as gastric ulceration, dysphagia and esophagitis [182, 183]. To enhance the bioavailability of BPs, several efforts have been made, for example, improvements in the design of drug delivery systems, use of absorption enhancers and structural modification of the drugs [184–188]. On the other hand, infected site targeting controlled release of BPs has the capacity to enhance effectiveness of drugs and minimize the associated side effects [189–192]. Therefore, BPs have an important function of drug-delivery-system (DDS) within the organism, effectively addressing therapeutic agents on bone tissues [193]. Ideal properties of a drug delivery system should include timely release and good control rate of drugs at the required sites through the physical and chemical characteristics of the carriers. Numerous delivery systems for bisphosphonates have been explored [194–201]. In order to improve the bioavailability of the drugs administered and to decrease (or avoid) the side effects associated with them, new types of

DDS have been studied and developed, in which the BPs are no longer carriers but are conveyed through biological matrices, organic or inorganic. Depending on the type of support used, it will be possible to modulate the release speed of the active ingredient by acting on the chemical and physical characteristics of the carrier. The main strategies and techniques of administration studied today see the use of nanocapsules, copolymers, hydrogels, bioceramics, carbon nanotubes, fullerenes, liposomes, micelles and nanoparticles (NPs) of metal and non-metallic oxides [194, 202–209].

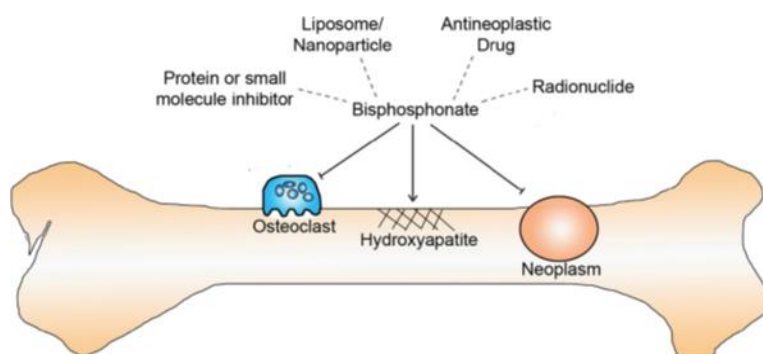


Figure 1.17: Schematic of bone-targeting bisphosphonate conjugates and effects of bisphosphonates.

Bisphosphonates alone inhibit osteoclasts, bind hydroxyapatite crystal structure, and negatively affect neoplasms. The addition of a conjugated drug may increase the efficacy of these functions or add further modes of action. This representation does not encompass all functions of bisphosphonates or conjugated moieties. [210]

Although the above-mentioned delivery systems have been reported to be useful for the delivery of bisphosphonates and other bioactive agents, they also suffer from some limitations. The conjugation of alendronate through the amines group to other drugs to form hybrid compounds compromises the therapeutic efficacy of the bisphosphonates. Also, the conjugation of chemotherapeutic agents with bisphosphonates for enhanced selectivity towards bone metastases tumors resulted in compounds that did not exhibit antitumor effects [211, 212], polymer-drug conjugates systems suffer from slow release of the drug, low drug loading that can reduce the therapeutic efficacy of the incorporated drugs and inability to control the polymer synthesis resulting in low yield [213, 214]. The application of liposomes for the encapsulation of bioactive agents is usually associated with low degrees of drug encapsulation and uncontrolled rates of drug release. However, the nanoparticles (NPs) of metal and non-metallic oxides are of high importance in pharmaceutical dosages on a nanometric scale: the therapeutic applications of NPs are in fact numerous, mainly comprising the diagnostic sector and the selective targeting of certain pathologies. [215]

1.5 Nanoparticles in the Biomedical Application

The novel drug-delivery systems would offer protection and improve the pharmacokinetics of easily degradable peptides and proteins that often have short half-lives in vivo. [216, 217]

Therefore, the development of techniques that could selectively deliver drugs to the pathological sites is currently one of the most important areas of drug research. The emergence of nanotechnology is likely to have a significant impact on the drug-delivery sector and nanoparticles (NPs) are at the leading edge, with many potential applications in clinical medicine and research. [218] A safe and targeted drug delivery could improve the performance of some classical medicines and moreover, will have implications for the development and success of new therapeutic strategies. In the last decade, several drug-delivery technologies have emerged, and a fascinating part of this field is the development of nanoscale drug delivery devices. The main interest in the use of NPs in the medical field is due to the ability to absorb and transport many classes of molecules defined by the high surface-to-mass ratio and their quantum properties. The nanoparticles are characterized by a diameter ranging from 10 to 100nm and can be formulated with different materials and structures functional to the type of application [219]. Although the definition identifies nanoparticles as having dimensions below 100 nm, especially in drug delivery relatively large (size>100 nm) nanoparticles may be needed for loading a sufficient amount of drug onto the particles. Recent advances in biotechnology and related areas are aiding the discovery and rational design of many new classes of drugs, however most of them are limited by their poor solubility, high toxicity, high dosage, aggregation due to poor solubility, nonspecific delivery, in vivo degradation and short circulating half-lives. The encapsulation or absorption of drugs and macromolecules on NPs has the main purpose of increasing their therapeutic index and bioavailability, decreasing their toxicity towards other organs and their side effects. Moreover, NPs increase the aqueous solubility of the drug, protect the drug from degradation, produce a prolonged release of the drug, improve the bioavailability, provide a targeted delivery, decrease the toxic side effects of the drug, offer appropriate form for all routes of administration and allow rapid-formulation development. Drugs can be loaded onto NPs by various methods, such as encapsulation, surface attachment or entrapment. NPs, in addition to acting within the blood flow, thanks to their small size can penetrate cell membranes by releasing the therapeutic agents in tissues and cells in a controlled manner, thus providing specific and targeted therapies [220]. Therefore, the unwanted side effects and the toxicity of the therapeutic agents reduced, and the therapeutic efficacy is enhanced. Furthermore, they can carry useful contrast agents in non-invasive diagnostic investigations such as positron emission tomography (PET) and computed tomography (CT) (Fig.18). In order to design specific and targeted nanoparticle structures, some characteristics such as the loading and molecular delivery kinetics within NPs, the stability of these molecules in the vector, the biocompatibility of NPs and the biodistribution within the organism (if the possible elimination of residual material is used only as a vector). The aims for nanoparticle entrapment of drugs are either enhanced delivery to, or uptake by, target cell and/or a reduction in the toxicity of the free drug to non-target organs. Both situations will result in an increase of therapeutic index, the margin between the doses resulting in a therapeutic efficacy and toxicity to other organ systems. For these aims, creation of long-lived and target-specific nanoparticles is needed.

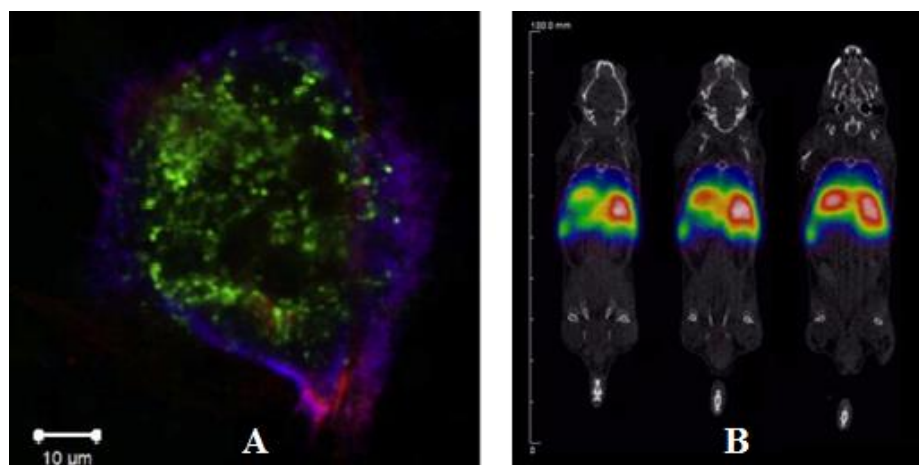


Figure 1.18 (A) Laser scanning confocal microscopy of an osteoclast of animal origin (rabbit) to which a fluorescent BP (green) has been added; (B) PET sections of three mouse specimens following the administration of ^{68}Ga -DOTA-ZrNPs: the clear section indicates a higher concentration of radioisotope in the liver and spleen.

Biocompatibility is extremely important because the NPs must be able to integrate with the biological system without eliciting any immune response: the eventual activation would result in an inflammatory reaction by the body with the consequent inactivation of the nanoparticles through phagocytosis. The undesirable effects caused by NPs depend mainly on their shape, the hydrodynamic radius, the amount administered, the residence time, the surface chemical properties (charge) and the material they are made of [221]. The main materials of biological origin used in the synthesis of NPs are chitosan, phospholipids, lipids, lactic acid and dextran while for the formulation of inorganic NPs metals (Au, Fe, Ag), metalloids (Si) are used, and transition metals (Zr, Ti) [18]. Typically, the drugs are loaded onto inorganic supports having high surface area values and interact with them through weak non-covalent interactions such as hydrogen bonds, electrostatic interactions, and physical absorption. Variations of some parameters of the physiological environment such as pH, temperature or the intervention of some specific enzymes can cause the breakdown of the weak links between drug and support characterizing the release of these molecules within the organism [222].

The therapeutic applications of NPs are diverse, ranging from cancer therapeutics, antimicrobial actions, vaccine delivery, gene delivery and site-specific targeting to avoid the undesirable side effects of the current therapeutics. Many chemotherapeutic drugs such as carboplatin, paclitaxel, doxorubicin and etoposide, etc., have been successfully loaded onto NPs and these nanoparticulate systems are very potent against various cancers. In addition, multifunctional NPs with surface functionalized biomolecules are also being synthesized and serve as potential therapeutic agents. The ability to track and image the fate of any nanomedicine from the systemic to the subcellular level becomes essential. NPs can be successfully exploited to improve the utility of fluorescent markers for medical imaging and diagnostic purposes. While various fluorescent markers are widely used in research and clinical diagnostic applications, current techniques have several disadvantages, such as the requirement of color-matched lasers,

fluorescence bleaching and lack of discriminatory capacity of multiple dyes, etc. Fluorescent NPs can greatly overcome these problems and a major advance toward clinical applicability is the use of NPs to image tumors and other diseases in vivo.

1.5.1 Zirconium Oxide: a new frontier of Inorganic Biomaterials

From last decade, the formulation of inorganic supports with applications in the clinical field has seen the prevalent use of silica-based materials. However, due to the narrow chemical and physical stability of such materials, transition metals have been developed such as titania, bismuth and zirconia (titanium oxides, bismuth oxide and zirconium oxide, respectively) having great technological potential, outstanding mechanical, chemical, optical, and electrical properties [223] Among those mentioned, ZrO_2 superior in terms of mechanical performance (strength, toughness, fatigue resistance) when compared to other materials, that make the zirconium-derived materials of great interest in the formulation of NPs and biomedical ceramics. Zirconia (ZrO_2) has mechanical properties comparable to stainless steel. [224, 225] Zirconia could stabilize in tetragonal metastable phase when cooling down the material from cubic to monoclinic phase. This unique mechanism makes ZrO_2 a potentially better material in the dentistry and biomedical fields. The high biocompatibility of zirconium oxide and its substantial non-toxicity [226] allows its use as a biomaterial in the construction of dental implants, in bone replacement, in nanocomposite coatings and as a drug-delivery-system in the form of powder either of sintered material or as a composite ceramic configuration in conjunction with inorganic oxides such as titanium oxide, alumina and hydroxyapatite. [226] [227] Zirconia ceramics have several advantages over other ceramic materials, Zirconia blades are used to cut Kevlar, magnetic tapes, cigarette Alters (because of their reduced wear). High temperature ionic conductivity makes zirconia ceramics suitable as solid electrolytes in fuel cells and in oxygen sensors. Good chemical and dimensional stability, mechanical strength and toughness, coupled with a Young's modulus in the same order of magnitude of stainless-steel alloys was the origin of the interest in using zirconia as a ceramic biomaterial. The research on the use of zirconia ceramics as biomaterials started about twenty years ago, and now zirconia (Y-YZP) is in clinical use in THR, but developments are in progress for application in other medical devices. Mesoporous oxide systems are attractive to their high surface area, tunable pore size, controllable particle size and shape, and dual-functional exterior and interior surfaces [228]. Moreover, mesoporous zirconia-based materials have further additional properties, such as catalytic activity and selectivity, better chemical stability than alumina or silica, amphoteric and redox properties [229-231].

Synthesis of the family of Bis-phosphonic (BPs) Acids

Bis-phosphonic acids (BP) are a well-known class of organic molecules that represents the typical scaffold present in the most common drugs for osteoporosis and bone diseases treatments.[232] Bis-phosphonic acids can be prepared with a series of synthetic approaches and among these, the reaction of vinylidene bisphosphonate ester with nucleophiles through Michael or hetero-Michael addition is one of the most straightforward thus ensuring a wide range of possible products with simple commercially available nucleophiles. To synthesis new classes of bisphosphonates, the synthesis of methylene bisphosphonate ethyl ester was pivotal because this building block allow to synthesize a wide range of precursors characterized by the presence of vinyl units namely an unsubstituted double bond (VBP) and a wide range of mono and di-substituted precursors (Figure 2.1.).

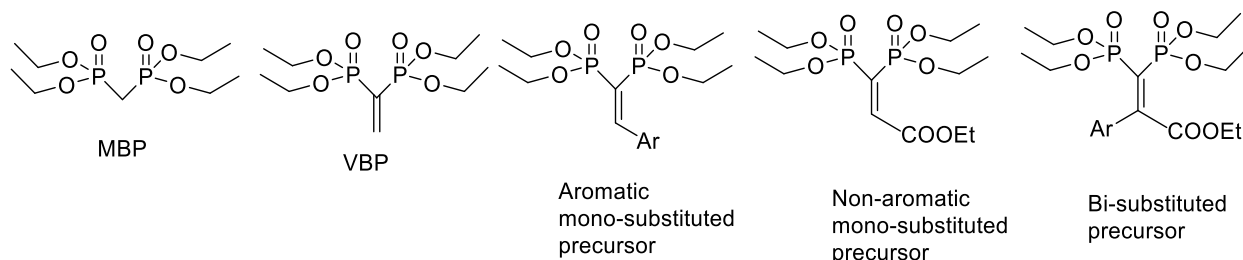
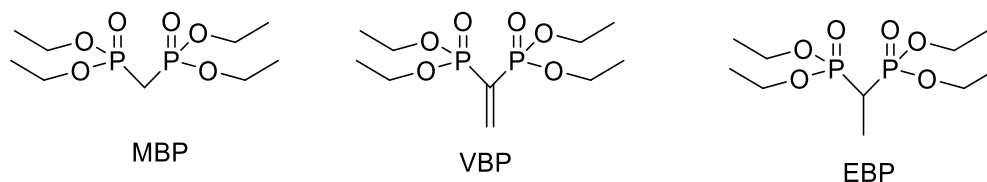


Figure 2.1: Different types of unsaturated BP precursors.

2. Results and Discussion

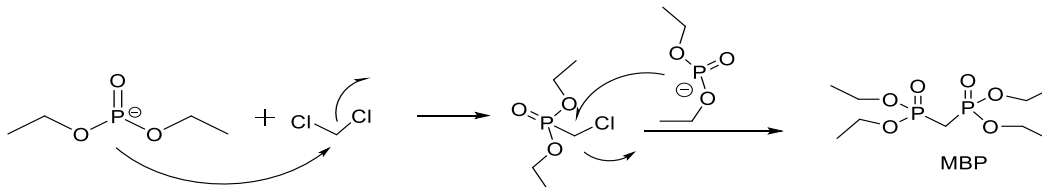
In this section the results obtained during the synthesis of Bis-phosphonic acids are presented. I will first report the results obtained in the syntheses of the precursor followed by the results obtained in the syntheses of new BP ester molecules containing Sulfur atoms. Finally reported the results obtained in the deprotection of ethyl ester to get BPs acid molecules.

2.1 Synthesis of BPs Precursors



2.1.1 Tetraethyl methylenebis(phosphonate) (MBP)

Methylene bisphosphonate tetraethyl ester (MBP) is the main building block that can produce a wide range of other BP precursors. This molecule is the simplest BP precursor, where R_1 and R_2 chains are both hydrogen atoms. It looks very similar to pyrophosphoric acid, where oxygen atom is replaced by a carbon atom and the acidic moieties are protected with four identical alkyl groups. In the literature some synthesis procedure of MBP have been reported using carbon disulfide [233] or diazomethane, [234] reagents requiring special precautions and use under severe restrictions: in fact, they are toxic, highly flammable and suspected carcinogens.



Scheme 2.1: Synthesis of MBP

Another problem limiting the experimental use of tetra alkyl methylene bisphosphonate as starting materials in syntheses is its high commercial price. We used a one pot procedure described by Hormi and co-workers [235] for the preparation of MBP starting from cheap materials. The synthesis of this precursor takes place with two subsequent nucleophilic attack by deprotonated phosphites on a dichloromethane molecule. The addition order of the reagents is crucial. The deprotonation of the phosphites occurs using a very strong Brønsted base (sodium ethylates) created *in situ* by addition of metallic sodium to ethanol used as the solvent.

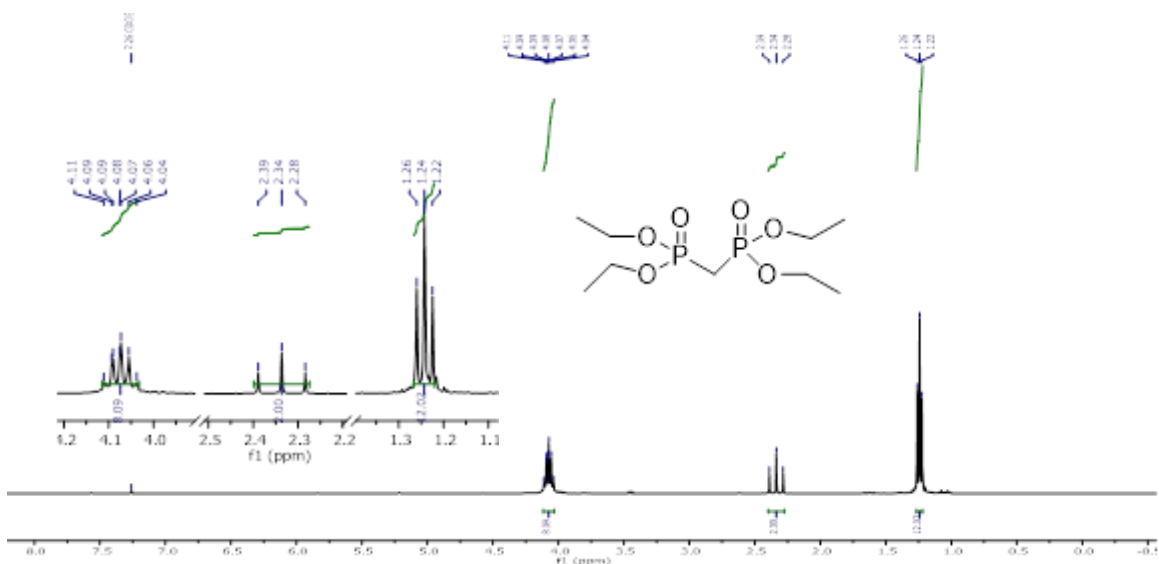


Figure 2.2: $^1\text{H-NMR}$ of MBP

Then diethyl phosphite is added that is deprotonated and is thus able to nucleophilically attack dichloromethane that is added at the end of the reaction. The reaction can proceed for two weeks. Recently Meziane and collaborators reported a faster procedure using microwave technologies to synthesize the same product. [236] It is noteworthy that the major product is MBP although a large excess of methylene chloride is used because the intermediate diethyl chloromethyl phosphonate is more reactive than methylene chloride in the subsequent nucleophilic substitution. This methodology described and shown in Scheme 2.1 could be performed in 10 g scale and allowed to obtain the product in 54% yield.

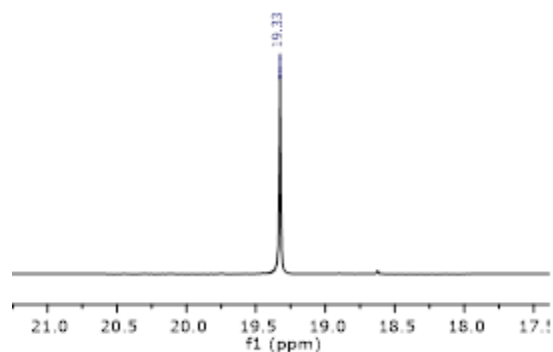
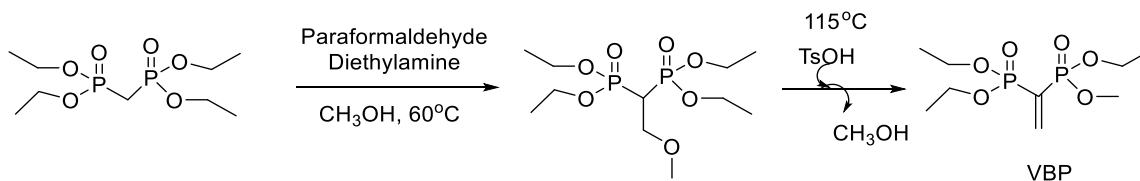


Figure 2.3: ^{31}P $\{^1\text{H}\}$ -NMR of MBP

2.1.2 Diethyl (1-(ethoxy(methoxy)phosphoryl)vinyl)phosphonate (VBP)

VBP is a versatile synthetic intermediate that allows access to a variety of highly functionalized compounds bearing the bisphosphonic moiety. Due to the presence of electron-deficient alkene moiety this compound can undergo conjugate addition with a variety of reagents including strong nucleophiles, such as organometallic reagents and enolates, as well as mild nucleophiles, such as amines, thiols and alcohols.



Scheme 2.2: Synthesis of VBP

VBP acts as a dipolarophile or dienophile in 1,3-dipolar cycloadditions or Diels–Alder reactions, to produce five- or six-membered rings containing the bisphosphonic unit. [237] The synthesis of this precursor occurs by reaction between MBP and formaldehyde [238] in two steps: the first one proceeds at 60°C with depolymerization of paraformaldehyde and deprotonation of the α carbon atom of MBP by diethylamine followed by attack to formaldehyde to give 2-methoxyethan-1,1 bisphosphonate intermediate (Scheme 2.2). The second step carried out at 115°C is characterized by the synthesis of the final VBP product by elimination of a methanol

molecule by acid catalysis in the presence of p-toluene sulfonic acid. The reaction was performed in gram scale and the product was obtained with a yield higher than 90%.

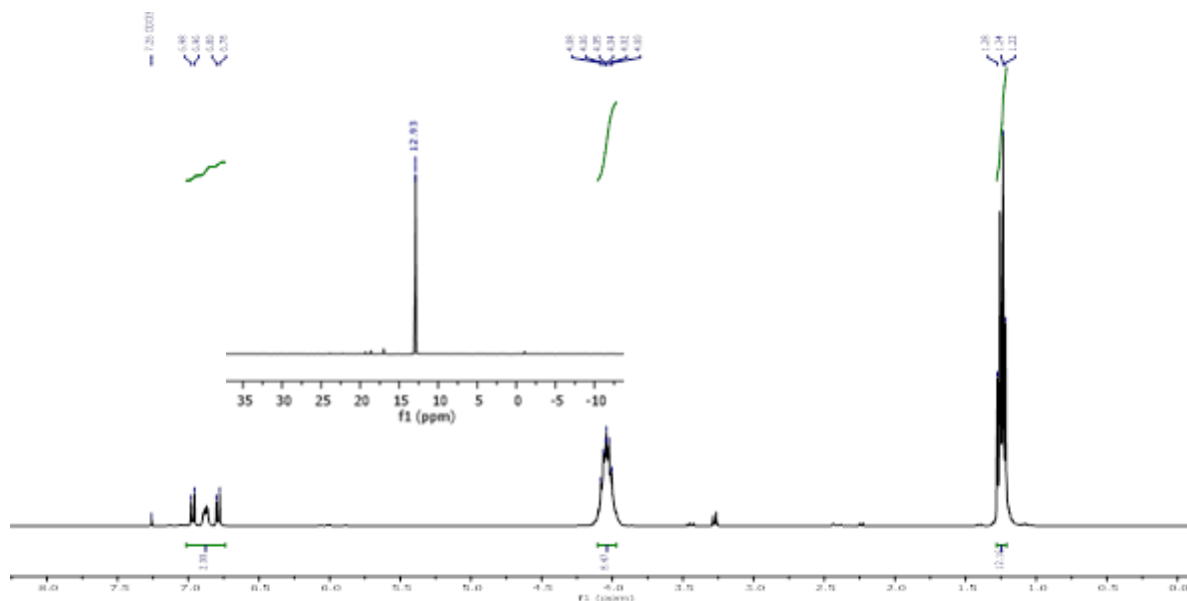
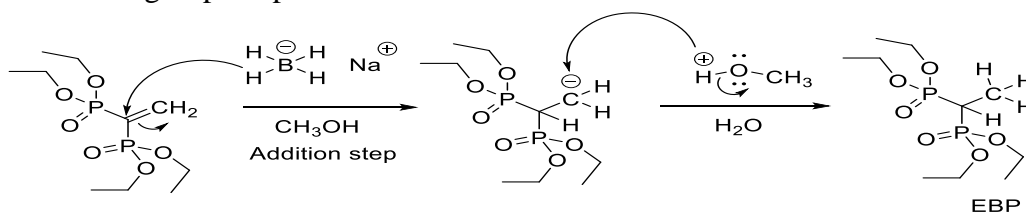


Figure 2.4: ^1H -NMR and $^{31}\text{P}\{^1\text{H}\}$ -NMR (inside) of VBP

^1H NMR spectra shows typical resonance for vinylic proton doublet of doublet at down field. $^{31}\text{P}\{^1\text{H}\}$ -NMR represent a sharp singlet. The obtained VBP was used, as described below, as a precursor for the synthesis of new BP through Michael addition reactions.

2.1.3 Tetraethyl ethane-1,1-diylbis(phosphonate) (EBP)

The synthesis of BP compound with short alkyl chain namely EBP is done by using Sodium borohydride (NaBH_4) as a reducing agent and VBP as precursor since it has electron deficient alkene group. NaBH_4 is relatively mild reducing agent, primarily used for the reduction of reactive functional groups in protic solvents.



Scheme 2.3: Synthesis of EBP

The mechanism of the reaction of sodium borohydride with VBP proceeds in two steps. In the first step, nucleophilic attack of a hydride (H^-) ion on the electron deficient carbon. This form the C-H bond and breaks the C-C bond, resulting in a new lone pair on the carbon, which makes the carbon negatively charged (carbanion). In the second step, a proton from water is added to the

carbanion to make the alkane. This is performed at the end of the reaction, the step referred to as protonation. The product was obtained with a yield 95%.

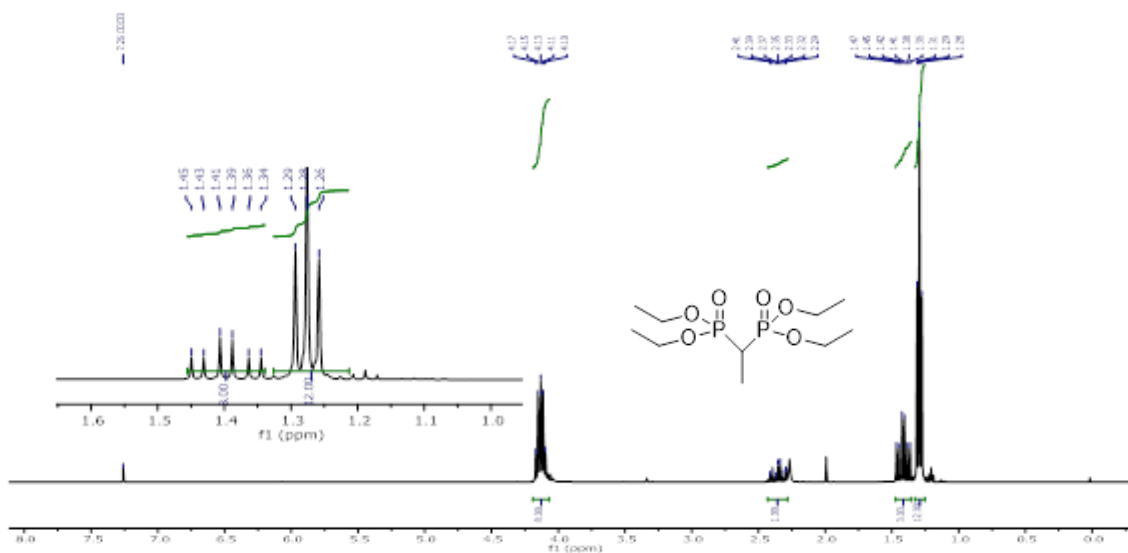


Figure 2.5: ^1H -NMR of EBP

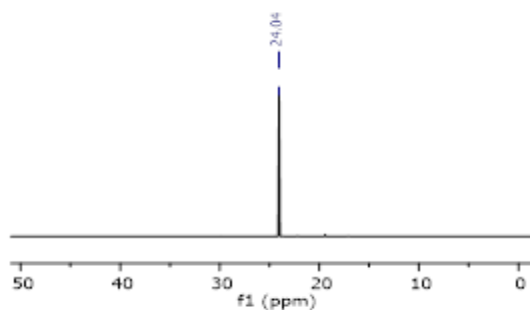
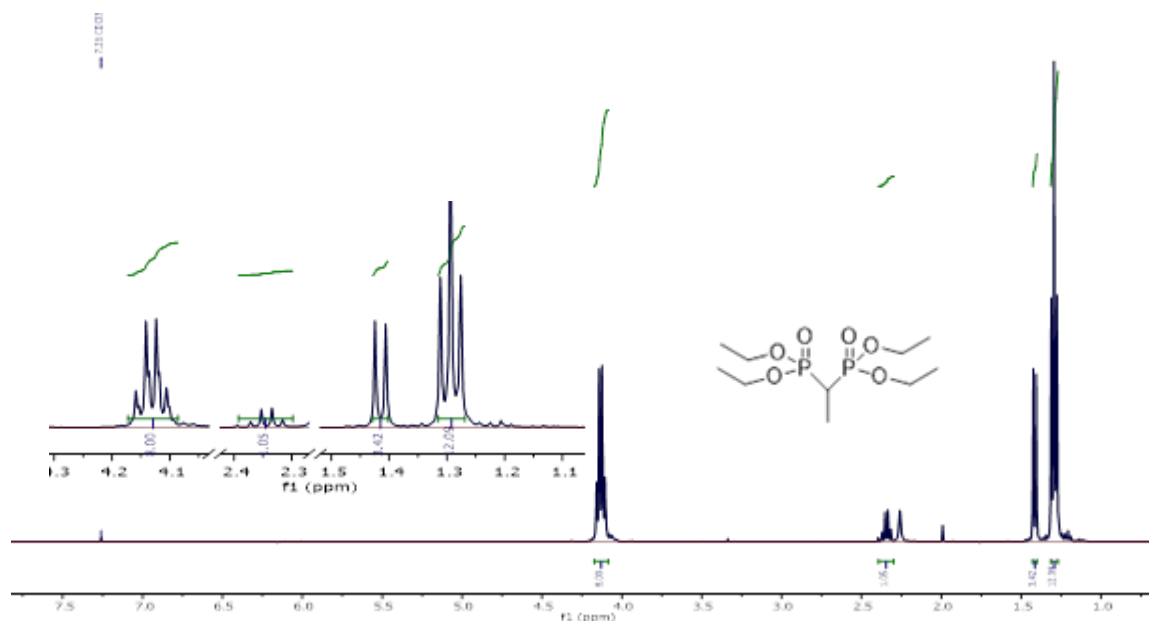
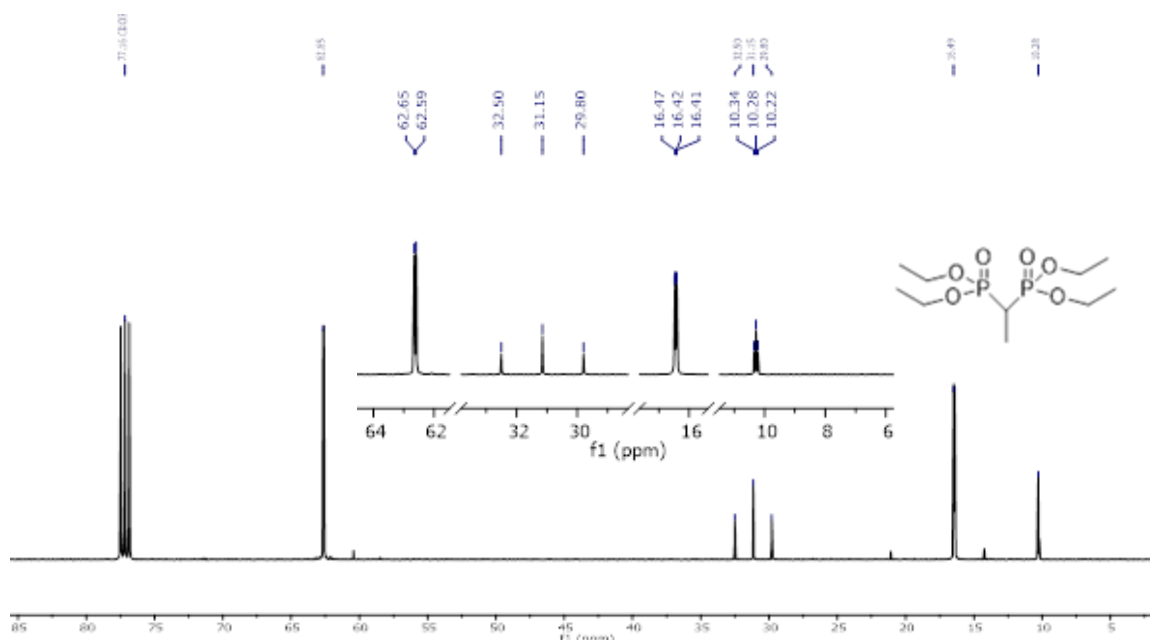


Figure 2.6: $^{31}\text{P}\{^1\text{H}\}$ -NMR of EBP

^1H NMR spectra represents typical resonance for β -proton triplet of doublet at high field 1.40 ppm. A sharp singlet at 24.04 ppm appears in $^{31}\text{P}\{^1\text{H}\}$ indicating two identical phosphate moieties. $^1\text{H}\{^{31}\text{P}\}$ -NMR spectra shows simplification of the resonance peaks, for example a doublet with small coupling constant 7.4 Hz instead of triple of doublet with high coupling constant at 17.2 Hz for ethylene proton (Figure 2.7).

Figure 2.7: ^1H $\{^{31}\text{P}\}$ -NMR of EBP

^{13}C -NMR of EBP shows the typical resonance peaks. The ethyl ester carbon represents the most downfield doublet at 62.53 ppm because of deshielding effect by electronegative oxygen atom. The signal of the carbon atom attach with two Phosphorous atom gives a triple at 31.06 ppm by coupling effect of phosphorous atoms. 2D-NMR HMBC showed long range ^{13}C - ^1H resonances, helping to assign ^{13}C signals as reported on Figure 2.10

Figure 2.8: ^{13}C -NMR of EBP

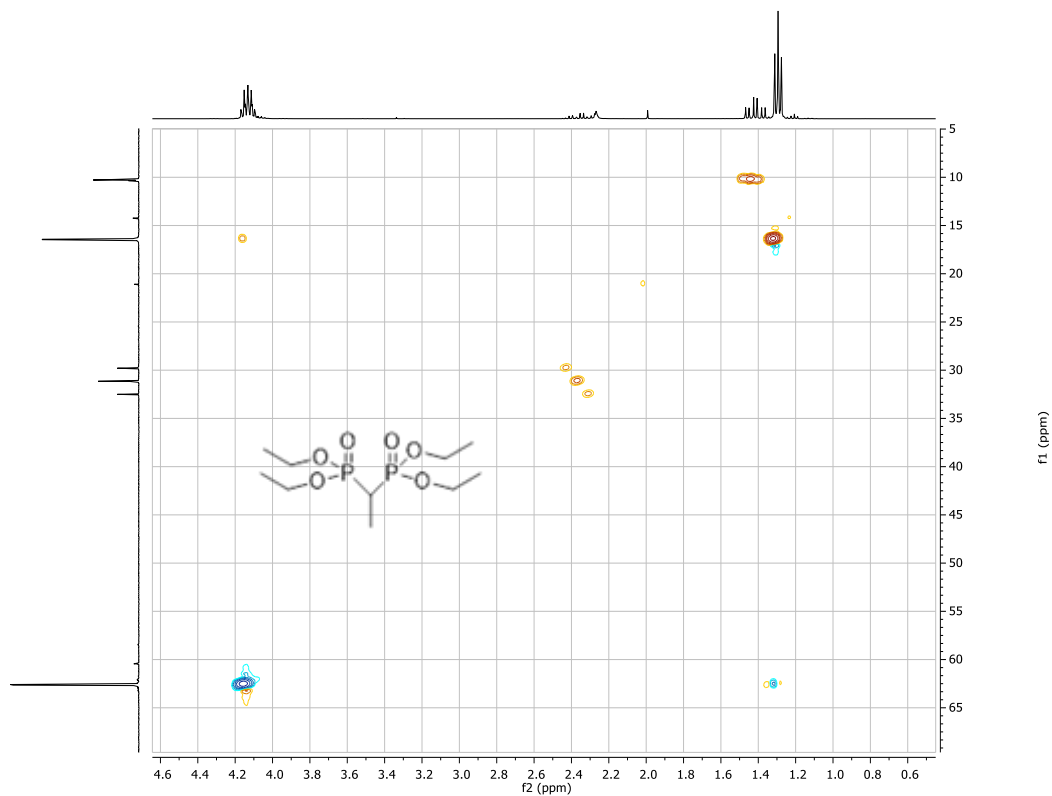


Figure 2.9: 2D-NMR HSQC of EBP

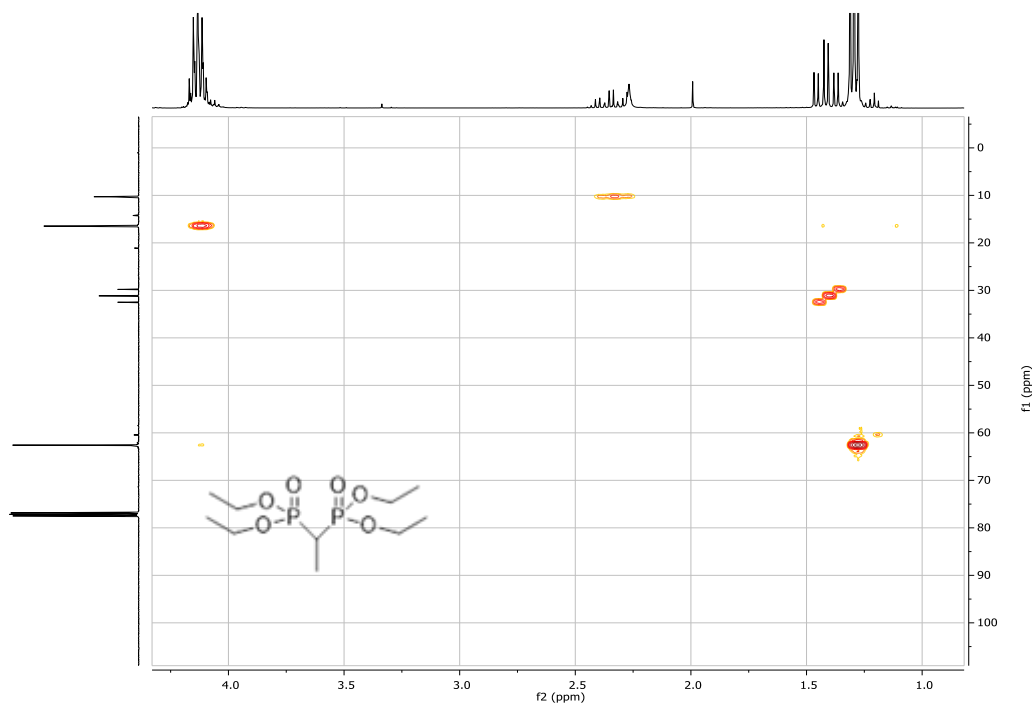


Figure 2.10: 2D-NMR HMBC of EBP

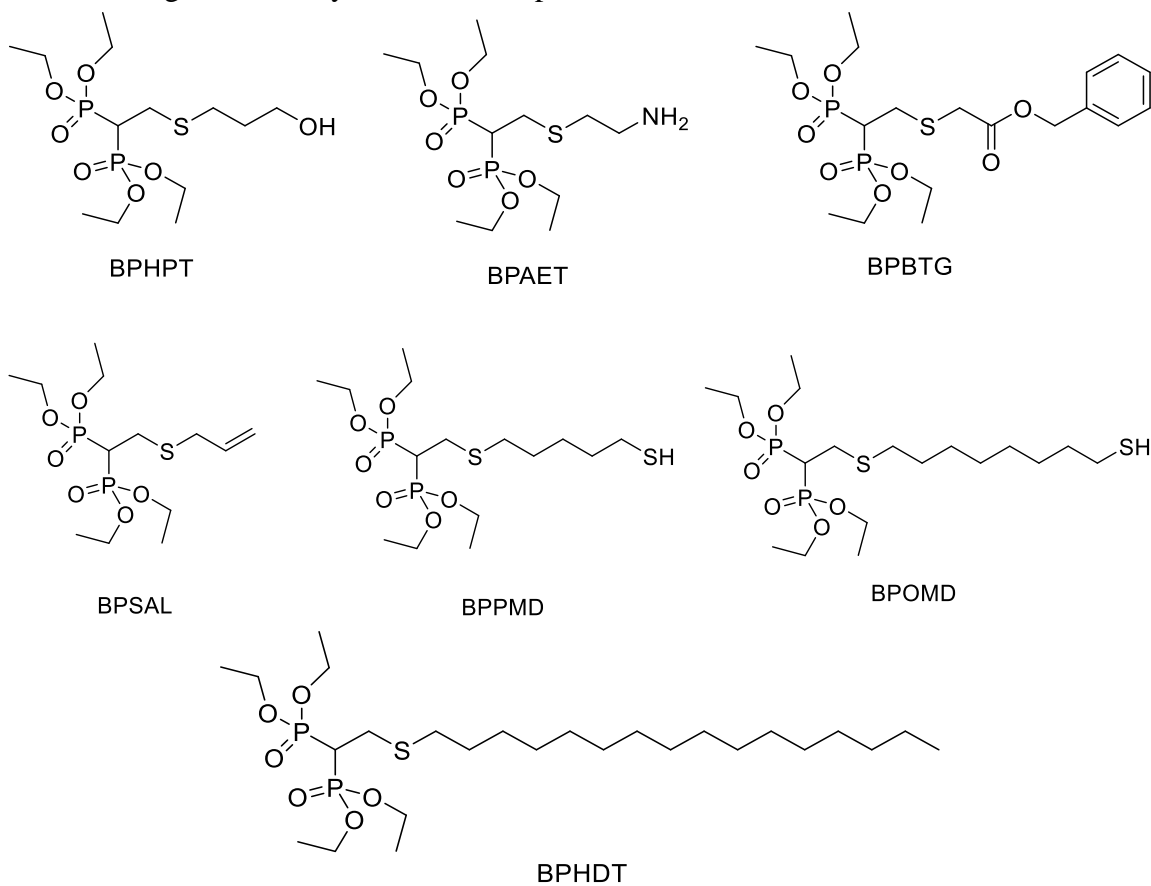
2.2 Synthesis of Sulfur Containing Bisphosphonate Ester

Bisphosphonates (BPs) are the most potent inhibitors of bone resorption clinically available to humans. Based on the components of their side chains, BPs divided into two categories: nitrogen-containing and non-nitrogenous. Tiludronate is only one non-nitrogenous commercially available BP, containing a sulfur atom in the β -position. Like other non-N-containing BPs, tiludronate can be incorporated into molecules of ATP, creating non-hydrolysable cytotoxic analogs of ATP molecules, which can disrupt phosphorylation thereby disrupting the activation and deactivation of regulatory enzymes. Though, tiludronate has low cellular potency and low mineral affinity in comparison to the more potent N-containing BPs and its clinical use is limited to the treatment of Paget's disease or in veterinary orthopedics. [239]

S-containing BPs can be synthesized by anion-mediated thiol-Michael reactions with Sulphur nucleophiles bearing different functional groups to give γ -substituted BPs (C-S bond). The thiol-Michael addition reaction or the conjugate addition of thiols or thiolate anions, to electron-deficient C=C bonds has attracted significant attention over the past decade due to its enhanced level of control over reaction parameters to ensure both spatial and temporally modifiable materials-be it the in vivo surface modification of biomaterials or photolithographic patterning of a substrate. [240–243]. Unlike radical mediated thiol-ene reactions which produce radical-radical termination products, thiol-Michael addition both the nucleophile- and base-catalyzed mechanisms do not lead to the formation of significant side products even in very dilute systems. This ability to proceed to quantitative conversion without side product formation even under dilute conditions renders the thiol-Michael addition the reaction of choice for many materials' chemistry applications. Generally, these reactions are carried out under the promotion of phosphorus- or nitrogen-centered nucleophiles. The phosphorus-centered reagents, such as tripropyl phosphine, are more effective as compared to the nitrogen-centered reagents, but they are environmentally sensitive and toxic. [244, 245] The main difference between base and nucleophile catalysts resides in the initiation process related with the production of thiolate anions (RS^-) resulting from deprotonation of a thiol (Michael donor). Strong base catalysts, such as tertiary amines (NEt_3), pick up the hydrogen atom directly from the thiol, whereas in the case of nucleophile catalysts, such as phosphines and primary (or secondary) amines, an intermediary zwitterionic enolate species is formed instead via nucleophilic attack to an electron-deficient vinyl (Michael acceptor), which in turn deprotonates the thiol ascribed to the strong basic character of zwitterions.[246]

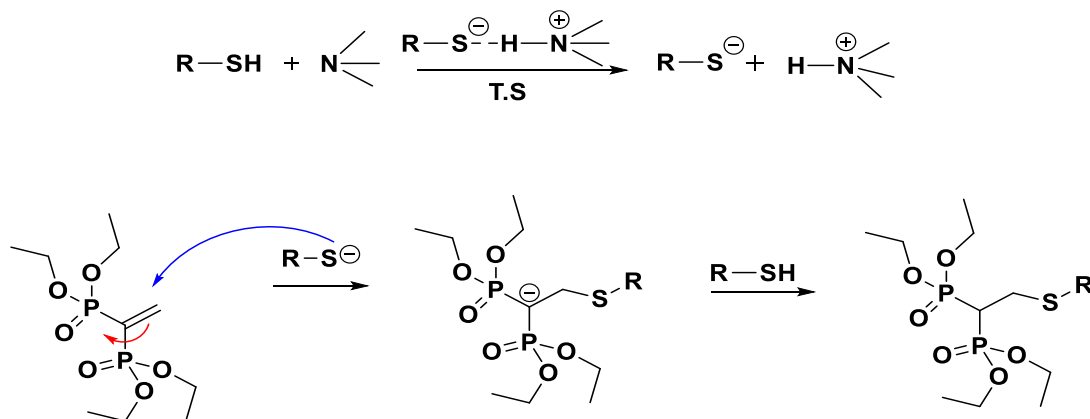
S-containing BPs are an under investigated class of BPs. Recent literature showed only a limited number of contributions, a new synthetic procedure reported is based on a rapid and solvent-free microwave-assisted method. [247] Studies on Thienopyrimidine-based bisphosphonates showed that these sulfur-nitrogen containing BPs were identified as a new class of inhibitors of the human farnesyl pyrophosphate synthase (FPPS). [248] Thiol BP products could be readily isolated and deprotected removing the phosphonic ester moieties to give the corresponding bisphosphonic acids. In particular, our research group reported a comparative study on the toxicity

and osteoclast inhibition activity of a known N-containing BPs with respect to a new S containing BP demonstrating good antiosteoclast activity of the latter while maintaining a low toxicity level, which is a really positive aspect for the development of new drugs. [249] Hence, new S-containing BPs were synthesized as reported below.



Scheme 2.4. Chemical structure of S-containing bisphosphonates Ester

General thiol-Michael Addition Reaction Mechanism with Base Catalyst

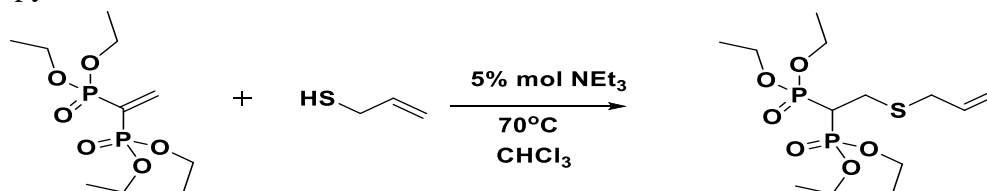


Scheme 2.5: The base-catalyzed thiol-Michael addition reaction pathway shows the hydrothiolation of an activated C=C bond via the addition of the anion across the electron-deficient β -Carbon of the vinyl group

Till now the most efficient catalysts with the minimal side reactions that have been used to initiate the thiol-Michael addition reactions are the base and nucleophile-based catalysts, although Lewis acids such as gadolinium triflate-based tetrafluoroborate also successfully initiate the thiol-Michael addition reactions.[250] Moreover, Moghaddam et al.[251] showed that a mixture of $\text{KF}/\text{Al}_2\text{O}_3$ yield an efficient ionic liquid to catalyze the thiol-Michael reaction while Movassagh et al.[252] demonstrate ideal conditions the absence of a solvent for the thiol-Michael addition reaction

2.2.1 Tetraethyl (2-(allylthio)ethane-1,1-diyl)bis(phosphonate) (BPSAL)

The synthesis of BPSAL was accomplished by reaction of allyl mercaptan with VBP under triethylamine catalysis, providing almost quantitative yield for the corresponding BP tetraethyl ester precursor. The product was purified by flash chromatography and characterized by NMR spectroscopy.



Scheme 2.6: Synthesis of BPSAL.

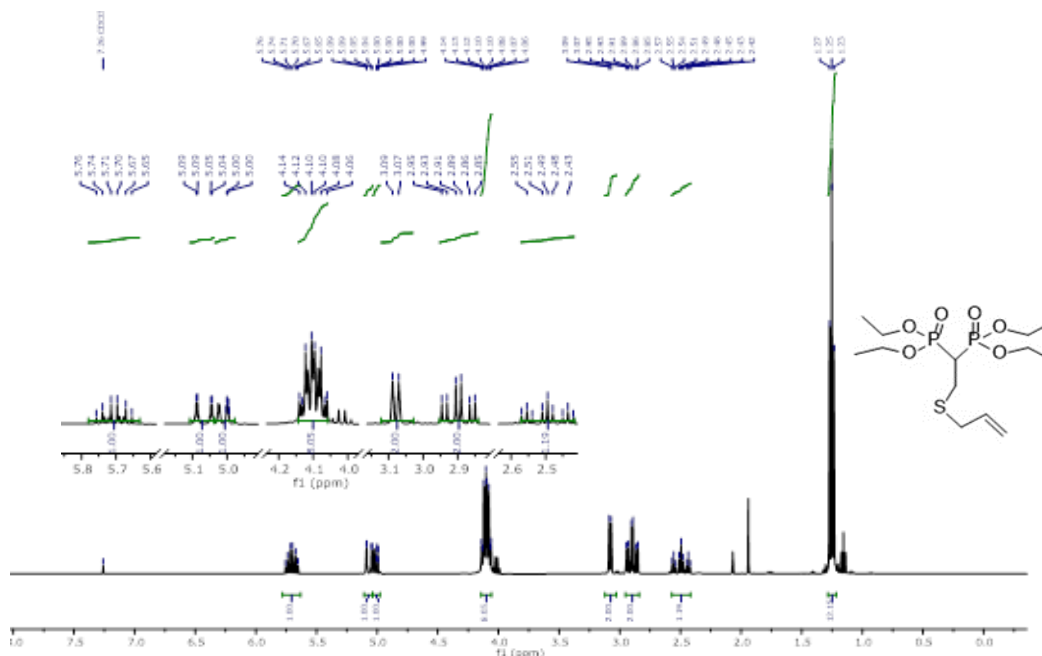
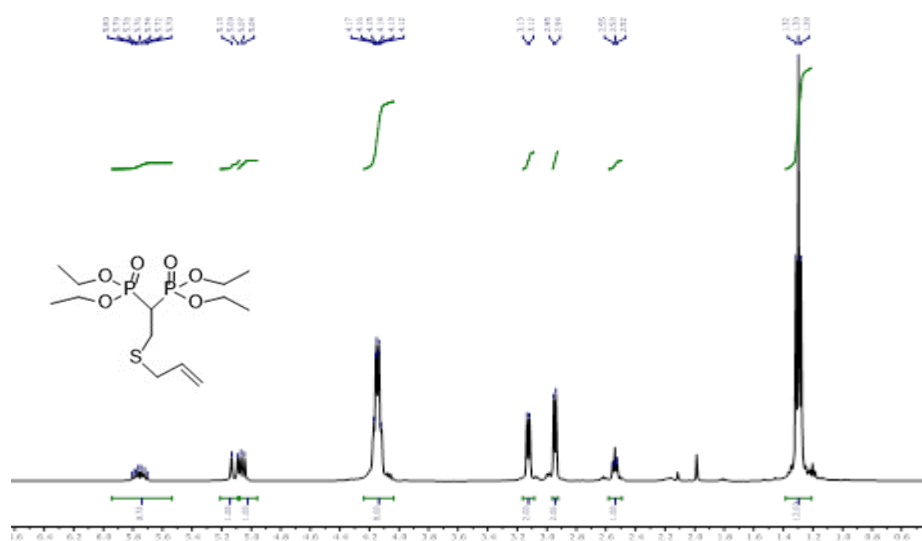
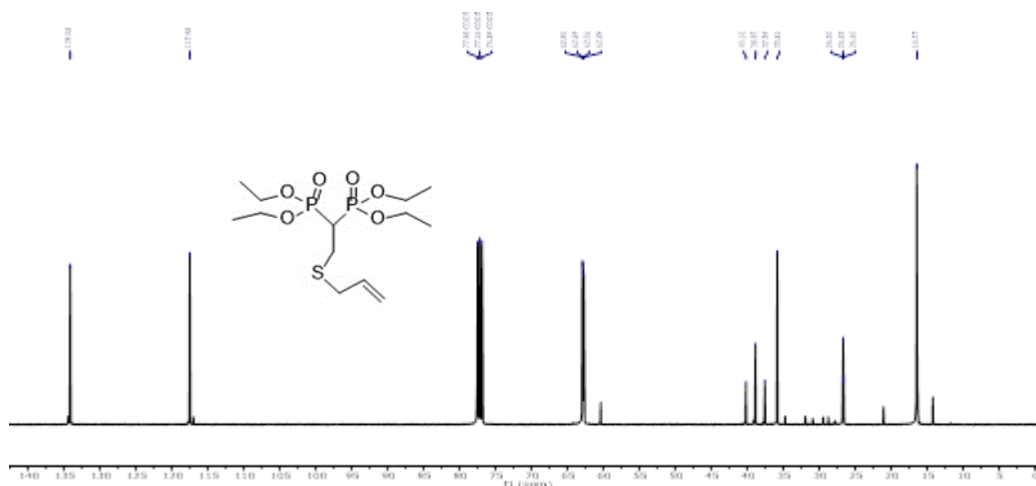
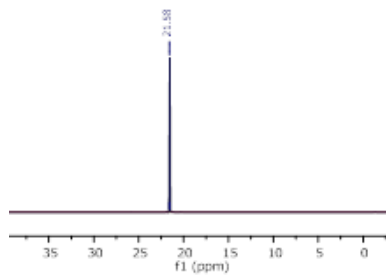


Figure 2.11: $^1\text{H-NMR}$ of BPSAL

Figure 2.12: $^1\text{H}\{^{31}\text{P}\}$ -NMR of BPSALFigure 2.13: ^{13}C -NMR of BPSAL

^1H NMR spectra shows typical resonance for allyl proton in the product at δ 5.75 ppm (triplet of doublet), 5.10 ppm (doublet of doublet) and 5.04 ppm (doublet of doublet) respectively. $^1\text{H}\{^{31}\text{P}\}$ -NMR spectra shows simplification of the resonance peaks (Figure).

Figure 2.14: ^{31}P -NMR of BPSAL

A sharp singlet appears at lower field 21.58 ppm in $^{31}\text{P}\{^1\text{H}\}$ spectra compare to that of singlet at 12.93 ppm for VBP. 2D-NMR HMBC showed long range ^{13}C - ^1H resonances, helping to assign ^{13}C signals as reported on (Figure 2.13) The 2D-NMR NOESY (Figure 2.15) experiment revealed a cross-peak between ethyl proton to methylene in the ester portion.

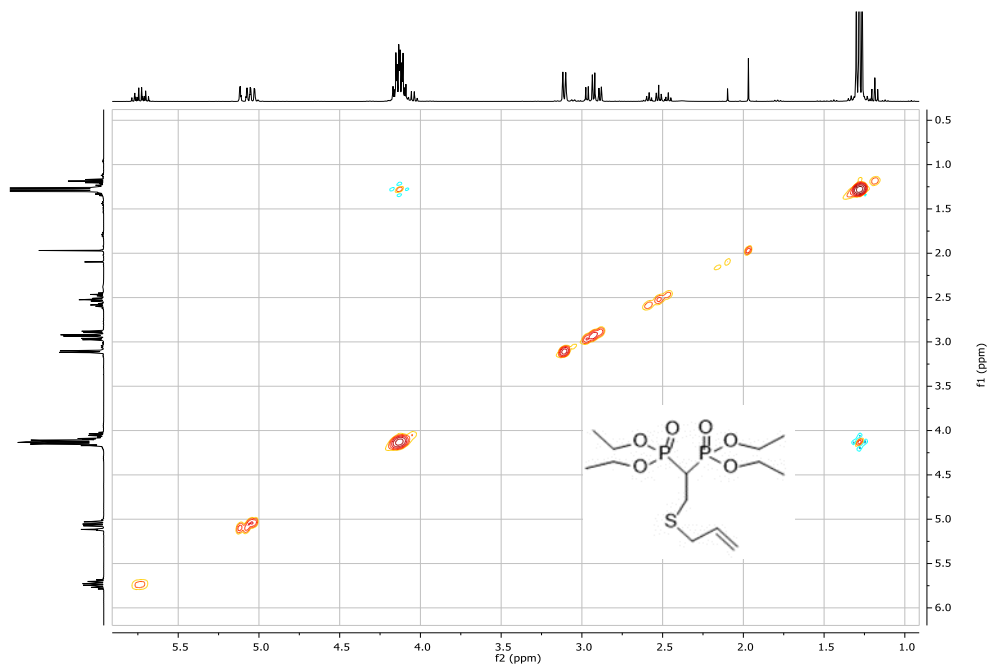


Figure 2.15: 2D-NMR NOESY of BPSAL

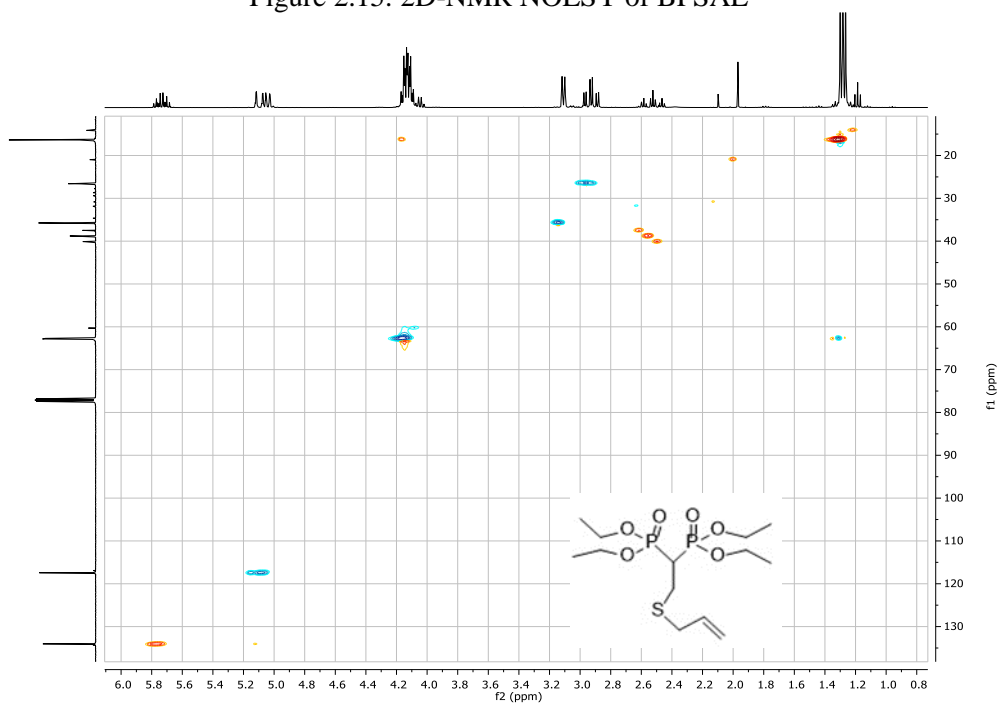


Figure 2.16: 2D-NMR HSQC of BPSAL

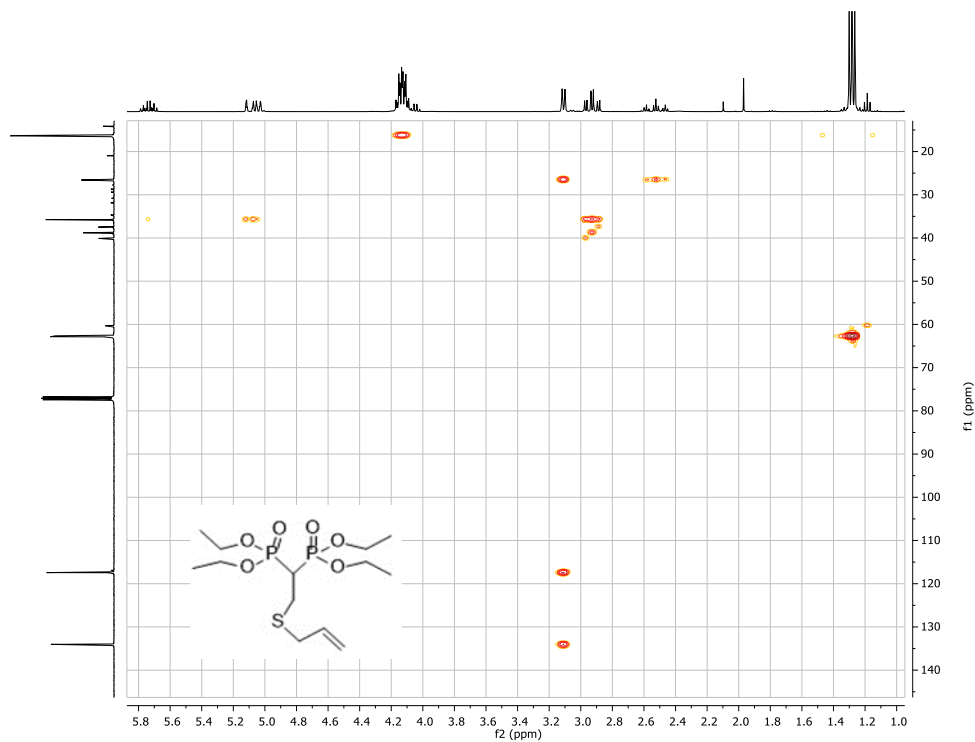
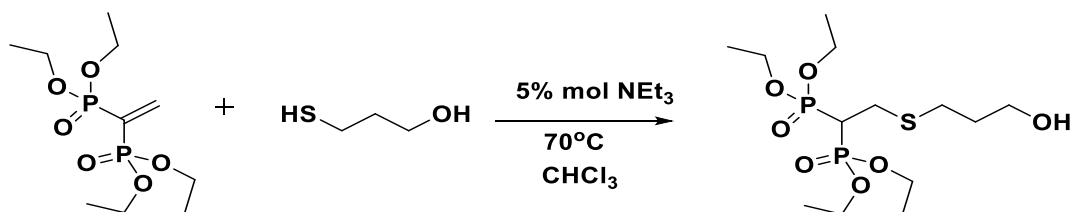


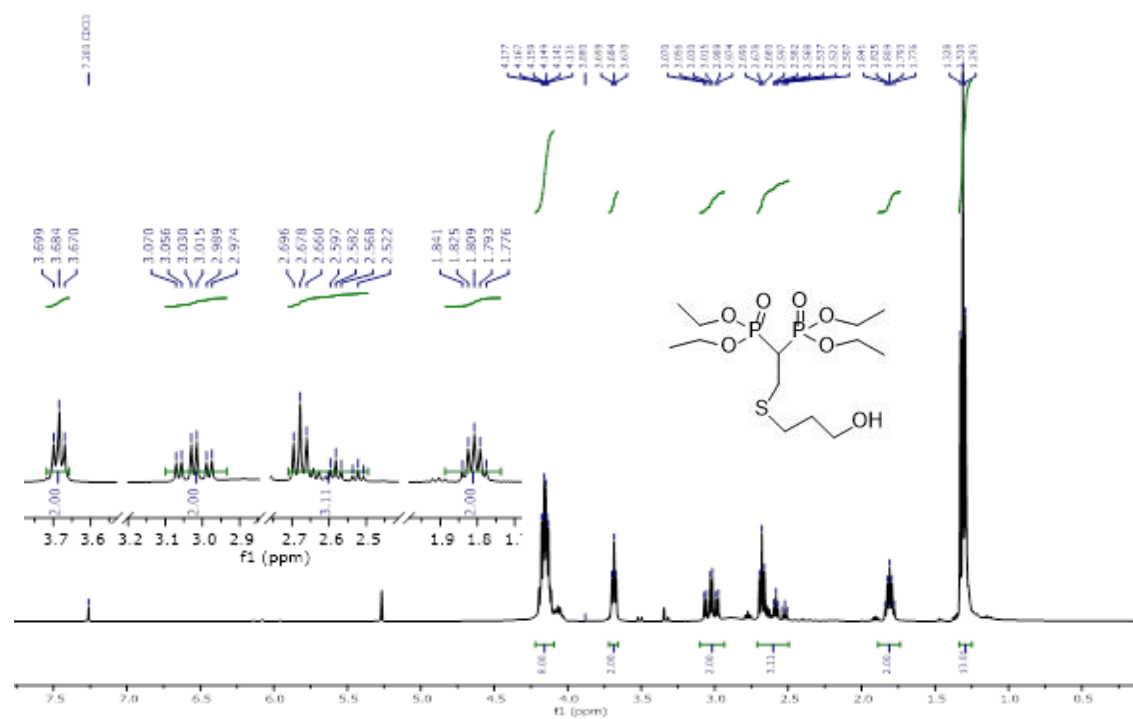
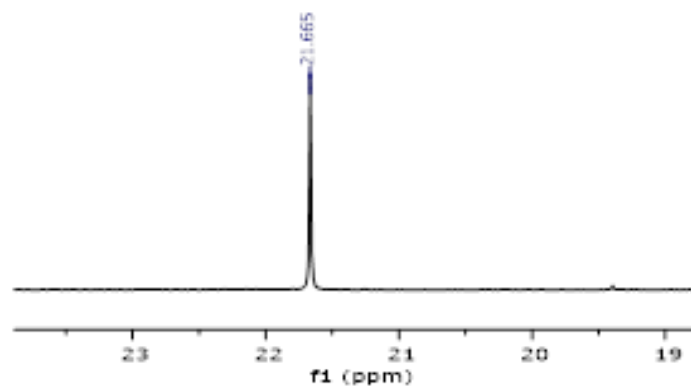
Figure 2.17: 2D-NMR HMBC of BPSAL

2.2.2 Tetraethyl (2-((3-hydroxypropyl)thio)ethane-1,1-diyl)bis(phosphonate) (BPHPT)



Scheme 2.7: Synthesis of BPHPT.

¹H-NMR spectra show typical resonances for vinylic proton (doublet of doublets) at high field (Figure 2.18). 2D-NMR -COSY showed typical ¹H-¹H cross resonances among the ethyl ester protective groups. The HMBC 2D-NMR spectrum show long range ¹³C-¹H resonances, helping to assign ¹³C signals as reported on Figure 2.20.

Figure 2.18: $^1\text{H-NMR}$ of BPHPTFigure 2.19: $^{31}\text{P-NMR}$ of BPHPT

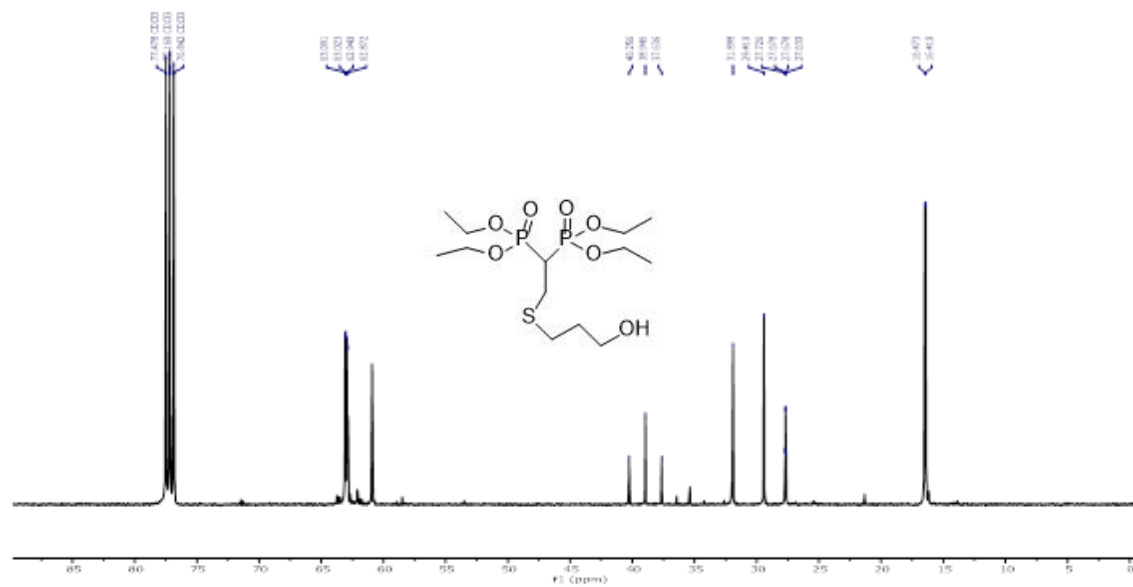
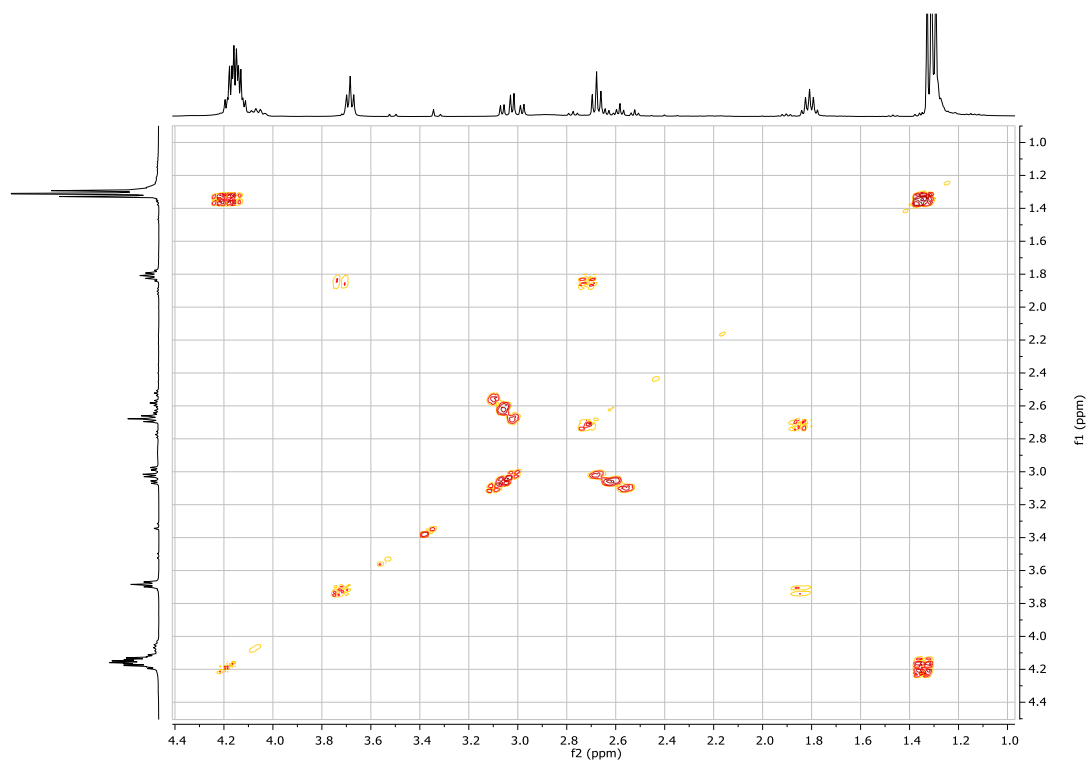
Figure 2.20: ^{13}C -NMR of BPHPT

Figure 2.21: 2D-NMR COSY of BPHPT

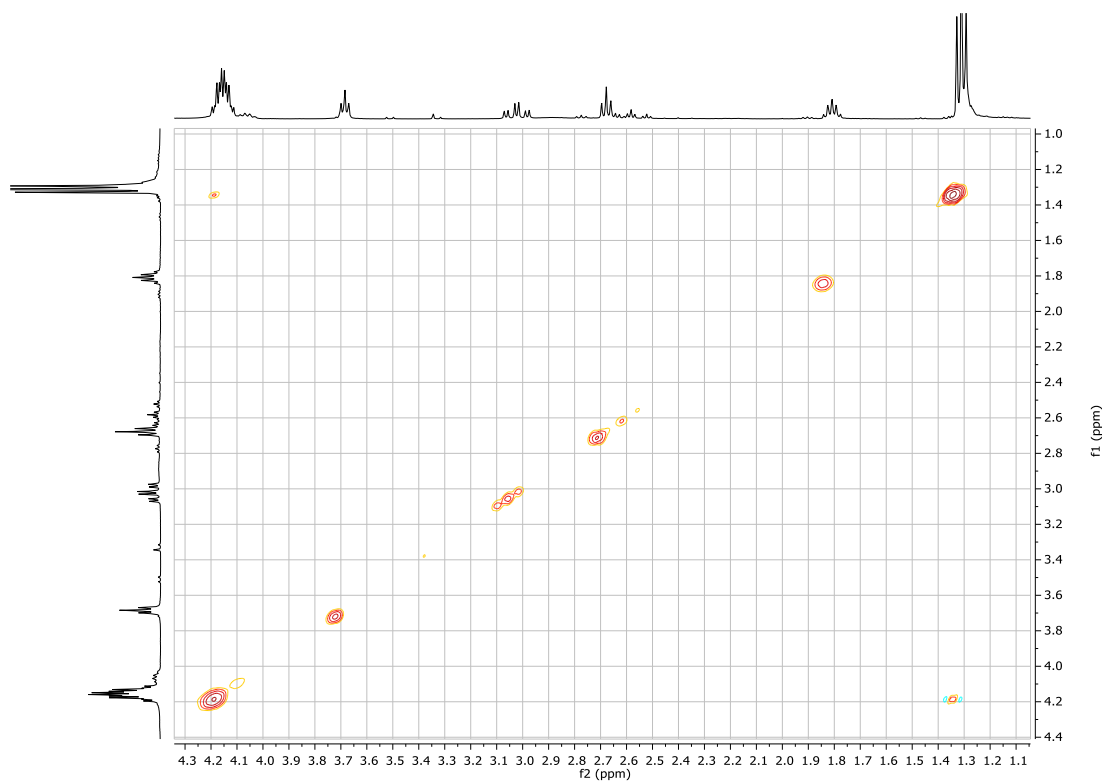


Figure 2.22: 2D-NMR NOESY of BPHPT

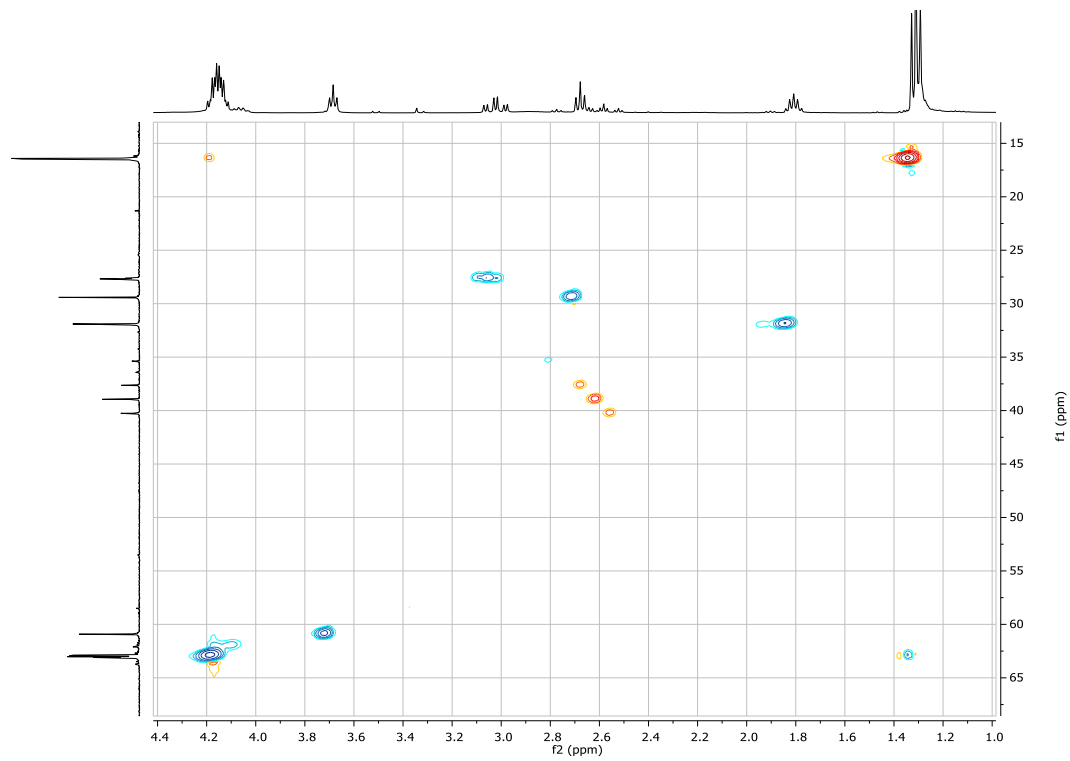


Figure 2.23: 2D-NMR HSQC of BPHPT

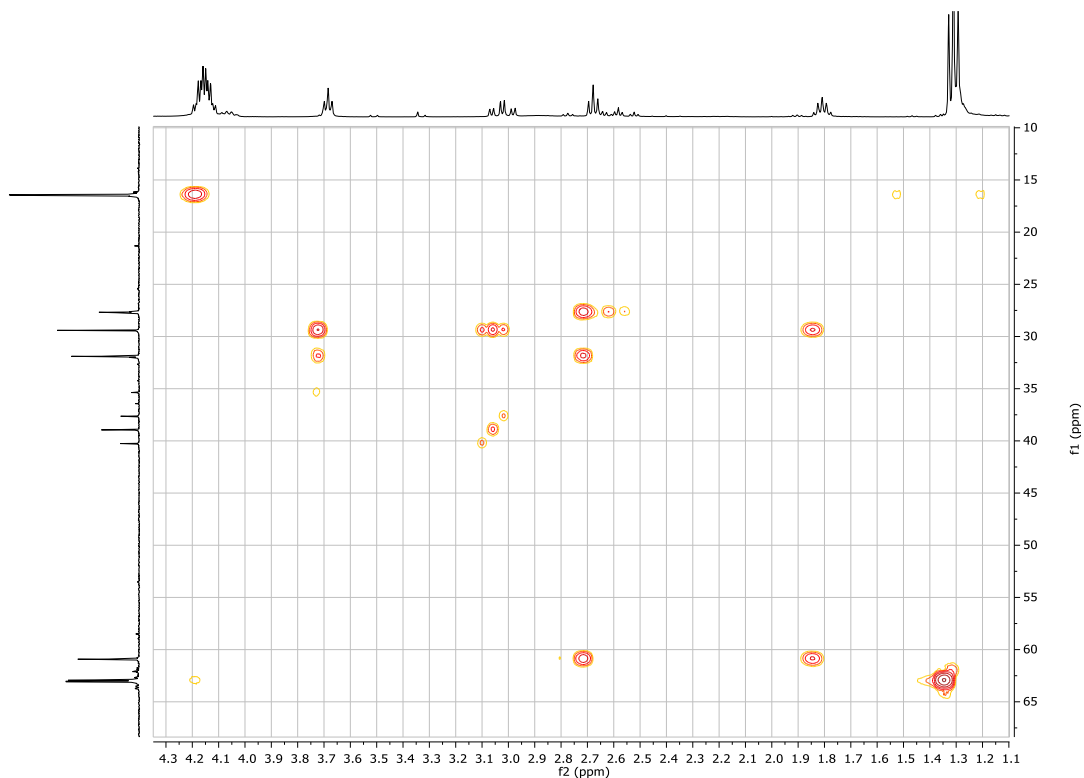
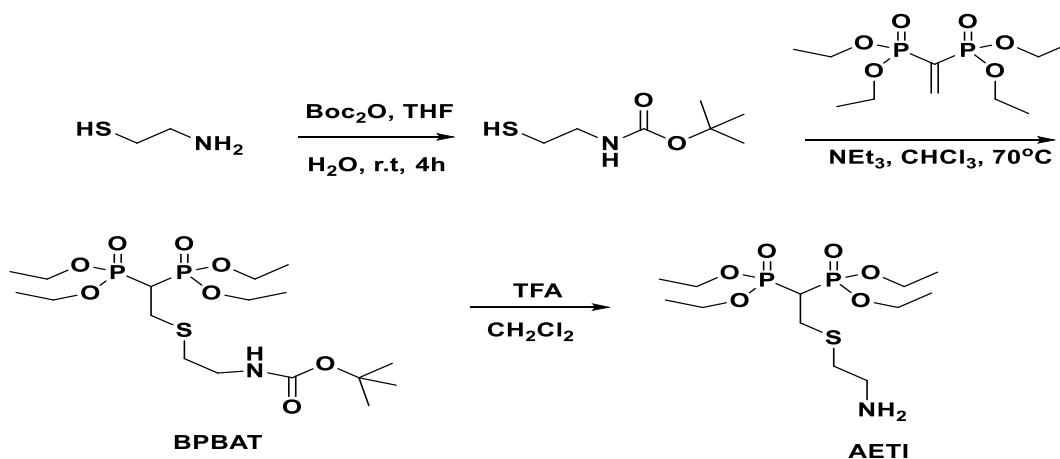


Figure 2.24: 2D-NMR HMBC of BPHPT

2.2.3 tetraethyl (2-((2-aminoethyl)thio)ethane-1,1-diyl)bis(phosphonate) (AETI)

In the case of the amino substituted BP (AETI) the commercially available 2-aminoethanethiol turned out to react with VBP forming a mixture of N and S β -substituted bis-phosphonic esters.



Scheme 2.8: Synthesis of AETI.

Because of this it was necessary to preliminarily protect the amino functionality with Boc forming the protected thiol that was further reacted with VBP forming the intermediate tetraethyl

2-((2-Boc-amino) ethanethiol) ethane-1,1-diylidiphosphonate (BPBAT). Then the deprotection of Boc group is done by trifluoroacetic acid (TFA) to get AETI with good yield. (Scheme 2.8).

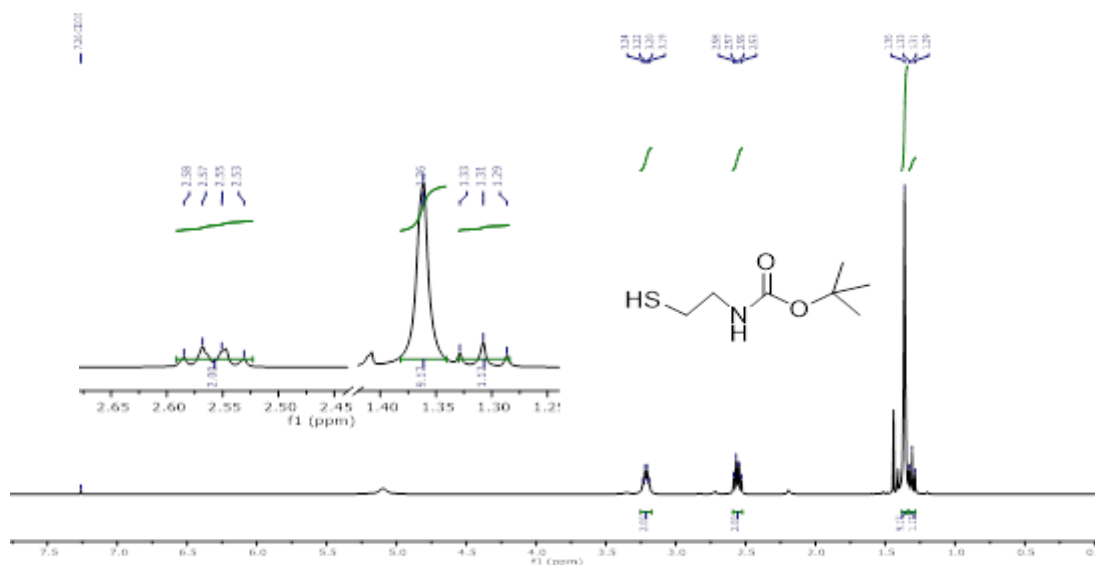


Figure 2.25: $^1\text{H-NMR}$ of 2-(Boc-amino) ethanethiol

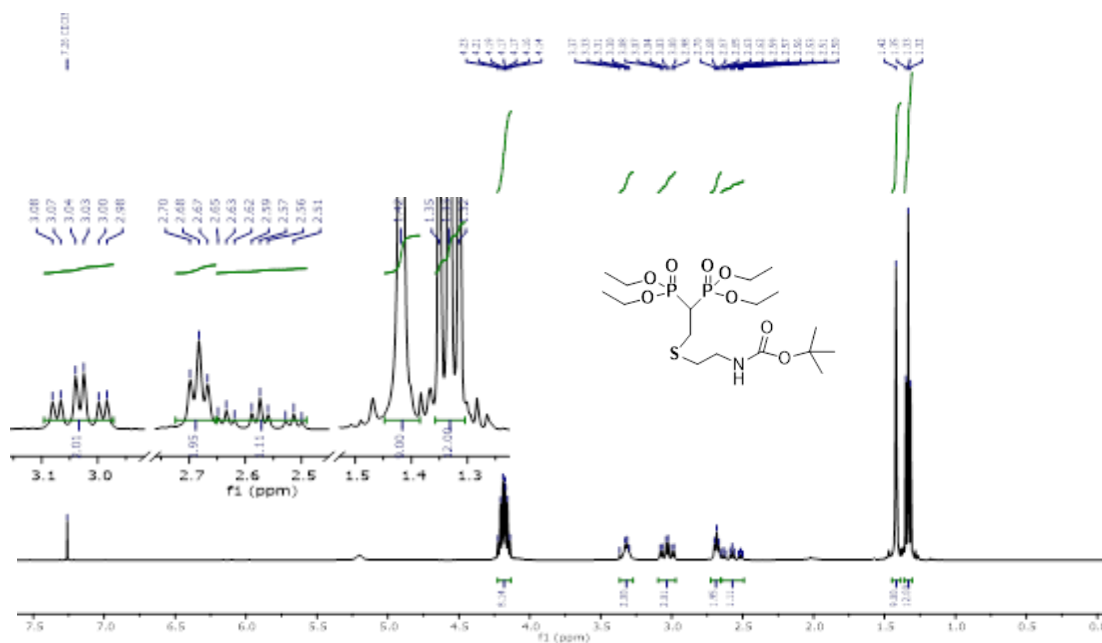


Figure 2.26: $^1\text{H-NMR}$ of BPBAT

$^1\text{H NMR}$ spectra represents a sharp singlet at high field 1.42ppm that confirmed the protection of amino group by Boc and shows typical triplet of triplet and triplet of doublet that belongs to α - and β - protons respectively (Figure 2.26). A comparison is reported between the traditional $^1\text{H-NMR}$ spectrum of BPBAT and the phosphorous decoupled $^1\text{H} \{^{31}\text{P}\}$ -NMR spectrum (Figure

2.28) in order to underline the presence of ^1H - ^{31}P couplings. Only S-containing β -substituted bis-phosphonic esters is formed confirmed by the ^{31}P NMR spectra that shows one singlet at 21.56 ppm due to symmetry of the intermediate BPBAT compound.

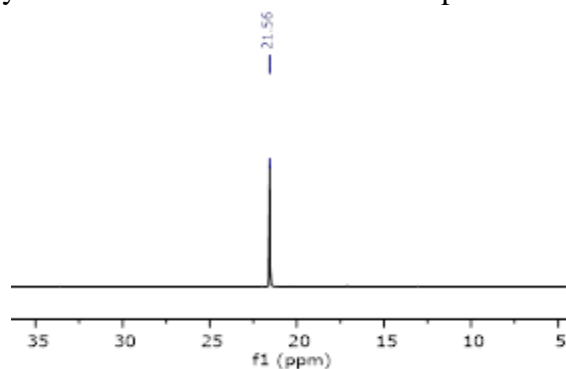


Figure 2.27: ^{31}P -NMR of BPBAT

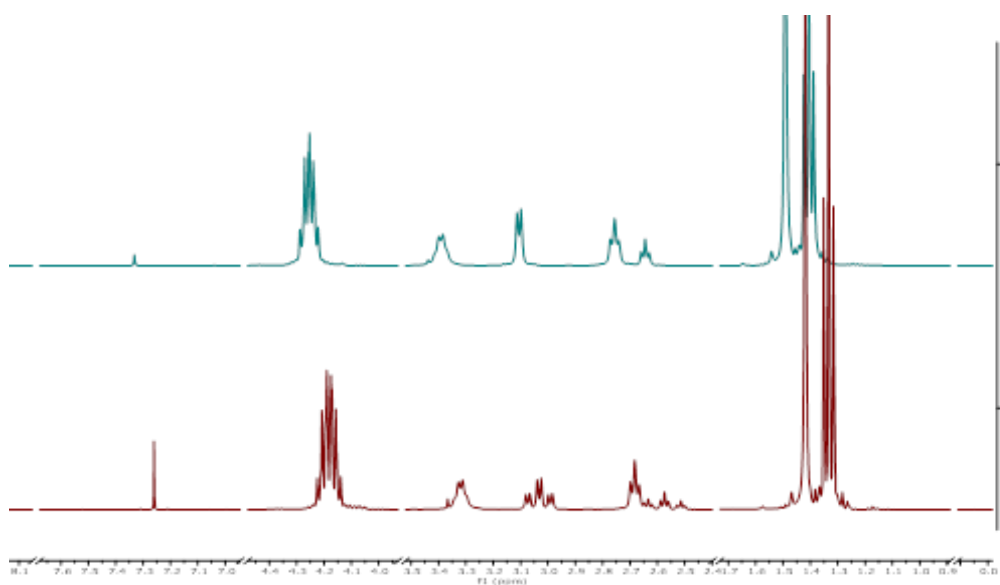


Figure 2.28: Comparison of ^1H NMR (red) & $^1\text{H}\{^{31}\text{P}\}$ NMR (blue) of BPBAT

2D-NMR COSY (Figure 2.30) showed usual cross-peak between ethyl ester protections protons highlighting ^1H - ^1H resonances between α and β -protons. 2D-NMR HSQC (Figure 2.32) and HMBC (Figure 2.33) helped to confirm the synthesis of desired Boc protected amino-BP product, giving the possibility to verify ^{13}C assignments.

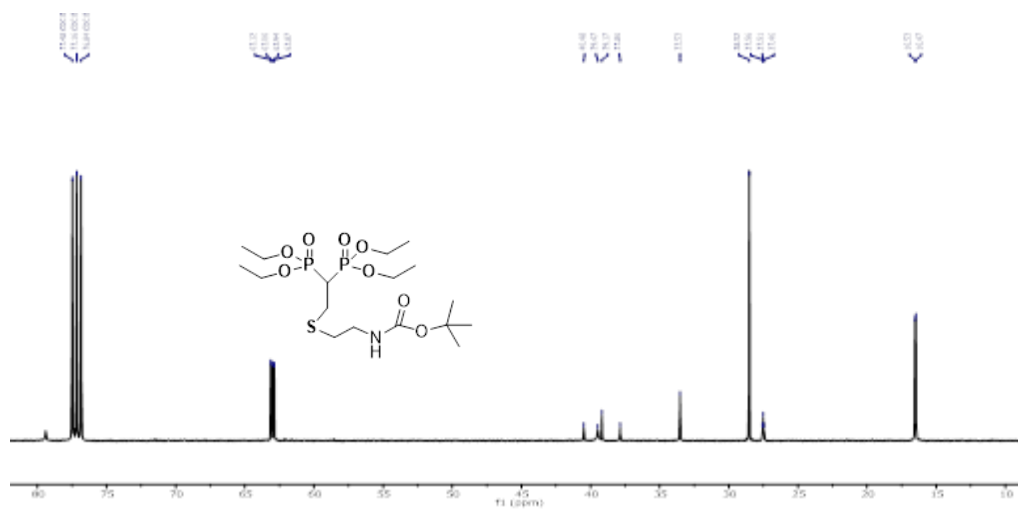
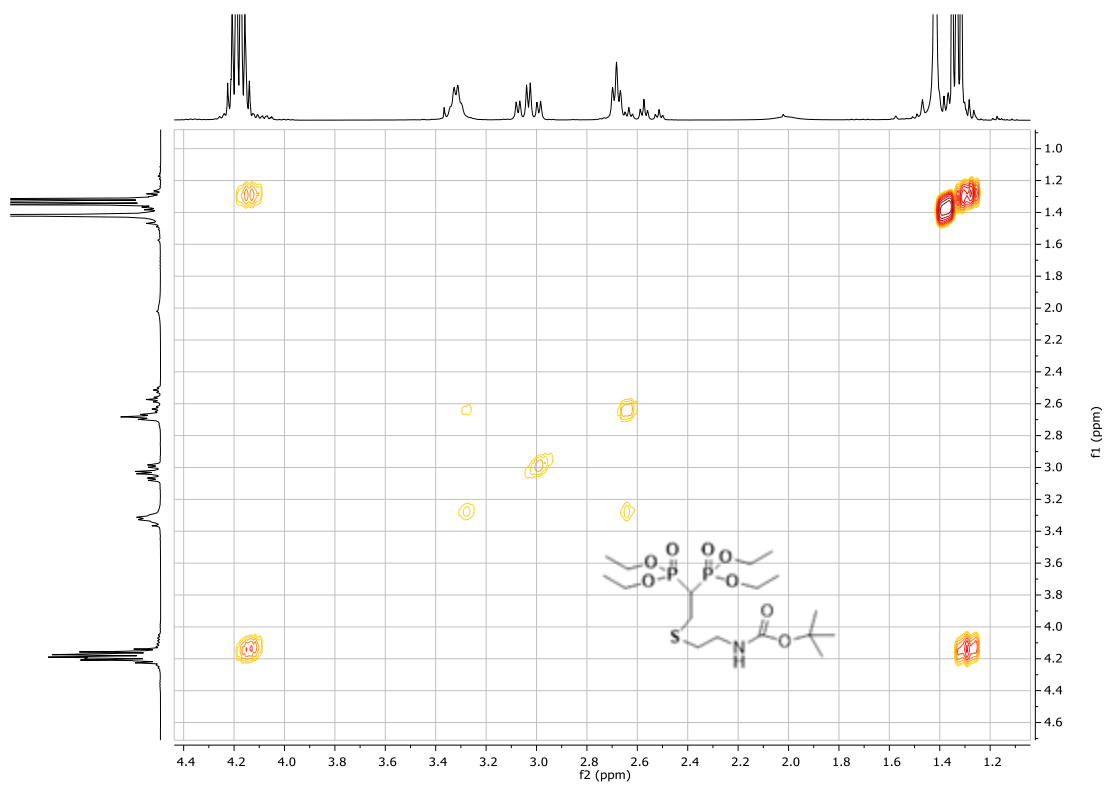
Figure 2.29: ^{13}C NMR of BPBAT

Figure 2.30: 2D-NMR COSY of BPBAT

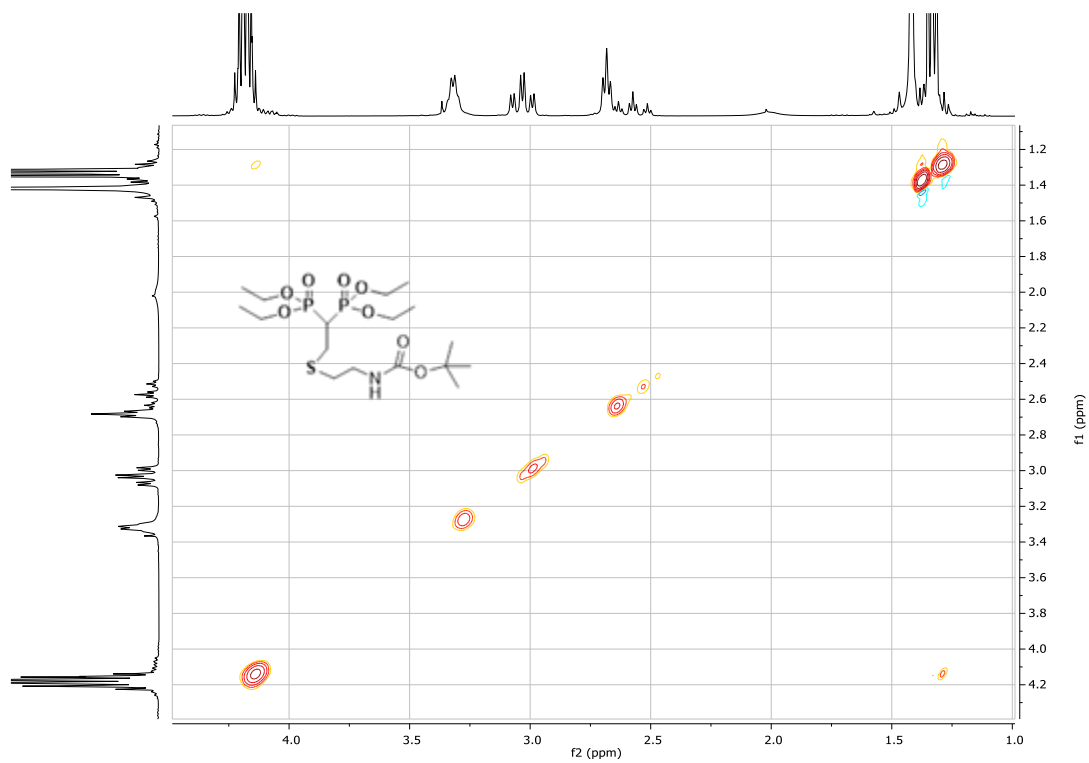


Figure 2.31: 2D-NMR NOESY of BPBAT

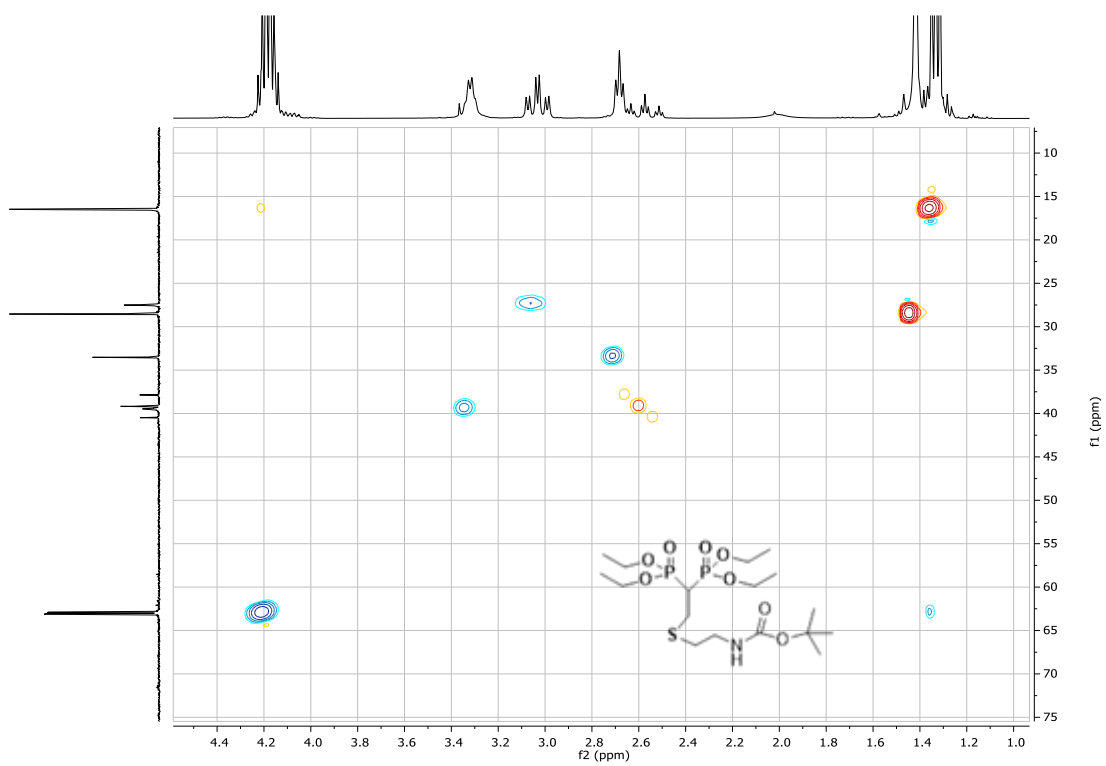


Figure 2.32: 2D-NMR HSQC of BPBAT

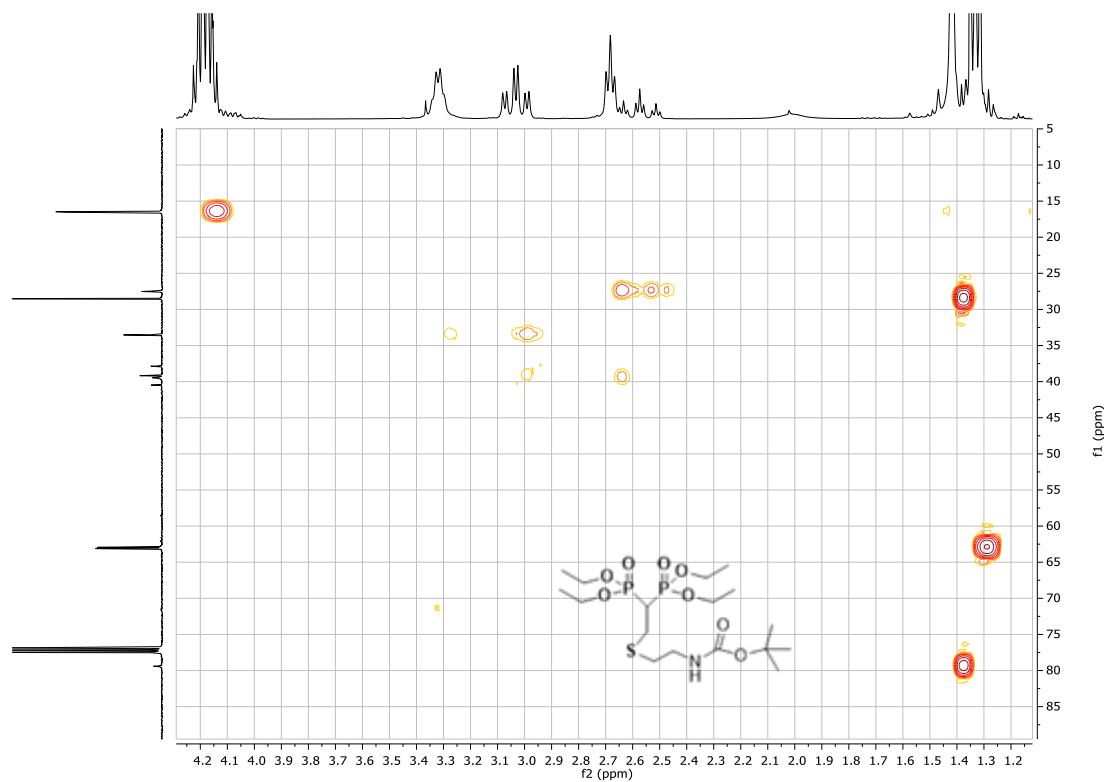


Figure 2.33: 2D-NMR HMBC of BPBAT

The corresponding Boc deprotected amino-bisphosphonic compound (AETI) was isolated in good yields and characterized by ^1H and ^{31}P -NMR spectroscopy in CHCl_3 . The absence of sharp singlet at high field proved the deprotection of amino group (Figure 2.34).

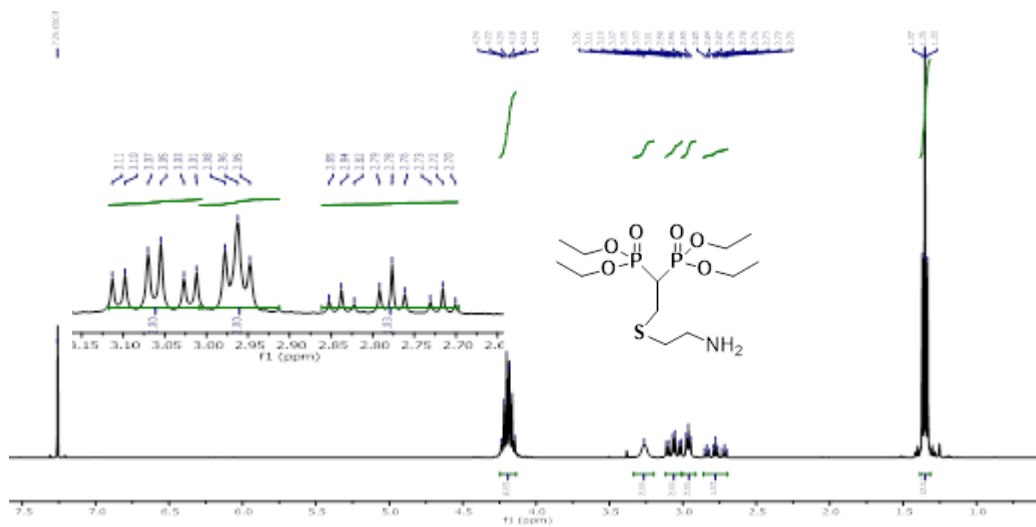


Figure 2.34: ^1H -NMR of AETI

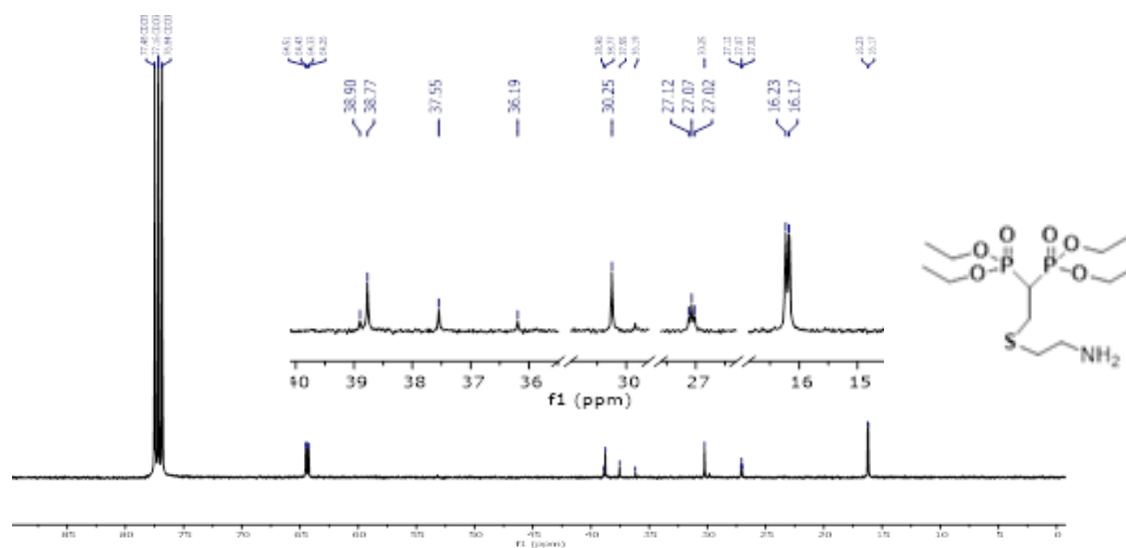
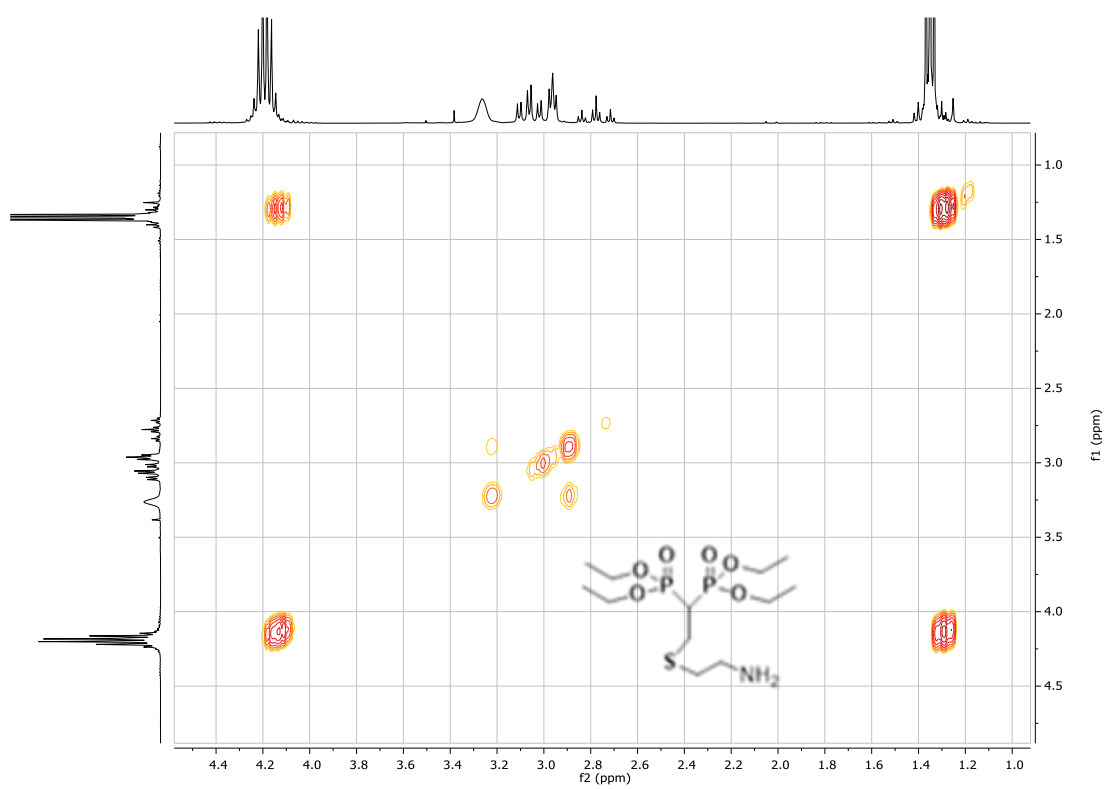
Figure 2.37: ^{13}C NMR of AETI

Figure 2.38: 2D-NMR COSY of AETI

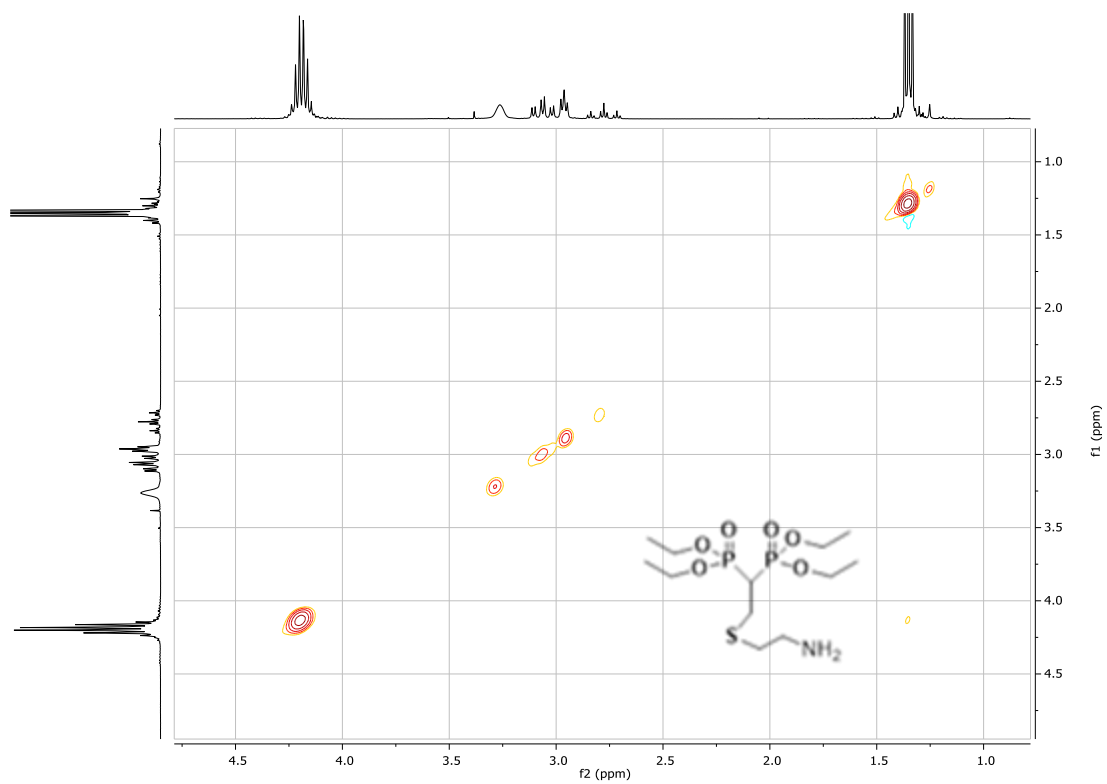


Figure 2.39: 2D-NMR NOESY of AETI

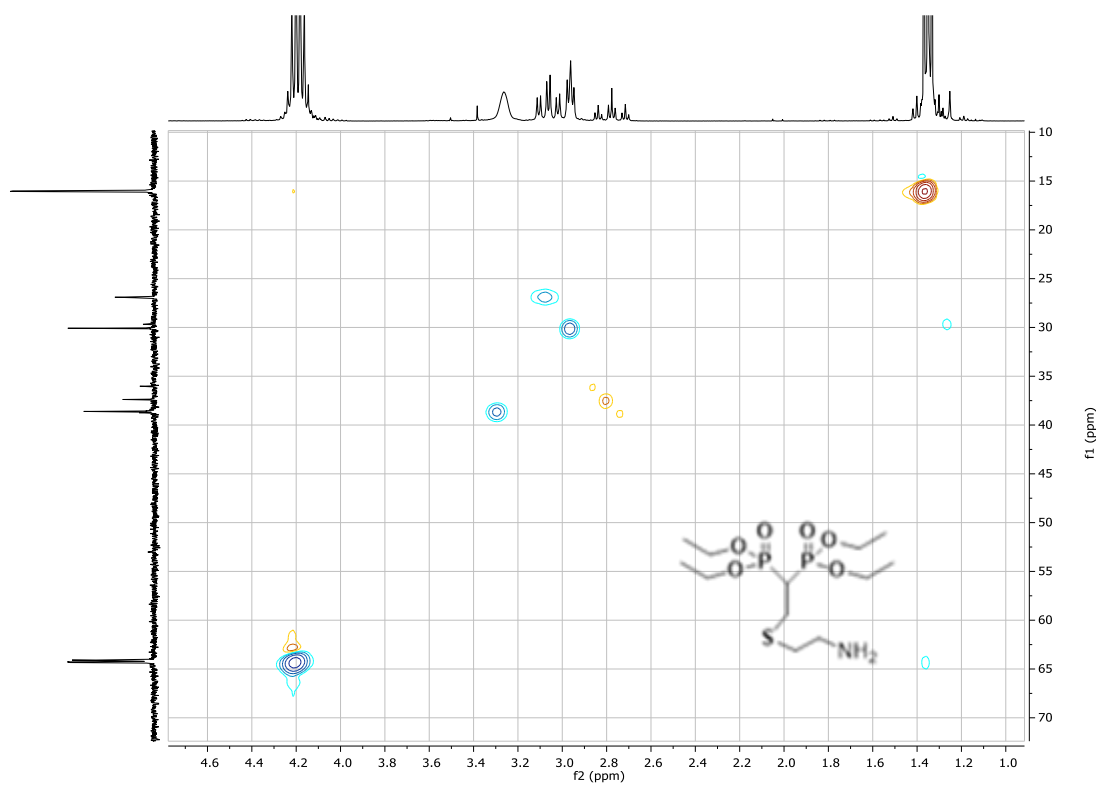


Figure 2.40: 2D-NMR HSQC of AETI

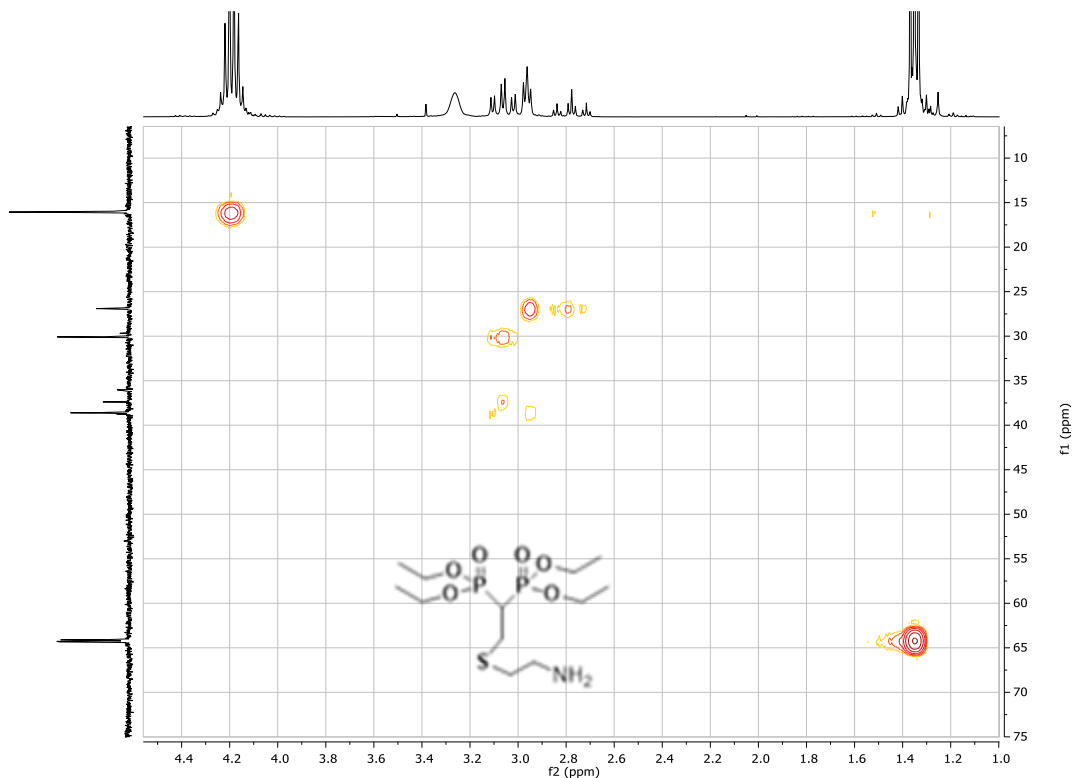
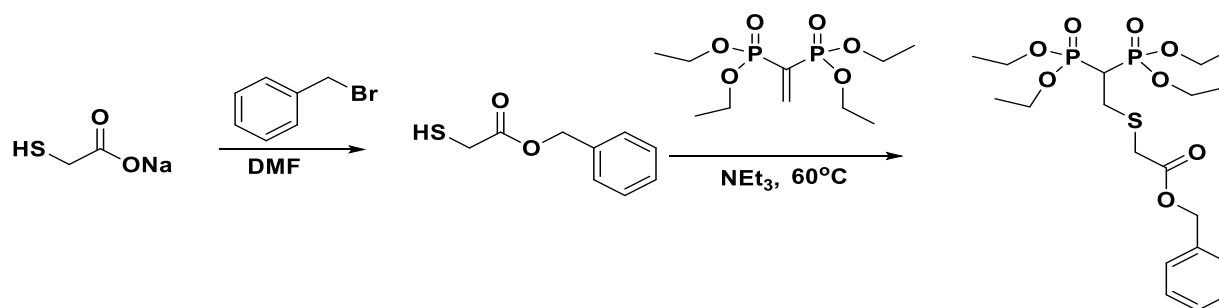


Figure 2.41: 2D-NMR HMBC of AETI

2.2.4 Benzyl 2-((2,2-bis(diethoxyphosphoryl)ethyl)thio)acetate (BPBTG)

For the synthesis of BP compound containing free carboxylic end group, the reaction of sodium thioglycolate with VBP did not provide the desired product even using polar solvents like DMSO or DMF observing in all cases a series of products derived by O and S attack on the β position of VBP.



Scheme 2.9: Synthesis of BPBTG

In order to selectively protect the carboxylic unit sodium thioglycolate was reacted in DMF with benzyl bromide under inert atmosphere forming the corresponding benzyl ester with the free thiol moiety that was reacted with VBP directly without isolation, forming the desired thio-Michael addition product (BPBTG) (Scheme 2.9) that was eventually deprotected to form the free bis-phosphonic acid.

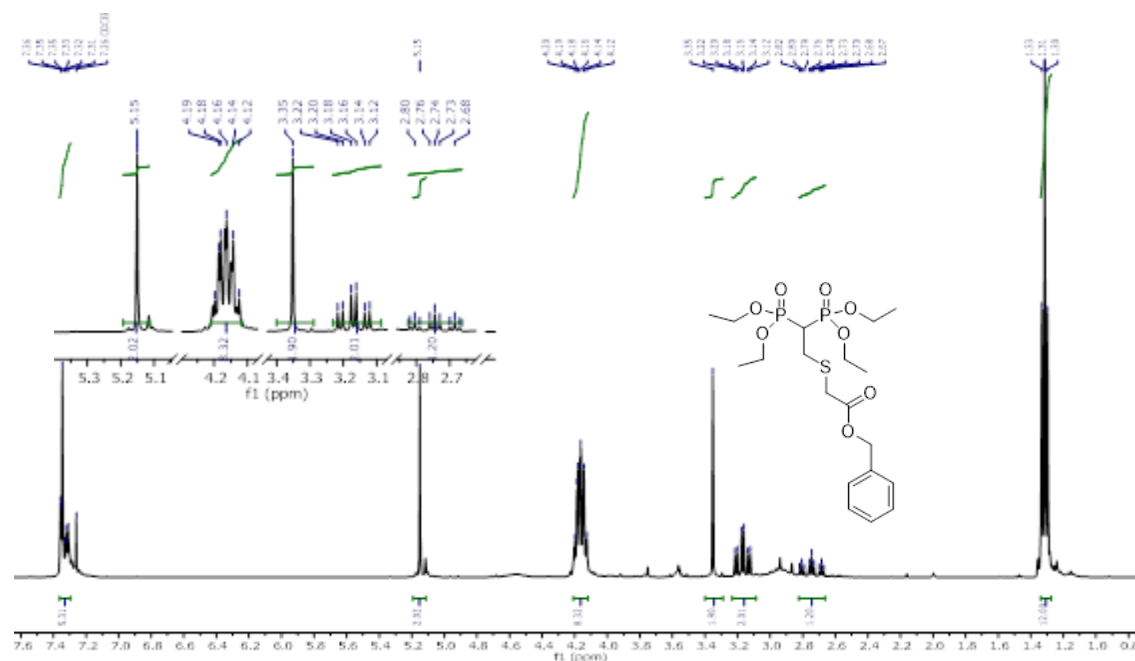


Figure 2.42: ^1H NMR of BPBTG

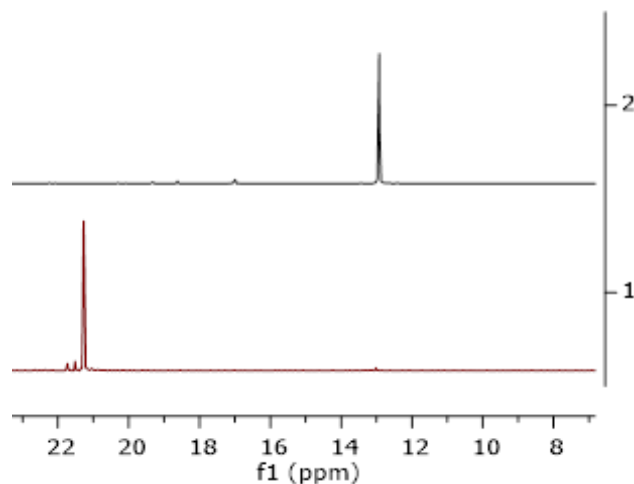


Figure 2.43: Comparison of $^{31}\text{P}\{^1\text{H}\}$ -NMR of BPBTG (red) & VBP (black)

^1H NMR spectra (Figure 2.43) represents typical resonance for benzyl-proton multiplet at low field 7.40 – 7.27 ppm. A comparison between the $^{31}\text{P}\{^1\text{H}\}$ NMR spectra of VBP (black) and BPBTG (red) confirmed the complete conversion of VBP to BPBTG. $^1\text{H}\{^{31}\text{P}\}$ -NMR spectra shows simplification of the resonance peaks, for example a triplet with small coupling constant 6.0 Hz instead of triple of triplet with high coupling constant at 24.0 Hz for α -proton (Figure 2.44). ^{13}C -NMR shows the typical resonance peaks at around 128 ppm for benzyl carbon. 2D-NMR NOESY (Figure 2.47) experiments revealed intense NOE cross-couplings between ethyl ester proton 2D-NMR HMBG (Figure) showed long range ^{13}C - ^1H resonances, helping to assign ^{13}C signals as reported on Figure 2.45

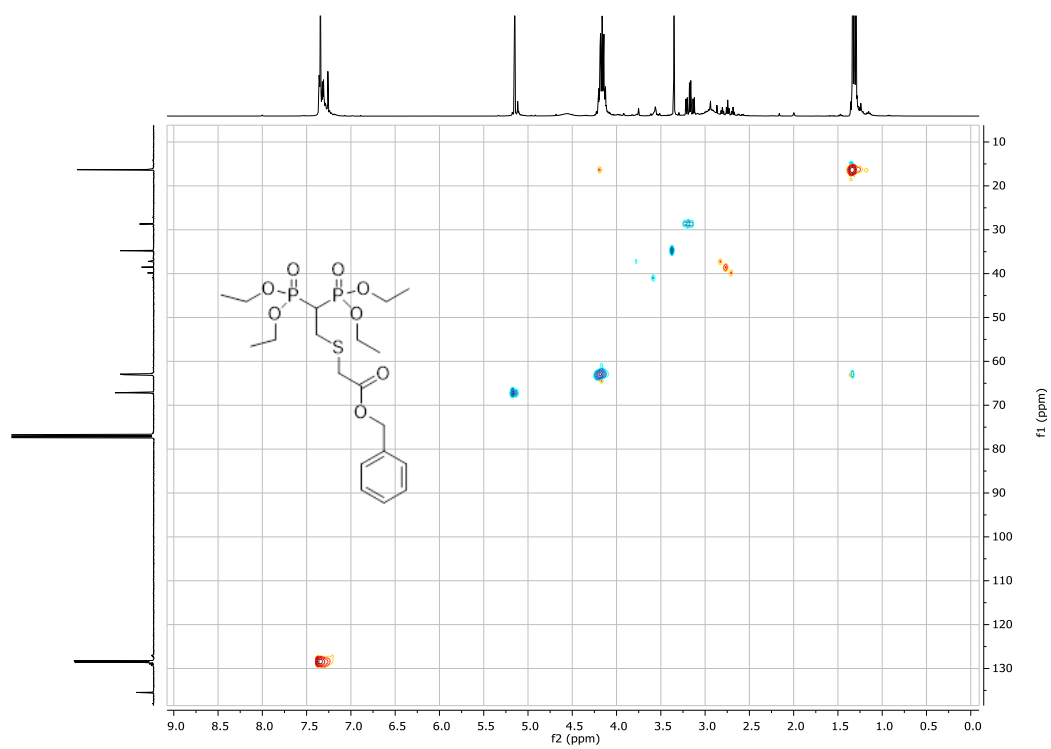


Figure 2.48: 2D-NMR HSQC of BPBTG

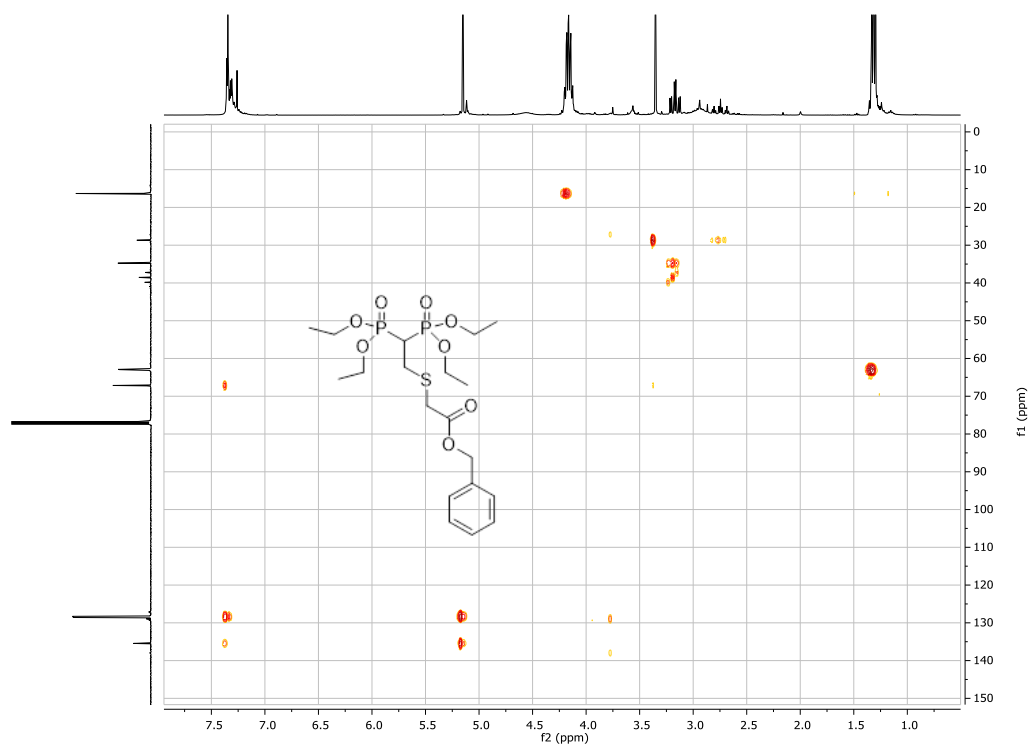
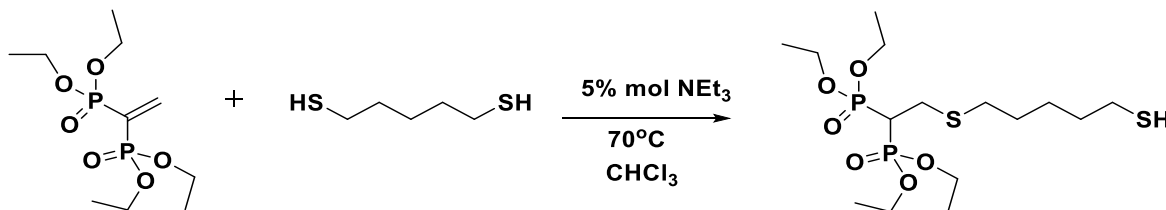


Figure 2.49: 2D-NMR HMBC of BPBTG

2.2.5 Tetraethyl (2-(pentamethylene dimercaptan) ethane-1,1-diyl)bis(phosphonate) (BPPMD)

The product was obtained in hundreds mg scale, purified by flash chromatography and characterized by NMR spectroscopy. BPPMD characterization is reported below



Scheme 2.10: Synthesis of BPPMD

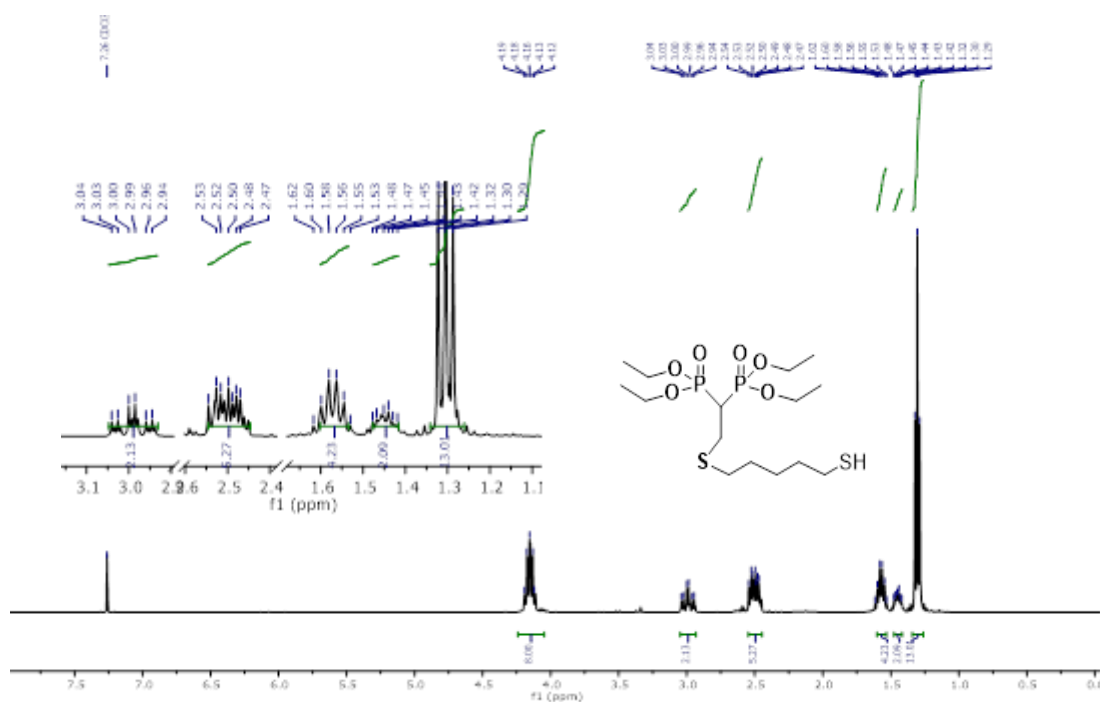
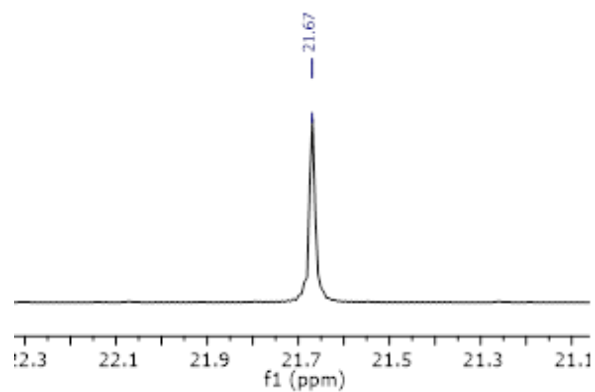
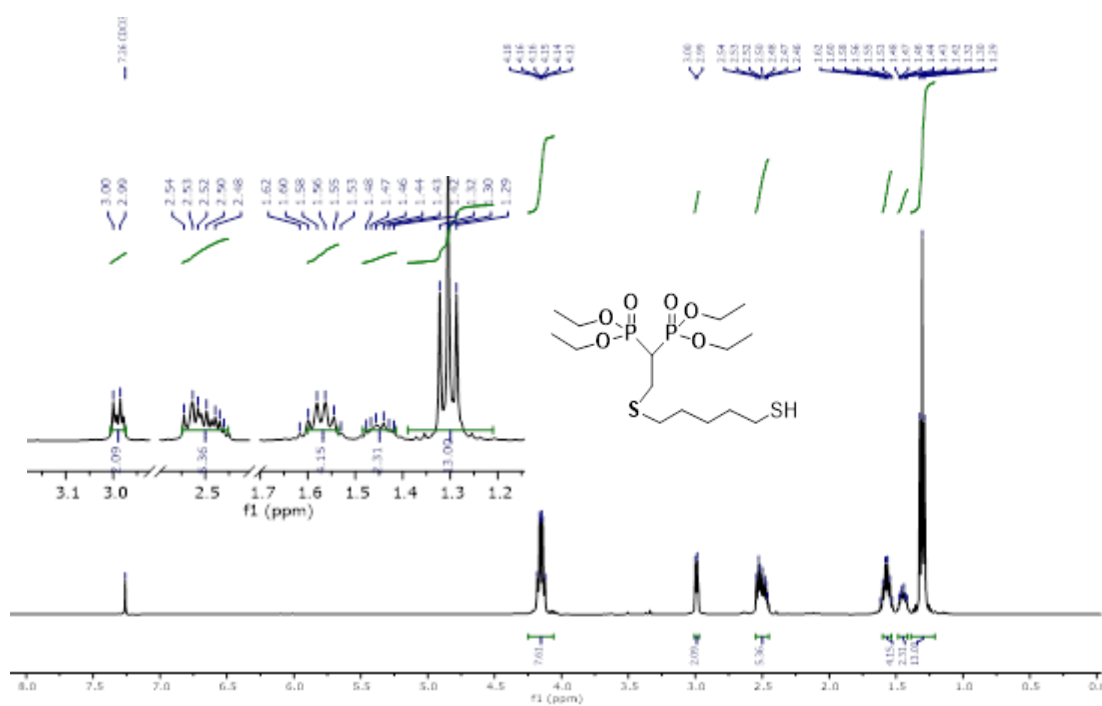


Figure 2.50: ¹H NMR of BPPMD

The characterization of the BPPMD compound is reported with comparison between ¹H-NMR & ¹H {³¹P}-NMR, simplification of the resonance peaks showed in the latter spectrum of α and β protons. The ³¹P {¹H}-NMR showed the presence of a strong singlet at downfield 21.67 ppm compare to VBP. The 2D-NMR COSY (Figure 2.55) showed usual cross-peak between ethyl ester protections protons highlighting ¹H-¹H resonances between α and β protons. 2D-NMR HMBC (Figure 2.57) helped to confirm the synthesis of desired BPPMD product, giving the possibility to verify ¹³C assignments (Figure 2.54).

Figure 2.51: $^{31}\text{P}\{^1\text{H}\}$ -NMR of BPPMDFigure 2.52: $^1\text{H}\{^{31}\text{P}\}$ -NMR of BPPMD

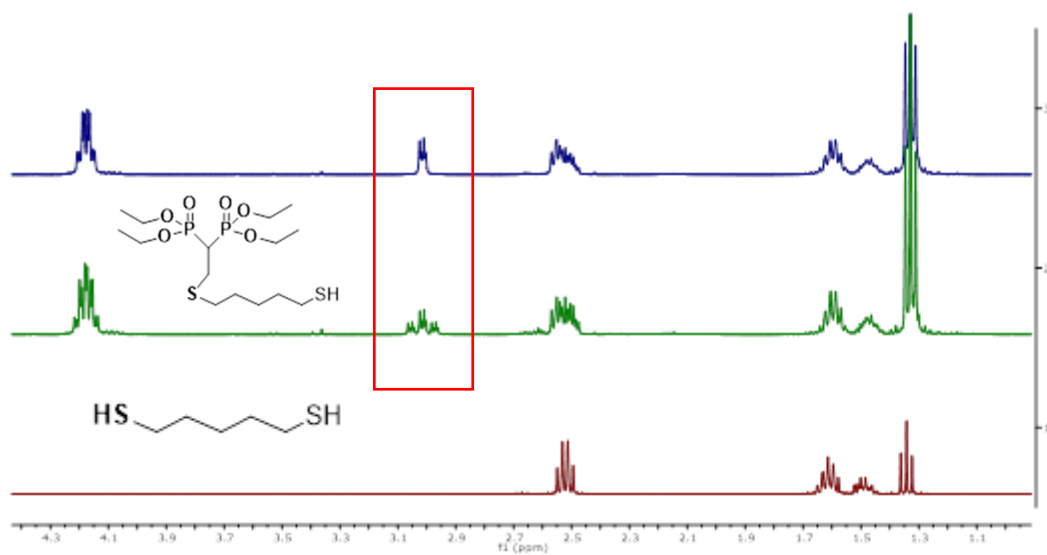


Figure 2.53: Comparison between ^1H -NMR (green) & $^1\text{H}\{^{31}\text{P}\}$ -NMR (blue) of BPPMD ester and ^1H -NMR of 1,5- Penta dithiol reagent (red)

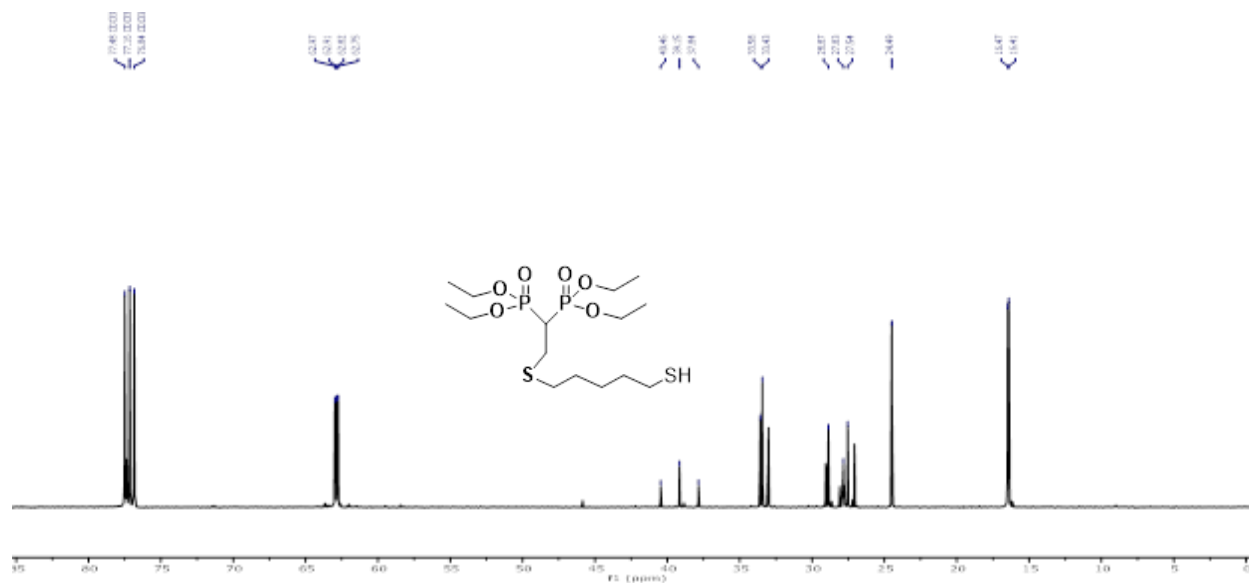


Figure 2.54: ^{13}C NMR of BPPMD

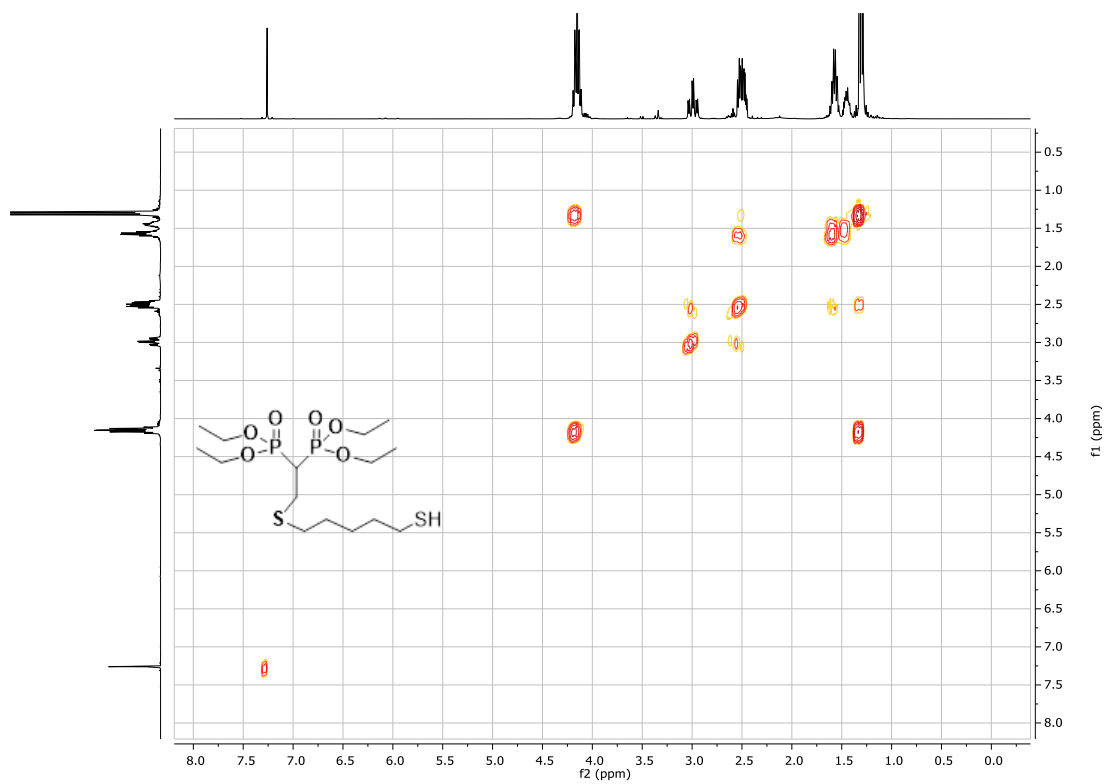


Figure 2.55: 2D NMR- COSY of BPPMD

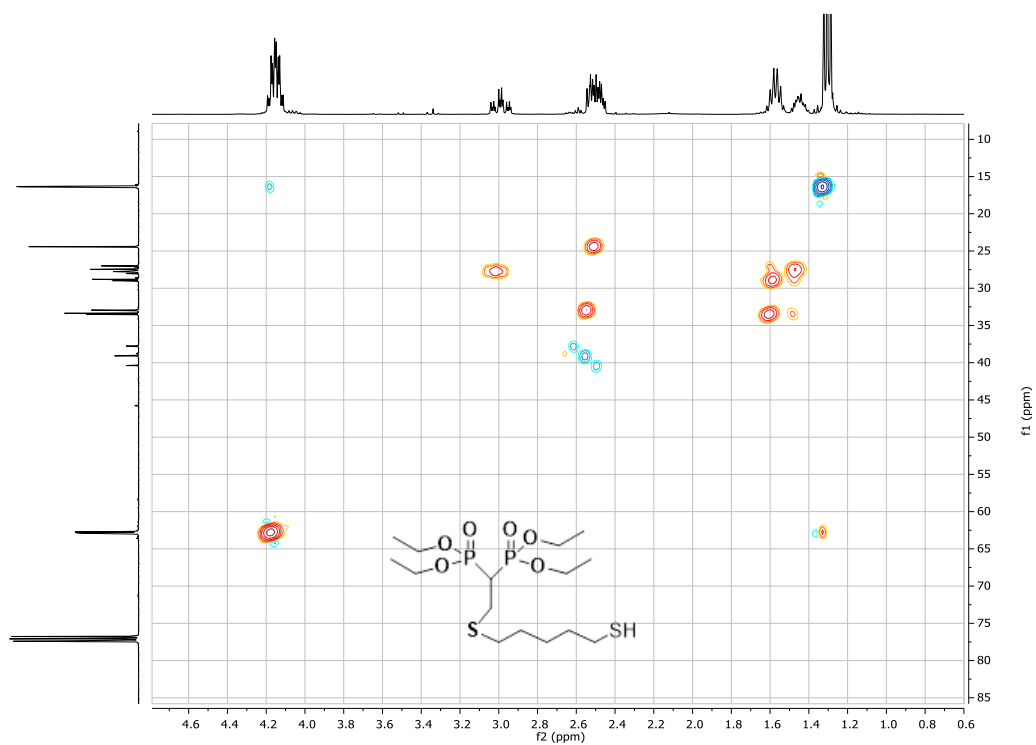


Figure 2.56: 2D NMR- HSQC of BPPMD

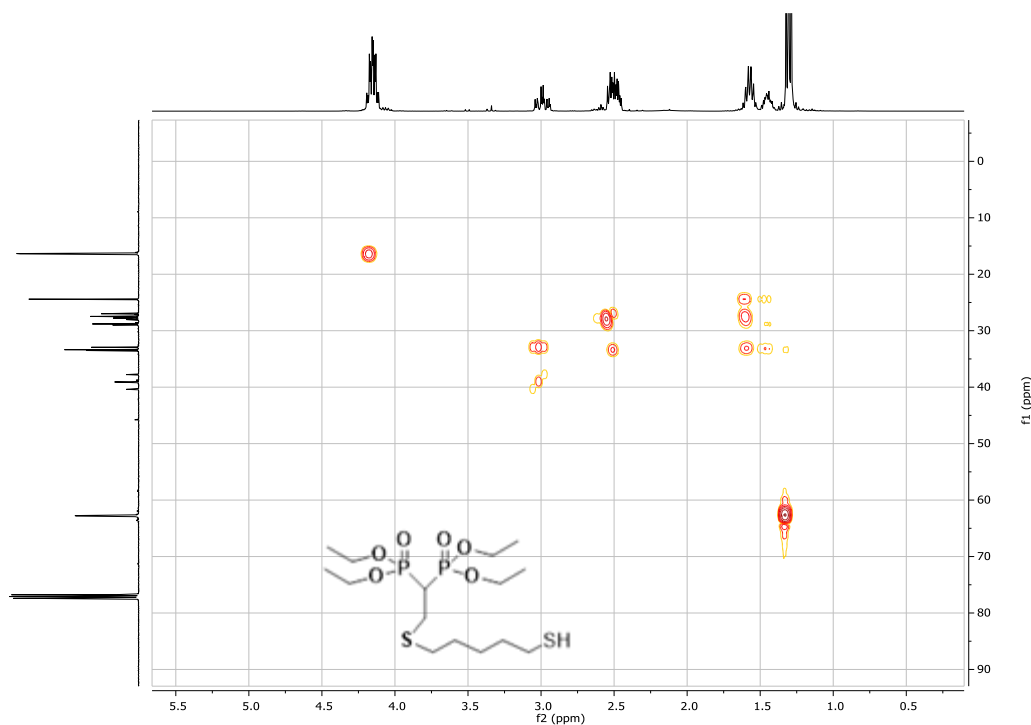
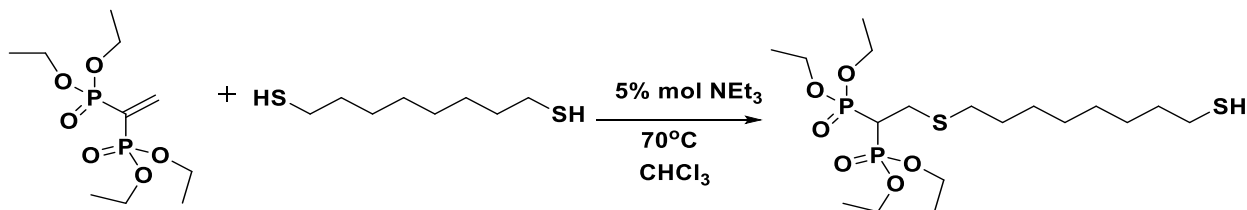


Figure 2.57: 2D NMR- HMBC of BPPMD

2.2.6 Tetraethyl 2-(octamethylene dimercaptan) ethane-1,1 diyl)bis(hosphonate) (BPOMD)

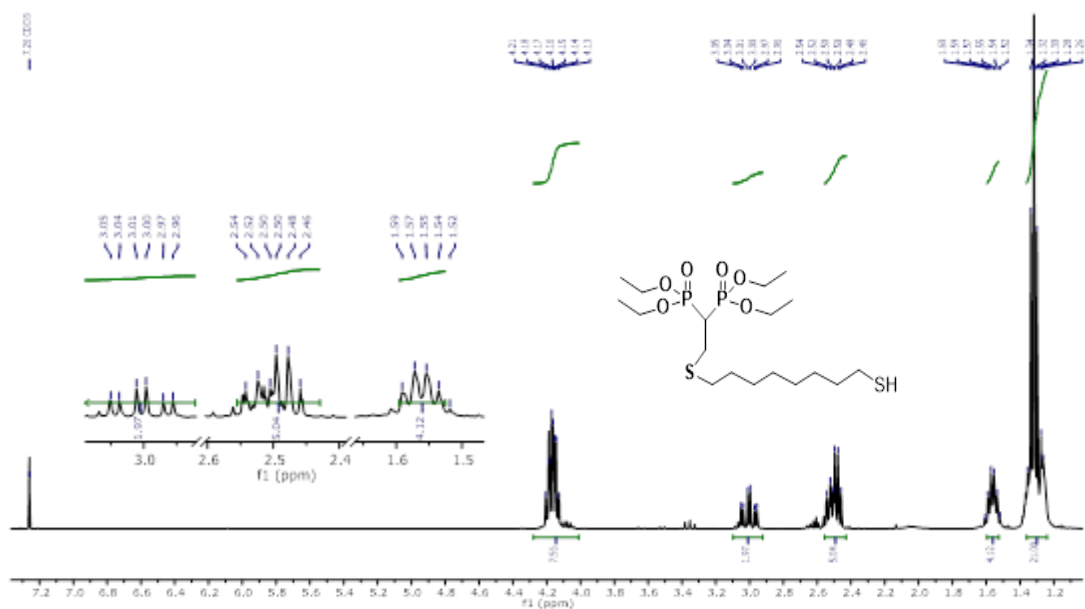
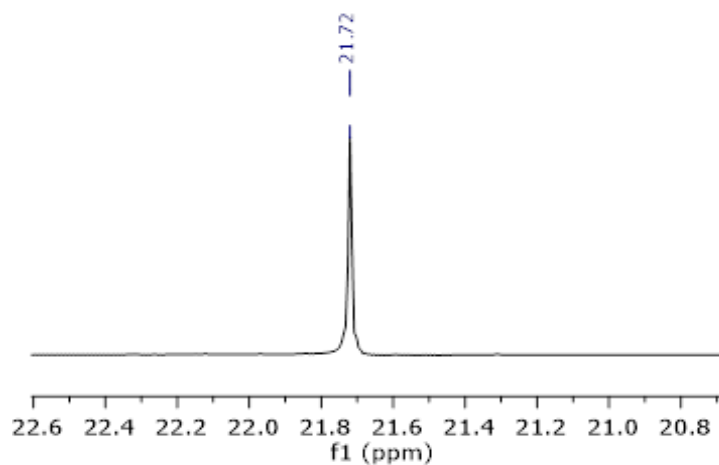
The desired product obtained by the reaction between VBP and 1,8-octane dithiol with 1: 1 molar ratio in the presence of base catalyst trimethyl amine. The product was obtained as colorless liquid with 96%.



Scheme 2.11: Synthesis of BPOMD

^1H NMR spectra showed several multiplets at 1.25 to 2.70 ppm to corresponding methylene proton in the ethyl ester portion along with long chain free thiol portion. $^{31}\text{P}\{^1\text{H}\}$ NMR represent a sharp singlet at 21.72 ppm.

2D-NMR HSQC (Figure 2.61) helped to confirm the synthesis of desired product by analyzing the correlations between a carbon and its attached protons. 2D-NMR HMBC of BPOMD showed long range ^{13}C - ^1H resonances that turned out to be very useful to assign ^{13}C resonances as reported in Figure 2.60.

Figure 2.58: $^1\text{H-NMR}$ of BPOMDFigure 2.59: $^{31}\text{P-NMR}$ of BPOMD

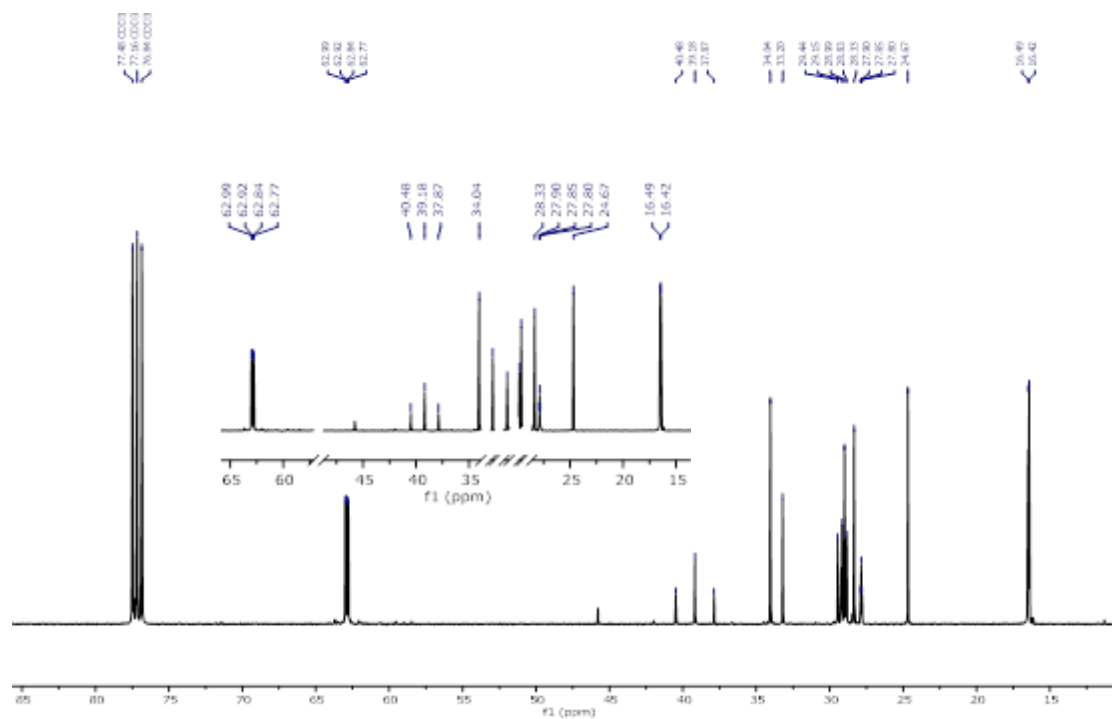
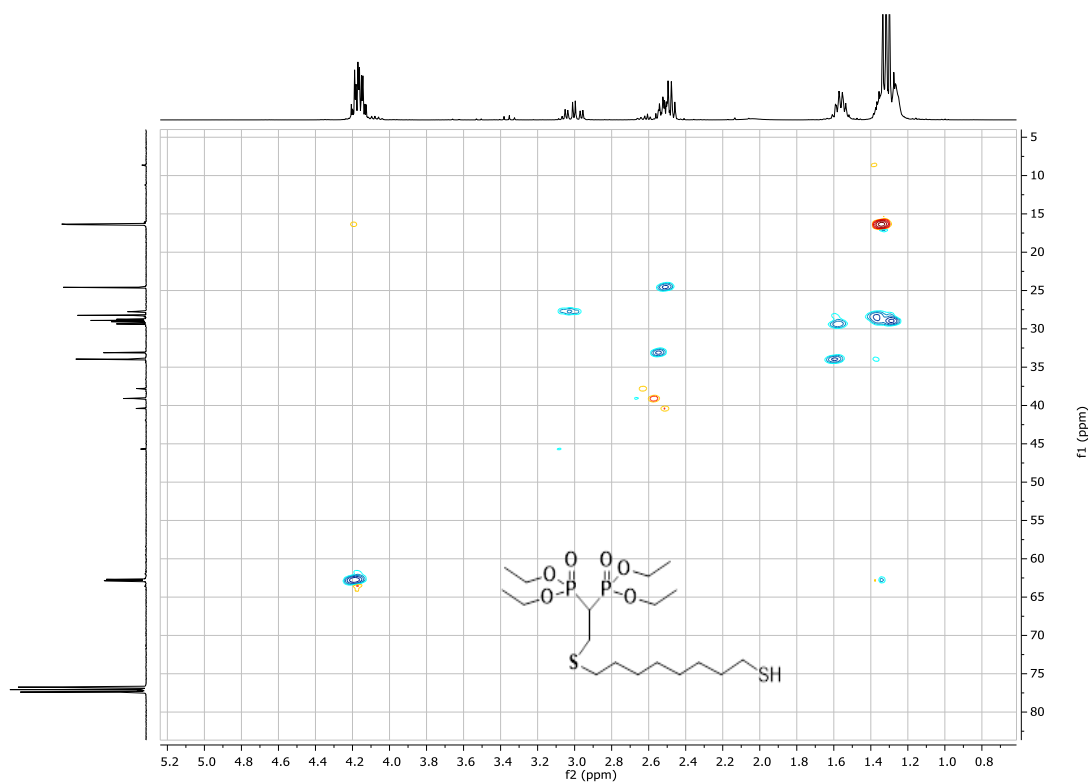
Figure 2.60: ^{13}C -NMR of BPOMD

Figure 2.61: 2D NMR- HSQC of BPOMD

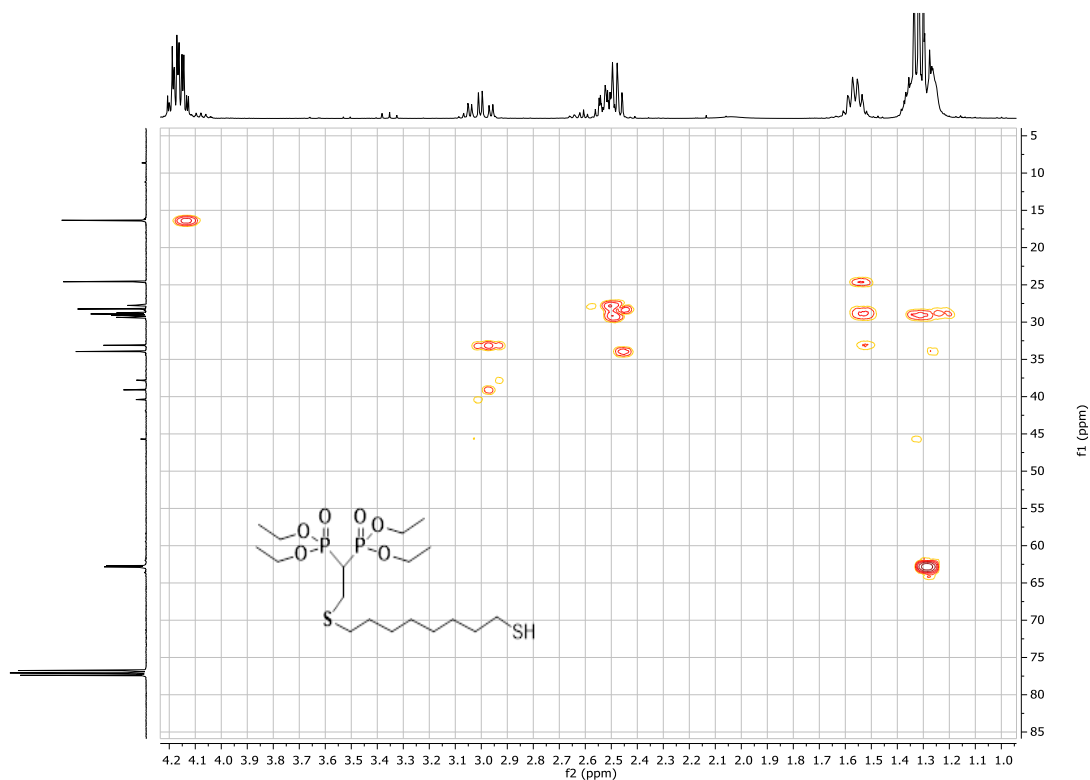
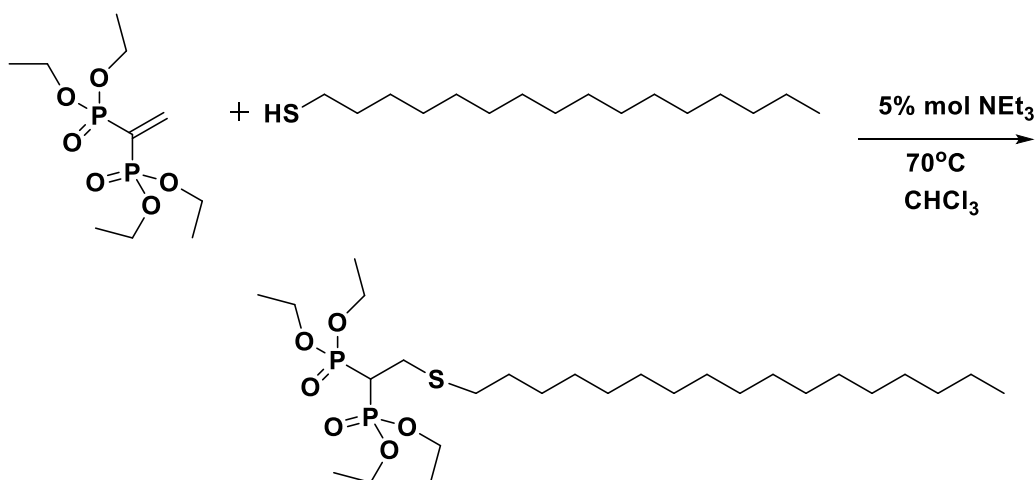


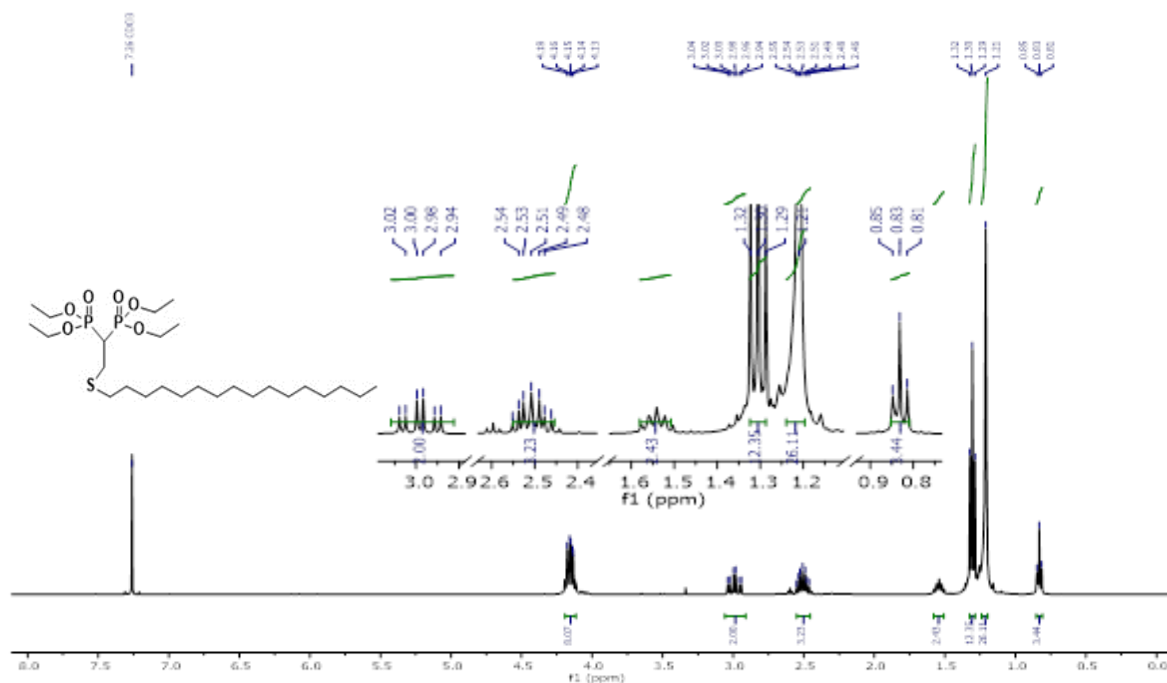
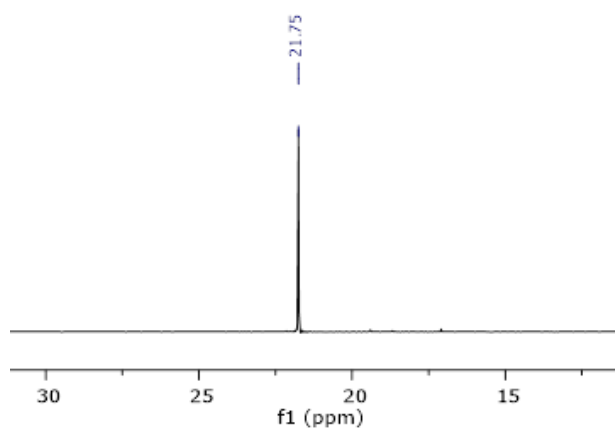
Figure 2.62: 2D NMR- HMBC of BPOMD

2.2.7 Tetraethyl (2-(1-hexadecane thiol) ethane-1,1 diyl)bis(phosphonate) (BPHDT)

To produce hydrophobic environment on the metal surface we need to prepare a BP compound with long alkyl chain. The S-containing BP compound with long alkyl chain BPHDT prepared with 1-hexadecane thiol in molar ratio. The product obtained with 93% yield.



Scheme 2.12: Synthesis of BPHDT.

Figure 2.63: ^1H NMR of BPHDTFigure 2.64: $^{31}\text{P}\{^1\text{H}\}$ -NMR of BPHDT

^1H NMR spectra represents typical resonance for α and β -proton doublet of doublet and triplet of doublet at high field respectively (Figure 2.63). A set of multiplet observed at 1.21 ppm that proved the presence of several methylene group in long chain of final product. A sharp singlet at 21.75 ppm appears in $^{31}\text{P}\{^1\text{H}\}$ indicating two identical phosphate moieties. The phosphorous decoupled $^1\text{H}\{^{31}\text{P}\}$ -NMR spectrum (Figure 2.64) revealed the absence of ^1H - ^{31}P couplings. 2D-NMR COSY (Figure 2.67) showed cross-peak between ethyl ester protections protons highlighting ^1H - ^1H resonances between α and β -protons.

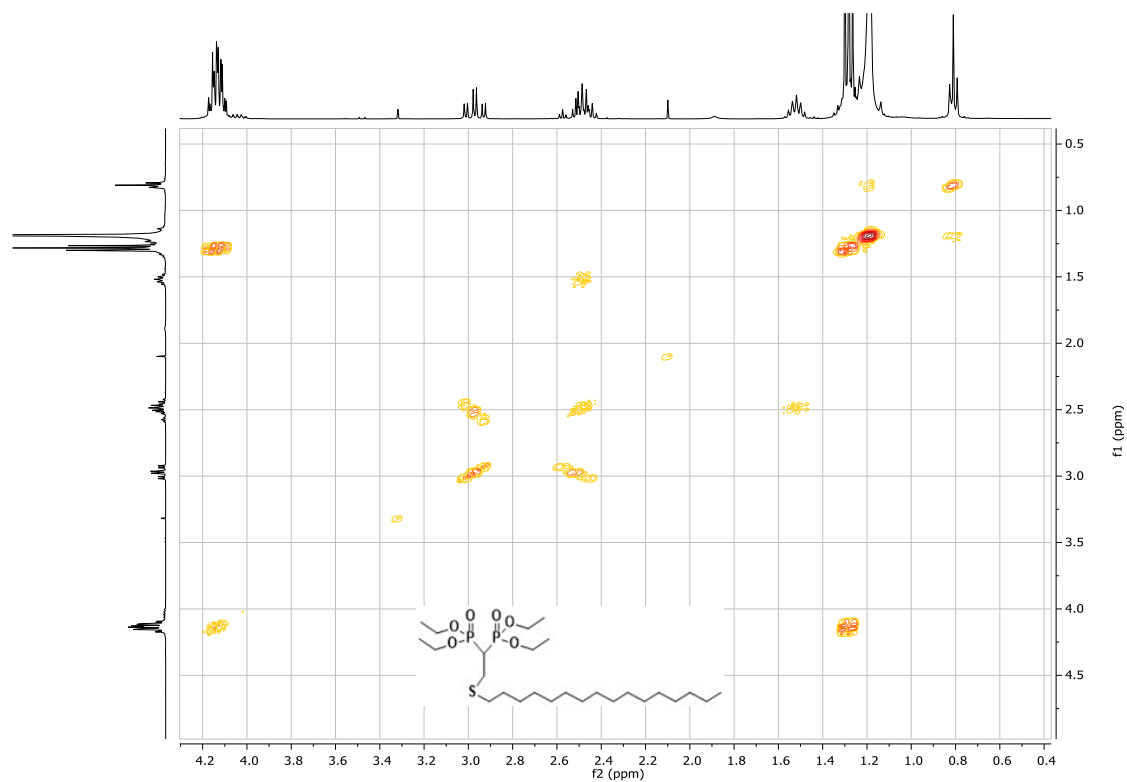


Figure 2.67: 2D-NMR COSY of BPHDT

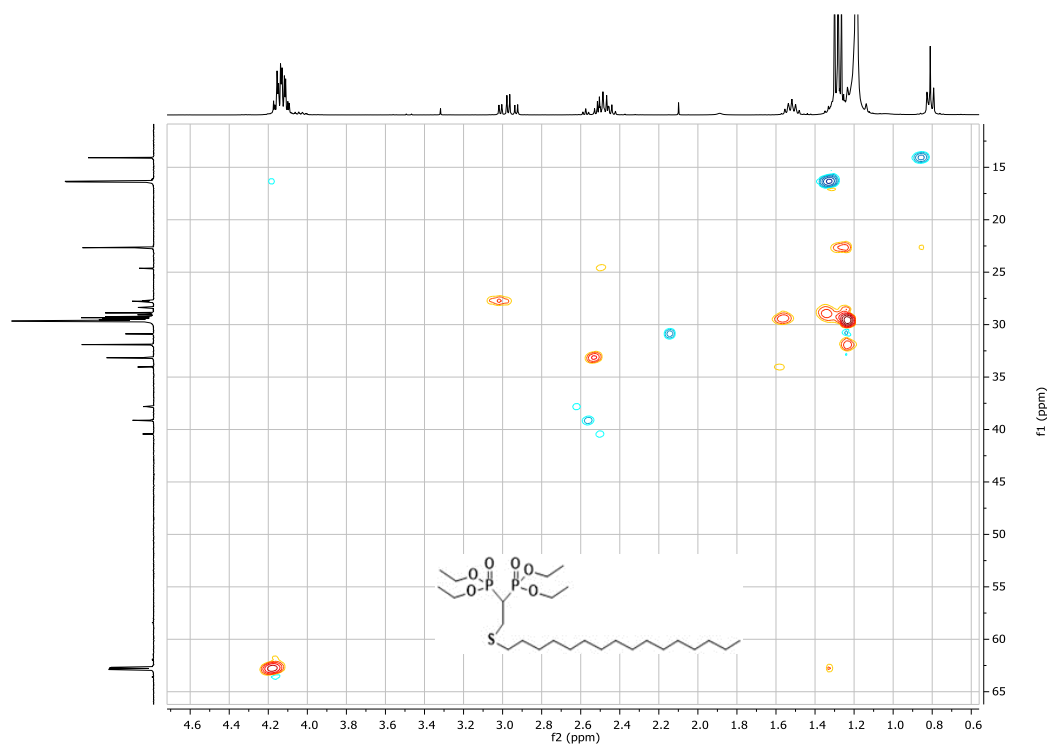


Figure 2.68: 2D-NMR HSQC of BPHDT

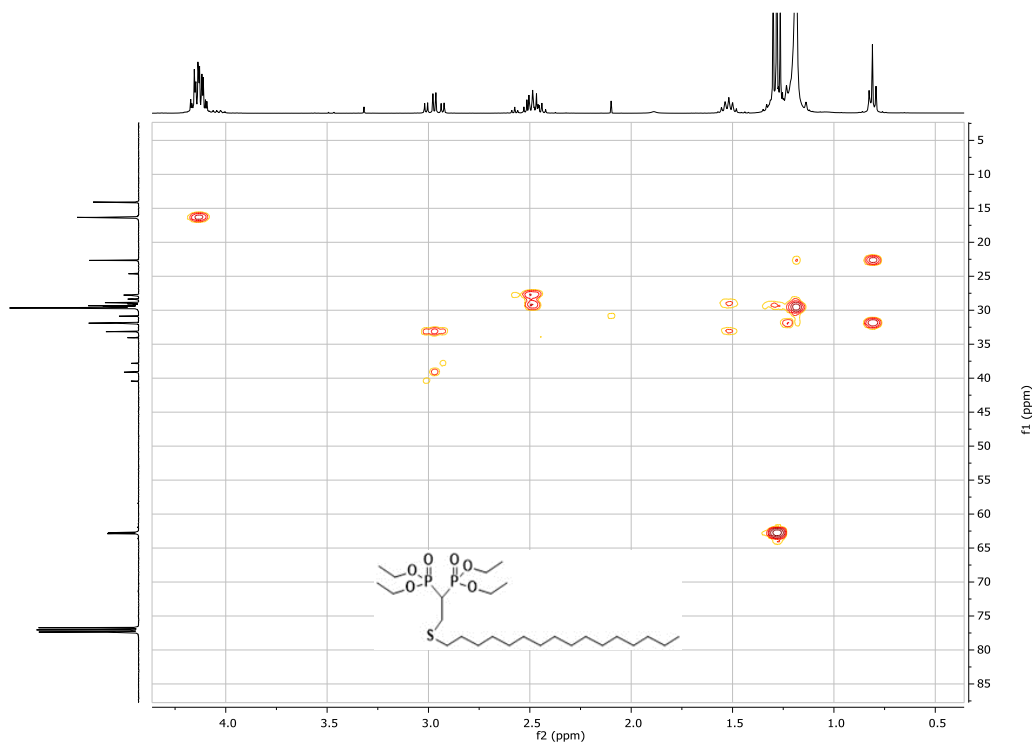
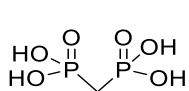


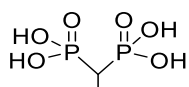
Figure 2.69: 2D-NMR HMBC of BPHDT

2D-NMR HMBC of represented long range ^{13}C - ^1H resonances that turned out to be very useful to assign ^{13}C resonances as reported in Figure 2.66

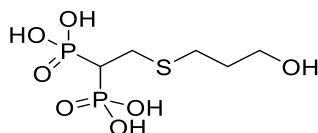
2.3 Synthesis of Bis-phosphonic Acids



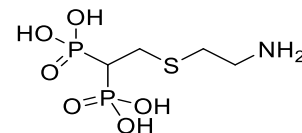
MBP, 1a



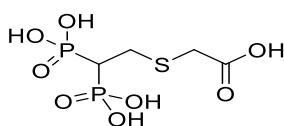
EBP, 1b



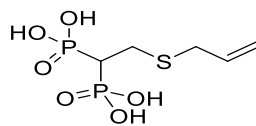
BPHPT, 1c



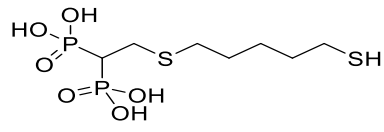
AETI, 1d



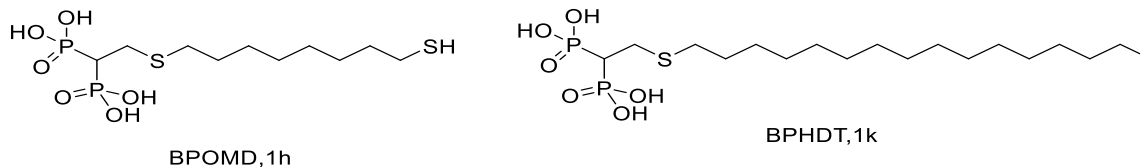
BPSC, 1e



BPSAL, 1f

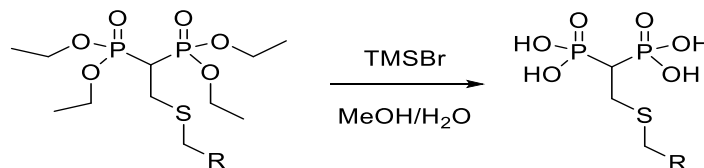


BPPMD, 1g

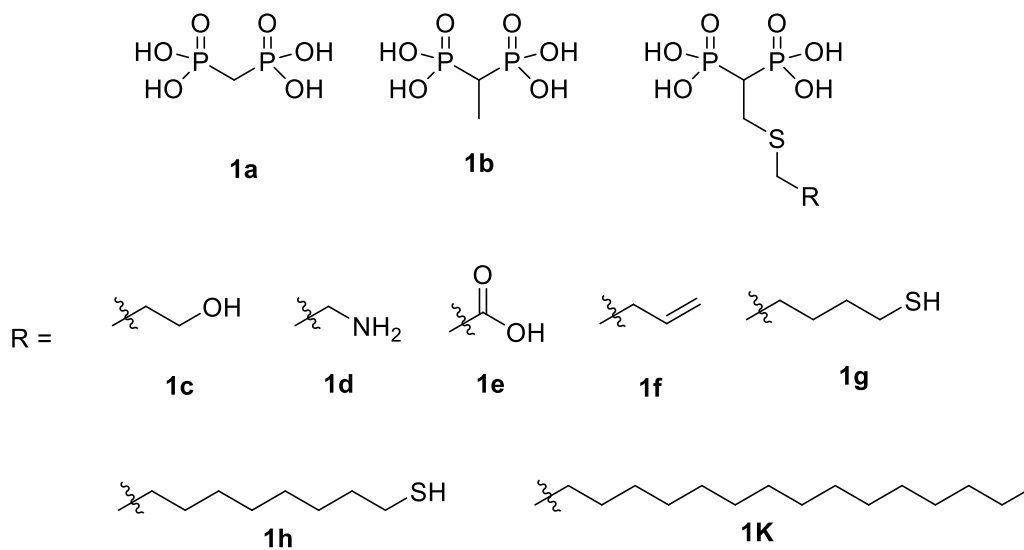


General Procedure 1(a-k)

General procedure for the deprotection of ethyl esters



Scheme 2.13: Synthesis of deprotected Bis-phosphonic acids.



2.3.1 Methylene Bis-phosphonic Acid (MBP, 1a)

^1H NMR spectra represents typical resonance for α -proton triplet at high field 2.12 ppm. A sharp singlet at 18.18 ppm appears in $^{31}\text{P}\{^1\text{H}\}$ in D_2O indicating no aggregation of nanoparticles. $^1\text{H}\{^{31}\text{P}\}$ -NMR spectra shows simplification of the resonance peaks, for example a singlet instead of triple for methylene proton (Figure 2.71). 2D-NMR HSQC (Figure 2.73) helped to confirm the synthesis of desired product by analyzing the correlations between a carbon and its attached protons.

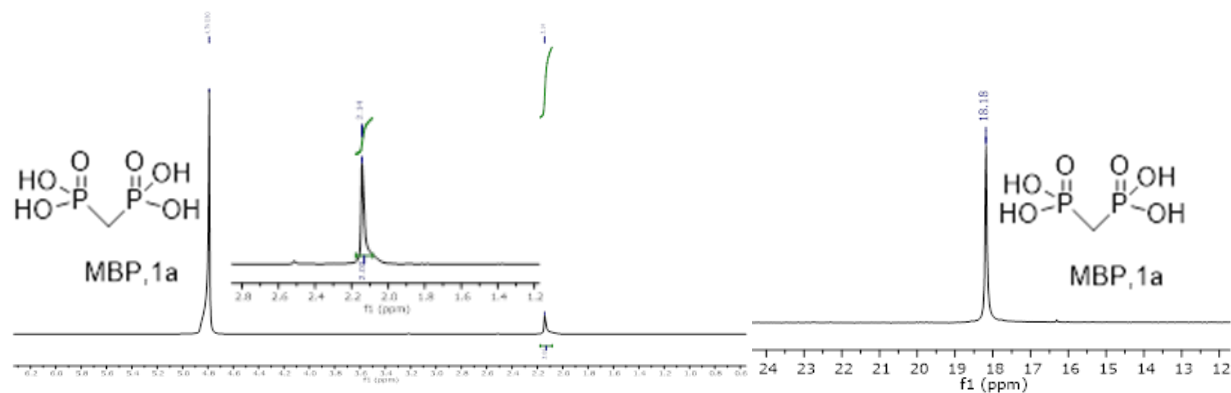
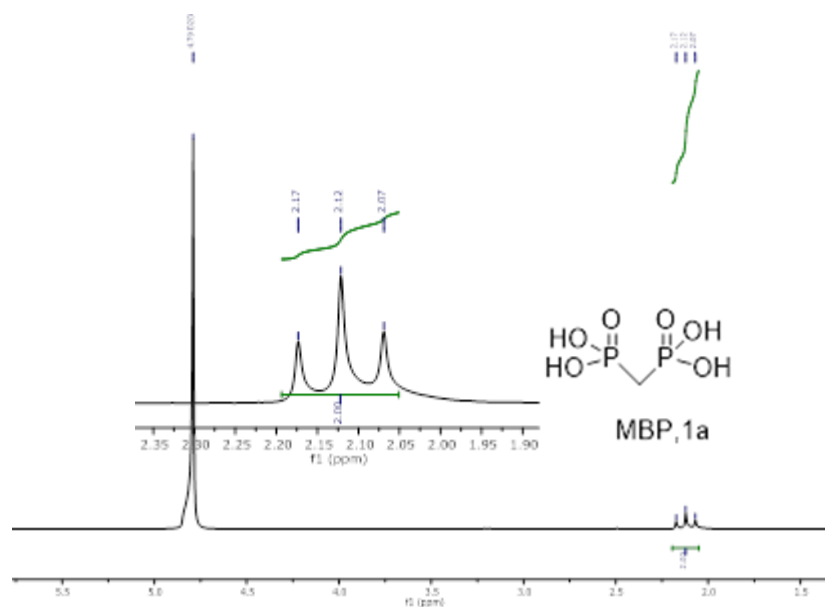


Figure 2.72: $^{31}\text{P}\{^1\text{H}\}$ -NMR of MBP, 1a

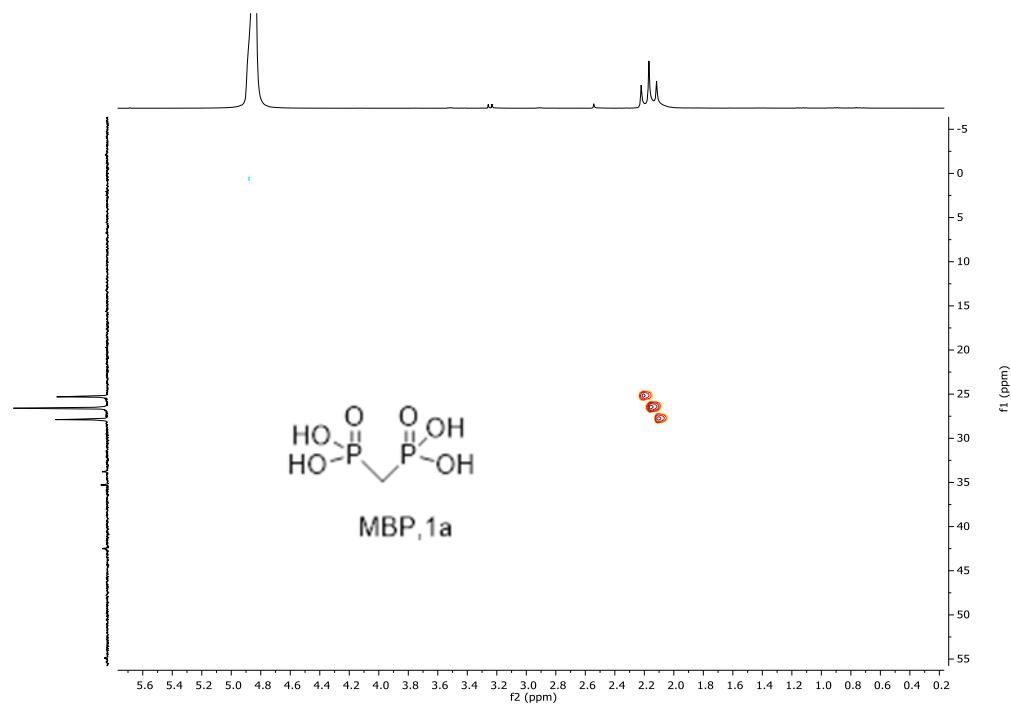
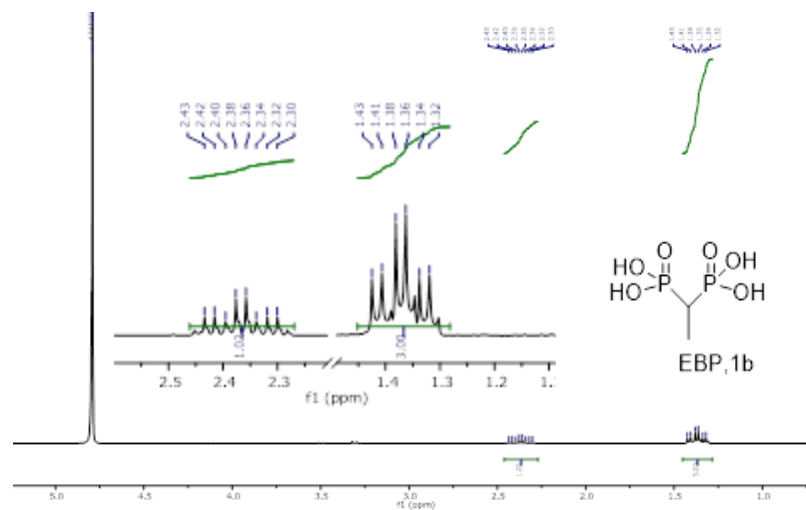


Figure 2.73: 2D NMR HSQC of MBP, 1a

2.3.2 *Ethan-1,1-diylbis(phosphonic Acid) (EBP, 1b)*

^1H NMR spectra shows only typical triplet of doublet and multiplet that belongs to α - and β -protons respectively (Figure 2.74).

Figure 2.74: ^1H NMR of EBP, 1b

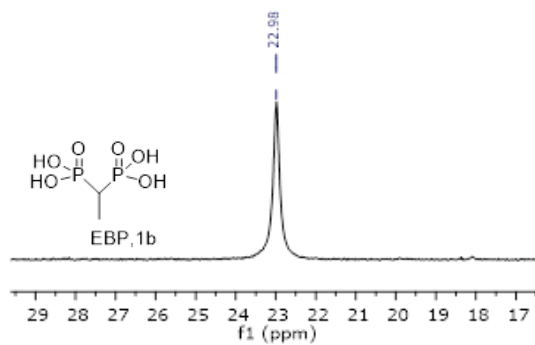
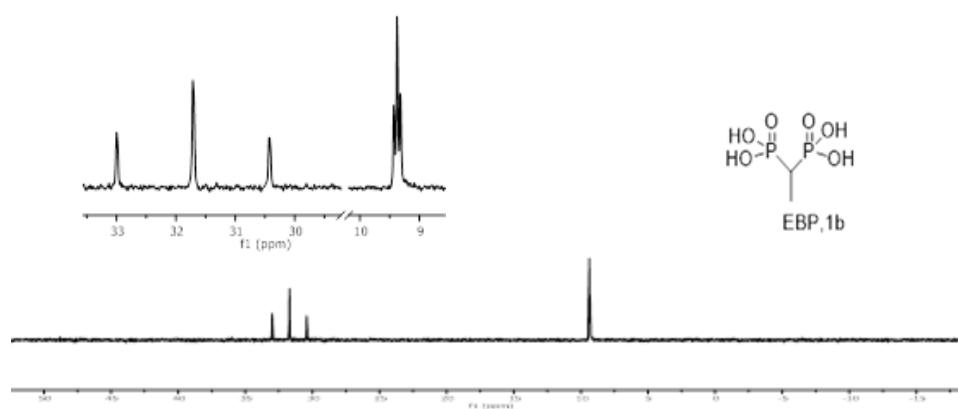
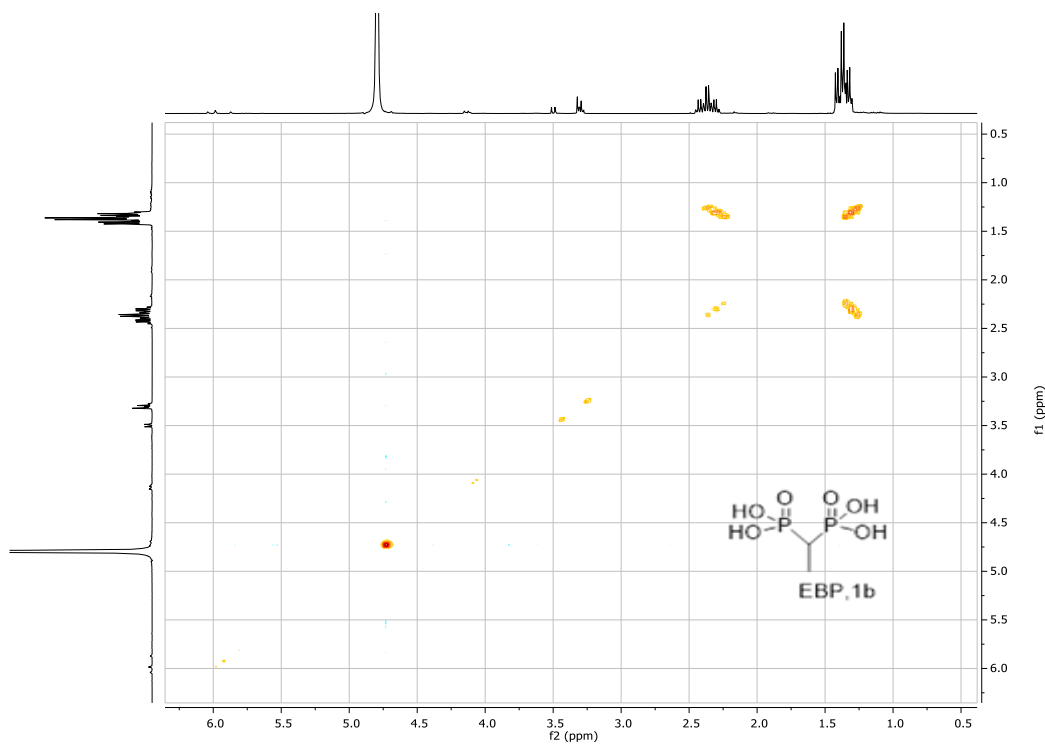
Figure 2.75: $^{31}\text{P}\{^1\text{H}\}$ NMR of EBP, 1bFigure 2.76: ^{13}C NMR of EBP, 1b

Figure 2.77: 2D NMR COSY of EBP, 1b

2D-NMR COSY (Figure 2.77) shows usual cross-peak highlighting ^1H - ^1H resonances between α and β -protons. 2D-NMR HSQC (Figure 2.78) helped to confirm the synthesis of desired product, giving the possibility to verify ^{13}C assignments in figure 2.76.

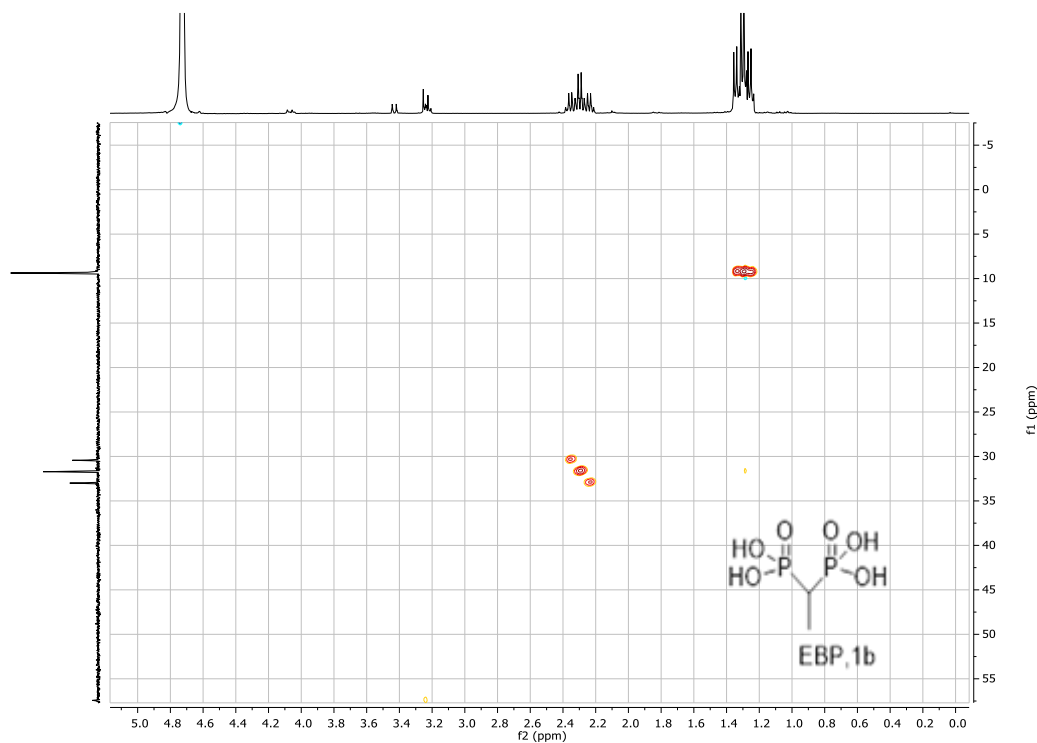


Figure 2.78: 2D NMR HSQC of EBP, 1b

2.3.3. 2-((3-hydroxypropyl) thiol)ethane-1,1- diyl)bis(phosphonic acid) (BPHT, 1c)

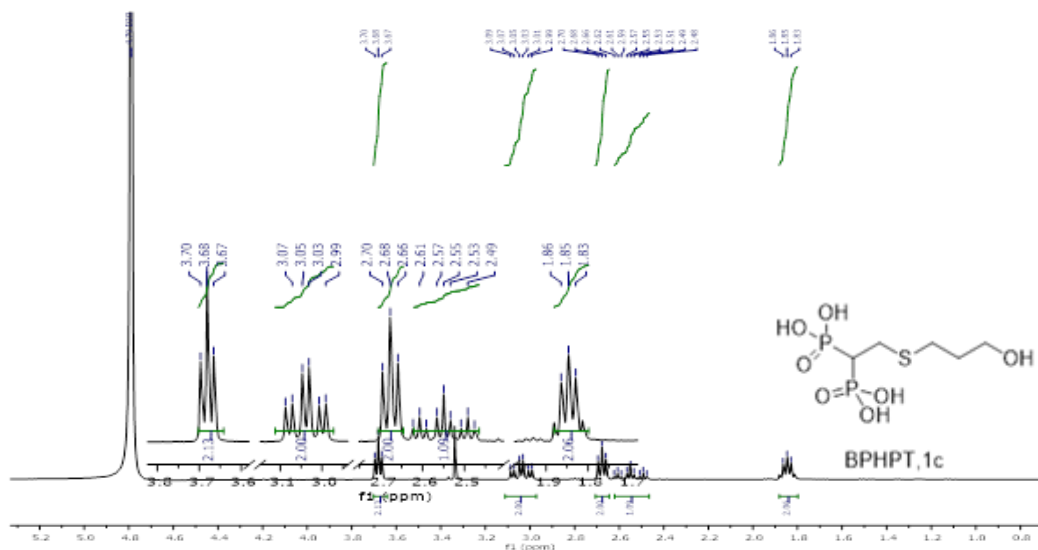


Figure 2.79: ^1H NMR of BPHT, 1c

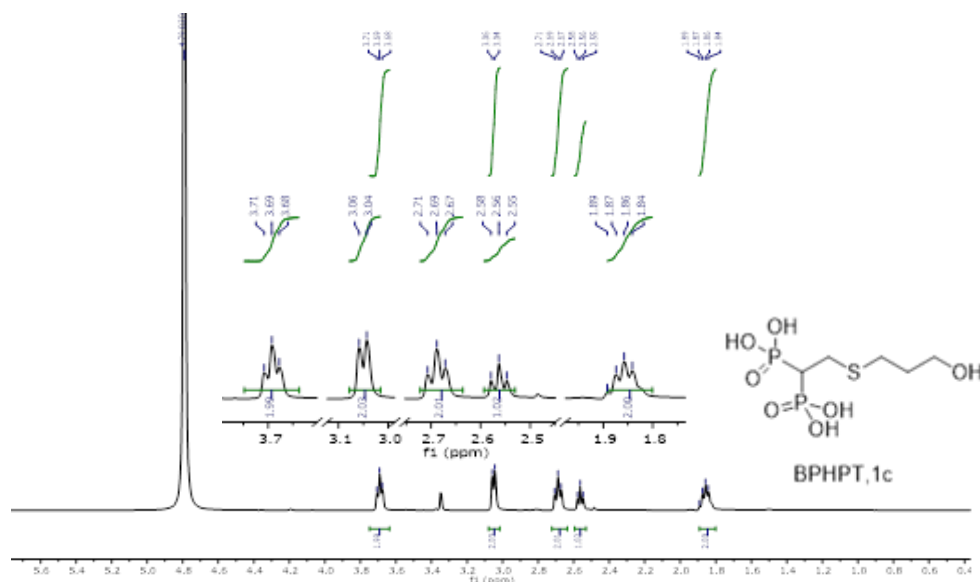


Figure 2.80: $^1\text{H}\{^{31}\text{P}\}$ NMR of BPHPT, 1c

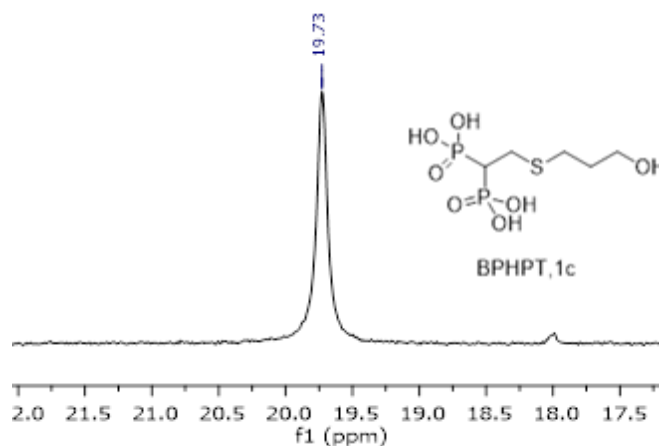


Figure 2.81: $^{31}\text{P}\{^1\text{H}\}$ -NMR of BPHPT, 1c

In ^1H -NMR spectra absence of typical resonances for ethyl ester proton at high field (Figure 2.79) confirmed the deprotection of ester group. 2D-NMR -COSY showed typical ^1H - ^1H cross resonances. The HMBC 2D-NMR spectrum (figure 2.84) show long range ^{13}C - ^1H resonances, helping to assign ^{13}C signals as reported on Figure 2.82. Proton decoupled Phosphorous NMR shows only one sharp signal to confirm complete conversion of ester to acid.

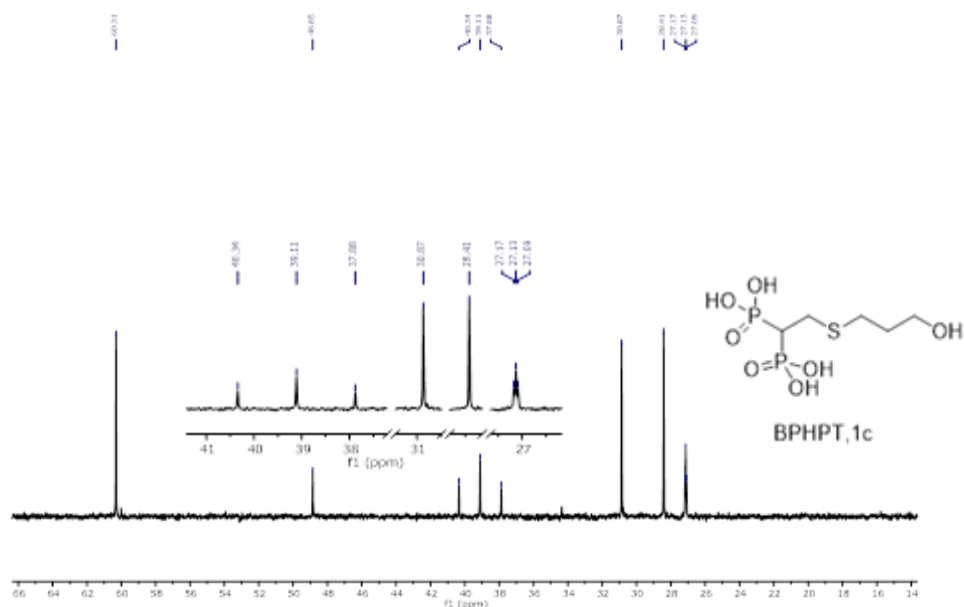
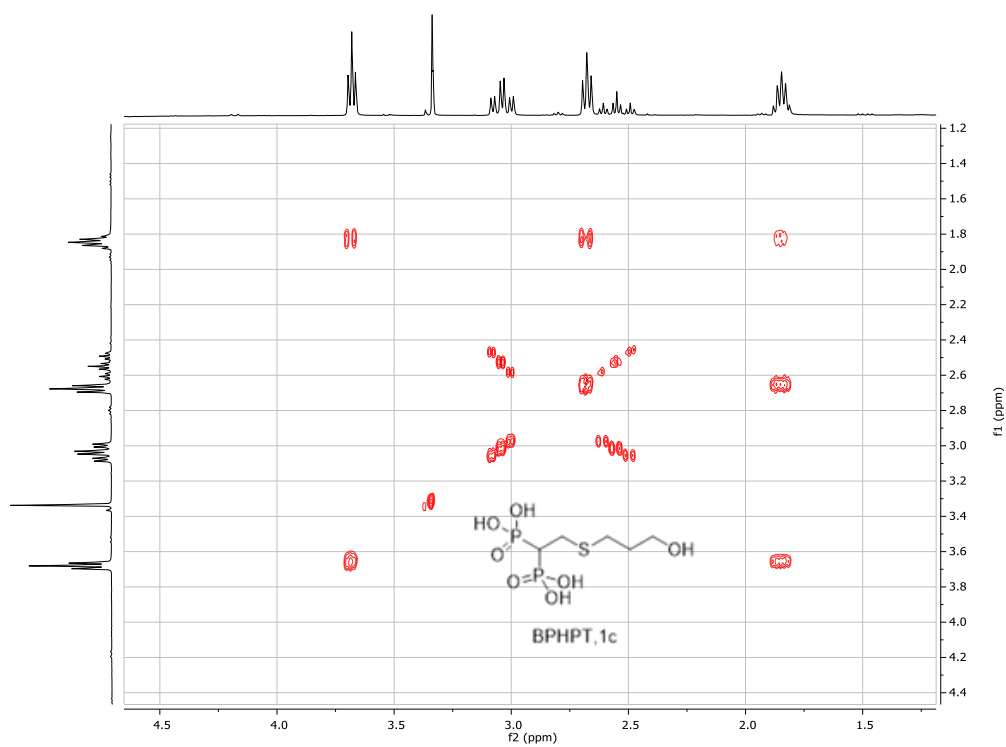
Figure 2.82: ^{13}C NMR of BPHPT, 1c

Figure 2.83: 2D NMR COSY of BPHPT, 1c

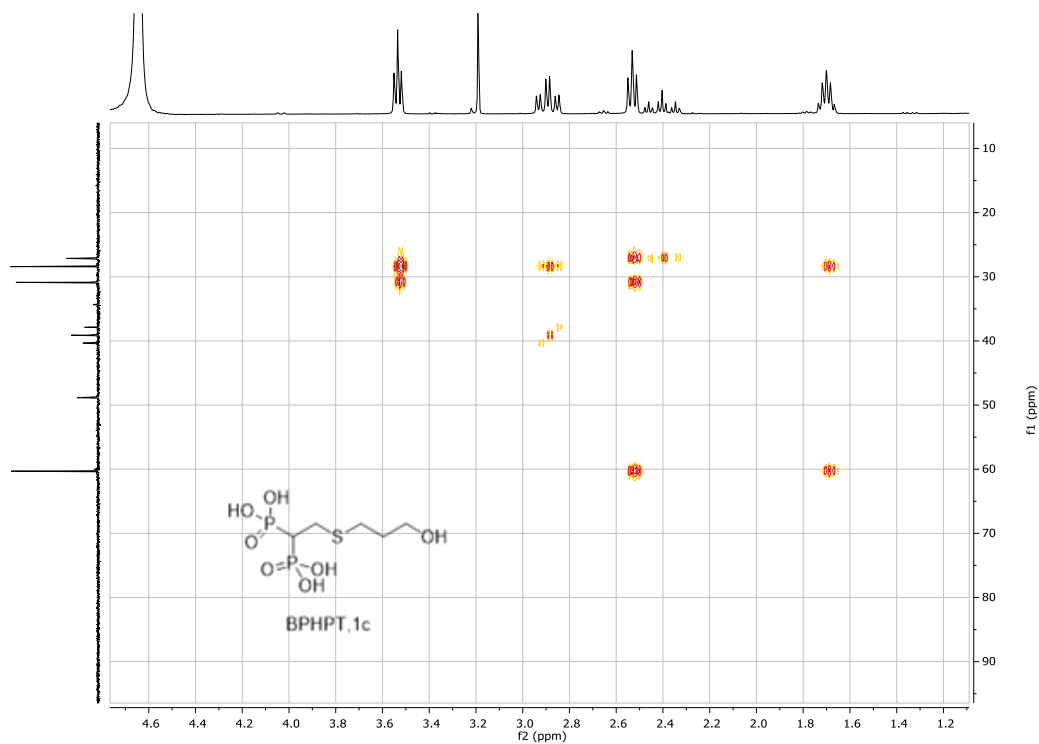


Figure 2.84: 2D NMR HMBC of BPHPT, 1c

2.3.4. (2-((2-aminoethyl)thio)ethane-1,1-diyl)bis(phosphonic acid) (AETI, 1d)

The characterization of the AETI compound is reported with ^1H -NMR, shows all typical resonance. A comparison between $^{31}\text{P}\{^1\text{H}\}$ -NMR of ester deprotected & $^{31}\text{P}\{^1\text{H}\}$ -NMR of ester protected amino-BP compound represented, the $^{31}\text{P}\{^1\text{H}\}$ -NMR showed the presence of a strong singlet at upfield 21.67 ppm compare to latter one.

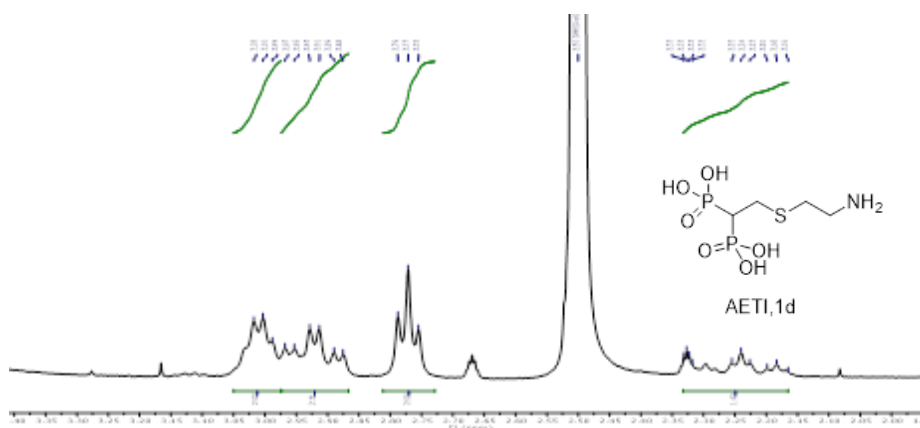


Figure 2.85: ^1H NMR of AETI, 1d

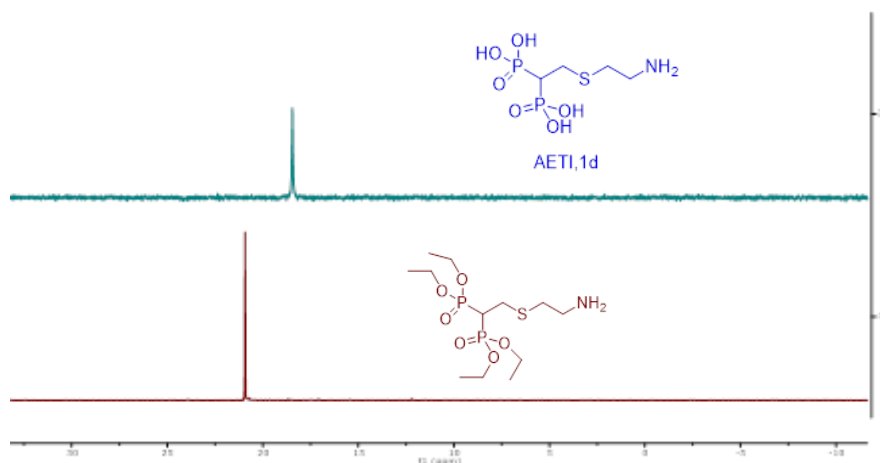
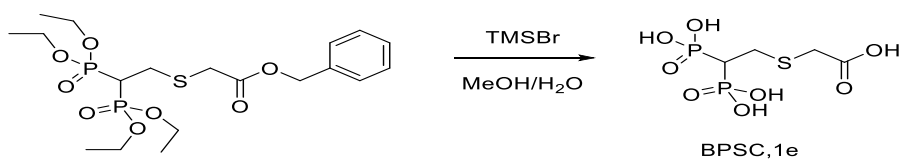


Figure 2.86: Comparison between $^{31}\text{P}\{^1\text{H}\}$ NMR of AETI ester and $^{31}\text{P}\{^1\text{H}\}$ NMR of AETI acid, 1d

2.3.5. 2-((2,2-diphosphonoethyl)thio)acetic acid (BPSC, 1e)



Scheme 2.14: Synthesis of deprotection BPSC acid

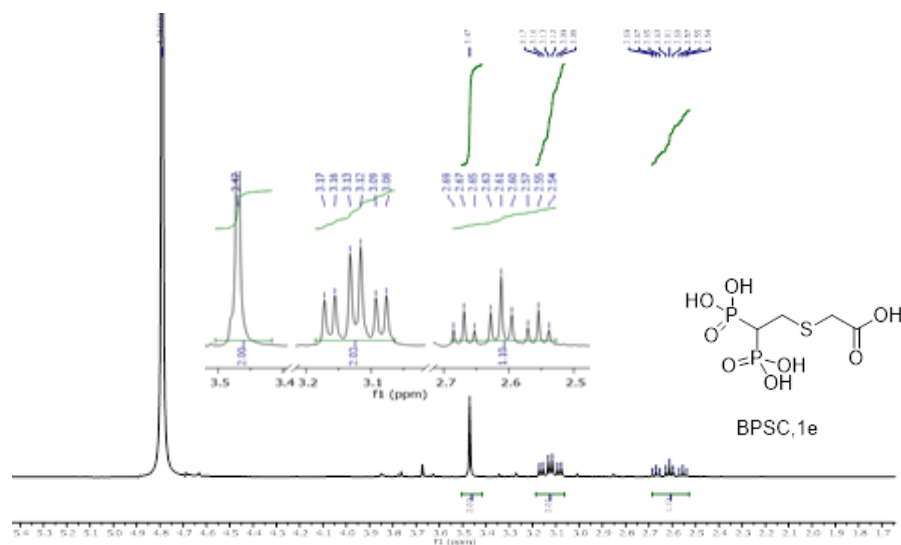


Figure 2.87: ^1H NMR of BPSC, 1e

In the presence of bromo trimethyl silane both the benzyl group and ester group deprotected from BPBTG compound. The product was obtained as colorless liquid with 98% yield. The characterization of the BPSC compound is reported with comparison of ^1H -NMR of deprotected BPBTG, absence of resonance of benzyl proton at low field and ethyl ester proton at high field confirmed the desired product. The ^{31}P $\{^1\text{H}\}$ -NMR showed the presence of a strong singlet at upfield 19.22 ppm compare to BPBTG (Figure 2.90)

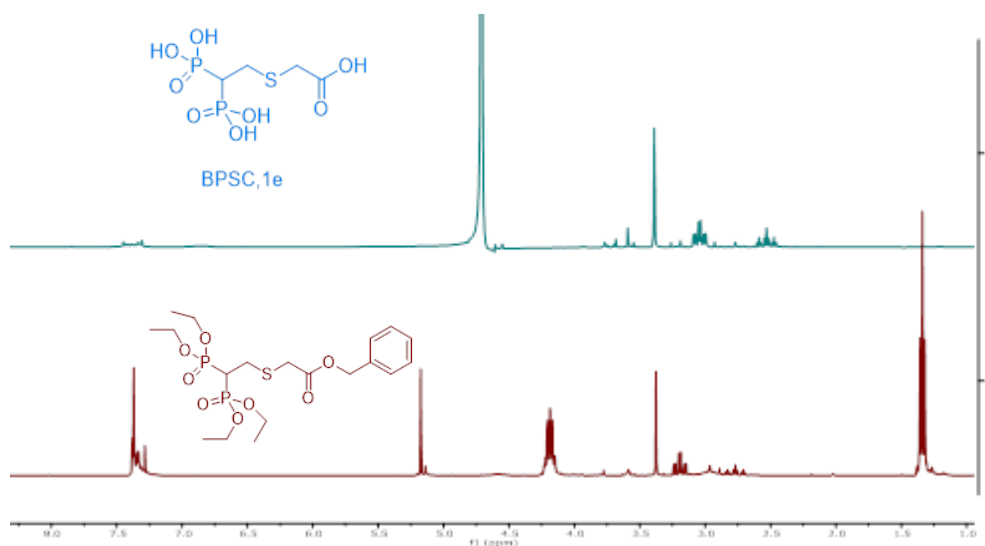


Figure 2.88: Comparison between ^1H NMR of BPBTG ester (red) and BPSC acid, 1e (green)

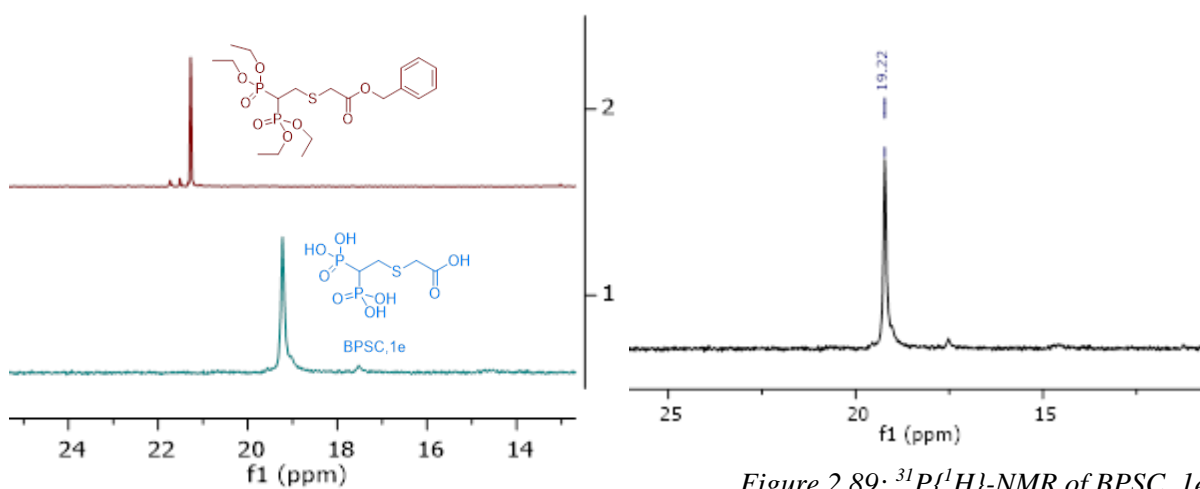


Figure 2.89: $^{31}\text{P}\{^1\text{H}\}$ -NMR of BPSC, 1e

Figure 2.90: Comparison between $^{31}\text{P}\{^1\text{H}\}$ -NMR of BPBTG ester (red) and BPSC acid, 1e (blue)

2.3.6. (2-(allylthio)ethane-1,1-diyl)bis(phosphonic acid) (BPSAL, 1f)

^1H NMR spectra shows typical resonance for allyl proton in the product triplet of doublet), doublet of doublet and doublet of doublet along with resonance of α and β - protons (Figure 2.91).

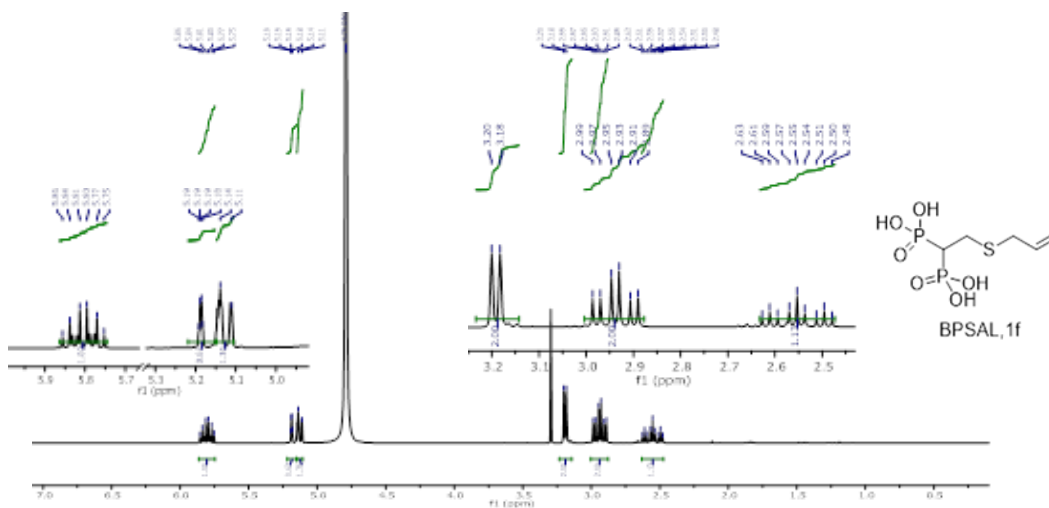


Figure 2.91: ^1H NMR of BPSAL,1f

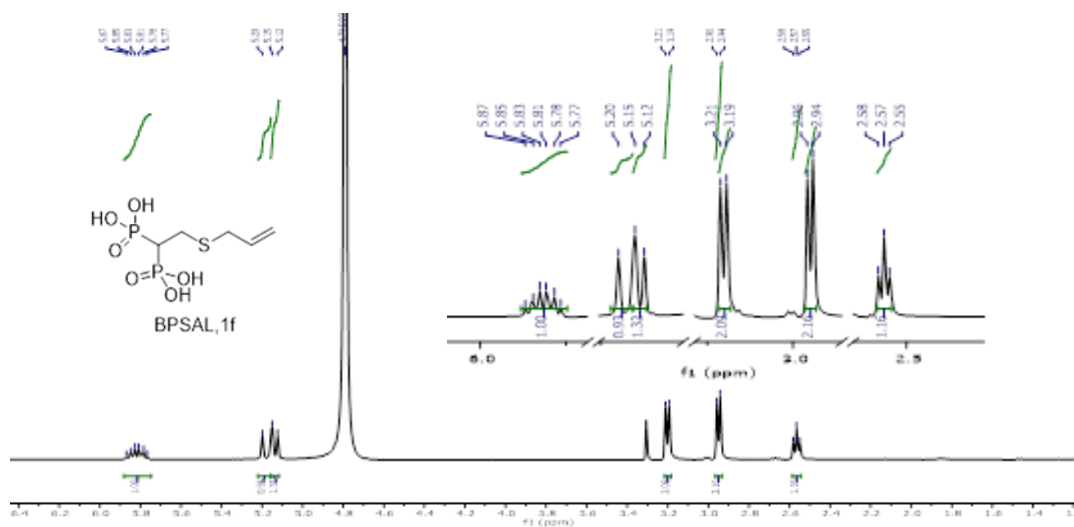
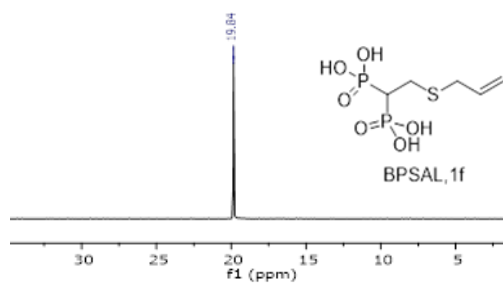
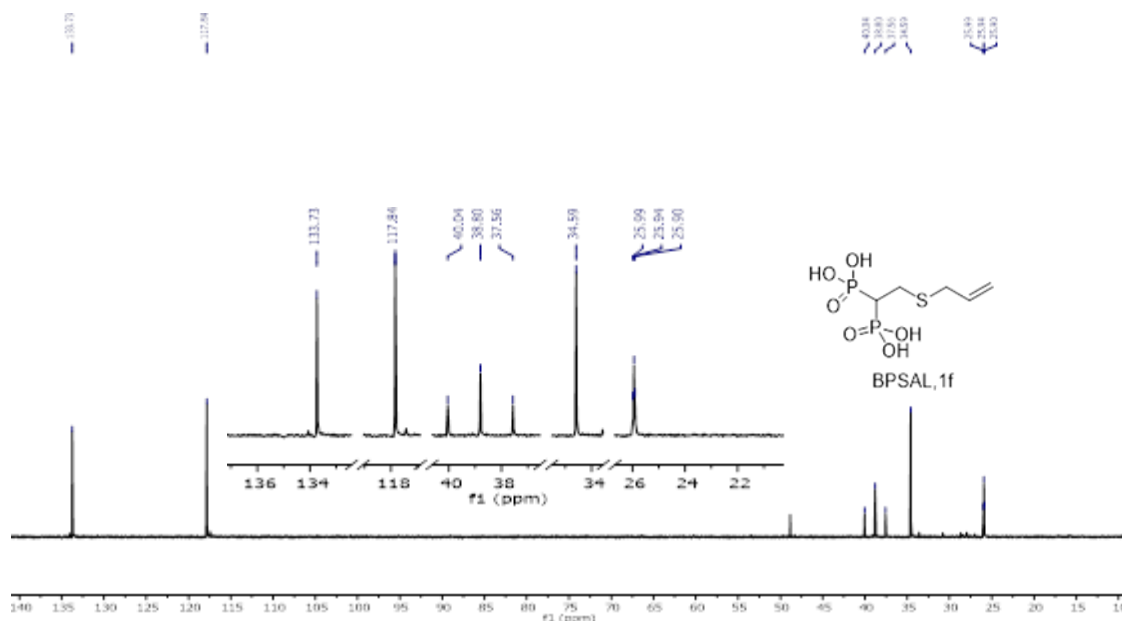


Figure 2.93: $^1\text{H}\{^{31}\text{P}\}$ - NMR of BPSAL,1f

$^1\text{H}\{^{31}\text{P}\}$ -NMR spectra shows simplification of the resonance peaks (Figure 2.93). A sharp singlet appears at lower field 19.84 ppm in $^{31}\text{P}\{^1\text{H}\}$ spectra. 2D-NMR HMBC showed long range ^{13}C -

^1H resonances, helping to assign ^{13}C signals as reported on (Figure 2.97). 2D-NMR COSY showed typical ^1H - ^1H cross resonances among the α and β - protons and allyl protons (Figure 2.95). Comparison between ^1H -NMR of BPSAL Ester and ^1H -NMR of BPSAL Acid (figure 2.98) confirmed the absence of ester group in latter one.



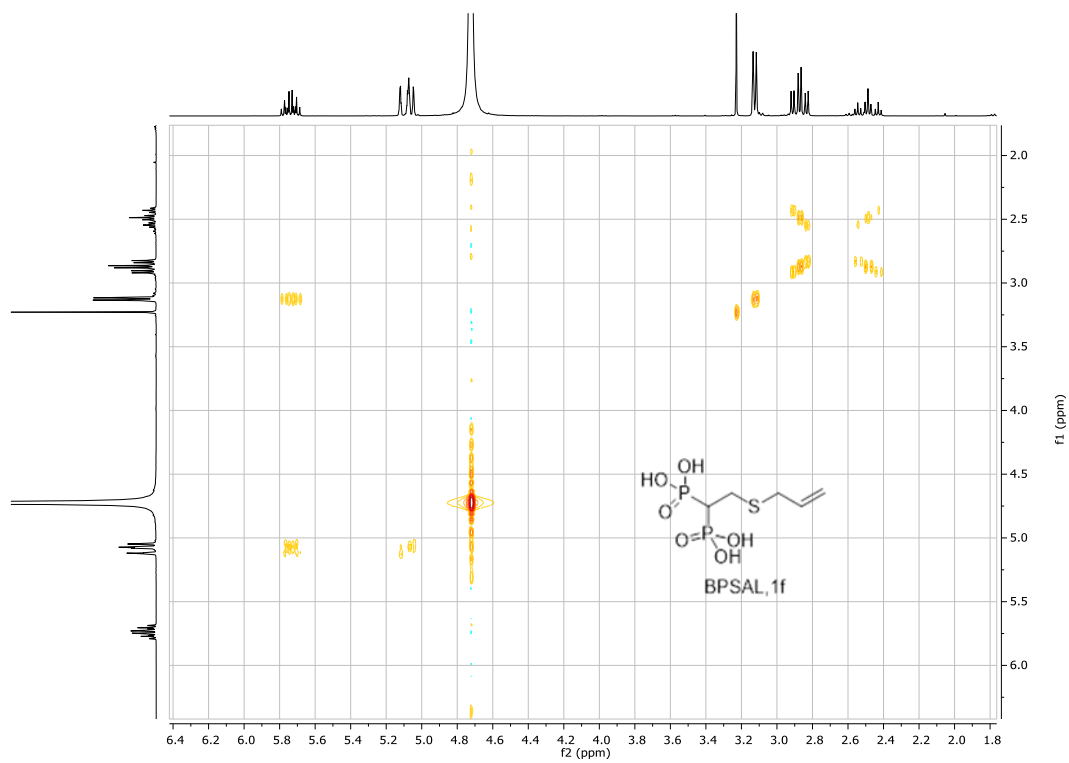


Figure 2.95: 2D NMR COSY of BPSAL,1f

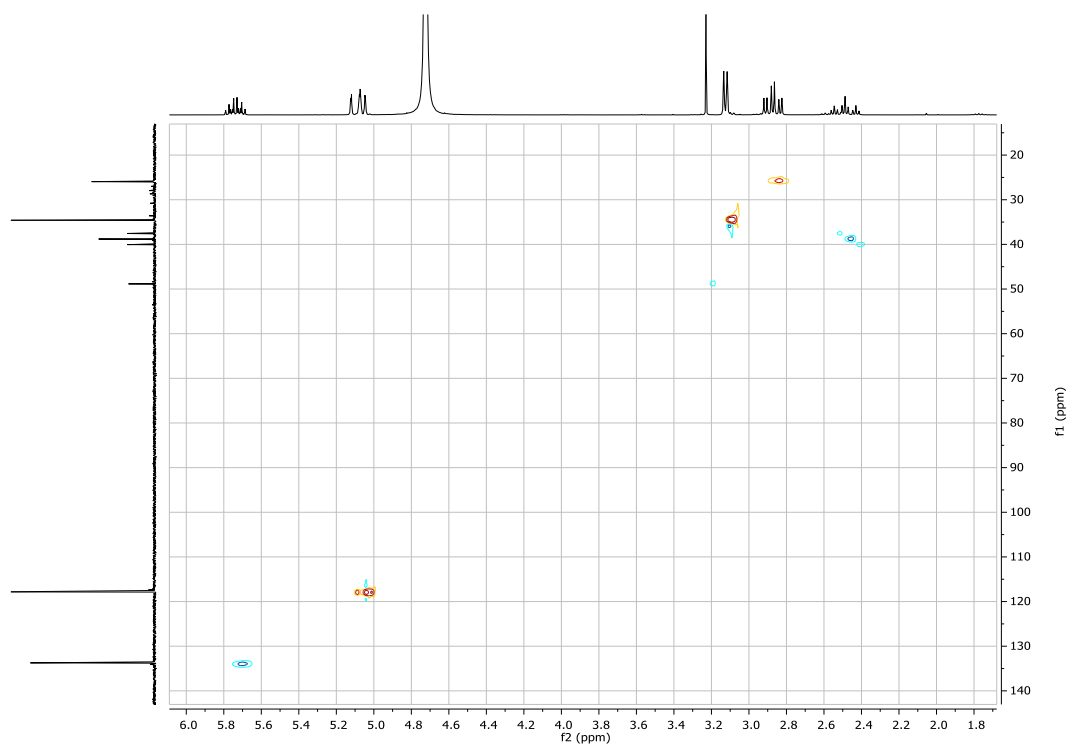


Figure 2.96: 2D NMR HSQC of BPSAL,1f

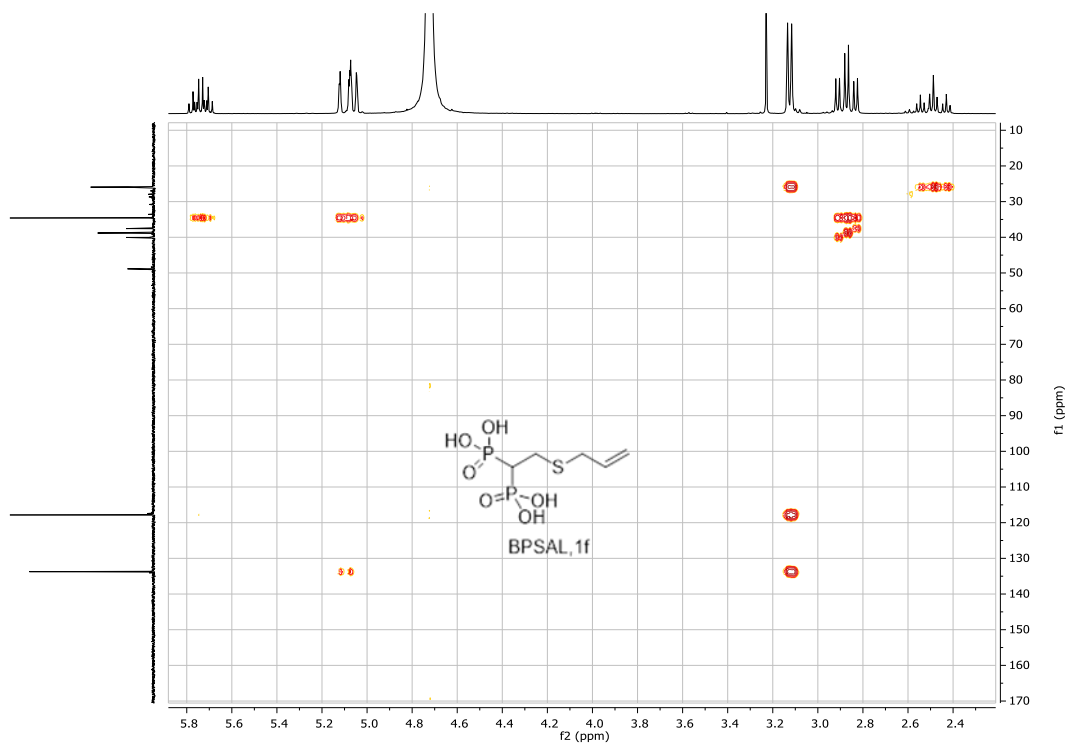
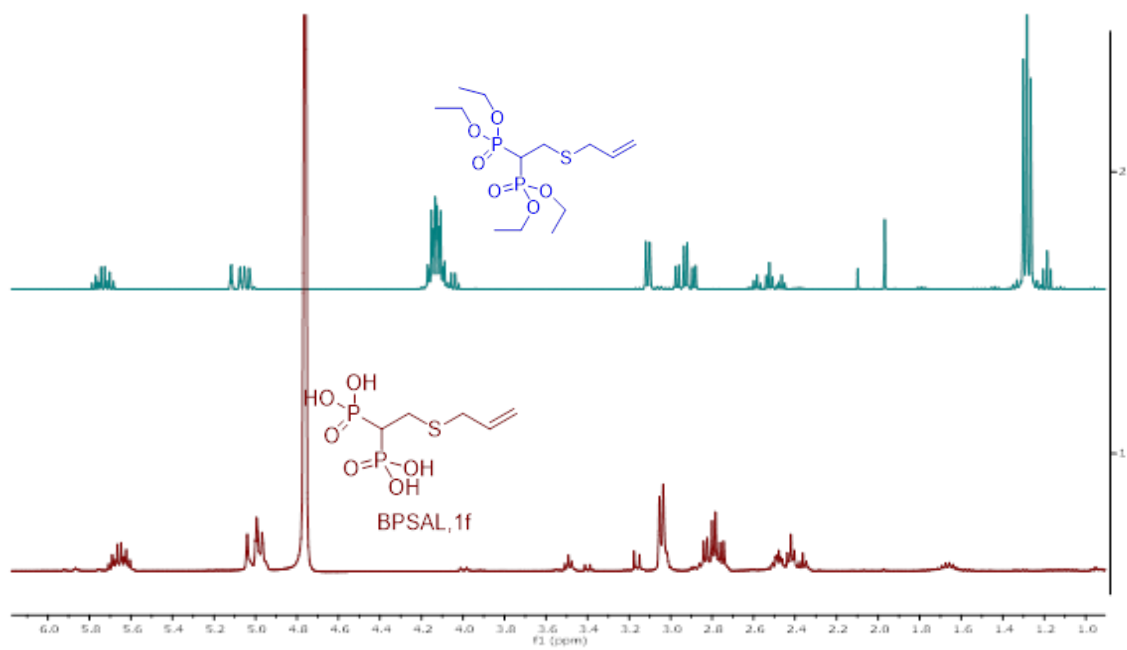


Figure 2.97: 2D NMR HMBC of BPSAL, 1f

Figure 2.98: Comparison between ^1H -NMR of BPSAL Acid, 1f (red) & ^1H -NMR of BPSAL Ester (blue)

2.3.7. (2- (pentamethylene dimercaptan)ethane-1,1- diyl)bis(phosphonic Acid) (BPPMD, 1g)

In Figure 2.102, comparison between ^1H -NMR of BPPMD ester, ^1H -NMR & ^1H - $\{^{31}\text{P}\}$ -NMR of BPPMD Acid clearly shows the deprotection of ester group since the triplet at 1.30ppm and set of multiplet at 4.21 – 4.11ppm are disappear.

2D-NMR COSY (Figure 2.103) showed usual cross-peak between methylene protons of thiol chain highlighting ^1H - ^1H resonances between α and β -protons.

2D-NMR NOESY (Figure 2.104) experiments revealed intense NOE cross-couplings between methylene proton. 2D-NMR HSQC (Figure 2.105) helped to confirm the synthesis of desired product, giving the possibility to verify ^{13}C assignments in Figure 2.101.

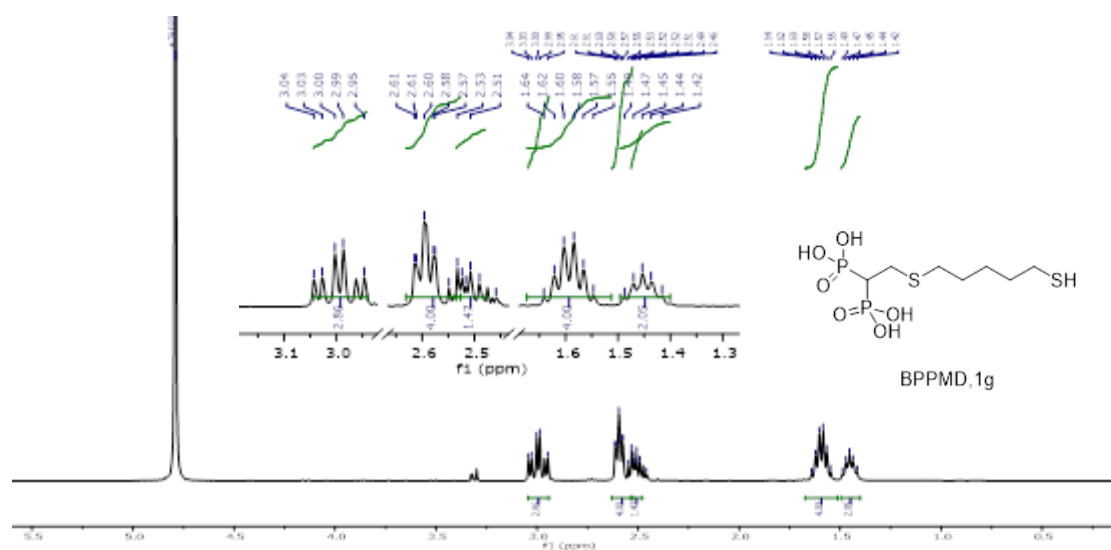


Figure 2.99: ^1H -NMR of BPPMD,1g

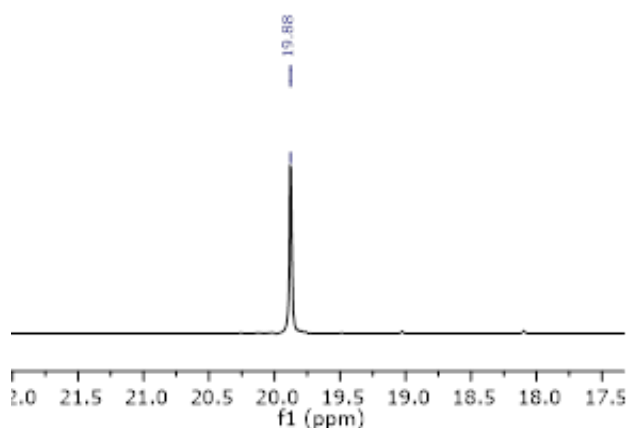
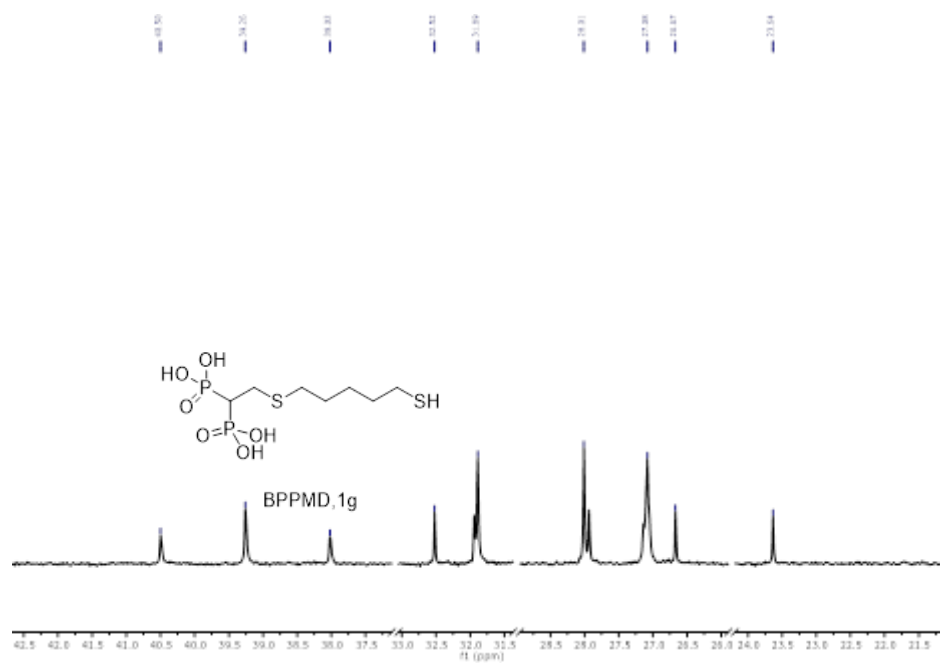
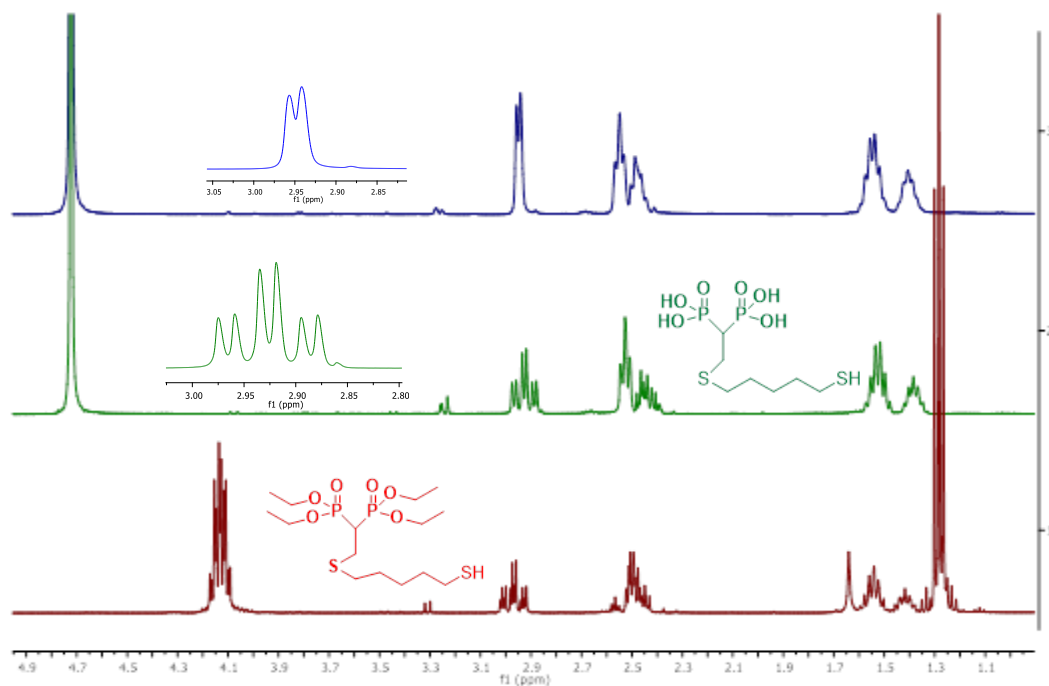


Figure 2.100: $^{31}\text{P}\{^1\text{H}\}$ -NMR of BPPMD,1g

Figure 2.101: ^{13}C NMR of BPPMD, 1gFigure 2.102: Comparison between ^1H -NMR of BPPMD ester (red) & ^1H -NMR (green) & ^1H - $\{^{31}\text{P}\}$ -NMR of BPPMD Acid, 1g (blue)

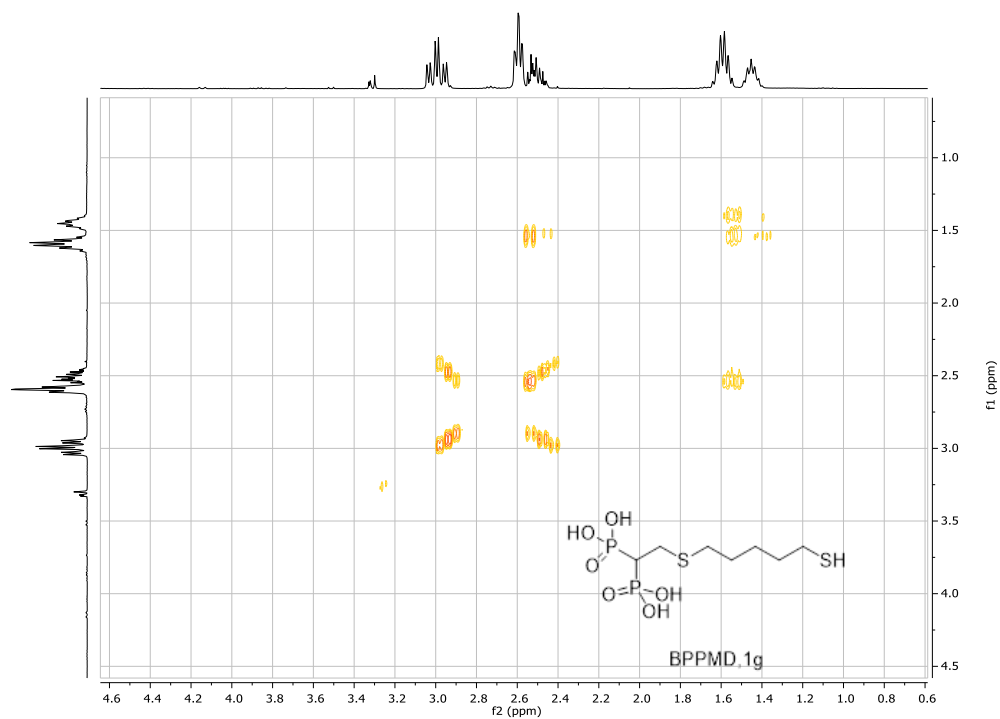


Figure 2.103: 2D NMR COSY of BPPMD Acid, 1g

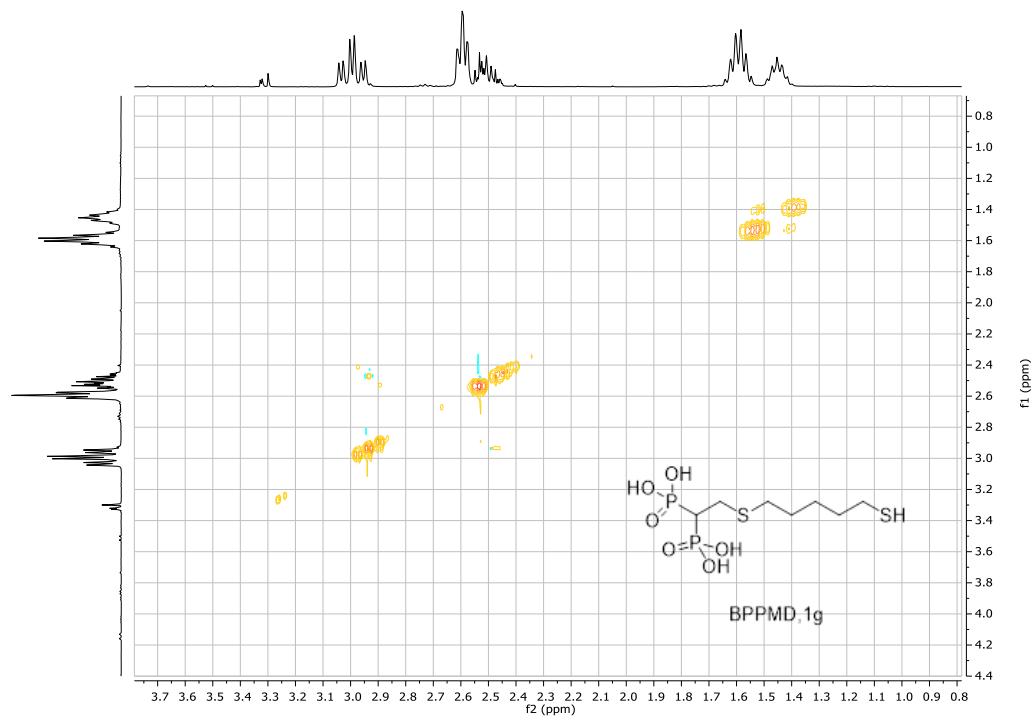


Figure 2.104: 2D NMR NOESY of BPPMD Acid, 1g

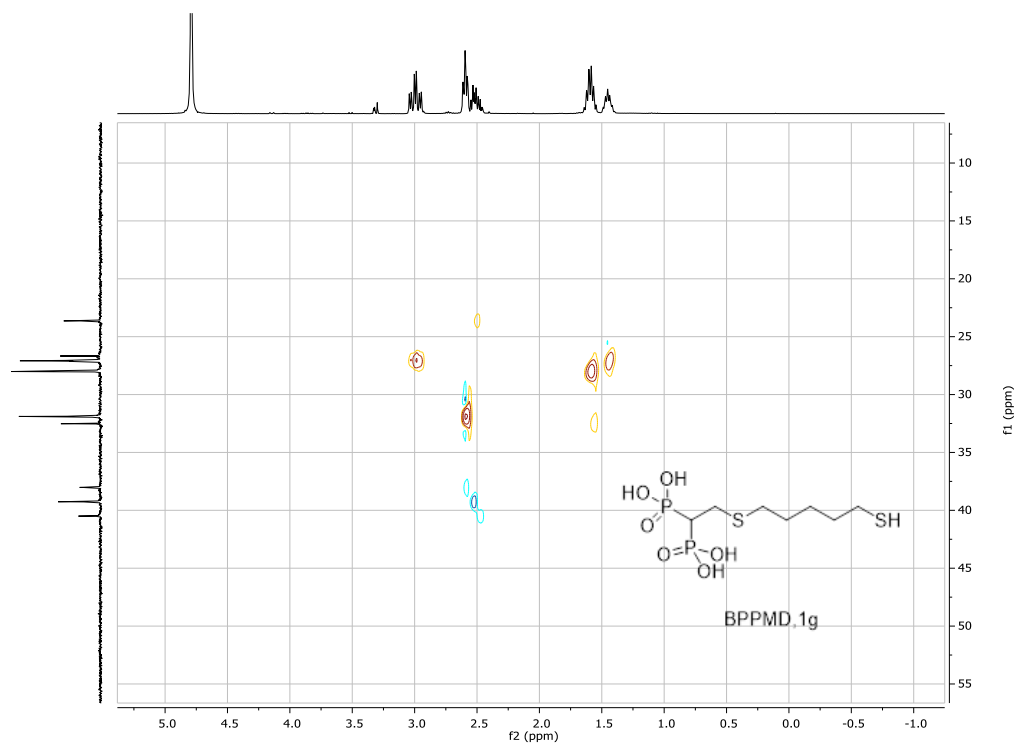


Figure 2.105: 2D NMR HSQC of BPPMD Acid, 1g

2.3.8. (2-(octamethylene dimercaptan)ethane-1,1-diyl)bis(phosphonic Acid) (BPOMD, 1h)

1D NMR (^1H , $^{31}\text{P}\{^1\text{H}\}$) and 2D NMR HSQC, HMBC revealed the production of desired product BPOMD with good yield.

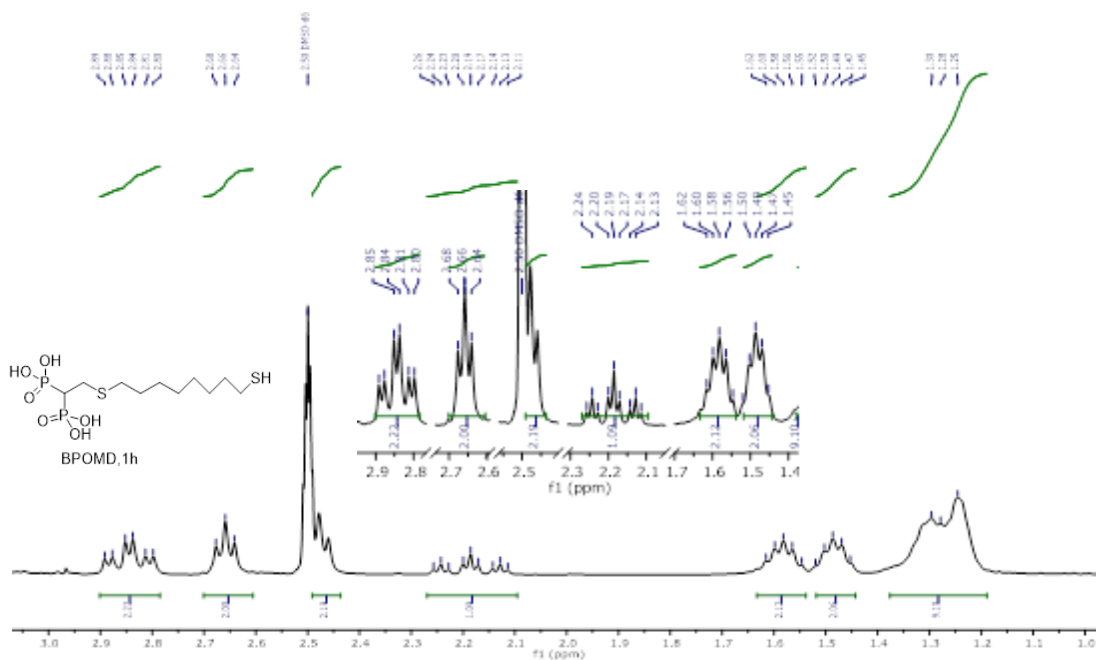


Figure 2.106: ^1H NMR of BPOMD, 1h

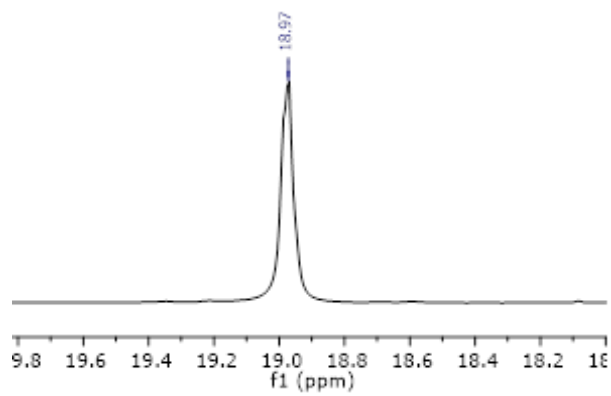
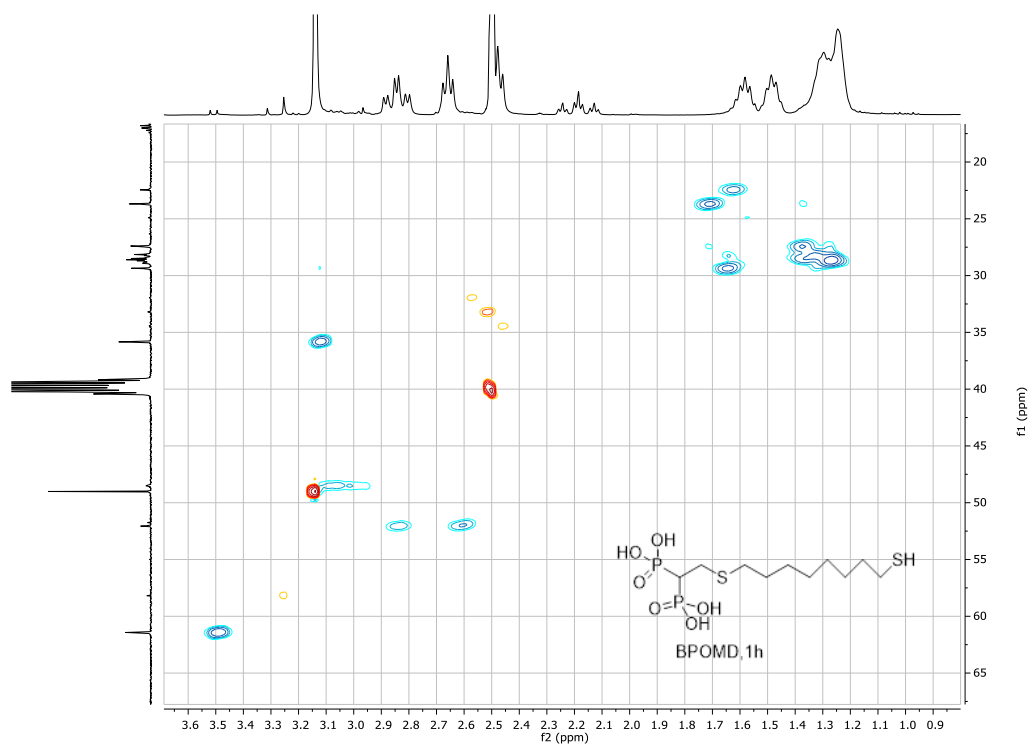
Figure 2.107: $^{31}\text{P}\{^1\text{H}\}$ -NMR of BPOMD, 1h

Figure 2.108: 2D NMR HSQC of BPOMD, 1h

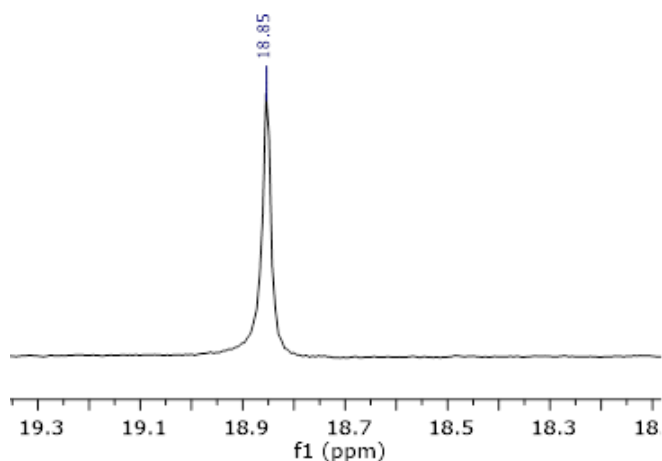


Figure 2.111: $^{31}\text{P}\{^1\text{H}\}$ NMR of BPHDT, 1k

2D-NMR HSQC (Figure 2.113) helped to confirm the synthesis of desired product by analyzing the correlations between a carbon and its attached protons. 2D-NMR HMBC of BPOMD (Figure 2.114) showed long range ^{13}C - ^1H resonances that turned out to be very useful to assign ^{13}C resonances.

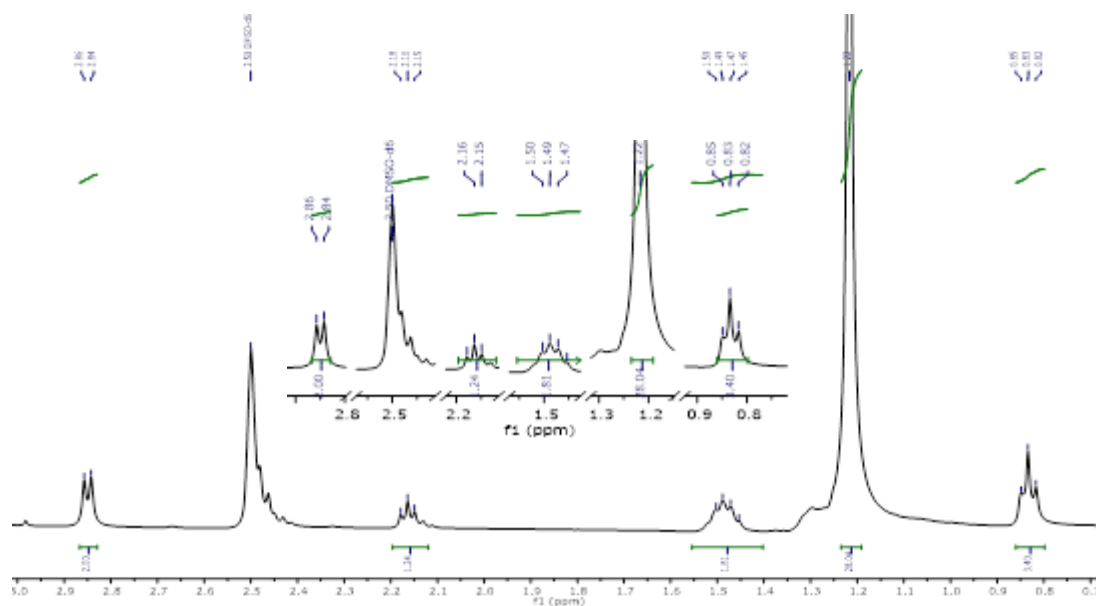


Figure 2.112: $^1\text{H}\{^{31}\text{P}\}$ NMR of BPHDT, 1k

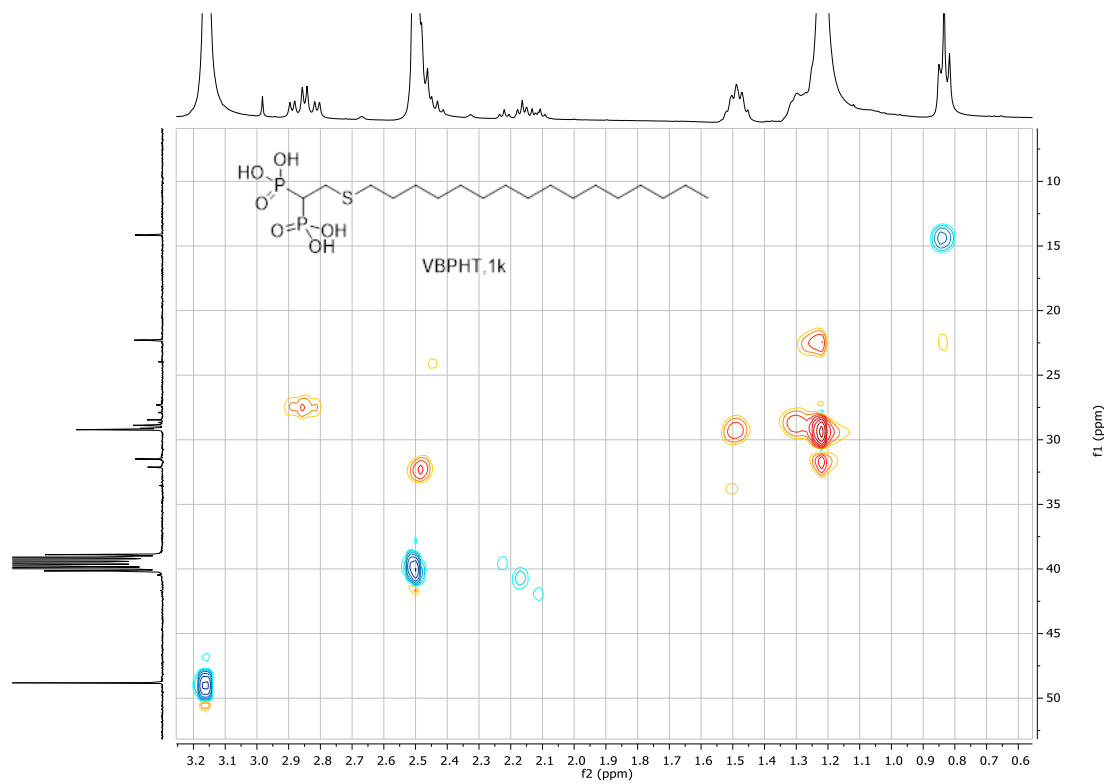


Figure 2.113: 2D NMR HSQC of BPHDT, 1k

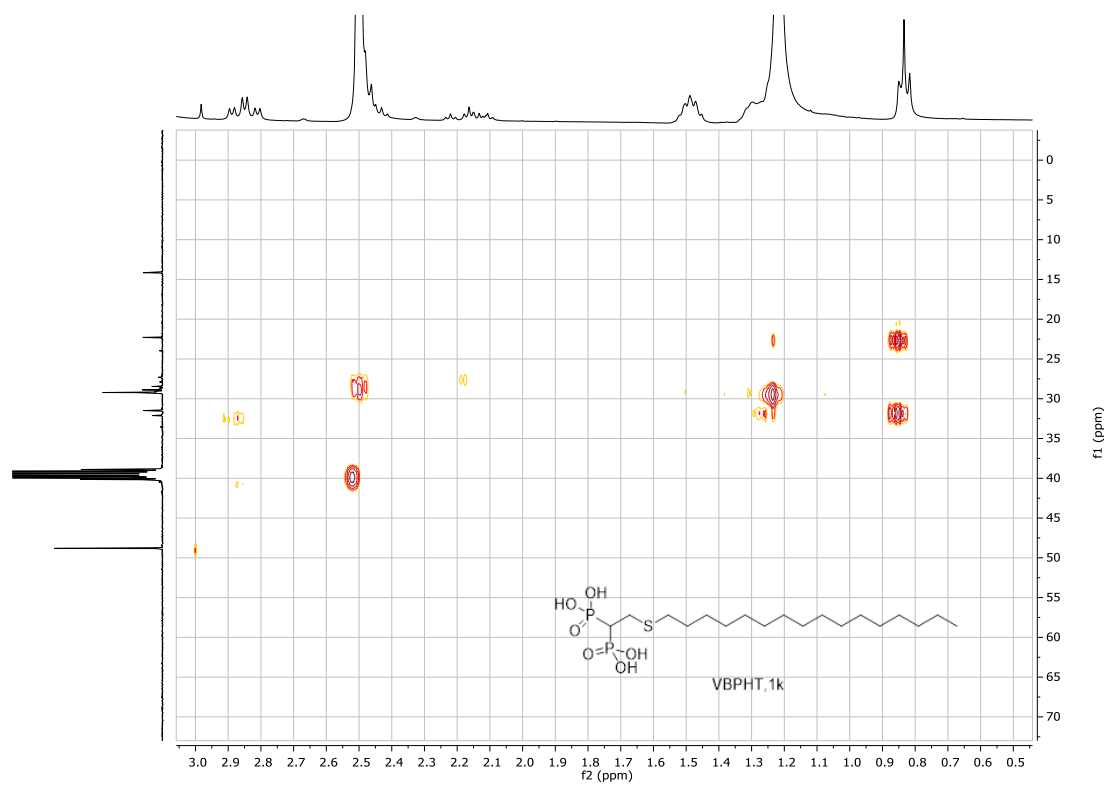


Figure 2.114: 2D NMR HMBC of BPHDT, 1k

2.4. Experimental Section

General Methods & Materials

The reactions were followed with TLC Polygram[®] Sil G/UV254, 0.25 mm thickness. ¹H NMR, ¹³C NMR, and 2D spectra were recorded with a Bruker Avance 300 and Ascend 400 spectrometers, working at 300-400 and 75-100 MHz respectively. Resonance frequencies are referred to tetramethyl silane.

Reagents and solvents with high purity degree purchased by the providers were used as given. Otherwise, they were purified following the procedures reported in literature. [253] Anhydrous solvents were prepared by adding activated 3 Å molecular sieves to the solvent under inert atmosphere. Molecular sieves were activated shortly before the use by continuous heating under vacuum. Flash chromatography were performed with silica gel Merk 60, 230-400 mesh, following procedures reported in literature. [254]

Reagents	Purity	M.W (g/mol)	Density (g/cm ⁻³)	Supplier
Aminoethanthiol	>95%	77.15		Tokyo Chemical Industry (TCI)
3-mercapto-1-propanol	>97%	92.16	1.067	Tokyo Chemical Industry (TCI)
Allyl mercaptan	>80%	74.14	0.90	Tokyo Chemical Industry (TCI)
Methyl mercaptan sodium salt	>95%	114.10	1.0	Tokyo Chemical Industry (TCI)
1,5-Pentanedithiol	>95%	136.28	1.016	Tokyo Chemical Industry (TCI)
1,8-Octanedithiol	>97%	178.36	0.97	Tokyo Chemical Industry (TCI)
1-Hexadecanethiol	>97%	258.52	0.846	Tokyo Chemical Industry (TCI)
Sodium borohydride	≥ 98%	37.83	1.07	Sigma-Aldrich
Bromo trimethylsilane	>97%	153.09	1.183	Sigma-Aldrich
Di-tert-butyl decarbonate	>98%	218.25	0.95	Sigma-Aldrich
Trifluoroacetic acid	>99%	114.02	1.48	Sigma-Aldrich
Benzyl bromide	>98%	171.03	1.44	Sigma-Aldrich

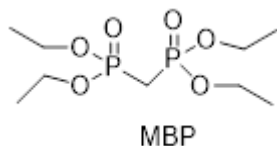
Quantitative ¹H NMR determinations

¹H NMR spectra for quantitative determinations were recorded with a Bruker Ascend 400 spectrometer operating at 400 MHz with saturation of the solvent peak of water at 4.79 ppm. Analyses were carried out preparing a standard solution of the BP 5 mM in D₂O buffered solutions 25 mM. Since the release tests were directly carried out in deuterated solvents, aliquots of 1 mL on the samples were withdrawn at fixed times (0, 30, 60, 90, 120, 240, 420, and 1440 minutes) removing the ZrNPs by centrifugation. The obtained solutions were directly analysed by quantitative NMR acquiring the ¹H NMR spectra of the samples and of the references with the same acquisition parameters such as number of scans 16 and d1 of 10 s on 0.6 mL of sample. The ¹H NMR spectra were analysed with the quantitative Eretic Bruker program considering

volume of the solution, the concentration of the mother solution as reference and the number of H atoms assigned to a certain resonance in the spectrum.

2.4.1. Tetraethyl methylenebis(phosphonate) (MBP)

The starting material was synthesised according to literature procedure [255]. Briefly, in a 500 mL round bottomed flask, small pieces of sodium metal (5 g, 220 mmol) were dissolved in 130 mL ethanol solvent under vigorous stirring, then diethyl phosphite (28 mL, 220 mmol) was added dropwise into the clear sodium ethoxide solution and then left the reaction mixture under stirring for 1h at room temperature. Then the resulting solution was concentrated under rotavapor and then dissolved in anhydrous methylene chloride (10 mL, 156 mmol) and the solution was stirred for 15 days at room temperature. After that the solution was washed with saturated brine (3 X 50 mL). The organic phase was diluted with CH₂Cl₂ (30 mL) and dried with NaSO₄ and then precipitate was filtered. Methylene dichloride was removed from mother liquors with rotavapor. The residue was distilled at high vacuum through Kugelrohr (0.1 mm Hg). The product was obtained as colorless oil (54% yield).



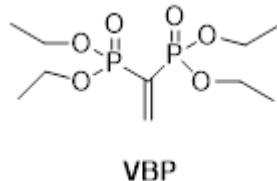
¹H NMR (400 MHz, Chloroform-*d*) δ 4.16 – 3.97 (set of m, 8H), 2.34 (t, *J* = 21.0 Hz, 2H), 1.24 (t, *J* = 7.1 Hz, 12H).

³¹P NMR (162 MHz, Chloroform-*d*) δ 19.33 (s, 2p).

¹³C NMR (101 MHz, Chloroform-*d*) δ 62.62 (t, *J* = 3.0 Hz), 25.43 (t, *J* = 136.9 Hz), 16.36 (d, *J* = 3.2 Hz) ppm.

2.4.2. diethyl (1-(ethoxy(methoxy)phosphoryl)vinyl)phosphonate (VBP)

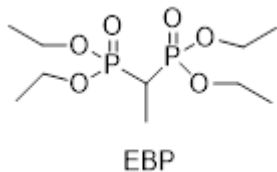
In a 500 mL round bottomed flask, paraformaldehyde (3.18 g, 106 mmol) and diethylamine (2.2 mL, 21mmol) were dispersed in 60 mL of methanol and the flask was topped with a reflux condenser. The apparatus was purged with nitrogen and the suspension refluxed until clearness. The resulting solution was cooled to room temperature. Then tetraethyl (methylene) bisphosphonate (5 ml, 20 mmol) was added dropwise into the cooled solution and then reflux for overnight. After that the completeness of the intermediate reaction was verified by ¹H & ³¹P NMR analysis. Then the solution was concentrated under rotavapor and the crude solution was diluted with methanol (30 mL) and then concentrated. The concentrated solution was diluted with toluene and concentrated again. Then the solution was dissolved in anhydrous toluene and p-toluene sulfonic acid (15 mg, 0.09 mmol) was added to the solution. A pressure-equalizing dropping funnel filled with activated 3 Å molecular sieves was placed over the flask and topped with a reflux condenser. The apparatus was purged with nitrogen and the suspension refluxed for 24 hours. The completeness of the reaction was verified by ¹H & ³¹P NMR analysis. The resulting solution was cooled to room temperature and concentrated under rotavapor. Then the residue was dissolved in CH₂Cl₂, washed twice with H₂O, dried with NaSO₄, and finally CH₂Cl₂ was removed from mother liquor with rotavapor. The product was obtained as light-yellow oil (5.3 g, 17.6 mmol, 90% yield).



^1H NMR (400 MHz, Chloroform-*d*) δ 6.88 (dd, $J = 71.6, 9.3$ Hz, 2H), 4.17 – 3.89 (set of m, 8H), 1.24 (t, $J = 7.1$ Hz, 12H).
 $^{31}\text{P}\{^1\text{H}\}$ NMR (162 MHz, Chloroform-*d*) δ 12.93 (s, 2P).
 ^{13}C NMR (101 MHz, Chloroform-*d*) δ 149.29 (s), 132.17 (t, $J = 166.6$ Hz), 62.78 (t, $J = 2.8$ Hz), 16.38 (t, $J = 3.3$ Hz) ppm.

2.4.3. Tetraethyl ethane-1,1-diylbis(phosphonate) (EBP)

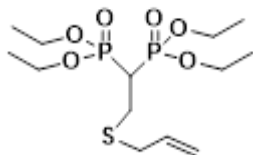
In a 100 mL round bottom flask equipped with magnetic stirring bar, vinylidene bisphosphonate tetraethyl ester (VBP, 500 mg, 1.67 mmol) was added in 5 mL methanol. Then NaBH_4 (63 mg, 1.67 mmol) was added to the solution and left stirred for 3h at room temperature under inert atmosphere. Then 1 mL deionized H_2O was added to the reaction mixture and continued stirred for 30 min. After that methanol was removed with rotavapor. The crude was dissolved in 10 mL ethyl acetate and then washed with saturated brine (2X 50 mL), dried with NaSO_4 and then precipitate was filtered. Finally, ethyl acetate solvent was removed with rotavapor. The product was obtained as colorless liquid (450 mg, 1.49 mmol, 95% yield).



^1H NMR (400 MHz, Chloroform-*d*) δ 4.18 – 4.02 (set of m, 8H), 2.44 – 2.26 (set of m, 1H), 1.40 (td, $J = 17.2, 7.4$ Hz, 3H), 1.28 (t, $J = 7.1$ Hz, 12 H).
 $^{31}\text{P}\{^1\text{H}\}$ - NMR (162 MHz, CDCl_3) δ 24.04 (s, 2P).
 $^1\text{H}\{^{31}\text{P}\}$ -NMR (400 MHz, Chloroform-*d*) δ 4.16 – 4.06 (set of m, 8H), 2.33 (q, $J = 7.4$ Hz, 1H), 1.40 (d, $J = 7.4$ Hz, 3H), 1.28 (t, $J = 7.1$ Hz, 12H).
 ^{13}C NMR (101 MHz, Chloroform-*d*) δ 62.53 (d, $J = 6.7$ Hz), 31.06 (t, $J = 136.2$ Hz), 16.39 (d, $J = 1.7$ Hz), 16.32 (d, $J = 1.7$ Hz), 10.19 (t, $J = 6.2$ Hz).

2.4.4. Tetraethyl (2-(allylthio)ethane-1,1-diyl)bis(phosphonate) (BPSAL)

In a 100 mL round bottom flask equipped with magnetic stirring bar, vinylidene bisphosphonate tetraethyl ester (VBP, 500 mg, 1.67 mmol) was dispersed in 2.5 mL CHCl_3 . Then allyl mercaptan (137 μL , 1.67 mmol) and triethyl amine (12 μL , 5% in mol) were added to the solution. The apparatus was purged with nitrogen and the reaction mixture was refluxed for overnight. The resulting solution was cooled to room temperature and concentrated under rotavapor. The crude was dissolved in 10 mL CH_2Cl_2 and washed with deionized H_2O (2x 25 mL). The organic phase was dried with NaSO_4 and precipitate was filtered and CH_2Cl_2 solvent was removed with rotavapor. The crude mixture was purified by flash chromatography with 1:1 ethyl acetate/Methanol as eluent. The product was obtained as pale-yellow oil (556 mg, 1.51 mmol, 89% yield).

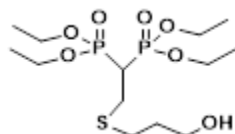


^1H NMR (400 MHz, CDCl_3) δ 5.75 (1H, td, $J = 17.0, 8.5$ Hz, 1H), 5.10 (dd, $J = 17.0, 1.5$ Hz, 1H), 5.04 (dd, $J = 9.9, 1.6$ Hz, 1H), 4.14 – 4.06 (set of m, 8H), 3.09 (d, $J = 7.1$ Hz, 2H), 2.91 (td, $J = 16.2, 6.1$ Hz, 2H), 2.49 (tt, $J = 23.8, 6.1$ Hz, 1H), 1.25 (t, $J = 7.1$ Hz, 12H).
 $^{31}\text{P}\{^1\text{H}\}$ - NMR (162 MHz, Chloroform-*d*) δ 21.58 (s, 2P).

^1H $\{^{31}\text{P}\}$ -NMR (400 MHz, Chloroform-*d*) δ 5.83 – 5.68 (set of m, 1H), 5.11 (d, J = 15.9 Hz, 1H), 5.06 (d, J = 9.9 Hz, 1H), 4.21 – 4.10 (m, 10H), 3.13 (d, J = 7.1 Hz, 2H), 2.95 (d, J = 6.1 Hz, 3H), 2.52 (s, 0H), 1.30 (t, J = 7.1 Hz, 14H).
 ^{13}C NMR (101 MHz, Chloroform-*d*) δ 134.08, 117.48, 62.87 (d, J = 6.6 Hz), 62.72 (d, J = 6.7 Hz), 38.85 (t, J = 131.6 Hz), 35.81, 26.65 (t, J = 4.9 Hz), 16.40 (d, J = 6.2 Hz).

2.4.5. Tetraethyl (2-((3-hydroxypropyl)thio)ethane-1,1-diyl)bis(phosphonate) (BPHPT)

In a 100 mL round bottom flask, vinylidene bisphosphonate tetraethyl ester (VBP, 500 mg, 1.67 mmol) was dispersed in 2.5 mL CHCl_3 . Then 3- mercapto-1-propanol (146 μL , 1.67 mmol) and triethyl amine (12 μL , 5% in mol) were added to the solution. The apparatus was purged with nitrogen and the reaction mixture was refluxed for overnight. The resulting solution was cooled to room temperature and concentrated with rotavapor. The crude was dissolved in 10 mL CH_2Cl_2 and washed with deionized H_2O (2x 25 mL). The organic phase was dried with NaSO_4 and precipitate was filtered. Then CH_2Cl_2 solvent was removed with rotavapor. The crude mixture was purified by flash chromatography with 1:1 ethyl acetate/Methanol as eluent. The product was obtained as colorless liquid (619 mg, 1.58 mmol, 95% yield).



^1H NMR (400 MHz, Chloroform-*d*) δ 4.21 – 4.08 (set of m, 8H), 3.68 (t, J = 5.9 Hz, 2H), 3.02 (td, J = 16.3, 5.9 Hz, 2H), 2.71 – 2.50 (set of m, 3H), 1.81 (p, J = 6.5 Hz, 2H), 1.31 (t, J = 7.1 Hz, 13H).

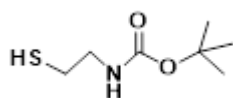
^{31}P $\{^1\text{H}\}$ - NMR (162 MHz, Chloroform-*d*) δ 21.6 (s, 2P).

^1H $\{^{31}\text{P}\}$ - NMR (400 MHz, , Chloroform-*d*) δ 4.17 – 4.09 (set of m, 8H), 3.69 – 3.64 (t, 2H), 3.00 (d, J = 5.7 Hz, 2H), 2.65 (t, J = 6.9 Hz, 2H), 2.56 (t, J = 5.1 Hz, 1H), 1.82 – 1.74 (p, 2H), 1.28 (t, J = 6.9 Hz, 12H).

^{13}C NMR (101 MHz, Chloroform-*d*) δ 63.06 (d, J = 6.9 Hz), 62.91 (d, J = 6.8 Hz), 38.95 (t, J = 131.8 Hz), 31.90 (s), 29.41 (S), 27.68 (t, J = 4.8 Hz), 16.44 (d, J = 6.4 Hz).

2.4.6a. Synthesis of 2-(Boc-amino) ethanethiol

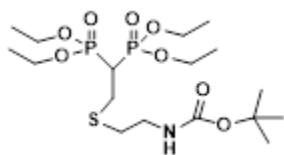
In a 500 mL round bottle flask equipped with magnetic stirring, a solution of 2-amino ethanol (200 mg, 2.6 mmol) in water (3 mL) and a THF solution of di-tert-butyl decarbonate $(\text{BOC})_2\text{O}$ (597 μL , 2.6 mmol) were added. The reaction mixture was stirred under N_2 atmosphere at room temperature for 4 h. Then solution was extracted with 10 mL of CH_2Cl_2 and washed twice with 25 mL of water. The organic phase was dried with NaSO_4 and precipitate was filtered. Then CH_2Cl_2 solvent was removed with rotavapor. The product was obtained as colorless liquid ((451 mg, 2.49 mmol, 98% yield).



^1H NMR (400 MHz, Chloroform-*d*) δ 3.21 (q, J = 6.1 Hz, 2H), 2.56 (q, J = 8.0, 7.3 Hz, 2H), 1.36 (s, 9H), 1.31 (t, J = 8.5 Hz, 1H).

2.4.6b. *Tert-butyl (2-((2,2-bis(diethoxyphosphoryl)ethyl)thio)ethyl)carbamate (BPBAT)*

In a 100 mL round bottom flask, vinylidene bisphosphonate tetraethyl ester (VBP, 500 mg, 1.67 mmol) was dispersed in 2.5 mL CHCl₃. Then (2-boc-amino) ethanethiol (301 μL, 1.67 mmol) and triethyl amine (12 μL, 5% in mol) were added to the solution. The apparatus was purged with nitrogen and the reaction mixture was refluxed for overnight. The resulting solution was cooled to room temperature and concentrated with rotavapor. The crude was dissolved in 10 mL CH₂Cl₂ and washed with deionized H₂O (2x 25 mL). The organic phase was dried with NaSO₄ and precipitate was filtered. Then CH₂Cl₂ solvent was removed with rotavapor. The crude mixture was purified by flash chromatography with 1:1 ethyl acetate/Methanol as eluent. The product was obtained as colorless liquid (678 mg, 1.42 mmol, 85% yield).



¹H NMR (400 MHz, Chloroform-*d*) δ 4.24 – 4.13 (set of m, 8H), 3.38 – 3.28 (m, 2H), 3.03 (td, *J* = 16.5, 5.8 Hz, 2H), 2.68 (t, *J* = 6.2 Hz, 2H), 2.57 (tt, *J* = 24.0, 5.9 Hz, 1H), 1.42 (s, 9H), 1.33 (t, *J* = 7.1 Hz, 12H).

³¹P{¹H}- NMR (162 MHz, Chloroform-*d*) δ 21.56 (s, 2P).

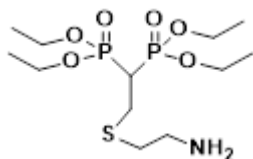
¹H {³¹P}- NMR (400 MHz, Chloroform-*d*) δ 4.26 – 4.11 (set of m, 8H), 3.32 (set of m, 2H), 3.03 (d, *J* = 5.7 Hz, 2H), 2.68 (t, *J* = 6.1 Hz, 2H), 2.57 (t, *J* = 5.8 Hz, 1H), 1.42 (s, 9H), 1.33 (t, *J* = 7.1 Hz, 12H).

¹³C NMR (101 MHz, Chloroform-*d*) δ 63.09 (d, *J* = 6.7 Hz), 62.91 (d, *J* = 6.7 Hz), 39.47 (s), 39.17 (t, *J* = 131.9 Hz), 33.53 (s), 28.52 (s), 27.51 (t, *J* = 4.9 Hz), 16.50 (d, *J* = 6.2 Hz).

2.4.6c. *Tetraethyl (2-((2-aminoethyl)thio)ethane-1,1-diyl)bis(phosphonate) (BPAET)*

In a 100 mL round bottom flask, tetraethyl 2-((2-boc-amino) ethanethiol) ethane-1,1-diyl diphosphonate (BPBAT, 500 mg, 1.05 mmol) was added in 3 mL of CH₂Cl₂. Then 4 mL of trifluoroacetic acid (TFA) was added slowly and the reaction mixture was left under stirred for one and half an hour at room temperature. The chloroform solvent was removed with rotavapor. The product was obtained as colorless liquid (388 mg, 1.03 mmol, 98% yield).

¹H NMR (400 MHz, Chloroform-*d*) δ 4.27 – 4.12 (set of m, 8H), 3.26 (set of m, 2H), 3.06 (td, *J* = 17.2, 6.1 Hz, 2H), 2.96 (t, *J* = 6.0 Hz, 2H), 2.78 (tt, *J* = 24.4, 6.0 Hz, 1H), 1.35 (t, *J* = 7.1 Hz, 12H).



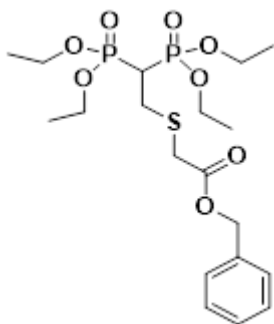
³¹P{¹H}- NMR (162 MHz, Chloroform-*d*) δ 20.93 (s, 2p).

¹H {³¹P}-NMR (400 MHz, Chloroform-*d*) δ 4.20 (p, *J* = 7.1 Hz, 8H), 3.28 (set of m, 2H), 3.07 (d, *J* = 6.0 Hz, 2H), 2.96 (t, *J* = 5.9 Hz, 2H), 2.79 (t, *J* = 5.9 Hz, 1H), 1.35 (t, *J* = 7.0 Hz, 12H).

¹³C NMR (101 MHz, Chloroform-*d*) δ 64.47 (d, *J* = 7.1 Hz), 64.29 (d, *J* = 7.0 Hz), 38.77 (s), 37.55 (t, *J* = 136.2 Hz), 30.25 (S), 27.07 (t, *J* = 5.0 Hz), 16.20 (d, *J* = 5.6 Hz).

2.4.7. Benzyl 2-((2,2-bis(diethoxyphosphoryl)ethyl)thio)acetate (BPBTG)

In a double neck 100 mL round bottle flask, sodium thioglycolate (250 mg, 2.19 mmol) was added in 3-4 mL of anhydrous DMF. The apparatus was purged with nitrogen gas immediately. Then benzyl bromide (260 mg, 2.19 mmol) and vinylidene bisphosphonate tetraethyl ester (VBP, 657 mg, 2.19 mmol) were added in solution using needle without disturbing the inert atmosphere and the reaction mixture was left at 60°C for overnight. After that, molar equivalent amount of triethyl amine (300 μ L) was added to the reaction mixture under inert atmosphere. Then the reaction mixture was left for 24h at 60°C. Then the reaction mixture was cooled to room temperature and diluted with 20 mL CH₂Cl₂ solvent. The organic phase was dried with NaSO₄ and precipitate was filtered. Then CH₂Cl₂ solvent was removed with rotavapor. The crude mixture was purified by flash chromatography with 1:1 ethyl acetate/Methanol as eluent. The product was obtained as yellow liquid (739 mg, 1.53 mmol, 70% yield).



¹H NMR (400 MHz, Chloroform-*d*) δ 7.40 – 7.27 (set of m, 5H), 5.15 (s, 2H), 4.23 – 4.07 (set of m, 8H), 3.35 (s, 2H), 3.17 (td, J = 16.1, 6.0 Hz, 2H), 2.74 (tt, J = 24.0, 6.0 Hz, 1H), 1.31 (t, J = 7.1 Hz, 12H).

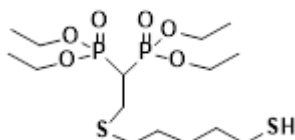
³¹P{¹H}-NMR (162 MHz, Chloroform-*d*) δ 21.27 (s, 2P).

¹H{³¹P}-NMR (400 MHz, Chloroform-*d*) δ 7.39 – 7.27 (set of m, 5H), 5.15 (s, 2H), 4.16 (q, J = 7.0 Hz, 8H), 3.35 (s, 2H), 3.17 (d, J = 6.0 Hz, 2H), 2.74 (t, J = 6.0 Hz, 1H), 1.31 (t, J = 7.1 Hz, 12H).

¹³C NMR (101 MHz, Chloroform-*d*) δ 128.70 (s), 128.50 (s), 128.39 (s), 67.26 (s), 63.19 (d, J = 6.6 Hz), 63.03 (d, J = 6.7 Hz), 38.64 (t, J = 131.8 Hz), 34.88 (s), 28.81 (t, J = 4.9 Hz), 16.45 (d, J = 6.2 Hz).

2.4.8. Tetraethyl (2-(pentamethylene dimercaptan) ethane-1,1-diyl)bis(phosphonate) (BPPMD)

In a 100 mL round bottom flask, vinylidene bisphosphonate tetraethyl ester (VBP, 500 mg, 1.67 mmol) was dispersed in 2.5 mL CHCl₃. Then 1,5 pentane dithiols (224 μ L, 1.67 mmol) and triethyl amine (12 μ L, 5% in mol) were added to the solution. The apparatus was purged with nitrogen and the reaction mixture was refluxed for overnight. The resulting solution was cooled to room temperature and concentrated under rotavapor. The crude was dissolved in 10 mL CH₂Cl₂ and washed with deionized H₂O (2x 25 mL). The organic phase was dried with NaSO₄ and precipitate was filtered. Then CH₂Cl₂ solvent was removed with rotavapor. The product was obtained as colorless liquid (704 mg, 1.63 mmol, 98% yield).



¹H NMR (400 MHz, Chloroform-*d*) δ 4.21 – 4.11 (set of m, 8H), 2.99 (td, J = 16.3, 5.9 Hz, 2H), 2.55 – 2.45 (set of m, 5H), 1.63-1.57 (set of m, 4H), 1.51 – 1.39 (set of m, 2H), 1.30 (t, J = 7.1 Hz, 13H).

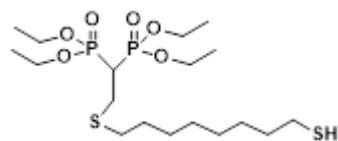
³¹P{¹H}-NMR (162 MHz, Chloroform-*d*) δ 21.67 (s, 2P).

$^1\text{H}\{^{31}\text{P}\}$ -NMR (400 MHz, Chloroform-*d*) δ 4.24 – 4.09 (set of m, 8H), 2.99 (d, $J = 5.9$ Hz, 2H), 2.58 – 2.42 (set of m, 5H), 1.61-1.53 (set of m, 4H), 1.51 – 1.39 (set of m, 2H), 1.30 (t, $J = 7.1$ Hz, 13H).

^{13}C NMR (101 MHz, Chloroform-*d*) δ 62.94 (d, $J = 6.6$ Hz), 62.78 (d, $J = 6.7$ Hz), 39.15 (t, $J = 131.5$ Hz), 33.58 (s), 33.43 (s), 28.87 (s), 27.83 (t, $J = 4.9$ Hz), 27.54 (s), 24.49 (s), 16.44 (d, $J = 6.2$ Hz).

2.4.9. Tetraethyl 2-(octamethylene dimercaptan) ethane-1,1 diylbis(hosphonate) (BPOMD)

In a 100 mL round bottom flask, vinylidene bisphosphonate tetraethyl ester (VBP, 500 mg, 1.67 mmol) was dispersed in 2.5 mL CHCl_3 . Then 1,8 octane dithiols (297 μL , 1.67 mmol) and triethyl amine (12 μL , 5% in mol) were added to the solution. The apparatus was purged with nitrogen and the reaction mixture was refluxed for overnight. The resulting solution was cooled to room temperature and concentrated under rotavapor. The crude was dissolved in 10 mL CH_2Cl_2 and washed with deionized H_2O (2x 25 mL). The organic phase was dried with NaSO_4 and precipitate was filtered. Then CH_2Cl_2 solvent was removed with rotavapor. The product was obtained as colorless liquid (766 mg, 1.60 mmol, 96% yield).



^1H NMR (400 MHz, Chloroform-*d*) δ 4.24 – 4.09 (set of m, 8H), 3.00 (td, $J = 16.0, 5.6$ Hz, 2H), 2.59 – 2.43 (set of m, 5H), 1.56 (set of m, 4H), 1.39 – 1.23 (set of m, 21H).

$^{31}\text{P}\{^1\text{H}\}$ -NMR (162 MHz, Chloroform-*d*) δ 21.72 (s, 2P).

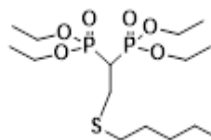
$^1\text{H}\{^{31}\text{P}\}$ - NMR (400 MHz, Chloroform-*d*) δ 4.24 – 4.09 (set of m, 8H), 3.00 (d, $J = 5.9$ Hz, 2H), 2.57 – 2.44 (set of m, 5H), 1.63 – 1.49 (set of m, 4H), 1.39 – 1.23 (set of m, 21H).

^{13}C NMR (101 MHz, Chloroform-*d*) δ 62.96 (d, $J = 6.6$ Hz), 62.80 (d, $J = 6.7$ Hz), 39.18 (t, $J = 131.5$ Hz), 34.04 (s), 33.20 (s), 29.44 (s), 29.15 (s), 28.99 (s), 28.83 (s), 28.33 (s), 27.85 (t, $J = 4.9$ Hz), 24.67 (s), 16.45 (d, $J = 6.2$ Hz).

2.4.10. Tetraethyl (2-(1-hexadecane thiol) ethane-1,1 diyl)bis(phosphonate) (BPHDT)

In a 100 mL round bottom flask, vinylidene bisphosphonate tetraethyl ester (VBP, 500 mg, 1.67 mmol) was dispersed in 2.5 mL CHCl_3 . Then 1-hexadecane thiol (508 μL , 1.67 mmol) and triethyl amine (12 μL , 5% in mol) were added to the solution. The apparatus was purged with nitrogen and the reaction mixture was refluxed for overnight. The resulting solution was cooled to room temperature and concentrated under rotavapor. The crude was dissolved in 10 mL CH_2Cl_2 and washed with deionized H_2O (2x 25 mL). The organic phase was dried with NaSO_4 and precipitate was filtered. Then CH_2Cl_2 solvent was removed with rotavapor. The product was obtained as colorless liquid (866 mg, 1.55 mmol, 93% yield).

^1H NMR (400 MHz, Chloroform-*d*) δ 4.20 – 4.11 (set of m, 8H), 2.99 (td, $J = 16.3, 5.9$ Hz, 2H), 2.57 – 2.43 (set of m,



3H), 1.60 – 1.49 (set of m, 2H), 1.30 (t, $J = 7.1$ Hz, 12H), 1.21 (set of m, 26H), 0.87 – 0.79 (t, $J = 6.8$ Hz, 3H).

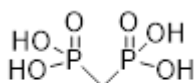
$^{31}\text{P}\{^1\text{H}\}$ - NMR (162 MHz, Chloroform- d) δ 21.75 (s, 2P).

$^1\text{H}\{^{31}\text{P}\}$ -NMR (400 MHz, Chloroform- d) δ 4.24 – 4.13 (set of m, 8H), 3.02 (d, $J = 5.9$ Hz, 2H), 2.59 – 2.47 (set of m, 2H), 1.64 – 1.51 (set of m, 2H), 1.33 (t, $J = 7.1$ Hz, 12H), 1.24 (set of m, 26H), 0.86 (t, $J = 6.8$ Hz, 3H).

^{13}C NMR (101 MHz, Chloroform- d) δ 62.97 (d, $J = 6.7$ Hz), 62.82 (d, $J = 6.7$ Hz), 39.24 (t, $J = 131.4$ Hz), 33.27 (s), 32.02 (s), 30.99(s), 29.79(s), 29.45(s), 29.00(s), 27.88 (t, $J = 5.0$ Hz), 22.78(s), 16.48 (d, $J = 6.3$ Hz), 14.20 (s).

2.4.11. Methylene Bis-phosphonic Acid (MBP, 1a)

In a 100 mL round bottom flask equipped with magnetic stirring bar, methylene bisphosphonate tetraethyl ester (500 mg, 1.78 mmol) was added in 4-5 mL $\text{C}_2\text{H}_4\text{Cl}_2$ solvent. Then bromotrimethylsilane ($\text{Si}(\text{CH}_3)_3\text{Br}$, 3.46 mL, 26.7 mmol) was added quickly to the solution. The mixture was refluxed under nitrogen atmosphere for an hour and a half. Then the flask was putted into high vacuum with N_2 for 1 h. Then vacuum was removed and solvent mixture (10 ml MeOH + 1 mL distilled water) was added to the flask and the reaction mixture was left stirred for 1h. After that, the solvent was removed with rotavapor. The product was obtained as colorless liquid (306 mg, 1.74 mmol, 98% yield).



MBP, 1a

^1H NMR (400 MHz, Deuterium Oxide) δ 2.12 (t, $J = 20.9$ Hz, 2H).

$^{31}\text{P}\{^1\text{H}\}$ - NMR (162 MHz, Deuterium Oxide) δ 18.18 (s, 2P).

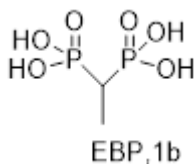
$^1\text{H}\{^{31}\text{P}\}$ - NMR (400 MHz, Deuterium Oxide) δ 2.14 (s, 2H).

^{13}C NMR (101 MHz, Deuterium Oxide) δ 26.59 (t, $J = 130.2$ Hz).

2.4.12. Ethan-1,1-diylbis(phosphonic Acid (EBP, 1b)

In a 100 mL round bottom flask equipped with magnetic stirring bar, ethylene bisphosphonate tetraethyl ester (350 mg, 1.76 mmol) was added in 3 mL $\text{C}_2\text{H}_4\text{Cl}_2$ solvent. Then bromotrimethylsilane ($\text{Si}(\text{CH}_3)_3\text{Br}$, 2.25 mL, 17.4 mmol) was added quickly to the solution. The mixture was refluxed under nitrogen atmosphere for an hour and a half. Then the flask was putted into high vacuum with N_2 for 1 h. Then vacuum was removed and solvent mixture (10 ml MeOH + 1 mL distilled water) was added to the flask and the reaction mixture was left stirred for 1h. After that, the solvent was removed with rotavapor. The product was obtained as colorless liquid (326 mg, 1.72 mmol, 98% yield).

^1H NMR (400 MHz, Deuterium Oxide) δ 2.46 – 2.26 (m, 1H), 1.37 (td, $J = 17.4, 4.7$ Hz, 3H).



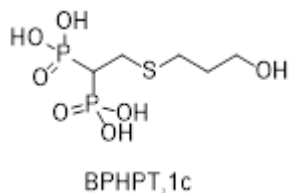
$^{31}\text{P}\{^1\text{H}\}$ - NMR (162 MHz, Deuterium Oxide) δ 22.98 (s).

$^1\text{H}\{^{31}\text{P}\}$ -NMR (400 MHz, Deuterium Oxide) δ 2.46 – 2.29 (m, 1H), 1.39 (d, J = 6.9 Hz, 3H).

^{13}C NMR (101 MHz, Deuterium Oxide) δ 31.71 (t, J = 129.3 Hz), 9.37 (t, J = 5.5 Hz).

2.4.13. 2-((3-hydroxypropyl) thiol)ethane-1,1- diyl)bis(phosphonic acid (BPHPT, 1c)

In a 100 mL round bottom flask equipped with magnetic stirring bar, ethylene bisphosphonate tetraethyl ester (500 mg, 1.28 mmol) was added in 4 mL $\text{C}_2\text{H}_4\text{Cl}_2$ solvent. Then bromotrimethylsilane ($\text{Si}(\text{CH}_3)_3\text{Br}$, 2.48 mL, 19.2 mmol) was added quickly to the solution. The mixture was refluxed under nitrogen atmosphere for an hour and a half. Then the flask was putted into high vacuum with N_2 for 1 h. Then vacuum was removed and solvent mixture (10 ml MeOH + 1 mL distilled water) was added to the flask and the reaction mixture was left stirred for 1h. After that, the solvent was remover with rotavapor. The product was obtained as colorless liquid (354mg, 1.27 mmol, 99% yield).



^1H NMR (400 MHz, Deuterium Oxide) δ 3.66 (t, 2H), 3.04 (td, J = 16.0, 6.4 Hz, 2H), 2.68 (t, J = 7.3 Hz, 2H), 2.55 (tt, J = 23.0, 6.4 Hz, 1H), 1.90 – 1.77 (set of m, 2H).

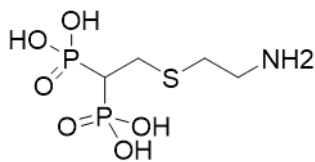
$^{31}\text{P}\{^1\text{H}\}$ - NMR (162 MHz, Deuterium Oxide) δ 19.73 (s, 2P).

$^1\text{H}\{^{31}\text{P}\}$ NMR (400 MHz, Deuterium Oxide) δ 3.69 (t, J = 6.1 Hz, 2H), 3.08 – 3.02 (d, J = 6.1, 2H), 2.69 (t, J = 7.1 Hz, 2H), 2.56 (t, J = 6.4 Hz, 1H), 1.90 – 1.80 (set of m, 2H).

^{13}C NMR (101 MHz, Deuterium Oxide) δ 60.31 (s), 48.85 (s), 39.11 (t, J = 123.7 Hz), 30.87 (s), 28.41 (s), 27.13 (t, J = 4.2 Hz).

2.4.14. (2-((2-aminoethyl)thio)ethane-1,1-diyl)bis(phosphonic acid) (AETI, 1d)

In a 100 mL round bottom flask equipped with magnetic stirring bar, tetraethyl 2-(amino ethanethiol) ethane-1,1-diyl diphosphonate (500 mg, 1.32 mmol) was added in 4 mL $\text{C}_2\text{H}_4\text{Cl}_2$ solvent. Then bromotrimethylsilane ($\text{Si}(\text{CH}_3)_3\text{Br}$, 2.57 mL, 19.87 mmol) was added quickly to the solution. The mixture was refluxed under nitrogen atmosphere for an hour and a half. Then the flask was putted into high vacuum with N_2 for 1 h. Then vacuum was removed and solvent mixture (10 ml MeOH + 1 mL distilled water) was added to the flask and the reaction mixture was left stirred for 1h. After that, the solvent was remover with rotavapor. The product was obtained as colorless liquid (332 mg, 1.25 mmol, 95% yield).



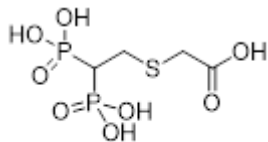
BPAET, 1d

^1H NMR (400 MHz, DMSO- d_6) δ 3.06 – 2.97 (set of m, 2H), 2.92 (td, J = 15.4, 5.8 Hz, 2H), 2.77 (t, J = 6.6 Hz, 2H), 2.34 (tt, J = 22.3, 5.8 Hz, 1H).

$^{31}\text{P}\{^1\text{H}\}$ - NMR (162 MHz, DMSO- d_6) δ 18.45 (s, 2P).

2.4.15. 2-((2,2-diphosphonoethyl)thio)acetic acid (BPSC, 1e)

In a 100 mL round bottom flask equipped with magnetic stirring bar, tetraethyl 2-(benzyl thioglycolate) ethane-1,1-diylidiphosphonate (500 mg, 1.04 mmol) was added in 4 mL $\text{C}_2\text{H}_4\text{Cl}_2$ solvent. Then bromotrimethylsilane ($\text{Si}(\text{CH}_3)_3\text{Br}$, 2.02 mL, 15.60 mmol) was added quickly to the solution. The mixture was refluxed under nitrogen atmosphere for an hour and a half. Then the flask was putted into high vacuum with N_2 for 1 h. Then vacuum was removed and solvent mixture (10 ml MeOH + 1 mL distilled water) was added to the flask and the reaction mixture was left stirred for 1h. After that, the solvent was removed with rotavapor. The product was obtained as colorless liquid (285 mg, 1.02 mmol, 98% yield).



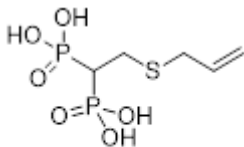
BPSC, 1e

^1H NMR (400 MHz, Deuterium Oxide) δ 3.47 (s, 2H), 3.12 (td, J = 15.9, 6.5 Hz, 2H), 2.61 (tt, J = 22.9, 6.5 Hz, 1H).

$^{31}\text{P}\{^1\text{H}\}$ - NMR (162 MHz, Deuterium Oxide) δ 19.22 (s, 2P).

2.4.16. (2-(allylthio)ethane-1,1-diyl)bis(phosphonic acid) (BPSAL, 1f)

In a 100 mL round bottom flask equipped with magnetic stirring bar, tetraethyl 2-(2-propene-1-thiol) ethane-1,1-diylidiphosphonate (200 mg, 1.29 mmol) was added in 4 mL $\text{C}_2\text{H}_4\text{Cl}_2$ solvent. Then bromotrimethylsilane ($\text{Si}(\text{CH}_3)_3\text{Br}$, 2.50 mL, 19.35 mmol) was added quickly to the solution. The mixture was refluxed under nitrogen atmosphere for an hour and a half. Then the flask was putted into high vacuum with N_2 for 1 h. Then vacuum was removed and solvent mixture (10 ml MeOH + 1 mL distilled water) was added to the flask and the reaction mixture was left stirred for 1h. After that, the solvent was removed with rotavapor. The product was obtained as colorless liquid (324 mg, 1.24 mmol, 96% yield).



BPSAL, 1f

^1H NMR (400 MHz, Deuterium Oxide) δ 5.80 (td, J = 17.2, 7.2 Hz, 1H), 5.19 (q, J = 1.2 Hz, 1H), 5.12 (d, J = 11.6 Hz, 1H), 3.19 (d, J = 7.2 Hz, 2H), 2.94 (td, J = 15.9, 6.6 Hz, 2H), 2.55 (tt, J = 23.1, 6.6 Hz, 1H).

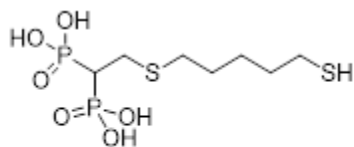
$^{31}\text{P}\{^1\text{H}\}$ -NMR (162 MHz, Deuterium Oxide) δ 19.84 (s).

$^1\text{H}\{^{31}\text{P}\}$ NMR (400 MHz, Deuterium Oxide) δ 5.81 (dt, J = 17.1, 7.4 Hz, 1H), 5.20 (s, 1H), 5.14 (d, J = 10.9 Hz, 1H), 3.20 (d, J = 7.2 Hz, 2H), 2.95 (d, J = 6.5 Hz, 2H), 2.57 (t, J = 6.5 Hz, 1H).

^{13}C NMR (101 MHz, Deuterium Oxide) δ 133.73 (s), 117.84 (s), 38.80 (t, $J = 125.2$ Hz), 34.59 (s), 25.94 (t, $J = 4.2$ Hz).

2.4.17. (2-(pentamethylene dimercaptan)ethane-1,1-diyl)bis(phosphonic Acid) (BPPMD, 1g)

In a 100 mL round bottom flask equipped with magnetic stirring bar tetraethyl 2-(pentamethylene dimercaptan) ethane-1,1-diyl diphosphonate (500 mg, 1.15 mmol) was added in 4 mL $\text{C}_2\text{H}_4\text{Cl}_2$ solvent. Then bromotrimethylsilane ($\text{Si}(\text{CH}_3)_3\text{Br}$, 2.23 mL, 17.25 mmol) was added quickly to the solution. The mixture was refluxed under nitrogen atmosphere for an hour and a half. Then the flask was putted into high vacuum with N_2 for 1 h. Then vacuum was removed and solvent mixture (10 ml MeOH + 1 mL distilled water) was added to the flask and the reaction mixture was left stirred for 1h. After that, the solvent was removed with rotavapor. The product was obtained as colorless liquid (358 mg, 1.10 mmol, 96% yield).



BPPMD, 1g

^1H NMR (400 MHz, Deuterium Oxide) δ 2.99 (td, $J = 16.1, 6.4$ Hz, 2H), 2.63 – 2.56 (set of m, 4H), 2.57 – 2.43 (set of m, 1H), 1.58 (set of m, 4H), 1.45 (set of m, 2H).

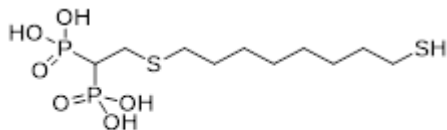
$^{31}\text{P}\{^1\text{H}\}$ NMR (162 MHz, Deuterium Oxide) δ 19.88 (s, 2P).

$^1\text{H}\{^{31}\text{P}\}$ -NMR (400 MHz, Deuterium Oxide) δ 3.02 (d, $J = 4.6$ Hz, 2H), 2.62 (t, $J = 7.1$ Hz, 1H), 2.55 (set of m, 4H), 1.62 (set of m, 4H), 1.48 (set of m, 2H).

^{13}C NMR (101 MHz, Deuterium Oxide) δ 39.26 (t, $J = 124.7$ Hz), 32.52 (s), 31.89 (s), 28.01 (t, $J = 4.9$ Hz), 27.08 (s), 26.67 (s), 23.64 (s).

2.4.18. (2-(octamethylene dimercaptan)ethane-1,1-diyl)bis(phosphonic Acid) 1h

In a 100 mL round bottom flask equipped with magnetic stirring bar tetraethyl 2-(octamethylene dimercaptan) ethane-1,1-diyl diphosphonate (500 mg, 1.05 mmol) was added in 4 mL $\text{C}_2\text{H}_4\text{Cl}_2$ solvent. Then bromotrimethylsilane ($\text{Si}(\text{CH}_3)_3\text{Br}$, 2.03 mL, 15.75 mmol) was added quickly to the solution. The mixture was refluxed under nitrogen atmosphere for an hour and a half. Then the flask was putted into high vacuum with N_2 for 1 h. Then vacuum was removed and solvent mixture (10 ml MeOH + 1 mL distilled water) was added to the flask and the reaction mixture was left stirred for 1h. After that, the solvent was removed with rotavapor. The product was obtained as colorless liquid (365 mg, 0.99 mmol, 95% yield).



BPOMD, 1h

^1H NMR (400 MHz, $\text{DMSO}-d_6$) δ 2.84 (td, $J = 15.8, 5.9$ Hz, 2H), 2.66 (t, $J = 7.1$ Hz, 2H), 2.53 – 2.43 (m, 2H), 2.19 (tt, $J = 22.9, 5.8$ Hz, 1H), 1.64 – 1.54 (set of m, 2H), 1.49 (p, $J = 6.8$ Hz, 2H), 1.38 – 1.19 (set of m, 9H).

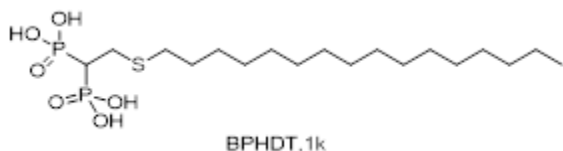
$^{31}\text{P}\{^1\text{H}\}$ NMR (162 MHz, $\text{DMSO}-d_6$) δ 18.97.

$^1\text{H}\{^{31}\text{P}\}$ NMR (400 MHz, DMSO) δ 2.98 (d, $J = 5.9$ Hz, 2H), 2.84 (m, 2H), 2.71 – 2.54 (m, 3H), 1.59 (m, 4H), 1.27 (m, 9H).

^{13}C NMR (101 MHz, $\text{DMSO-}d_6$) δ 35.84 (s), 29.36 (s), 28.61 (s), 28.50 (s), 28.15 (s, $J = 9.3$ Hz), 27.40 (t, 4.9 Hz), 23.69 (s).

2.4.19. (2-(1-hexadecane thiol)ethane-1,1-diylbis(phosphonic Acid) (BPHDT, 1k)

In a 100 mL round bottom flask equipped with magnetic stirring of tetraethyl 2-(1-hexadecane thiol) ethane-1,1-diylidiphosphonate (500 mg, 0.89 mmol) was added in 4 mL $\text{C}_2\text{H}_4\text{Cl}_2$ solvent. Then bromotrimethylsilane ($\text{Si}(\text{CH}_3)_3\text{Br}$, 1.74 mL, 13.35 mmol) was added quickly to the solution. The mixture was refluxed under nitrogen atmosphere for an hour and a half. Then the flask was putted into high vacuum with N_2 for 1 h. Then vacuum was removed and solvent mixture (10 ml MeOH + 1 mL distilled water) was added to the flask and the reaction mixture was left stirred for 1h. After that, the solvent was removed with rotavapor. The product was obtained as white liquid (381 mg, 0.85 mmol, 95% yield).



^1H NMR (400 MHz, $\text{DMSO-}d_6$) δ 2.85 (td, $J = 15.7, 6.0$ Hz, 2H), 2.16 (tt, $J = 23.4, 6.0$ Hz, 1H), 1.49 (p, $J = 7.1$ Hz, 2H), 1.22 (set of m, 28H), 0.83 (t, $J = 6.7$ Hz, 3H).

$^{31}\text{P}\{^1\text{H}\}$ -NMR (162 MHz, $\text{DMSO-}d_6$) δ 18.85 (s, 2P).

$^1\text{H}\{^{31}\text{P}\}$ NMR (400 MHz, $\text{DMSO-}d_6$) δ 2.85 (d, $J = 5.9$ Hz, 2H), 2.16 (t, $J = 5.9$ Hz, 1H), 1.54 – 1.43 (set of m, 2H), 1.22 (set of m, 28H), 0.83 (t, $J = 6.4$ Hz, 3H).

^{13}C NMR (101 MHz, $\text{DMSO-}d_6$) δ 32.12 (s), 31.48 (s), 29.22 (s), 29.18(s), 29.11(s), 28.88(s), 28.46 (s), 22.2 (s), 14.15 (s).

Synthesis of Metal Oxide Nanoparticles

3.1. Synthesis of ZrNPs:

The synthesis of mesoporous zirconia nanoparticles (MZNs) was adapted from the procedure proposed by Gabriele et al. [267] Briefly, the starting material was zirconium propoxide precursor and working at room temperature. The hexadecyl amine surfactant was dissolved in ethanol, then a correct quantity of distilled water and NaF solution were added to the surfactant solution and left it vigorous stirring at r.t. The precursor mixed with ethanol was added dropwise into surfactant solution under vigorous stirring. After overnight synthesis three EtOH washing cycles were performed. The dried powder was put into a Teflon bomb and heated at 170°C for 16 h with 6.25 ml of water and 12.5 ml of EtOH per gram of powder. The recovered powder was subjected to a heat vacuum extraction process at 120°C, to extract the surfactant without structural modifications. [268] The preferred molar ratio of the reagents ZP: EtOH: H₂O: NaF: HDA was 1: 750: 20: 0.02: 2.

3.2. ZrNPs Characterization:

Mesoporous Zirconia nanoparticles ZrNPs were successfully prepared by a neutral surfactant assisted sol-gel method in combination with NaF. It is worth to note that in order to obtain ZrNPs with a large surface area, while preserving the porosity, the surfactant was removed at 120°C in a vacuum extraction process rather than by calcination. The nanoparticles obtained by this method were spherical as observed by SEM and TEM analyses, monodispersed (with a mean diameter of 200±30 nm, Figure 4.2 C) and amorphous. The isotherms display the type IV profile with a H1 hysteresis loop (according to the IUPAC classification) which is typical for mesoporous materials. The surface area determined by BET equation was in the range 200-350 m²/g with a pore volume of 0.3 cm³/g and pore diameter distribution centred at 4.5 nm determined following the BJH equation. For this reason, these ZrNPs have the capability to host several types of molecules.

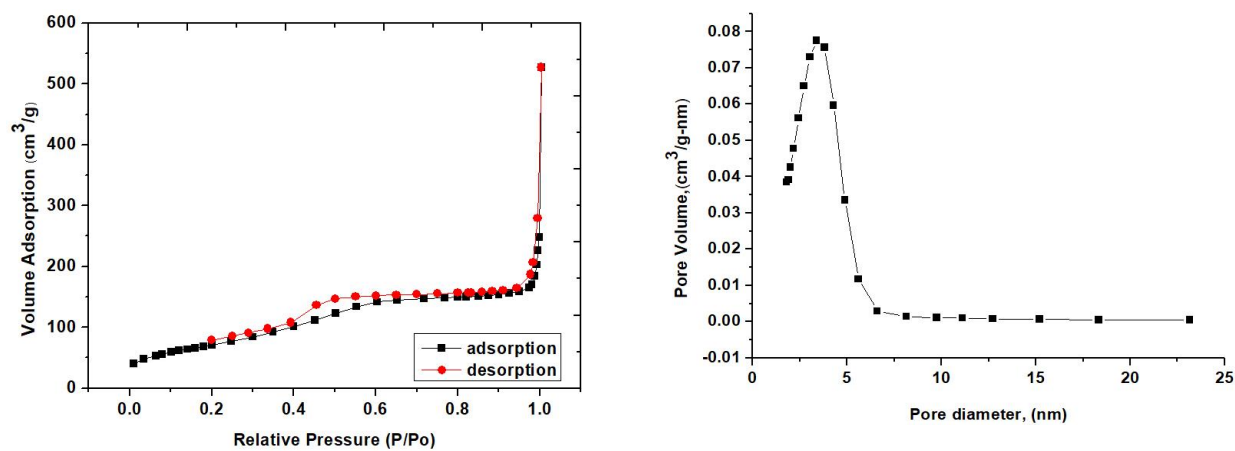


Figure 3.1. Characteristic adsorption–desorption curves of ZrNPs sample. The right-side graph shows the pore distribution curve.

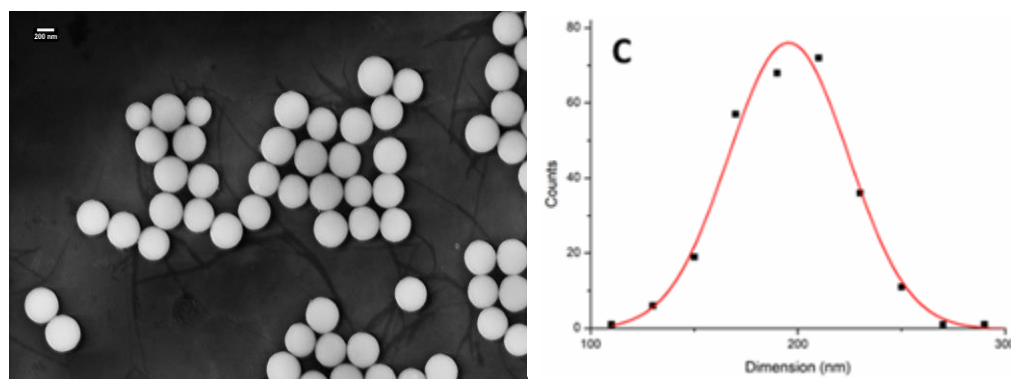


Figure 3.2: FE- SEM image of ZrNPs (left) & size distribution ($\langle d \rangle = 200 \pm 30$ nm) (right)

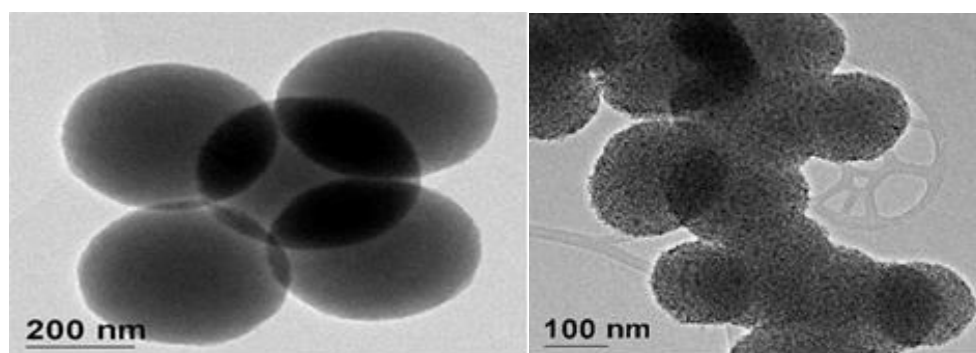


Figure 3.3: TEM image of as-synthesized ZrNPs

3.3. Synthesis of TiNPs:

In a typical process, certain amount of HDA was dissolved in 150 mL of anhydrous EtOH. Then 0.037 mol MilliQ water and 0.00185 mol KCl were added to the HAD solution. While the above mixture was being continuously stirred at room temperature, 3.7 mL of precursor Titanium isopropoxide (TIP) was dissolved into 22.25 ml EtOH. The precursor then added to the HAD solution with continuous stirring and left the mixture for overnight. The milky white suspension then washed with ethanol three times, then dried in air at room temperature. After that, the dried samples were transferred into a Teflon-lined autoclave and heated at 160°C for 16h by hydrothermal treatment with 30ml EtOH and 15ml H₂O per gram of powder. Finally, the recovered powder was subjected to a heat vacuum extraction process at 120°C, to extract the HDA. The preferred molar ratio of the reagents TIP: HAD: EtOH: H₂O: KCl: was 1:1: 236.5: 3: 5.5x10⁻³.

3.4 Characterization of TiNPs

As long as TiO₂ NPs are concerned, these were prepared following literature procedures obtaining the material with an average size of 100 nm and average surface area of 17 m²/g.

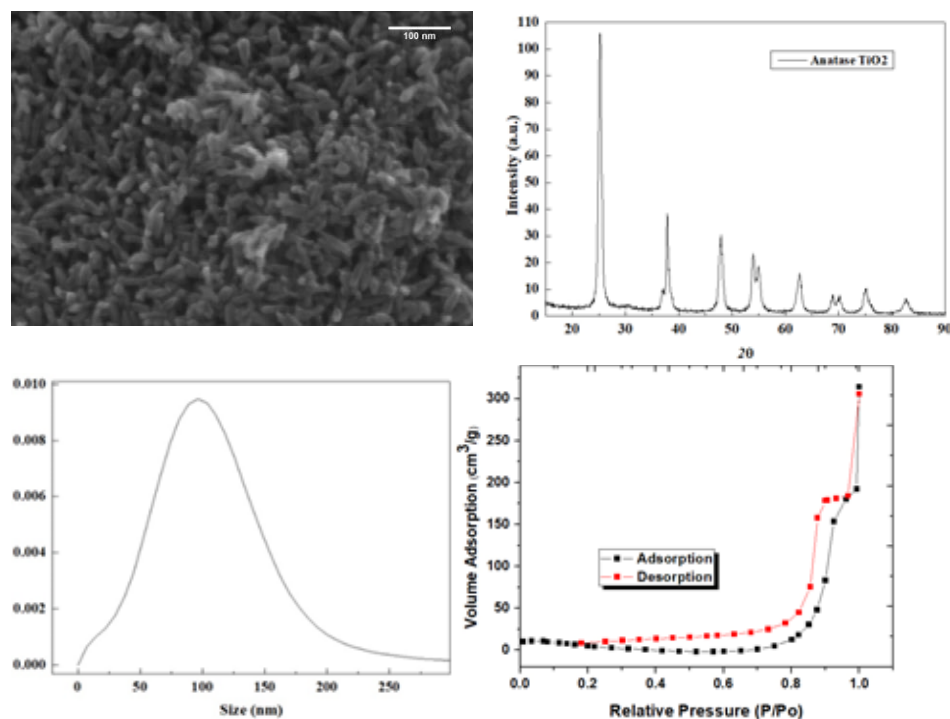


Figure 3.4: SEM image, XRD patterns, Particles size distribution and N₂- adsorption-desorption curves of TiNPs.

XRD patterns of TiNPs. The XRD peaks in the wide angle range of 2θ ($20^\circ < 2\theta < 90^\circ$) ascertained that the peaks in 25.267° , 37.823° , 37.909° , 48.158° , 54.051° , 55.204° , 62.867° , 68.976° , 70.479° , 75.303° , and 82.926° can be attributed to the 101, 103, 004, 112, 200, 105, 211, 204, 116, 220, 215, and 224 crystalline structures of tetragonal anatase synthesized TiNPs, respectively, (Anatase XRD JCPDS Card no. 78-2486).

3.5 Synthesis of FeNPs

The iron oxide nanoparticles were prepared according to an adapted co-precipitation method [289] Namely, a solution of both iron(II) and iron(III) chloride (50 and 100 mmol respectively) in 300 mL of deionised water were treated with ammonium hydroxide (25% NH_3 solution) under vigorous mechanical stirring until pH 11. The black precipitate was separated magnetically, washed with deionized water (2 x 50 mL) and with ethanol (2 x 50 mL), and dried under vacuum. The Fe_3O_4 nanoparticles obtained showed an average size of 5.4 nm and a surface area of $176 \text{ m}^2/\text{g}$ [290].

3.6 Synthesis of SiNPs & BiNPs: Silica and Bismuth oxide nanoparticles were collected from other member of our research group.

3.7 Characterization of BiNPs:

Due to its emerging interest in nanotechnology, we further investigated the interaction of **1a** with Bi_2O_3 NPs that were prepared following some literature procedures leading to the formation of solid non-porous NPs characterized by an average size of 123 nm and average surface area of about $15 \text{ m}^2/\text{g}$.

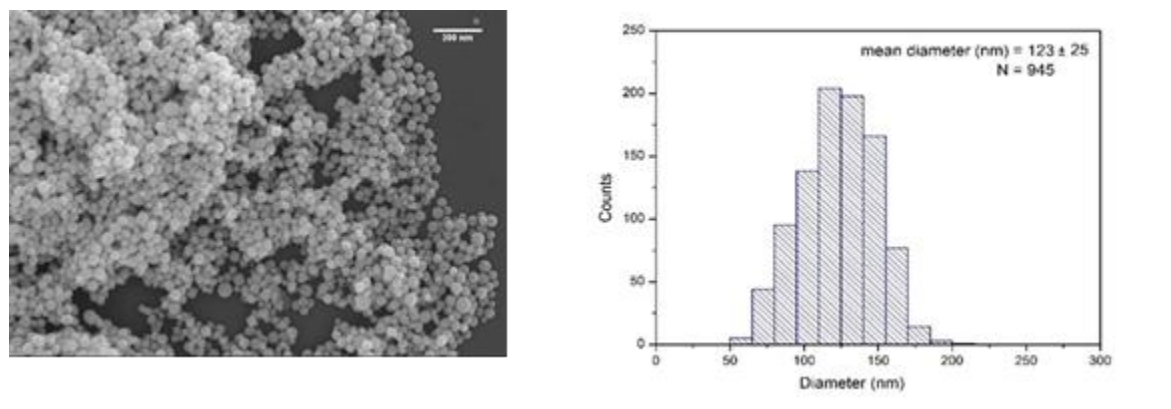


Figure 3.5: SEM image, Particle size distribution form DLS of BiNPs

Interaction of bis-phosphonic acid with Metal Oxide

In this part we introduce a versatile approach for the modification of the superficial properties of zirconia and other metal oxides (titania, silica, bismuth) based on the employment of a family of bis-phosphonic acids as synthesized in chapter 2 as derivatizing species. The latter organic molecules can be endowed with specific lateral functional groups such as amino, carboxy, cheto, thiol and many others and the interaction of the bisphosphonates with zirconia nanoparticles is efficient with high coverage of the oxide surface and stable over a wide range of pH. We further apply same procedure for others metal oxides.

4. Results and Discussion

4.1 Analysis and study of the interaction between buffer solutions and inorganic NPs

In order to quantitatively determine the interaction between the inorganic supports in analysis and the bis- and mono-phosphonic organic molecules in different buffered systems, preliminary tests have been carried out such as to show or not a possible affinity between the buffers and the zirconia, titania, silica and bismuth nanoparticles. Each buffer system formulated in deuterated water, such as acetic acid / sodium acetate (Acetate), MES, HEPES, TRIZMA and CAPS of 25mM concentration (Figure.4.1). ¹H NMR reference analysis was performed using the "BRUKER Advance" spectrometer 400 "operating 32 scans in D₂O and applying solvent suppression (such as not to identify in the spectrum the intense signal of non-deuterated water (at 4.79ppm) present in solution). Subsequently, 1mL of buffer solution in D₂O and 10mg of nanoparticles were added respectively in different vials. All the samples were stirred for a time interval of 24h by magnetic stirrer (600 rcf) and at the end of this interval centrifuged at 12000 rcf for ten minutes. The supernatant was analyzed in NMR using the same procedure described above. Once the analyzes on each sample were completed, a pH measurement was performed to verify if the addition of the support has modified this parameter.

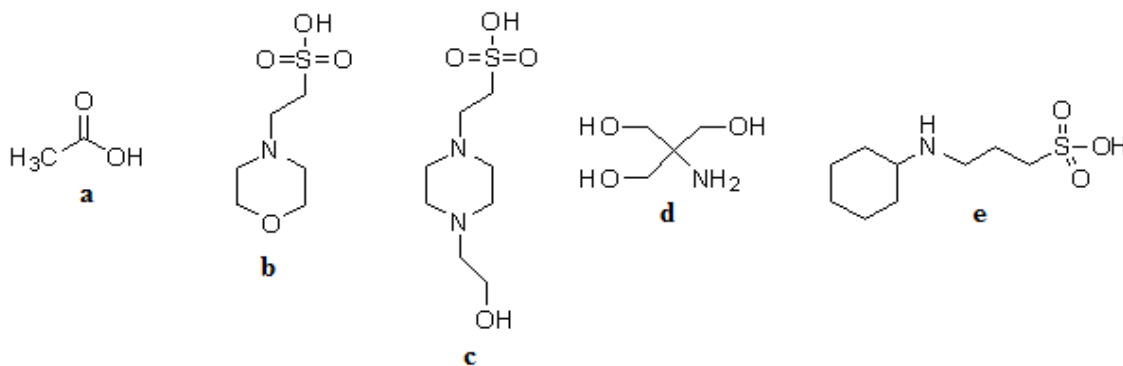


Figure 4.1: Graphical representation of the buffers used: (a) Acetic acid / sodium acetate; (b) MES; (c) HEPES; (d) TRIZMA; (e) CAPS

4.1.1 Buffer-Zirconia interaction (ZrO_2)

Following the addition of zirconia, the characteristic signals of each molecule have undergone a displacement at lower ppm (signal shielding) and a weak decrease in intensity (Figure 4.5). These phenomena allow us to consider a possible interaction between the buffers and the zirconia nanoparticles (ZrNPs). Table 1 shows the chemical shift values (δ) reported for each buffer under examination before and after the addition of the support and the $\Delta\delta$ calculated on the most significant signals present in the relative pairs of spectra (Figure.4.2).

	δ (ppm)		$\Delta\delta$	$\Delta\delta$ average
	Buffer	Buffer + Support		
Acetate pH 4.0	1,992	1,895	-0,097	-0,097
MES pH 5.5	3,894	3,788	-0,106	-0,107
	3,397	3,288	-0,109	
	3,301	3,196	-0,105	
	3,289	3,184	-0,105	
	3,28	3,174	-0,106	
	3,226	3,116	-0,11	
HEPES pH 7.0	3,817	3,717	-0,100	-0,099
	3,804	3,703	-0,101	
	3,789	3,689	-0,100	
	3,082	2,98	-0,102	
	3,016	2,923	-0,093	
	2,919	2,819	-0,100	
TRIZMA pH 8.8	3,490	3,408	-0,082	-0,082
CAPS pH 10.0	3,044	3,010	-0,034	-0,068
	3,025	2,991	-0,034	
	3,005	2,971	-0,034	
	2,952	2,862	-0,090	
	2,934	2,844	-0,090	
	2,914	2,825	-0,089	
	2,016	1,945	-0,071	
	1,997	1,926	-0,071	
	1,978	1,907	-0,071	
	1,727	1,651	-0,076	
	1,576	1,484	-0,092	
	1,209	1,146	-0,063	

Table 1 Chemical Shift related to the characteristic signals of the buffers examined before and after the addition of zirconia

The negative values expressed by $\Delta\delta$ are indicative of the shielding of the signals generated by the addition of zirconia, regardless of the pH value. This indicates that the effect of ZrNPs is to

increase the electronic density of the species in solution. As mentioned below, the surface of the NPs varies according to the pH and is clearly positive at low pH and clearly negative to the basic ones. Comparing the $\Delta\delta$ values for the various types of H atoms in the different buffers is observed as for MES and HEPES (and partly in that of CAPS) these values are almost constant indicating a uniform shielding of all the signals of the sample.

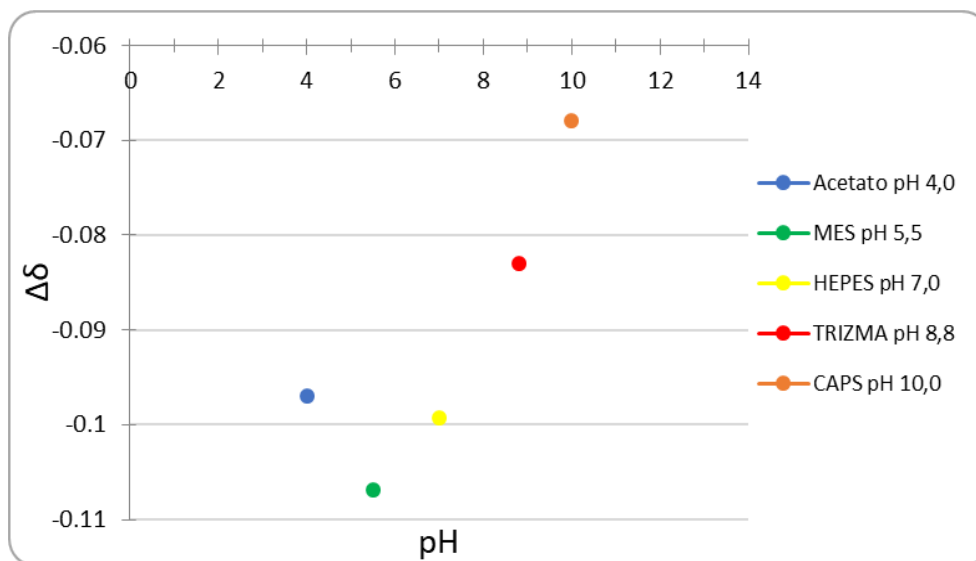


Figure 4.2: $\Delta\delta$ as a function of the pH of the respective buffers

As the pH increases, the separation between the pre and post-zirconia signals decreases (except for acetate). Using the "ERETIC" function present in the "BRUKER Advance 400" NMR spectrometer program it was possible to quantitatively determine the interaction between the buffers and the support by measuring the buffer concentration remaining in solution after interaction with the nanoparticles (Tab.2). The one of greatest intensity relative to the buffer was used as the reference signal before the addition of the NPs (initial concentration equal to 25mM). If there were no defined characteristic signals (both ends of the signal must intersect the base line) they were used as a reference for the multiplexes. The following table shows the results obtained:

	Signal	δ (ppm)	Buffer (mM)	Buffer + Support (mM)	%
CAPS pH 10.0	Triplet	3,07-2,99	25,00	24,88	0
	Multiplete	2,99-2,86	25,00	25,29	-1
	Multiplete	2,05-1,90	25,00	24,87	1
	Multiplete	1,79-1,67	25,00	24,82	1
	Multiplete	1,63-1,54	25,00	24,82	1
	Multiplete	1,32-1,04	25,00	25,13	-1
TRIZMA pH 8.8	singlet	3,49	25,00	22,61	10

HEPES pH 7.0	triplet	3,86-3,76	25,00	25,96	-4
	Multiplate	2,50-3,50	25,00	25,90	-4
MES pH 5.5	Singlet	4,03-3,77	25,00	25,4	-2
Acetate pH 4.0	singlet	2,04-1,92	25,00	23,88	4

Table 2 Experimental results related to quantitative determination of the ZrO₂ buffer interaction

In agreement with the experimental data, the hypothesis formulated to express these results takes into consideration the different type of interaction between the zirconia nanoparticles at the different pH and the buffers and the chelating character of the latter molecules with respect to the hydroxyl groups and metallic atoms present on the surface of the NPs. Zirconia in an acid environment is characterized by a positive surface charge (positive Z potential, Figure 4.3) while at basic pH from negative Z potential values. At operating pH, the amine, sulfonic and hydroxyl functions can be in cationic, anionic or neutral form (acid-base equilibrium dependent on the pK_a of the individual buffers) determining a possible interaction with the supporting NPs. The simultaneous presence of negative or positive charges in both species, however, would result in less interaction.

pH	Zeta P. ZrNPs (mV)
4.6	14.3
5.9	10.7
7.3	-7.9
8.5	-25.4
9.9	-31.4

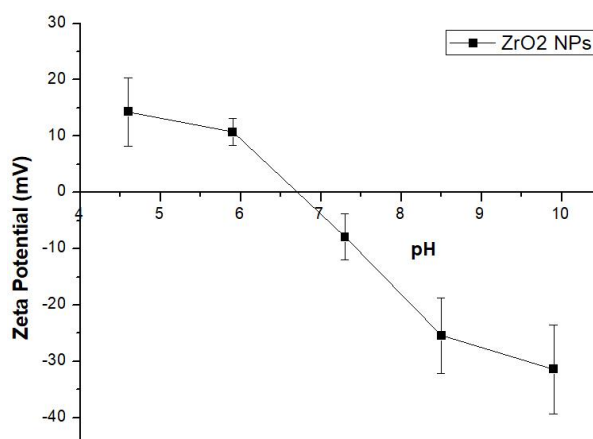


Figure 4.3 Measurements of the potential Z relative to the nanoparticles of ZrO₂ as a function of pH

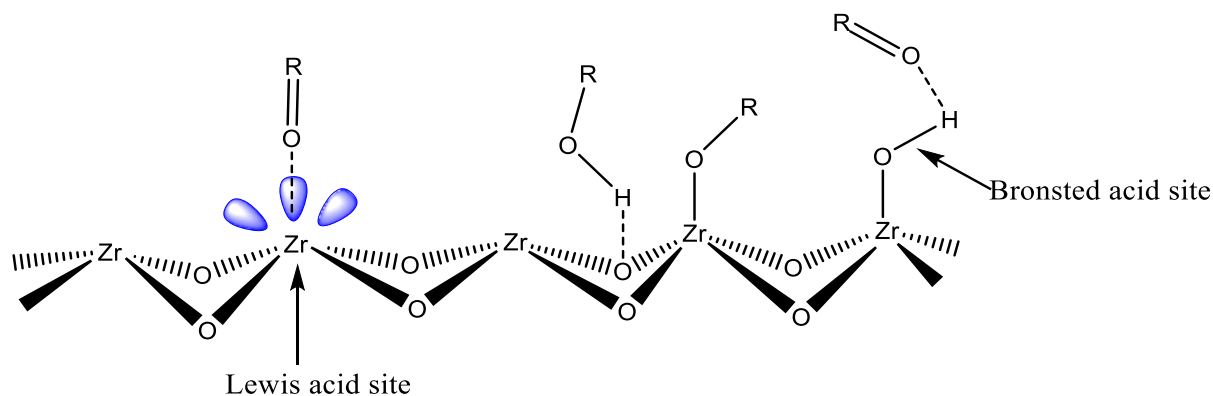


Figure 4.4 Graphical representation of the surface structure of the ZrNPs and of the possible types of interactions with the functionality of the buffers

The surface structure of zirconia has numerous hydroxyl groups and zirconium atoms (Lewis acid) which can interact with the functionalities present in the buffer molecules establishing hydrogen and coordination bonds, as shown in Figure 4.4. The strength of these bonds (and the consequent greater interaction) is determined by the number of reagent sites of both species (buffer-NPs) and by the coordinating capacity of the functional groups of the buffer.

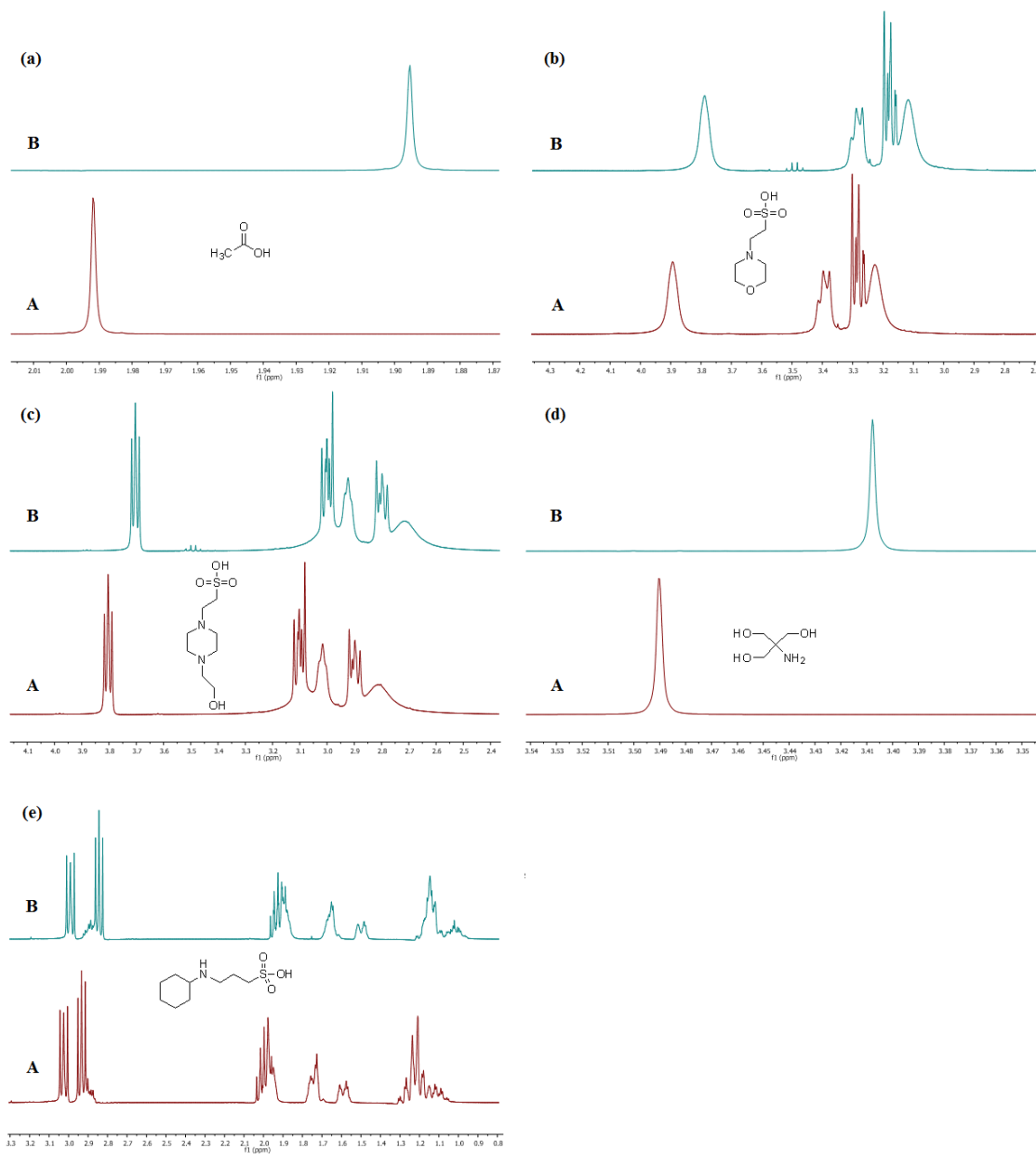


Figure 4.5 ¹H NMR spectra (400MHz, D₂O) related to the buffers examined first (A) and then (B) the addition of zirconia: (a) 25mM acetate pH 4.0. (b) MES 25mM pH 5.5. (c) HEPES 25mM pH 7.0. (d) TRIZAN 25mM pH 8.8. (e) CAPS 25mM pH 10.0.

The Acetate, HEPES and TRIZMA molecules present respectively one, two and three hydroxyl units, which can interact with the analogous surface groups of the NPs, characterizing an increasing structural stability the hypotheses formulated are confirmed by the experimental results reported in Tab.2. The percentages expressed represent the percentage amount of buffer that has interacted with the support. leading to the decrease in concentration in solution detectable by ^1H NMR analysis. Percentages less than 5% are not attributable to a support-buffer interaction as they coincide with the measurement error. Considering the instrumental error, it is possible to confirm an interaction (even if not excessive) of the TRIZMA buffer with the zirconia NPs. Once the analyzes on each sample were completed, a pH measurement was performed. From the results obtained we can confirm that the pH did not change following the addition of zirconia as evidence of the weak interaction between the buffer system and nanoparticles.

4.1.2 Silica-buffer interaction (SiO_2)

Preliminary tests performed on silica nanoparticles (SiNPs) were performed only on three of the five previously tested buffer solutions, one with Acetate acid pH, one HEPES neutral and one basic TRIZMA. Following the addition of the NPs, the ^1H NMR signals characteristic of the buffer molecules have undergone a major chemical shift, with the exception of the acetic acid / sodium acetate solution, indicating a signal de-shielded and a weak decrease in intensity (Figure 4.8). Such phenomena, as in the case of zirconia, allow to consider a possible interaction between the buffers and the supporting nanoparticles. Table 3 shows the values of chemical shift (δ) detected for each molecule under examination before and after the addition of silica (the values of $\Delta\delta$ calculated on the most significant signals present in the relative pairs of spectra are also shown (Figure 4.6).

	δ (ppm)			
	Buffer	Buffer + Support	$\Delta\delta$	$\Delta\delta$ average
Acetate pH 4.0	1,992	1,991	-0,001	-0,001
HEPES pH 7.0	3,824	3,839	0,015	0,013
	3,811	3,826	0,015	
	3,797	3,812	0,015	
	3,085	3,090	0,005	
	2,927	2,942	0,015	
TRIZMA pH 8.8	3,495	3,522	0,027	0,027

Table 3 Chemical Shift related to the characteristic signals of the swabs examined before and after the addition of silica

The positive values expressed by the $\Delta\delta$, except for the Acetate buffer, are an indication of the de-shielded of the signals due to the addition of the silica. The value of $\Delta\delta$ of the signal relative to the three methyl protons of the acetate buffer (singlet) is attributable to the error of the

measurement system and does not identify any interaction with the supporting NPs. In the case of HEPES and TRIZMA solutions, the characteristic signals of the molecules have undergone a shift at ppm greater determined by the de-shielding effect of the silica nanoparticles. Similarly, to what was done with the zirconia nanoparticles it was possible to quantitatively determine the interaction between the buffers and the supports using the "ERETIC" function present in the NMR spectrometer "BRUKER Advance 400" program.

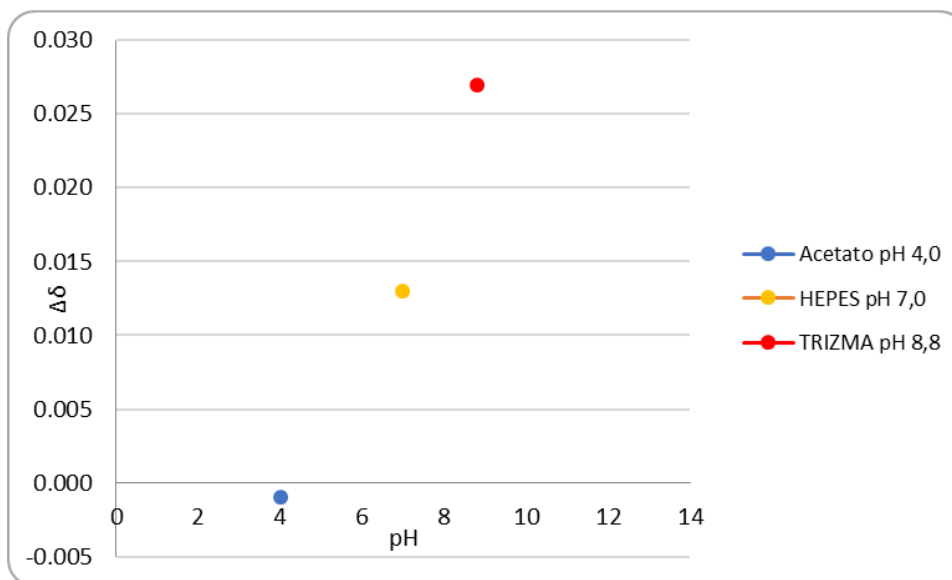


Figure 4.6 $\Delta\delta$ as a function of the pH of the respective buffers

As can be seen from the experimental results reported in Tab.4, considering the instrumental error, it is possible to confirm a non-negligible interaction of the buffers analyzed with silica NPs. The hypotheses previously formulated concerning zirconia can also be extended to silica. Silica has a surface area (determined by B.E.T. analysis) and a concentration of hydroxyl (silanol) groups greater than zirconia and these properties determine higher percentages of interaction than those identified for the Zr NPs (Figure 4.7).

	Signal	δ (ppm)	Buffer (mM)	Buffer + Support (mM)	%
TRIZMA pH 8.8	singlet	3,59-3,41	25,00	20,77	17
HEPES pH 7.0	triplet	3,86-3,76	25,00	23,59	6
	multiplate	2,50-3,50	25,00	23,78	5
Acetate pH 4.0	singlet	2,04-1,92	25,00	19,61	22

Table 4 Experimental results related to the quantitative determination of the buffer-SiO₂ interaction

Furthermore, such support for operational pH is characterized by a negative surface charge (paragraph 4.3) with the possible formation of electrostatic interactions between the surface anionic functionalities and the characteristic functional groups of the analyzed buffers. The high number of hydroxyl groups can justify the silly behavior that silica plays against buffer

molecules by subtracting greater electronic density from the protons present in the buffers with the consequent shift of the signals. Once the analyzes were completed, a pH measurement was performed on each sample and from the results obtained we can confirm that there were no variations of this parameter following the addition of silica.

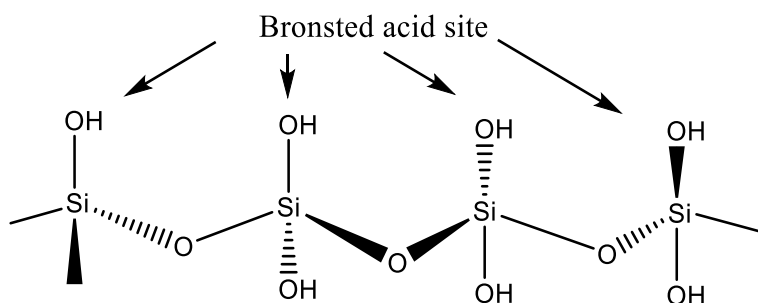


Figure 4.7: Graphical representation of the surface chemical structure of SiNPs

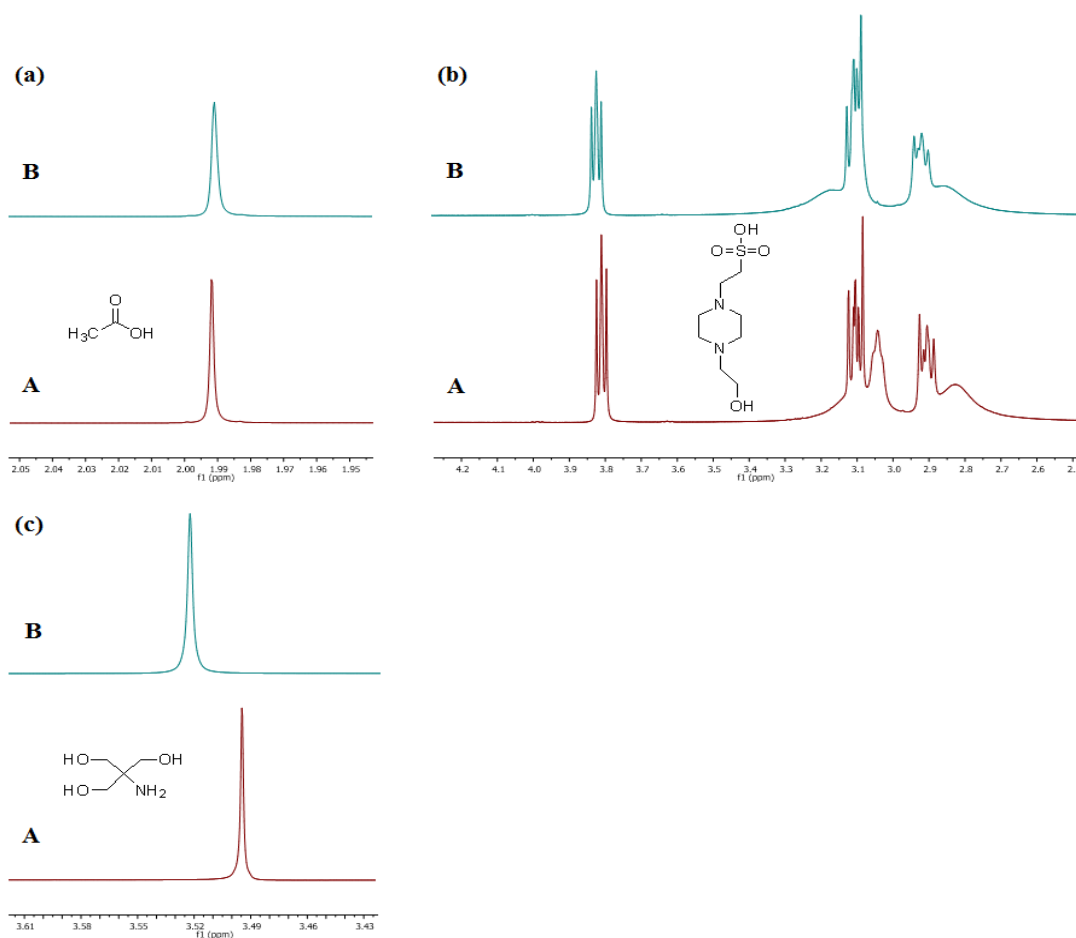


Figure 4.8: ^1H NMR spectra (400MHz, D_2O) related to the buffers examined first (A) and then (B) the addition of silica: (a) 25mM acetate pH 4.0. (b) HEPES 25mM pH 7.0. (c) TRIZMA 25mM pH 8.8.

4.1.3 Buffer-Bismuth interaction (Bi_2O_3)

It has not been possible to conduct preliminary tests such as to highlight any affinity between the buffers and the bismuth oxide nanoparticles, since the amount of support available has been limited. It was decided not to carry out the experiments similar to the other two supports and to dedicate the available batches to the quantitative determination of the interaction between the bismuth oxide and the methylene bis-phosphonic acid (MBP) in the different buffered systems (paragraph 4.2.1.3)

4.2 Analysis and study of the interaction between the nanoparticulate supports and the bis- and mono-phosphonic organic molecules under examination

In order to quantitatively determine the interaction between the bis- and mono-phosphonic molecules under examination and the inorganic supports consisting of zirconium, silicon, titanium and bismuth oxides in solution, different experimental tests were conducted in the buffered systems analyzed above (with the exception of MES and CAPS because they do not allow the correct integration of the reference signals) and in deuterated water (non-buffered system). The nanoparticles of support once added to the buffered solutions containing the organic molecules at a concentration of 5mM (shown in Figure 4.9a and Figure 4.9b) determined a decrease in intensity and a shift of the characteristic signals of the mono and bis-phosphonic molecules, an index of an interaction between the latter and the supports (functionalization of the nanoparticles). By analyzing these systems over time, it has been possible to define the different loading profiles that characterize the organic molecules under examination in accordance with the chemical-physical characteristics of the supports.

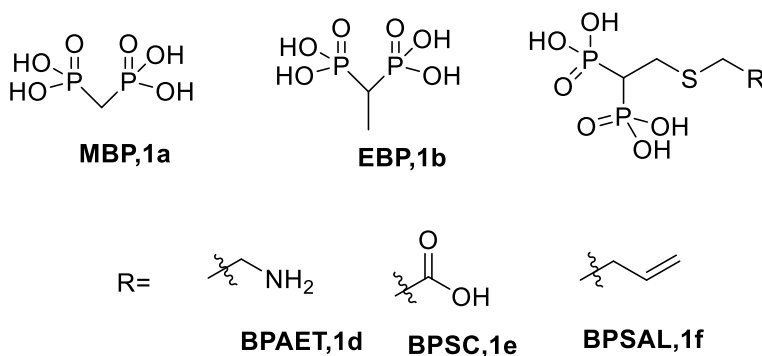


Figure 3.9a: Synthetic bis-phosphonic acids (BPs) used

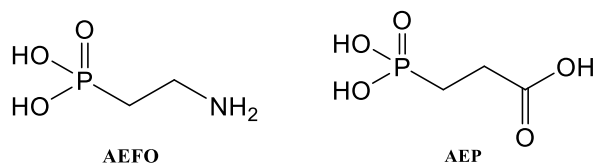


Figure 4.9b: Commercial Monophosphate Acids (AMPs) used

4.2.1 Methylene Bis-phosphonic acid (MBP, 1a)

To determine in detail the affinity between the bis- and mono-phosphonic molecules and the supports under examination, some preliminary tests were carried out, monitoring the decrease in the concentration of methylene bis-phosphonic acid (MBP) over time in the different buffered aqueous systems previously analyzed containing aliquots. Defined support, through quantitative analysis of the ^1H NMR signal relative to the methyl unit of the molecule (ERETIC functionality of the “Bruker Advance 400” spectrometer). Tests were performed starting from 5 ml of a 5 mM solution of MBP in the presence of 50 mg of support in a series of buffer at a concentration of 25 mM in the range of pH 4.0-8.8 (solution stirred by means of a magnetic stirrer at 600rcf). The non-buffered system of deuterated water following the addition of organic acid is characterized by a pH of 2.0 (strongly acidic). The concentration of analyte in solution was determined by withdrawing 1 ml of solution at 15-30-60-120-minute intervals, isolating the supernatant by centrifugation (10 minutes at 12000rcf) and analyzing this aliquot by quantitative ^1H NMR with respect to the original solution of the ‘analyte (MBP + buffer). The first measurement during loading analyzes was performed after 15 minutes, i.e. the shortest possible time for sample preparation (sampling and centrifugation) and NMR measurement (recording of signals). The 2.294ppm triplet area, attributed to the metabolic unit of the MBP molecule (Figure 4.10), was monitored over time and the analyte concentration measurements were made on this signal. The two protons identified in Fig. 4.10 from the letter (a) are characterized by a triplet in that, by means of a spin-spin interaction, they couple both with the two phosphorus atoms of the phosphonic units (^{31}P).

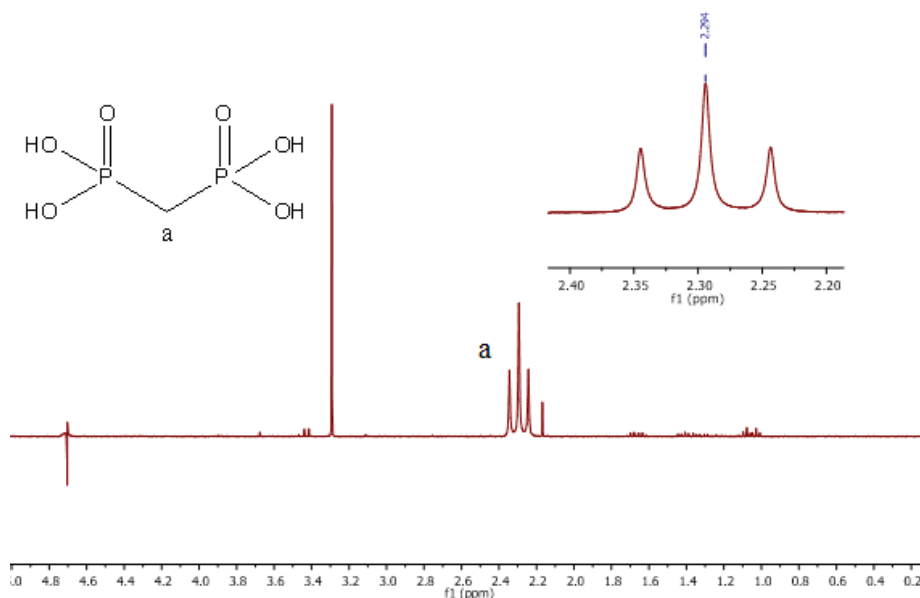


Figure 4.10: ^1H NMR spectrum (400MHz, D_2O) of methylenbephosphonic acid (MBP) 5mM

4.2.1.1 Zirconium oxide (ZrO_2)

In the presence of zirconia nanoparticles (ZrNPs) it is possible to notice a shift of the signals to higher fields (lower ppm) at pH 7 for HEPES and at pH 8.8 TRIZMA (shielding of signals). For Acetate and D_2O acid buffers, absorption of the MBP from ZrNPs was found to be complete in the time interval of 0-15 minutes, determining the lack of detection of a possible displacement of the characteristic signal. The increase in pH led to a decrease in the affinity between the molecules and the substrate identified by the presence of the signal at 15, 30, 60 and 120 minutes (Figure 4.12, Tab.5, Figure 4.13, Tab.6). The reason for this reduction is attributable to the repulsion between the negative charges held by both species to the operating pH and to the acid / base equilibrium established between the bound molecules and the support: zirconia, as reported in paragraph 3.1.1, has a Positive surface charge at acidic and negative pH (negative Z potential) for basic pH. The methyl bis-phosphonic acid molecule has four hydroxyl units in the two phosphonic groups which, depending on the pH, can be in an anionic or neutral form (Figure 3.11). The type of interaction hypothesized between the species in question concerns the possible coordination of the phosphate groups of MBP with the metallic zirconium atoms and with the hydroxyl units present on the surface of the nanoparticles through coordination and hydrogen bonds. The presence of superficial charges on the zirconia NPs at the different operating pHs, correlated with the values of potential Z, can determine a greater or lesser coordinating force.

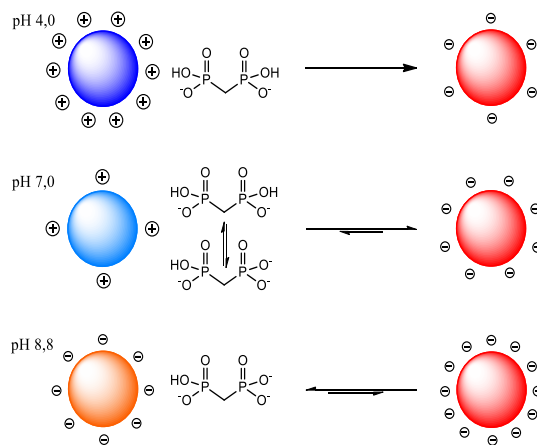


Figure 4.11: Schematic representation of the charge distribution on the ZrNPs before and after the interaction with the MBP

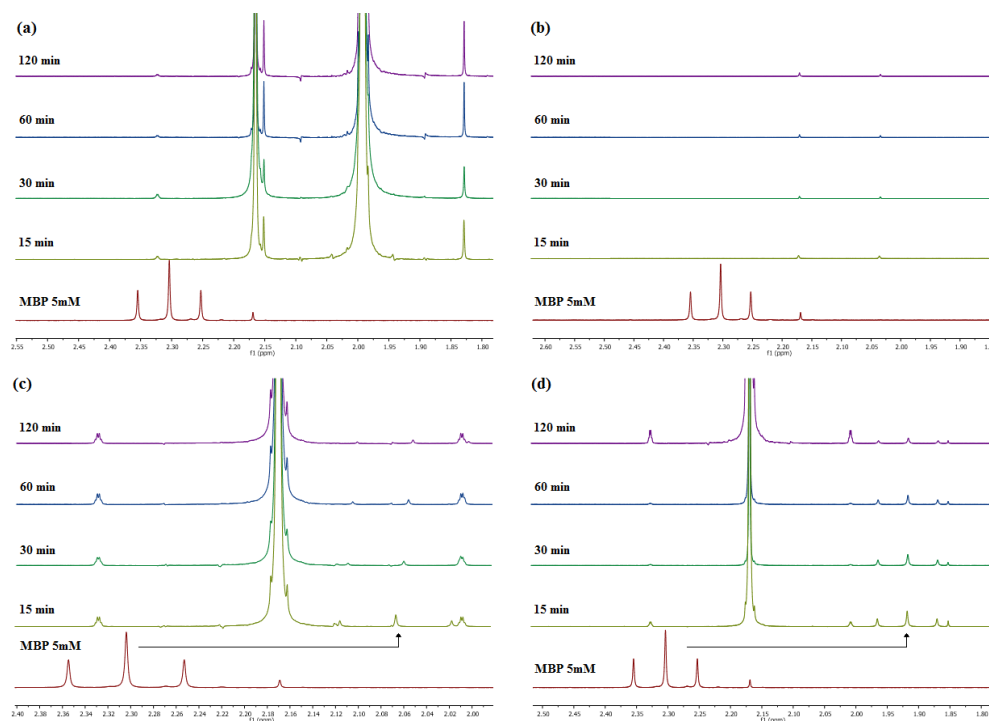


Figure 4.12: ^1H NMR spectra (400MHz, D_2O) related to the functionalization of ZrNPs with 5mM MBP in: (a) 25mM Acetate pH 4.0. (b) D_2O . (c) HEPES 25mM pH 7.0. (d) TRIZAN 25mM pH 8.8.

	Time	MBP	
Buffer	(min)	in solution (mM)	loaded (mM)
D_2O pH 2.0	0	5,00	0,00
	15	0,00	5,00
	30	0,00	5,00
	60	0,00	5,00
	120	0,00	5,00
Acetate pH 4.0	0	5,00	0,00
	15	0,00	5,00
	30	0,00	5,00
	60	0,00	5,00
	120	0,00	5,00
HEPES pH 7.0	0	5,00	0,00
	15	2,09	2,91
	30	0,93	4,07
	60	0,59	4,41
	120	0,22	4,78
TRIZMA pH 8.8	0	5,00	0,00

15	1,63	3,37
30	1,14	3,86
60	0,84	4,16
120	0,88	4,12

Table 5 Kinetics of loading the MBP to the different pH values

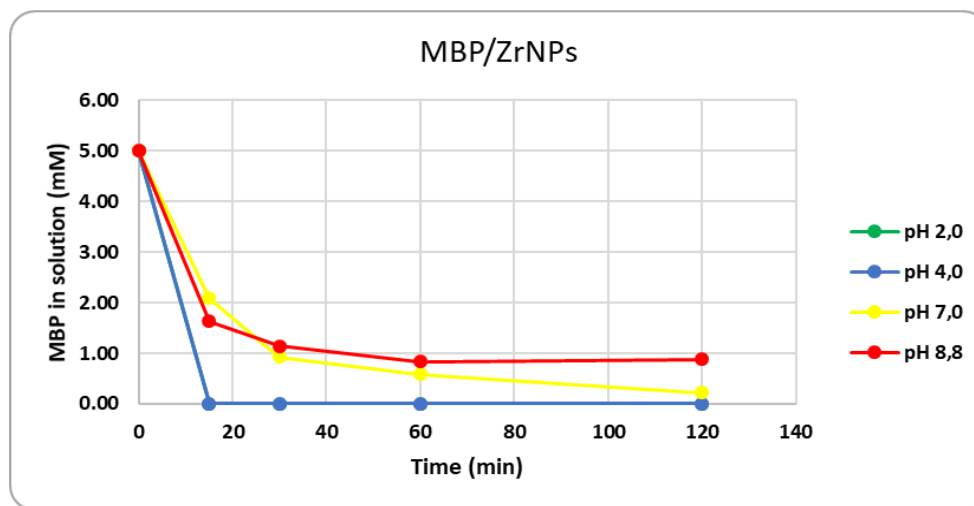


Figure 4.13: Graphical representation of the loading kinetics of the MBP molecule on ZrNPs at the different operating pHs

The operative pH, as evidenced by the experimental results, has a significant influence on the extent of the interaction between MBP and zirconia. In paragraph 4.3.1 the analysis of the interaction between the organic molecule under examination and the zirconia nanoparticles will be shown in detail, looking for, through the determination of the acid dissociation constants of the MBP, to verify and justify these behaviors.

Buffer	pH	Initial Conc. in sol. (mM)	Final Conc. in sol. (mM)	GD (mol/m ²)	GD %
D ₂ O	2,0	5,00	0,00	1,61E-06	47
Acetate	4,0	5,00	0,00	1,61E-06	47
HEPES	7,0	5,00	0,22	1,54E-06	45
TRIZMA	8,8	5,00	0,88	1,33E-06	38

Table 6: Binding efficiency of MBP on ZrNPs at different pH determined by ¹H quantitative NMR

From the results obtained in Acetate acidic conditions (pH 4.0), in order to determine the maximum concentration of MBP such as to fully functionalize the zirconia nanoparticles, the experiment was repeated using MBP solutions at 10mM and 25mM, observing respectively on 50mg of support, 100% and 70% of loading in the time interval of 120 minutes (Figure 4.15, Figure.4.16, Tab.7). The obtained results, considering the surface occupied by a molecule of MBP (approximate footprint equal to 48 Å² [256]) calculated through molecular models (Figure 4.14) and the chemical-physical characteristics of the zirconia used (surface area dependent on the batch used determined through BET analysis), can be expressed through Grafted Density

(mol MBP/m²), a parameter that can be related to the degree of surface coating of the nanoparticles. The experimental results obtained from the maximum 10mM and 25mM MBP loading tests are shown below

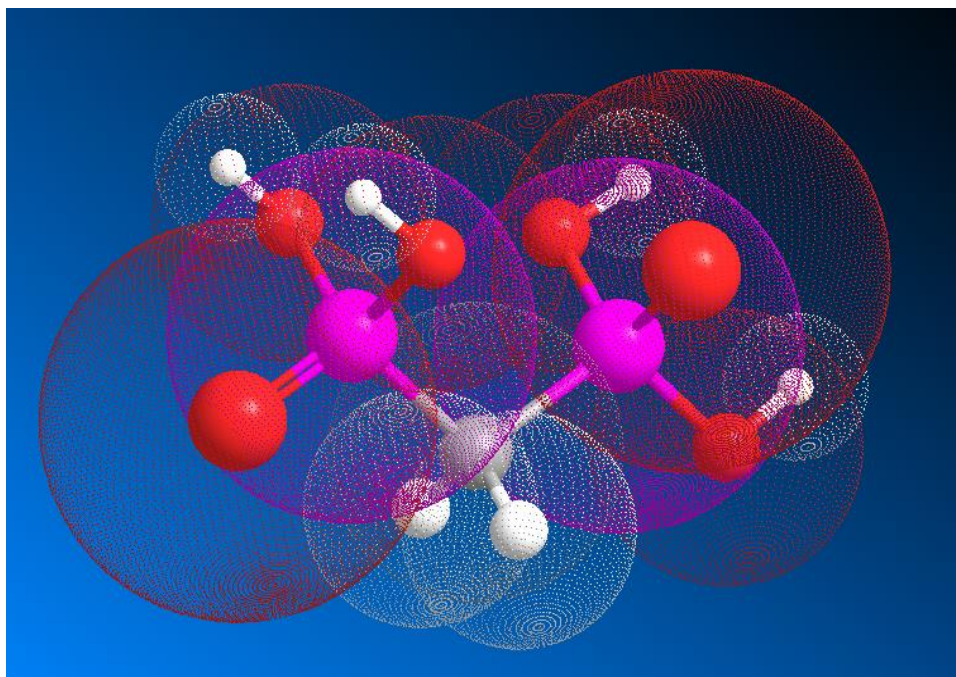


Figure 4.14: Three-dimensional structure representing the van der Waals rays of the MBP: Violet-Phosphorus, Red-Oxygen, Carbon-Gray, White-Hydrogen

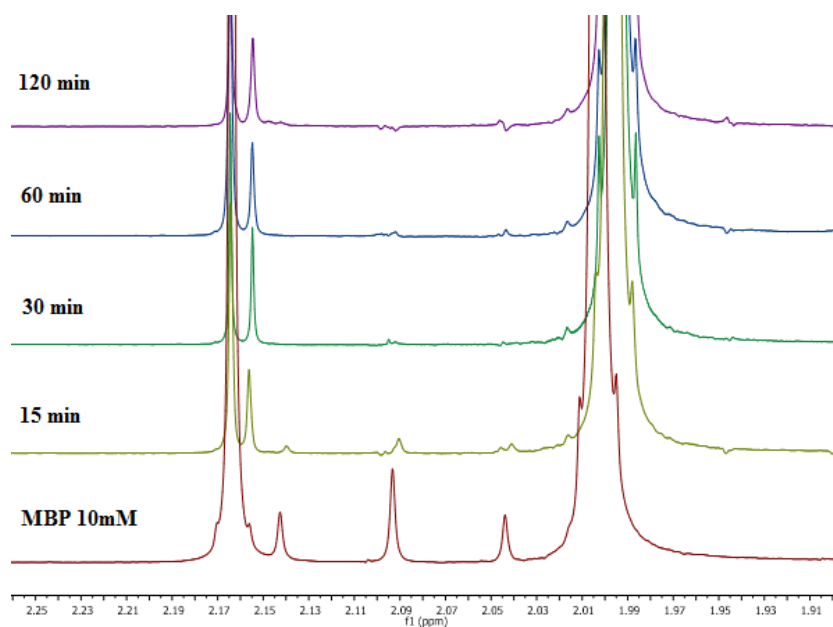


Figure 4.15: ¹H NMR spectra (400MHz, D₂O) related to the functionalization of ZrNPs with 10mM MBP in 25mM Acetate pH 4.0

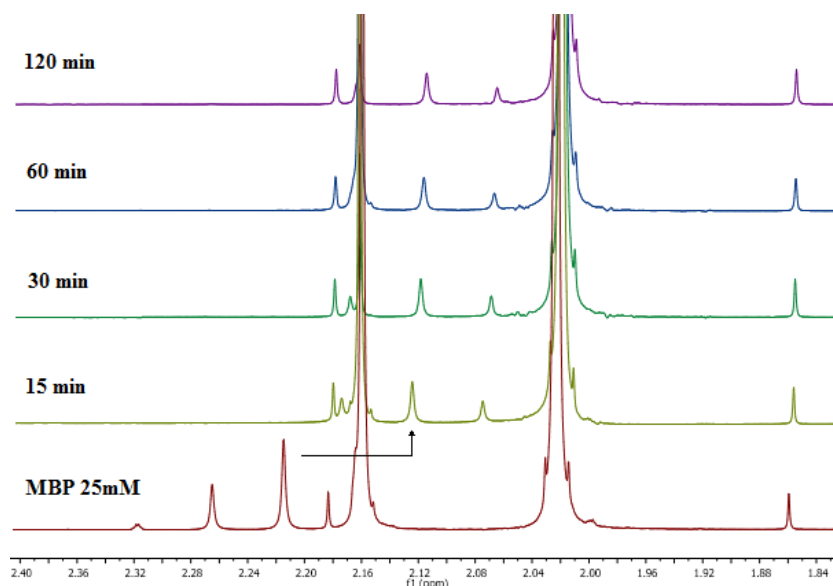


Figure 4.16: ^1H NMR spectra (400MHz, D_2O) related to the functionalization of ZrNPs with 25mM MBP in 25mM Acetate pH 4.0

Tampone	pH	Conc. Iniziale in sol. (mM)	Conc. Finale in sol. (mM)	GD (mol/m ²)	GD %
Acetate	4,0	10,00	0,00	3,27E-06	95
Acetate	4,0	25,00	7,40	5,77E-06	167

Table 7: Binding efficiency of MBP on ZrNPs at different concentration by ^1H quantitative NMR

From the results obtained it is possible to state that a 10mM MBP solution can determine the complete functionalization of zirconia nanoparticles (GD% equal to 95%). The value of Grafted Density related to the test carried out with the 25mM MBP solution in acidic conditions defines an over-loading of the nanoparticles (GD% 167%). This phenomenon can be explained through the coordinative interaction of only one of the two phosphate units of the MBP, allowing a greater number of molecules to bind to the surface of the ZrNPs (the values of GD% are calculated assuming that the bis-phosphonic acid interact with the bidentate binder support). Furthermore, there is the possibility of the formation of multiple MBP molecular layers on the substrate, resulting in a multi-layer coating of the nanoparticles favored by intermolecular hydrogen bonds between the phosphate units of the MBP. To test the stability of the interaction created between the MBP molecules and the zirconia nanoparticles, the functionalized support at pH 4.0 (complete loading of the 5mM MBP solution) was isolated by centrifugation, washed with distilled water and introduced in different buffered systems.

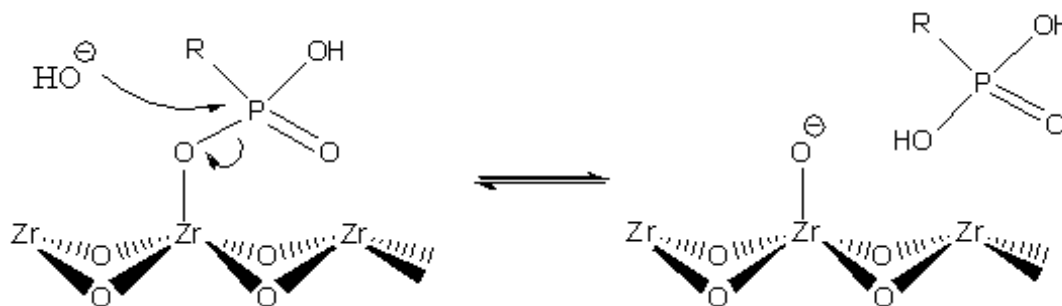


Figure 4.16: Reaction scheme related to equilibrium in a basic solution between the phosphonic molecules and the support

Through quantitative NMR analysis, after a time interval of 48h, no presence of MBP was found in the solution at pH 4.0 for Acetate while at pH 8.8 for TRIZMA, the concentration of MBP in solution was found to be 0,96mM, equal to a percentage release of 19%. (Figure 4.17, Tab.8) Only treating the functionalized support under strongly basic conditions for 100mM NaOH [257] it was possible to detect a consistent release in solution of the organic component, equal to 68% (time interval of 48h, Figure.4.19). The high pH of the buffer environment negatively affects the equilibrium established between MBP and the support: the electrostatic effects are less due to the deprotonation of the surface hydroxyl functionalities of the NPs and basic hydrolysis reactions of the previously formed bonds can occur (Figure .4.17).

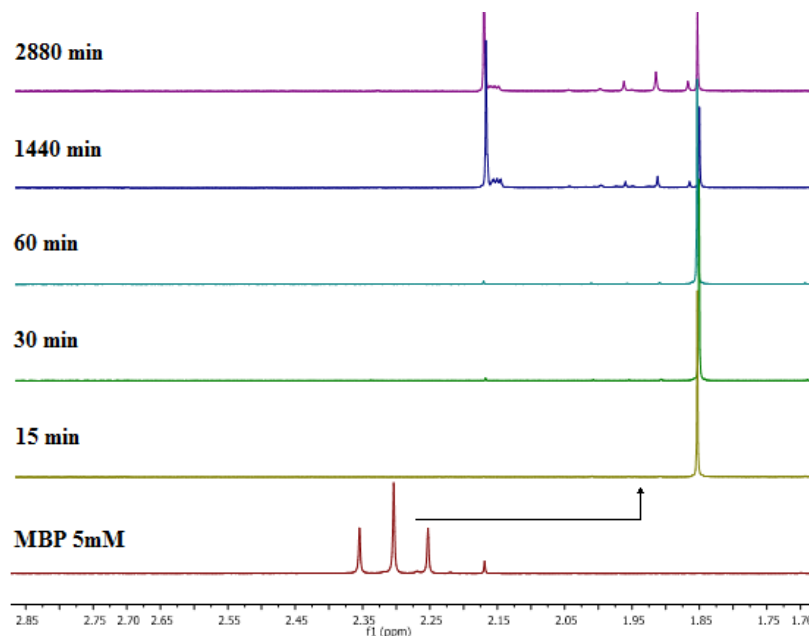


Figure 4.17: Release kinetics relative to the 5mM MBP molecule in 25mM Trizma (^1H NMR spectra: 400MHz, D₂O)

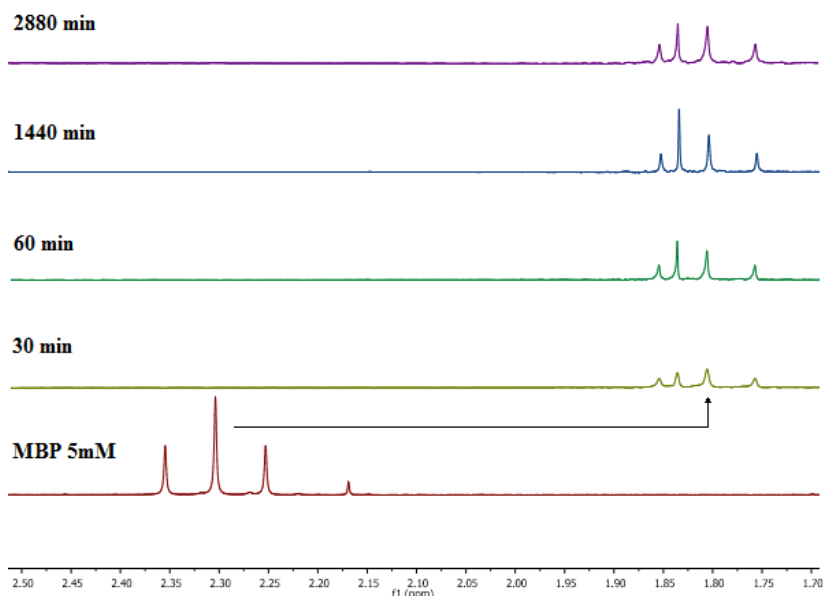


Figure 4.18: Release kinetics relative to the 5mM MBP molecule in 100mM NaOH (1H NMR spectra: 400MHz, D₂O)

Solution	Conc. Initial in sol. (mM)	Conc. Final in sol. (mM)	Release %
TRIZMA pH 8.8	0,00	0,96	19
NaOH 100mM	0,00	3,41	68

Table 8 Results concerning stability tests for MBM 5mM-ZrNPs

The study of the interaction between the methylene bis- phosphonic acid molecule and the nanoparticulate solid supports was extended to other inorganic oxides, replicating the described experiments for zirconia on silica (silicon oxide) and bismuth (bismuth oxide) nanoparticles.

4.2.1.2 Silicon oxide (SiO₂)

Following the addition of silica nanoparticles to buffered MBP solutions 5mM in the range of pH 2.0-8.8, the characteristic signal of the molecule under examination (triplet at 2.2ppm) has undergone a shift to larger fields (ppm lower) for the 25mM acetate solutions, 25mM HEPES and 25mM TRIZMA. Subsequently signal processing and integration, through the ERETIC functionality of the NMR spectrometer, different experimental results were found, if compared with what was found with the ZrNPs, an index of a different entity of interaction between the oxide and the MBP. At acidic pH (acetate and D₂O) the silica does not interact effectively (loading complete) with the organic molecule under consideration, defining load percentages of 5% and 50%. At basic pH for TRIZMA and pH neutral for HEPES, the loading percentages were

found respectively 62% and 69% (Figure 4.19, Figure 4.20, Tab.9). Considering the high surface area of the silica nanoparticles such results correspond to low values of Grafted Density, defining a lower degree of superficial covering.

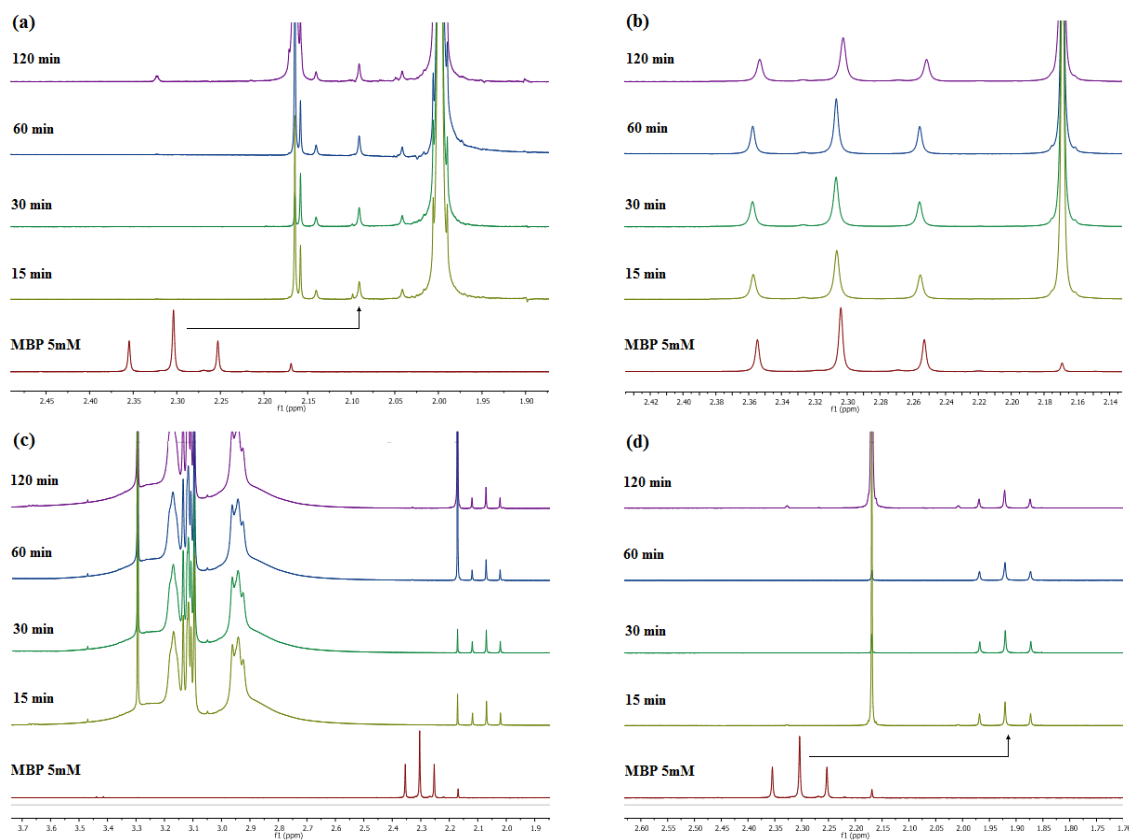


Figure 4.19: ^1H NMR spectra (400MHz, D_2O) related to the functionalization of SiNPs with 5mM MBP in: (a) 25mM Acetate pH 4.0. (b) D_2O . (c) HEPES 25mM pH 7.0. (d) TRIZAN 25mM pH 8.8.

Buffer	pH	Initial Conc. in sol. (mM)	Final Conc. in sol. (mM)	GD (mol/m ²)	GD %
D₂O	2,0	5,00	4,76	2,53E-08	1
Acetate	4,0	5,00	2,50	2,63E-07	8
HEPES	7,0	5,00	1,55	3,63E-07	10
TRIZMA	8,8	5,00	1,91	3,25E-07	9

Table 9: Binding efficiency of MBP on SiNPs at different pH determined by ^1H quantitative NMR

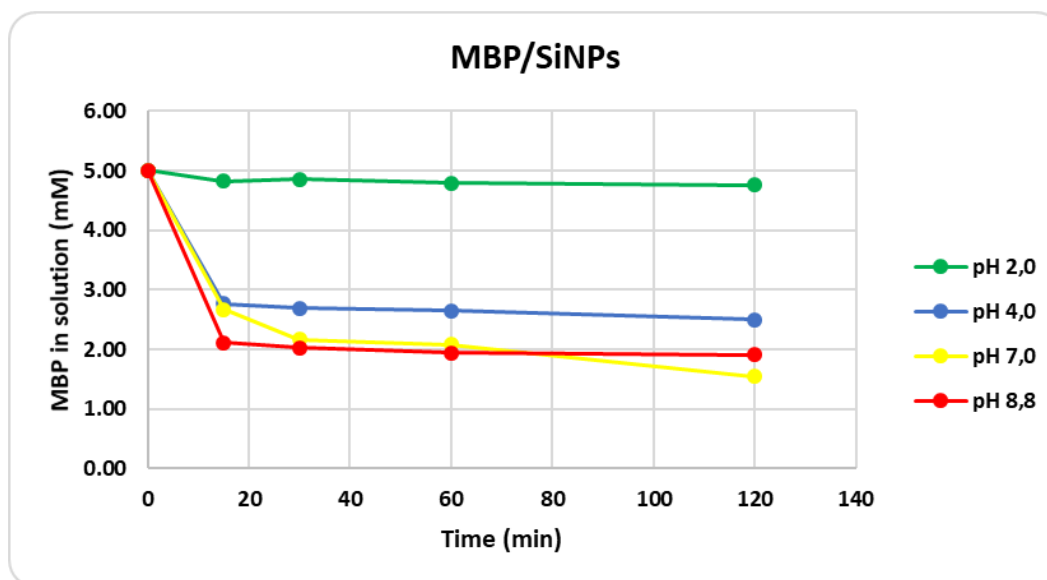


Figure 4.20: Graphical representation of the loading kinetics of the MBP molecule on SiNPs at different operating pHs

Solution	Initial Conc. in sol. (mM)	Final Conc in sol. (mM)	release %
TRIZMA pH 8.8	0,00	5,00	100

Table 10 Results regarding stability tests for MBM 5mM- SiNPs

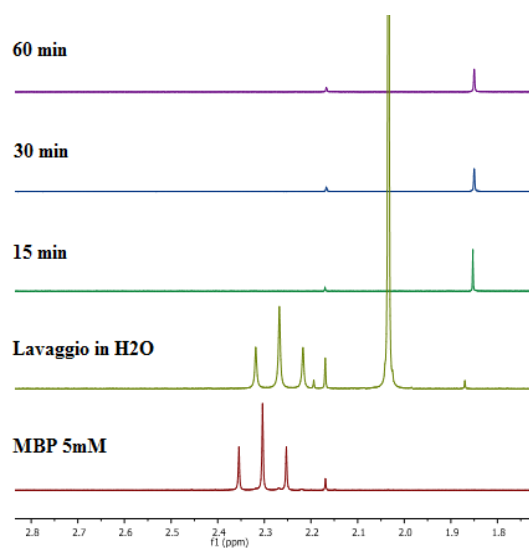


Figure 4.21: Release kinetics relative to the 5mM / SiNPs MBP molecule in TRIZMA 25mM (1H NMR spectra: 400MHz, D₂O)

Performing tests to verify the stability of the interaction between MBP molecules and silica nanoparticles, like zirconia, the functionalized support was isolated, washed and introduced into different buffered systems. The experiments conducted showed a complete release of the previously loaded MBP simply by washing the substrate with distilled water, demonstrating a weak and reversible interaction between the surface of the silica nanoparticles and the methylene bis-phosphonic acid (Table 10, Figure.4.21). From the experimental results obtained it is possible to state that the functionalization of silica nanoparticles with bis-phosphonic acids does not allow the formation of systems stable due to the weak interaction between species. Possible treatments superficial effects on the support will increase their reactivity and the creation of new strong types of interaction.

4.2.1.3 Bismuth oxide (Bi_2O_3)

The identification signal of the MBP, following the addition of the bismuth oxide nanoparticles to the buffered solutions and in D_2O , underwent a shorter ppm shift, identifying a possible interaction between the support and the methylene bis-phosphonic acid.

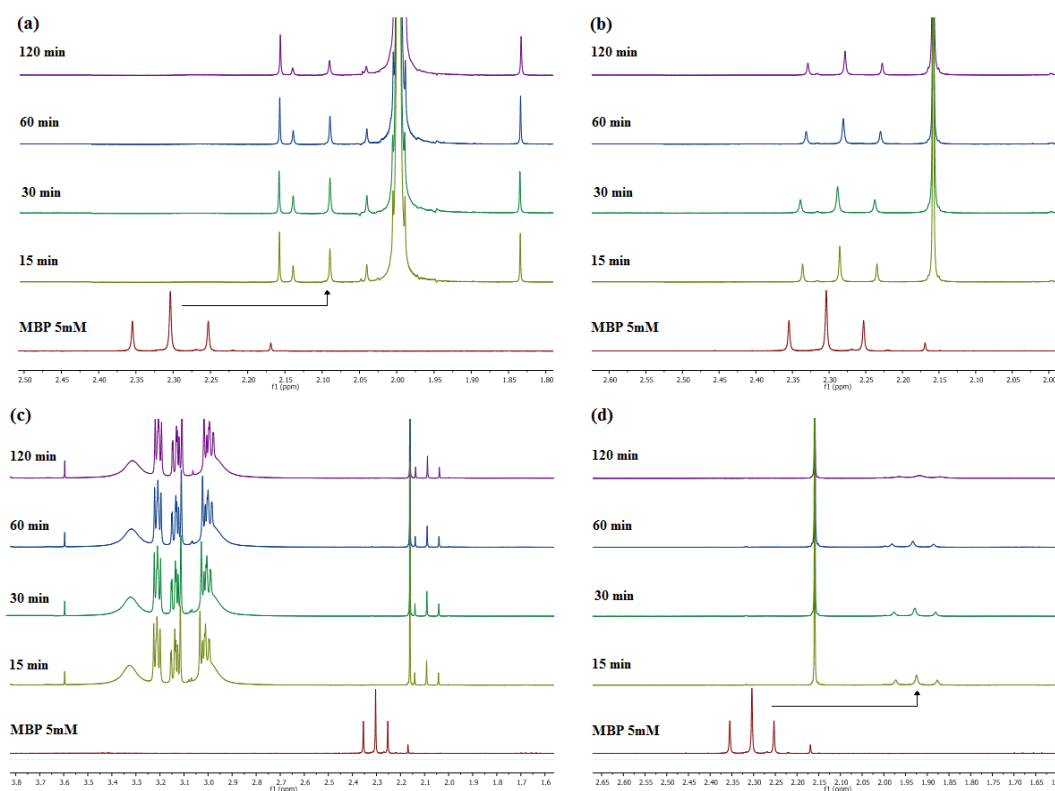


Figure 4.22: ^1H NMR spectra (400MHz, D_2O) related to the functionalization of BiNPs with 5mM MBP in: (a) 25mM Acetate pH 4.0. (b) D_2O . (c) HEPES 25mM pH 7.0. (d) TRIZAN 25mM pH 8.8

From the integration of the experimental signals, except for the buffered solution at pH 4.0 and in deuterated water, not all the organic molecules present in the solution interacted with the support, showing lower loading percentages compared to those found in the other oxides tested (Figure 4.22, Figure 4.23). Considering the reduced surface area of the nanoparticles used ($15 \text{ m}^2/\text{g}$), much lower than zirconia ($310.4 \text{ m}^2/\text{g}$) and silica ($949.9 \text{ m}^2/\text{g}$), the values related to Grafted Density% highlight an over-loading of the particles, like what was found in the case of the functionalized ZrNPs with acidic pH with 25mM MBP (Tab.11). These results underline how the type of metal influences the interaction model and the coordinating force between support and BPs. The high GD% can be justified considering the formation of numerous surface molecular layers of MBP (multi-layer): the reduced steric encumbrance and the weak amphiphilic character of these molecules in fact, together with the intermolecular hydrogen bonds between the phosphonic units, contribute to stabilize the creates structure (Figure. 4.24).

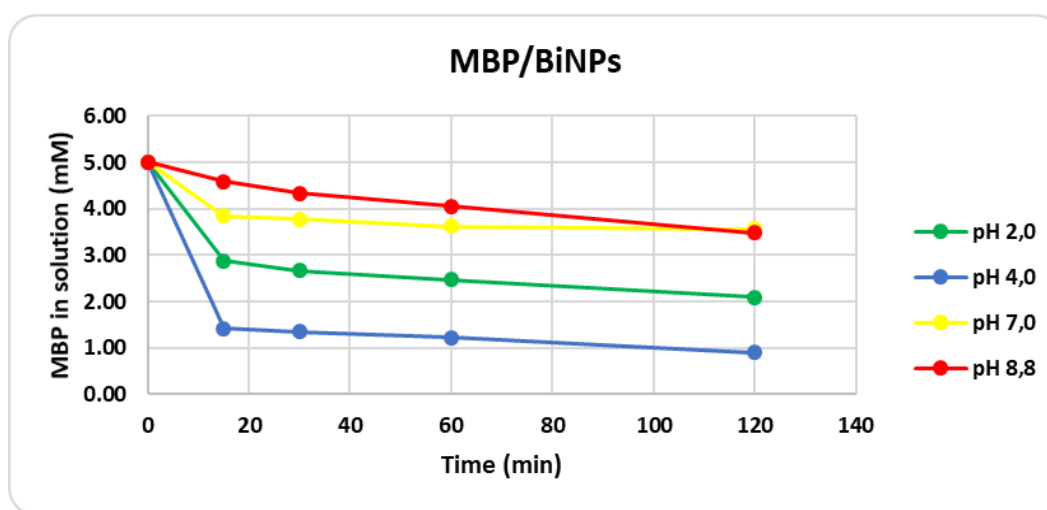


Figure 4.23: Graphical representation of the loading kinetics of the MBP molecule on BiNPs at different operating pHs

Buffer	pH	Initial Conc. in sol. (mM)	Final Conc. in sol. (mM)	GD (mol/m ²)	GD %
D ₂ O	2,0	5,00	2,09	2,09E-05	605
Acetate	4,0	5,00	0,90	2,95E-05	853
HEPES	7,0	5,00	3,56	1,04E-05	299
TRIZMA	8,8	5,00	3,48	1,09E-05	316

Table 11. Binding efficiency of MBP on BiNPs at different pH determined by ¹H quantitative NMR

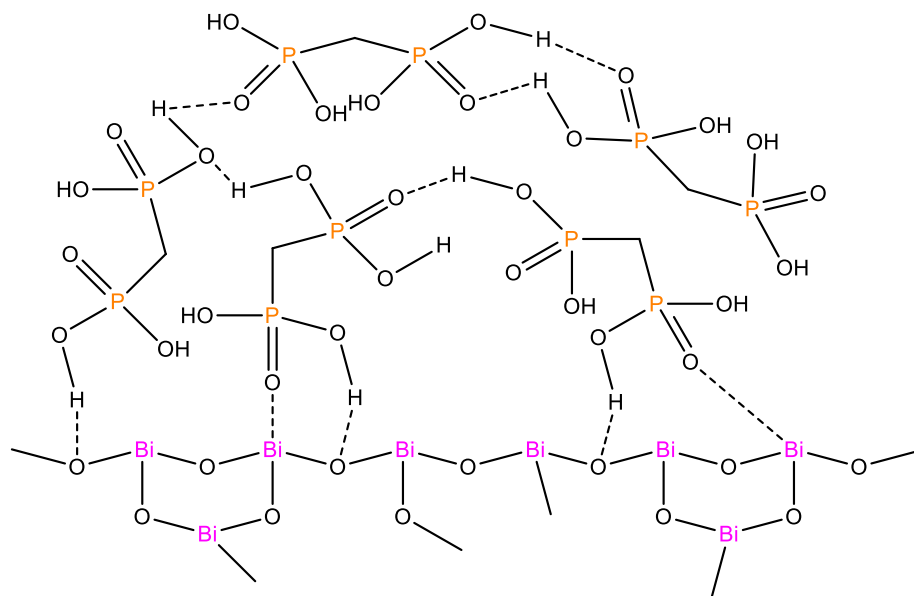


Figure 4.24: Graphical representation of the possible interactions formed between BiNPs and MBP

In order to test the stability of the interactions established between the MBP molecules and the bismuth nanoparticles, the functionalized support at pH 4.0 was isolated by centrifugation, washed with distilled water and introduced in the different buffered systems. Through quantitative NMR analysis, after a time interval of 48h, no presence of MBP was found in the solution at pH 4.0 for Acetate while at pH 8.8 for TRIZMA, the concentration of MBP in solution was found to be of 0.48mM equal to a 10% percentage release. (Tab.12, Figure.4.25).

Solution	Initial Conc. in sol. (mM)	Final Conc. in sol. (mM)	Release %
TRIZMA pH 8.8	0,00	0,48	10

Table 12 Results related to stability tests for MBM 5mM-SiNPss

Although it does not characterize a complete loading with acidic pH and follow, as in the case of zirconia, a loading kinetics dependent on the pH of the system, the oxide of bismuth defines strong interactions with the bis-phosphonic species in solution delineating a pH 8.8 for TRIZMA a lower release percentage (if compared with how much obtained for the ZrNPs). The MBP-support systems formed, because of their stability in aqueous solution they will be widely used in clinical and research fields.

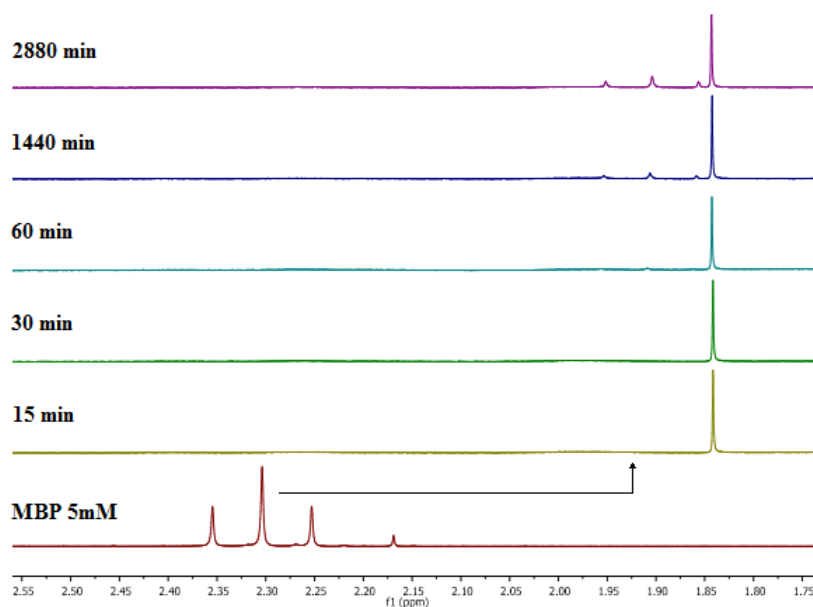


Figure 4.25: Release kinetics relative to the 5mM / BiNPs MBP molecule in TRIZMA 25mM (1H NMR spectra: 400MHz, D2O)

4.2.1.4 Titanium Oxide (TiO_2)

The loading tests with MBP showed a rapid uptake within 30 min of about 90% and 93% after 1h. This is in fact an expected result since examples of functionalization of TiO_2 surface with monophosphonates are known in the literature. The very high GD observed is possibly due to multilayer formation on the TiO_2 NPs similarly to what observed for Bi_2O_3 .

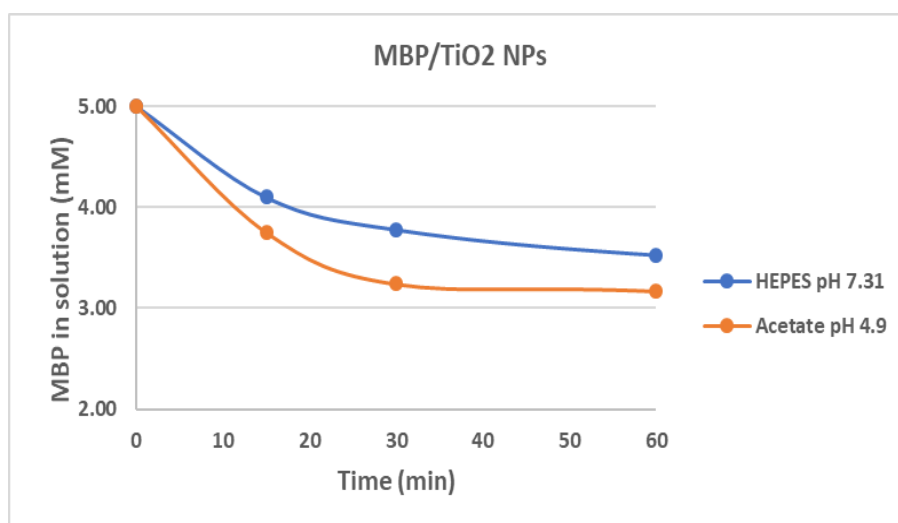


Figure 4.26: Graphical representation of the loading kinetics of the MBP molecule on TiNPs at different operating pHs

Buffer	pH	Initial Conc. in sol. (mM)	Final Conc. in sol. (mM)	GD (mol/m ²)	GD Molecules/nm ²
Acetate	4,9	5,00	2,89	2,95E-05	7.40
HEPES	7,3	5,00	3,28	1,04E-05	6.03

Table 13: Binding efficiency of MBP on TiNPs at different pH determined by ¹H quantitative NMR

4.2.2 Functionalized bis-phosphonic acids

The study of the interaction between methylene bis-phosphonic acid and zirconia nanoparticles was also extended to the other bis-phosphonic molecules represented in Figure 3.9a. These molecules differ from each other by the different central carbon binding substituents, characterized by carboxyl (BPSC), amine (BPAET), allylic (BPSAL) and methyl (EBP) functionalities. The molecules were tested in a buffered system at pH 4.0 for acetic acid / 25mM sodium acetate where 50 mg of support was added to 5 ml of a 5mM solution of BPs. The choice to perform the tests at pH 4.0 was determined by the fact that this pH provided the best results in terms of functionalizations and loading percentages in the experiments conducted with the MBP and the ZrNPs. Furthermore, most of the pure BPs rates available for experimental tests did not allow such large-scale tests to be conducted as they consisted of a few mg / μ L.

The BPSC molecule, in addition to the acidic environment for acetate, has also been tested in neutral (HEPES), basic (TRIZMA) and D₂O conditions to compare the results obtained with those obtained using the commercial analogue mono-phosphonic acid (paragraph 4.2). .3). The concentration of analyte in solution was determined in a similar way to that made with the MBP or taking an aliquot of solution at regular time intervals, isolating the supernatant by centrifugation and analyzing this solution by quantitative ¹H NMR with respect to the analyte's original solution (BP + buffer). In the integration phase the characteristic signals were used which showed a greater symmetry. The experimental results relating to each bis-phosphonic acid and the ¹H NMR spectra representing the loading kinetics of the test molecules are reported below (loading profiles and complete stability tests of all the experimental results are reported in the Appendix).

4.2.2.1 Ethane-1,1-diylbis(phosphonic acid) (EBP, 1b)

In the quantitative determination of the concentration in solution of the EBP molecule through the ¹H NMR analysis the disappearance of the split triplet (1.25-1.45ppm) relative to the methyl protons in position β with respect to the phosphonic groups was monitored over time (Figure 4.27b, b). In the time interval of 120 minutes, this molecule led to a complete loading and a functionalization of 44% of the accessible surface of the zirconia nanoparticles (Figure 4.28, Tab.14).

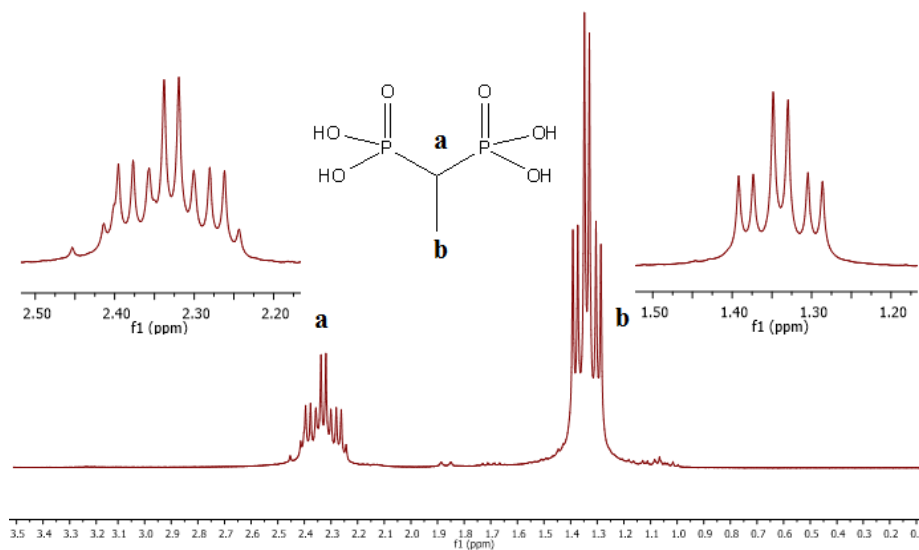


Figure 4.27: ^1H NMR spectrum (400MHz, D_2O) of the 5mM EBP molecule

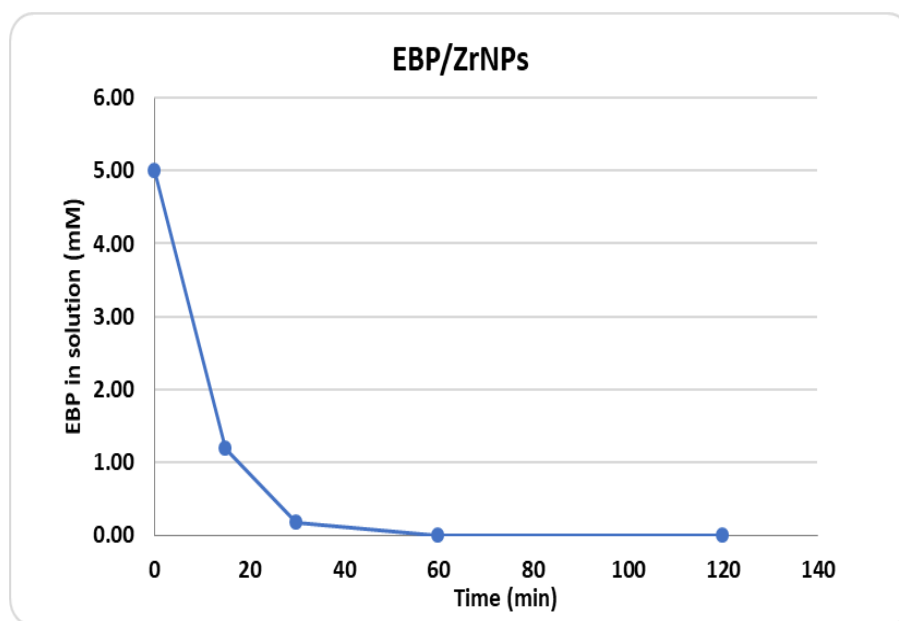
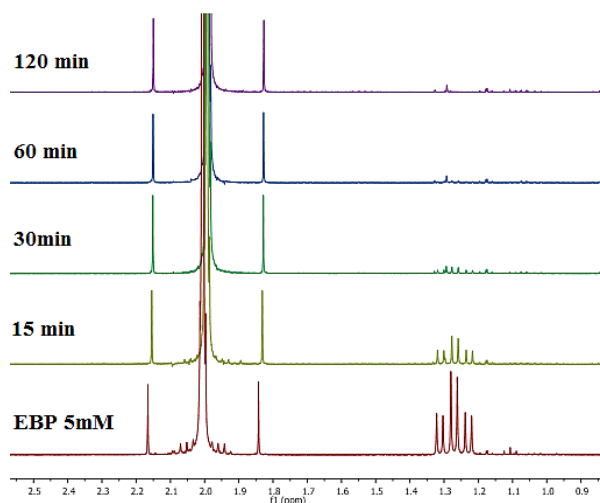


Figure 4.28: Graphical representation of the loading kinetics of the EBP molecule on ZrNPs

Buffer	pH	Initial Conc. in sol. (mM)	Final Conc. in sol. (mM)	GD (mol/m ²)	GD %
Acetate	4,0	5,00	0,00	1,52E-06	44

Table 14: Binding efficiency of EBP on ZrNPs at pH 4.0 determined by ^1H quantitative NMR



4.2.2.2. (2-((2-aminoethyl)thio)ethane-1,1-diyl)bis(phosphonic acid) (AETI, 1d)

In order to determine the concentration of AETI in solution, through the analysis of the characteristic molecular signals, the integration operation was carried out on the triplet located in the interval 3.16-3.24ppm characterizing the two protons identified by the letter "d" in figure 3.29. By monitoring this signal over time, after a two-hour time interval, 98% of the molecules present in the solution interacted with the ZrNPs, defining a GD% of 39% (Figure.4.30, Tab.15).

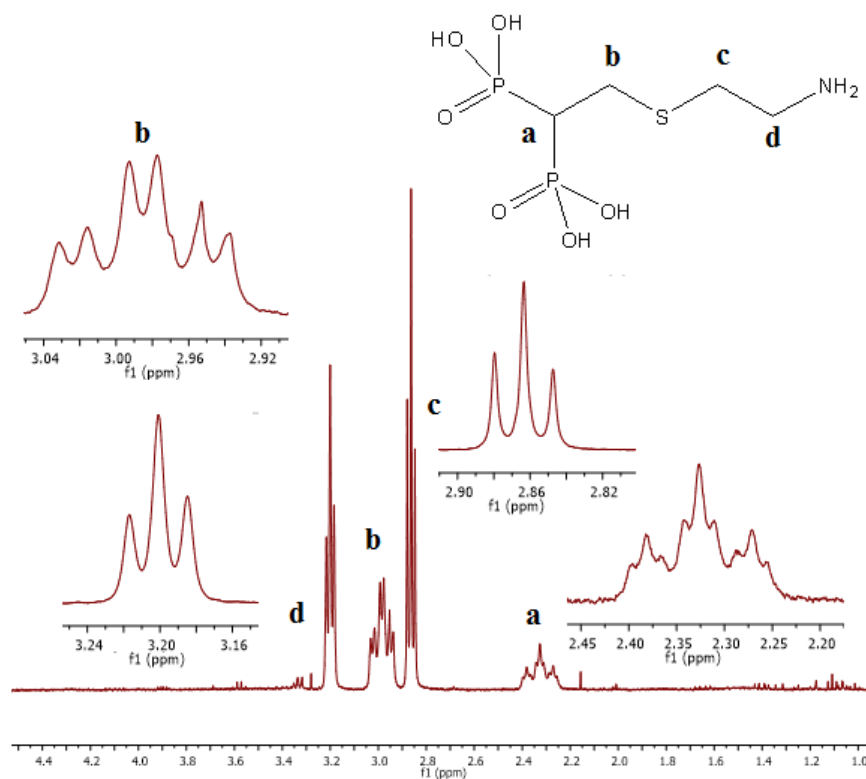


Figure 4.29: ^1H NMR spectrum (400MHz, D_2O) of the 5mM AETI molecule

Buffer	pH	Initial Conc. in sol. (mM)	Final Conc. in sol. (mM)	GD (mol/m ²)	GD %
Acetate	4,0	5,00	0,15	1,35E-06	39

Table 15: Binding efficiency of AETI on ZrNPs at pH 4.0 determined by ¹H quantitative NMR.

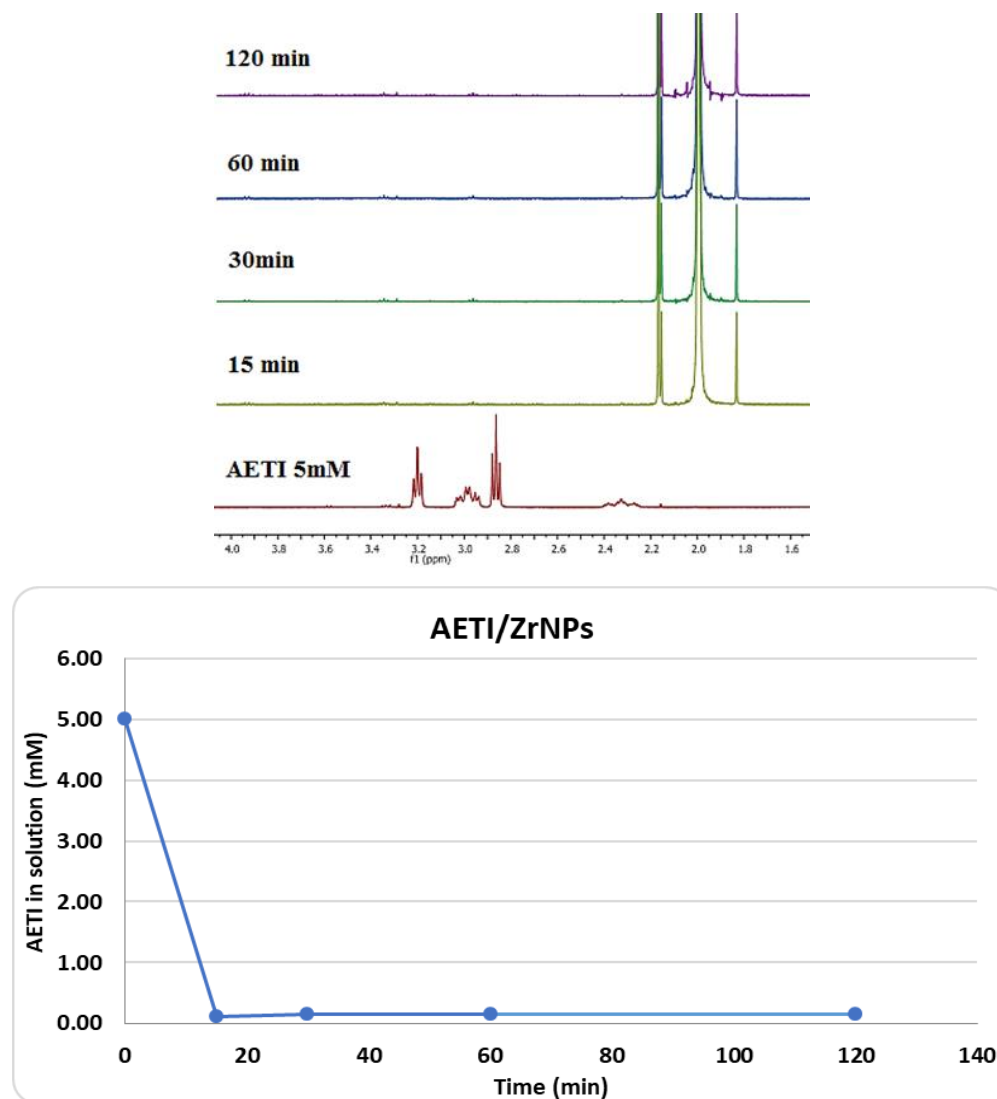


Figure 4.30: Graphical representation of the loading kinetics of the AETI molecule on ZrNPs

4.2.2.3. 2-((2,2-diphosphonoethyl)thio)acetic acid (BPSC)

The BPSC molecule, monitoring over time the signal related to protons in position β with respect to the phosphonic groups in the interval 2.97-3.12ppm (Figure 4.31, b) defined a quantitative loading in acidic environment for acetic acid / sodium acetate and in a non-buffered solution of deuterated water. By increasing the pH instead, the percentage of molecules in solution not

interacting with the support is increased up to 50% for TRIZMA (pH 8.8) and the percentage of overcoating decreased to 22% (Figure 4.32, Tab.16)

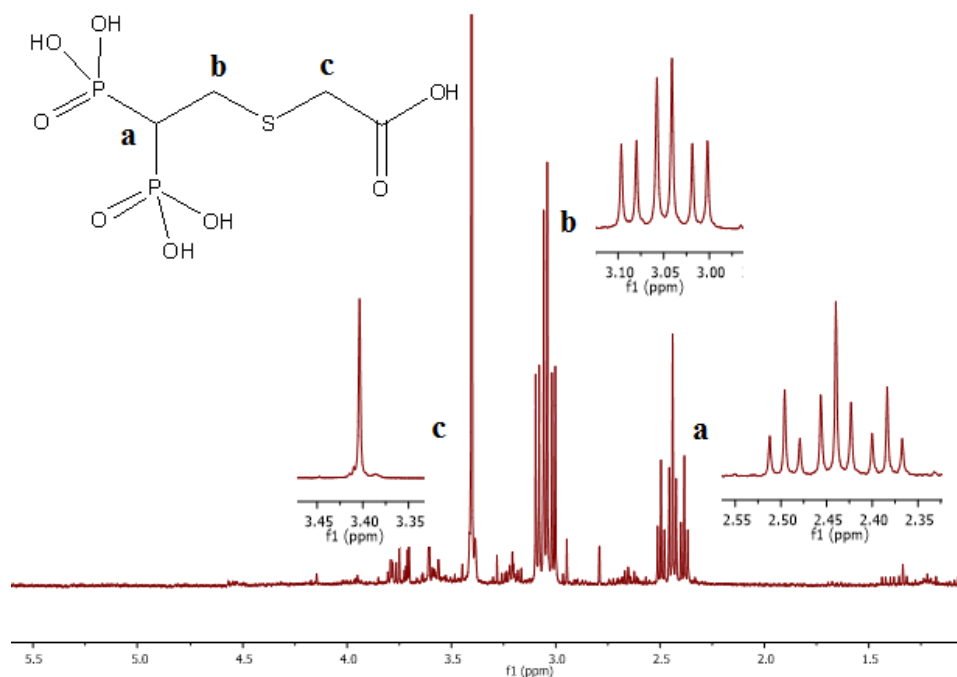


Figure 4.31: ¹H NMR spectrum (400MHz, D₂O) of the 5mM BPSC molecule

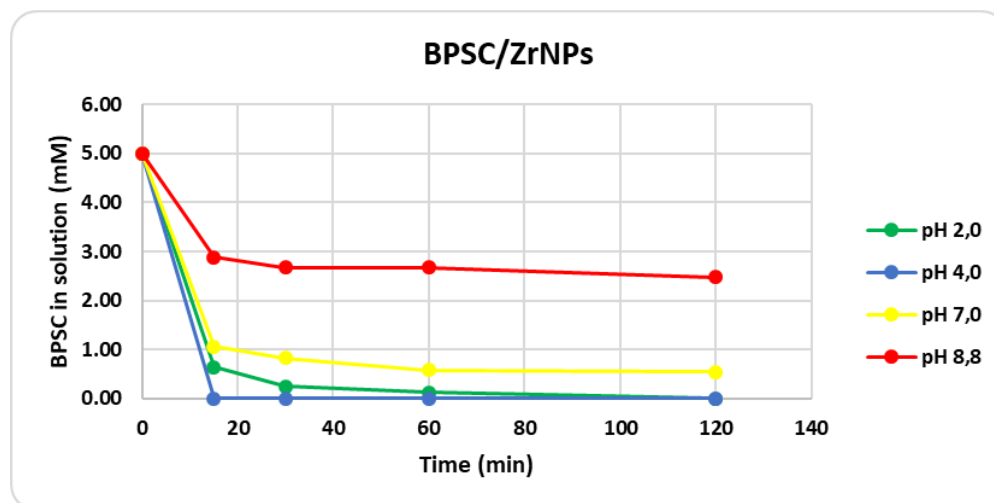
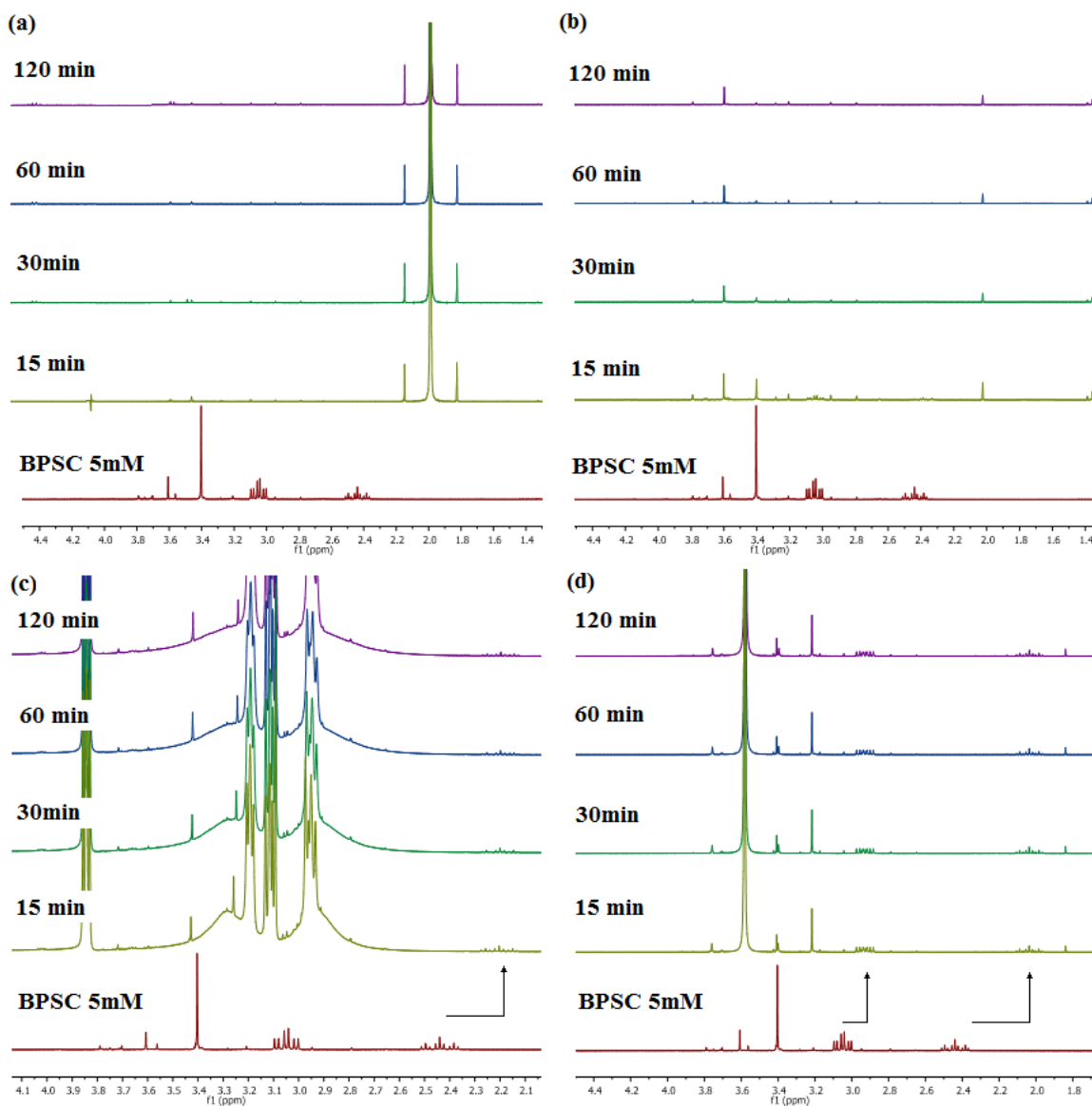


Figure 4.32: Graphical representation of the loading kinetics of the BPSC molecule on ZrNPs



(a) Acetato 25mM pH 4.0; (b) D₂O pH 2.0; (c) HEPES 25mM pH 7.0; (d) TRIZMA 25mM pH 8.8

Buffer	pH	Initial Conc in sol. (mM)	Final Con. in sol. (mM)	GD (mol/m ²)	GD %
D ₂ O	2,0	5,00	0,00	1,52E-06	44
Acetate	4,0	5,00	0,00	1,52E-06	44
HEPES	7,0	5,00	0,55	1,36E-06	39
TRIZMA	8,8	5,00	2,48	7,69E-07	22

Table 16: Binding efficiency of BPS on ZnNPs at different pH determined by ¹H quantitative NMR.

4.2.2.4 2-(2-propene-1-thiol) ethane-1,1-diyldiphosphonic acid (BPSAL)

The quantitative determination of the loading profile of the BPSAL molecule in buffered solution at pH 4.0 was performed by monitoring the ^1H NMR signal related to the protons characterized by the letter "b" in Figure 4.34 (2.82-2.95ppm). In the time interval of 120 minutes, this molecule showed a complete loading and a functionalization of 44% of the surface of the zirconia nanoparticles (Figure 4.33, Tab.17).

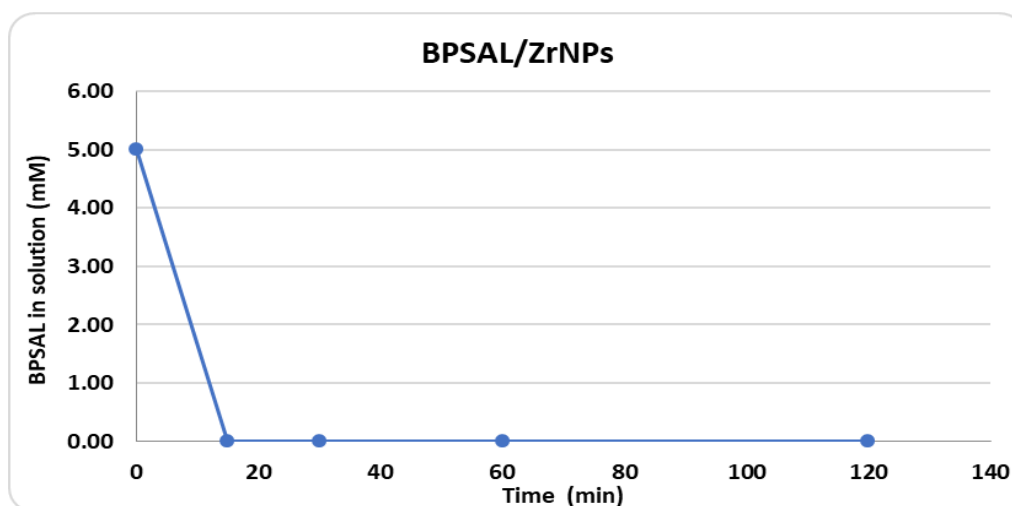


Figure 4.33: Graphical representation of the loading kinetics of the BPSAL molecule on ZrNPs

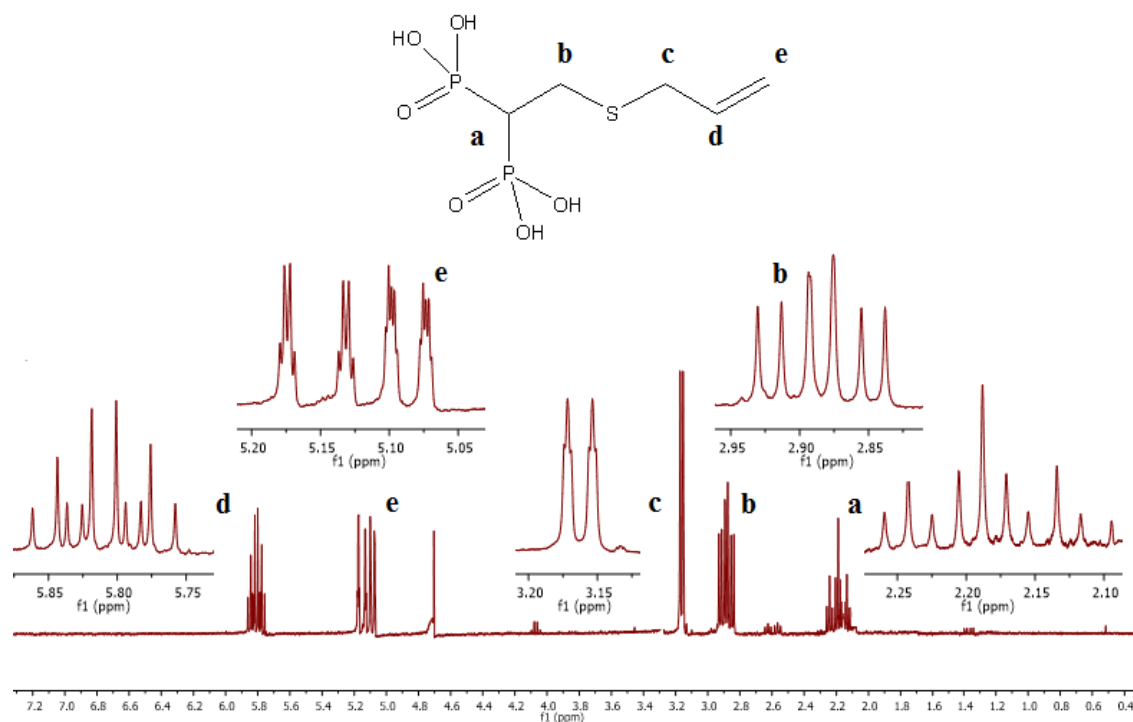
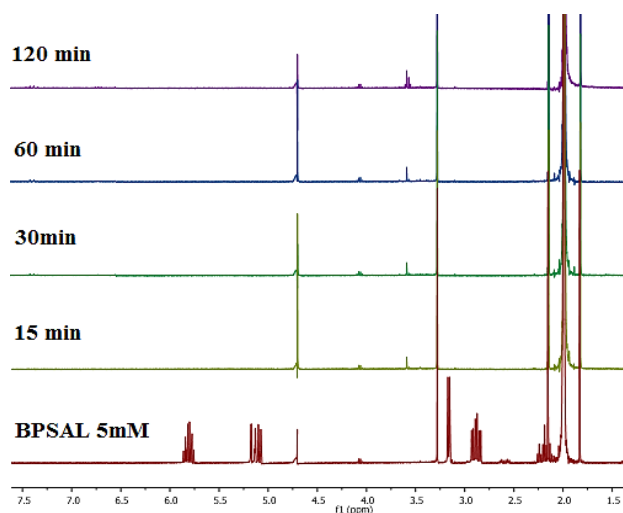


Figure 4.34: ^1H NMR spectrum (400MHz, D₂O) of the BPSAL 5mM molecule



Buffer	pH	Initial Conc. in sol. (mM)	Final Conc. in sol. (mM)	GD (mol/m ²)	GD %
Acetate	4,0	5,00	0,00	1,52E-06	44

Table 17 Binding efficiency of BPSAL on ZrNPs at pH 4.0 determined by ¹H quantitative NMR.

4.2.2.5 Comparison of the affinity between the various BPs and ZrNPs

Over the time interval of 120 minutes at acidic pH for acetic acid / 25mM sodium acetate, considering the error related to the experimental measurement, the bisphosphonic acids tested are substantially all characterized by 100% loading percentages indicating a quantitative interaction between the molecules and support. These results are also confirmed by the values of Grafted Density% equal to 44%. The results relative to the BPAET molecule differ from a few percent units from the other molecules in both the parameters taken into consideration (loading%: 98, GD%: 39) defining in each case a high interaction between ZrNPs and BPAET. The decrease in affinity between the two species can be attributed to forces of an electrostatic nature: the amine function present in the side chain of the BP at the acidic pH is positively charged (Figure 4.35) and the electrostatic repulsion between this charge and the support too positive and between chains close together can lead to less interaction.

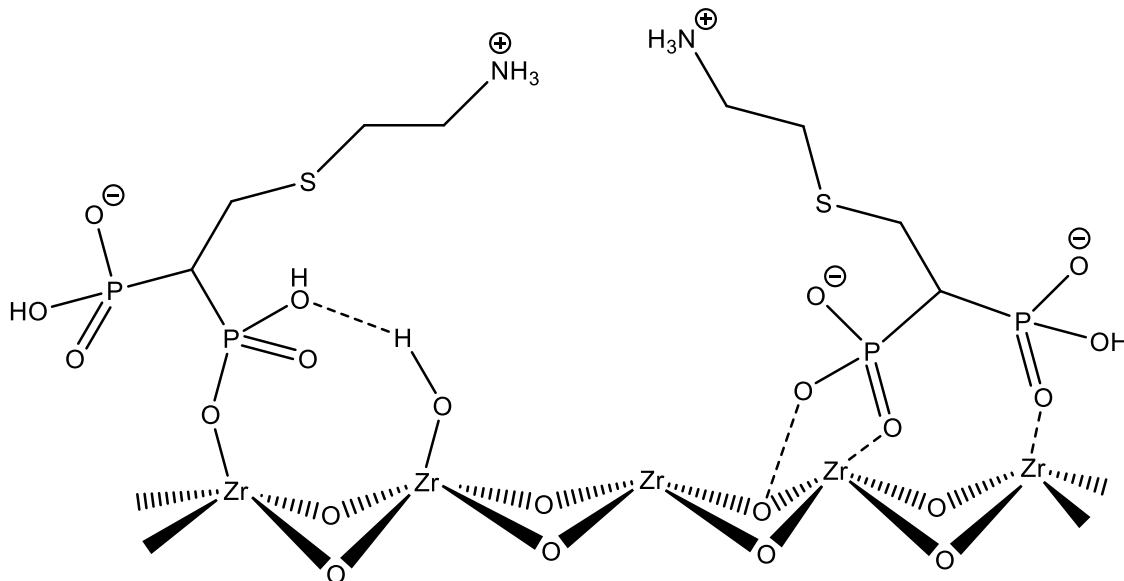


Figure 4.35: Graphical representation of the possible repulsion between the BPAET molecules coordinated with the ZrNPs which determines the reduction of the loading percentage

Furthermore, the steric encumbrance of the substituents contributes to these forces, increasing their effect. The increase in pH, similar to what has been verified with the MBP, destabilizes the equilibrium established between organic molecules and the increasingly less positive support leading to a lower percentage of loading (50% for TRIZMA 25mM). The other bis-phosphonic acids tested, not having charged functions, did not suffer too much from such interactions and their loading was complete. To test the stability of the interaction created between the zirconia molecules and nanoparticles, the functionalized supports were isolated by centrifugation, washed with distilled water and introduced into a buffered system at pH 8.8 for TRIZMA 25mM. Through quantitative NMR analysis, after a time interval of 48h, the presence of EBP and BPAET molecules resulting from the slow release was found in solution, which stands at a percentage equal to 9% and 23% respectively. The supports functionalized with the molecules of BPSAL and BPSC, in the time interval considered, did not show any release in solution of the organic component, demonstrating a stable and strong interaction between support and BPs (Tab.17). The EBP molecule and the allyl-substituted BPSAL differ from the other molecules due to the hydrophobic character of the side chain. This feature may affect the lower release percentage caused by the relative decrease in solubility of the molecule in the aqueous solvent used. Furthermore, it is known that bisphosphonates containing hydrophobic groups tend to aggregate in solution with a behavior like that of surfactants (amphiphilic molecules) in the formation of micelles or of structures with lower energy content and the contribution of the hydrophobic effect on the stability of the bond of the BPs with ZrNPs can justify such results. The amine group of the BPAET molecule present in cationic form at the operative pH can destabilize the intermolecular interaction between the neighboring molecules and impart a

greater solubility in the aqueous solvent to the bis-phosphonic acid, determining a more marked percentage of release, as can be seen from the values reported in Tab.18.

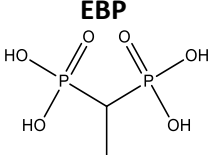
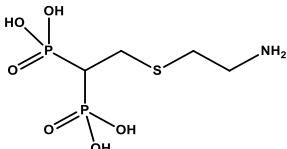
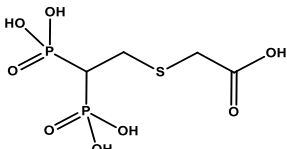
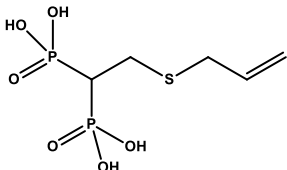
Buffer	Molecule	Initial Conc. in sol. (mM)	Final Conc.in sol. (mM)	Release %
TRIZMA pH 8.8	<p>EBP</p> 	0	0,43	9
	<p>BPAET</p> 	0	1,15	23
	<p>BPSC</p> 	0	0,00	0
	<p>BPSAL</p> 	0	0,00	0

Table 18 Results related to stability tests for 5mM-ZrNPs BPs in TRIZMA 25mM

4.2.3 Commercial monophosphate acids

In order to compare the affinity with respect to the zirconium oxide nanoparticles between the bis-phosphonic molecules BPSC and BPAET and the mono-phosphonic analogs (MPs) AFP and AEFO, for the latter molecules some tests have been conducted in different buffered systems. In fact, the AFP and AEFO molecules have a carboxylic group and an amino group as a terminal function, in accordance with the previously mentioned bisphosphonates. The affinity tests were performed using buffer solutions at pH 4.0 for acetic acid / 25mM sodium acetate, pH 7.0 for HEPES 25mM, pH 8.8 for TRIZMA 25mM and in D₂O, according to what was done in the experiments previous. Due to the high cost of AEFO commercial mono-phosphonic acid, only one test was carried out at pH 4.0, as this pH provided the best results in terms of functionalizations and loading percentages in tests conducted for the other molecules.

4.2.3. 3-phosphono-1-propanoic acid (AFP)

In the quantitative determination of the concentration in solution of the AFP molecule through the ^1H NMR analysis, the decrease in the signal relative to the methyl protons in position β with respect to the phosphonic group (interval 2.52-2.62ppm, Figure 4.36, b) was monitored over time. According to the BPSC, this molecule showed an operating pH dependent loading with a 94% loading in the non-buffered system (D_2O). By increasing the pH, the percentage of non-interacting molecules in the solution is increased up to 60% for TRIZMA (pH 8.8). These results led to the calculation of very low GD% values compared to what was found with the analogous BPs (Figure 4.37, Tab.19).

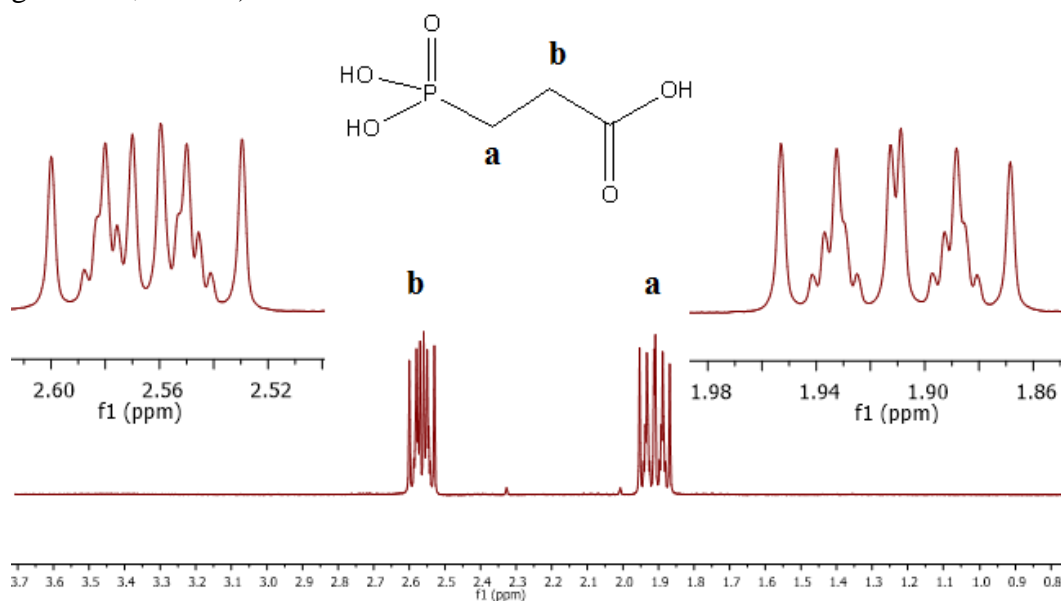


Figure 4.36: ^1H NMR spectrum (400MHz, D_2O) of the 5mM AFP molecule

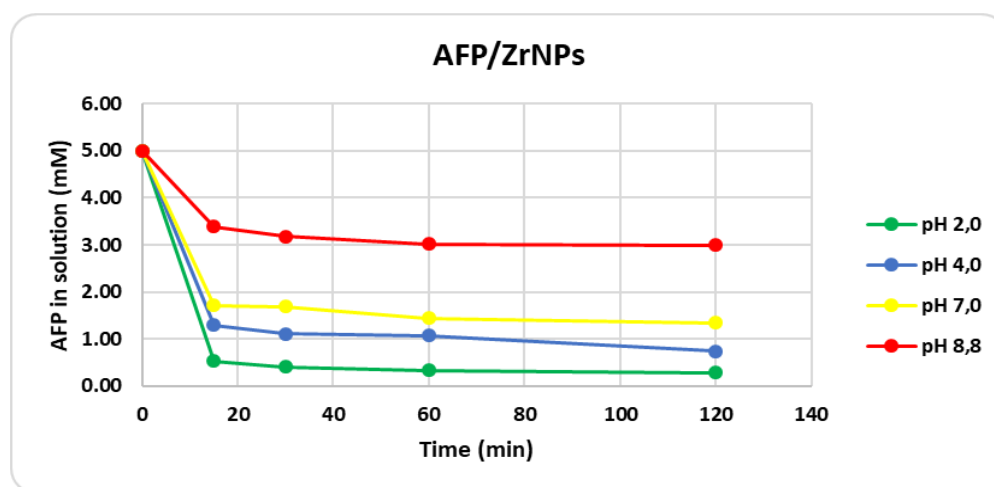


Figure 4.37: Graphical representation of the loading kinetics of the AFP molecule on ZrNPs at the different operating pHs

Buffer	pH	Initial Conc. in sol. (mM)	Final Conc. in sol. (mM)	GD (mol/m ²)	GD %
D ₂ O	2,0	5,00	0,28	1,30E-06	19
Acetato	4,0	5,00	0,74	1,17E-06	17
HEPES	7,0	5,00	1,35	1,00E-06	15
TRIZMA	8,8	5,00	3,00	5,51E-07	8

Table 19 : Binding efficiency of AFP on ZrNP at pH 4.0 determined by ¹H quantitative NMR

4.2.3. 2 Acid (2-aminoethyl) phosphonic acid (AEFO)

The AEFO molecule, monitoring over time the signal related to protons in position β with respect to the phosphonic group in the interval 3.06-3.26ppm (Figure 4.38, b), showed an acidic charge for acetic acid / sodium acetate 82%. Overall, in the time interval of 120 minutes, 17% of the surface area of the nanoparticles was functionalized (Figure 4.39, Tab.20).

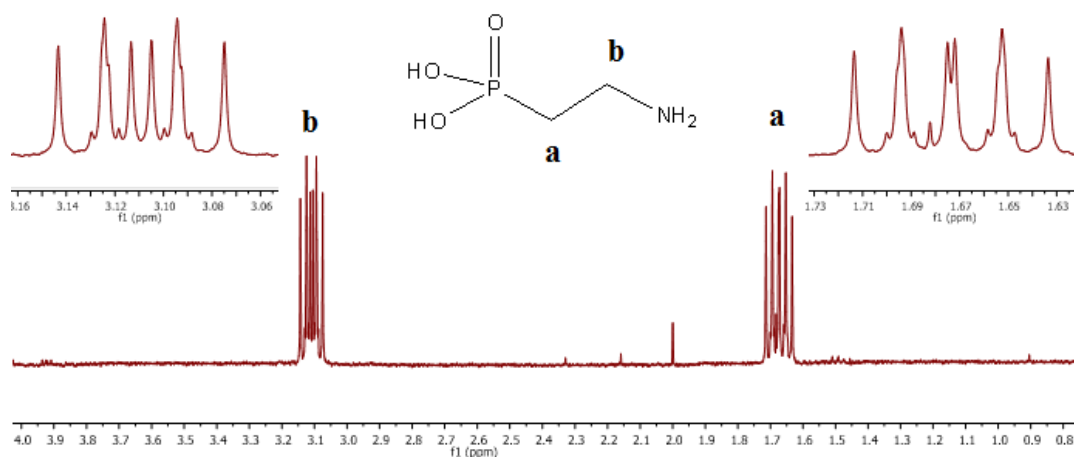


Figure 4.38: ¹H NMR spectrum (400MHz, D₂O) of the 5mM AEFO molecule

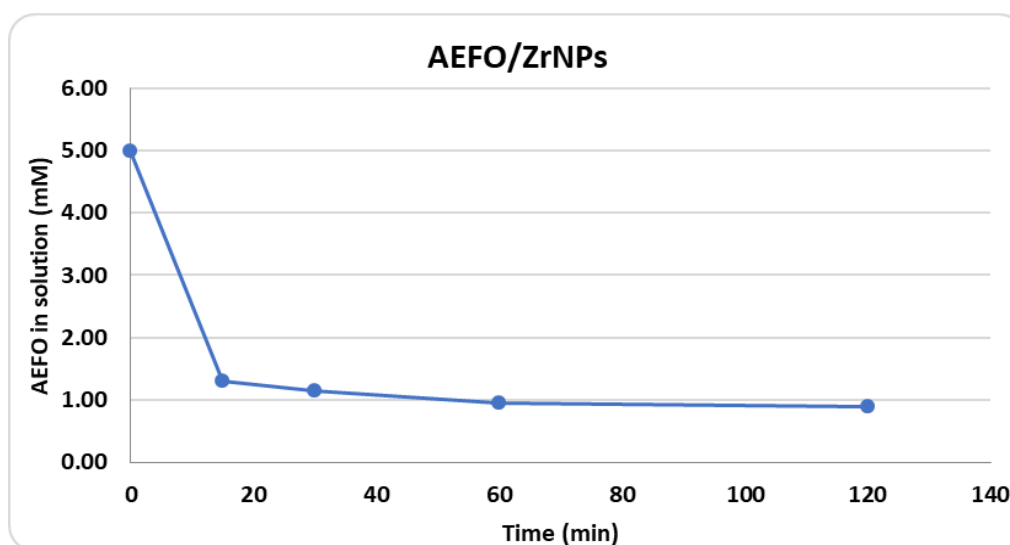


Figure 4.39: Graphical representation of the loading kinetics of the AEFO molecule on ZrNPs

Buffer	pH	Initial Conc. in sol. (mM)	Final Conc. in sol. (mM)	GD (mol/m ²)	GD %
Acetate	4,0	5,00	0,90	1,14E-06	17

Table 20: Binding efficiency of AEFO on ZrNPs at pH 4.0 determined by ¹H quantitative NMR.

4.2.3. 3 Comparison of affinity of monophosphonates and bisphosphonates against ZrNPs

The functionalization of zirconium oxide nanoparticles using commercial mono-phosphonates has determined different experimental results than as found with the respective bisphosphonates. The lower percentage of molecules organic that result in interacting with the ZrNPs can be attributed to the type interaction between the two species: mono-phosphonates are characterized by only one phosphonic functionality (hence the name) which attributes to these molecules the property of monodentate binders. The MPs-support adduct results to be less stable than the one established with the bisphosphonate analogues since the coordinating sites of these latter molecules are superior thanks to a greater number of bonds, both of electrostatic, covalent or hydrogen nature between MPs and NPs. These hypotheses were confirmed by the release tests carried out at basic pH for TRIZMA 25mM: thereafter processing and integration of ¹H NMR signals related to each acid mono-phosphonic, after a time interval of 48h, the molecules AFP and AEFO have determined a solution release of 1.18mM and 1.38mM respectively, equal to one percentage of 24% and 28% (Tab.21). If compared with the results obtained with the conforming bis-phosphonic acid (Tab.22), the percentage of solution release of the molecule of AFP results to be of much higher (BPSC 0%, AFP 24%) while the AEFO molecule instead, presents a value comparable to that obtained for BPAET, not subject to the latter by five percentage points.

Buffer	Molecule	Initial Conc. in sol. (mM)	Final Conc. in sol. (mM)	Release %
TRIZMA pH 8.8	AEFO	0,00	1,38	28
	AFP	0,00	1,18	24

Table 21 Results related to stability tests for MPs 5mM-ZrNPs in TRIZMA 25mM

Buffer	Final Conc. in sol. (mM)		Release % (5mM; pH 8.8)	
	BPSC	AFP	BPSC	AFP
Acetate	0,00	0,74	0	24
HEPES	0,55	1,35		
D2O	0,00	0,28		
TRIZMA	2,48	3,00		

Table 22 Experimental results related to BPSC and AFP molecules

The amino group characterizing the AEFO mono-phosphonate at the operating pH is present in cationic form: Positive charges in the side chain can destabilize the interaction intermolecular between vicinal molecules, increase the solubility of this molecule in aqueous solvent and in conjunction with the reversibility of the adduct due to the basic pH (competition between OH-

and phosphonic functionality), determine higher percentages of release. The comparative experiments carried out confirm the greater affinity of the bis-phosphonic acids compared to commercial monophosphate analogs in functionalization of nanoparticles consisting of inorganic oxides such as zirconia.

4.3 Study and determination of the MBP-NPs interaction in aqueous solution

In the functionalization of the zirconium oxide nanoparticles with the methylene bis-phosphonic acid, as can be seen from the experimental results, the operating pH significantly influences the loading percentages and the relative values of Grafted Density%. The charge possessed by the zirconia particles and the negative charges determined by the poly-phosphonic molecules of the MBP, as a result of their interaction, modify the surface charge of the support by characterizing a greater colloidal stability of the system, preventing aggregation in relatively long time periods (tests carried out with time intervals of 48h). To understand in depth, the type of interaction that is established between MBP and the support, some tests have been conducted in aqueous solvent such as to monitor the behavior of the organic acid as a function of pH. The analytical technique used was proton nuclear magnetic resonance spectroscopy (^1H NMR) and phosphorus (^{31}P NMR) because nuclear resonances are greatly influenced by acid-base equilibrium. This technique allows the determination of the acid dissociation constants of the MBP in an aqueous system (of 5mM concentration) monitoring the chemical shift of the proton triplet (in ^1H NMR) and of the singlet relative to the two phosphorus atoms (in ^{31}P NMR), characteristic of the methylene bis-phosphonic acid (Figure 4.40).

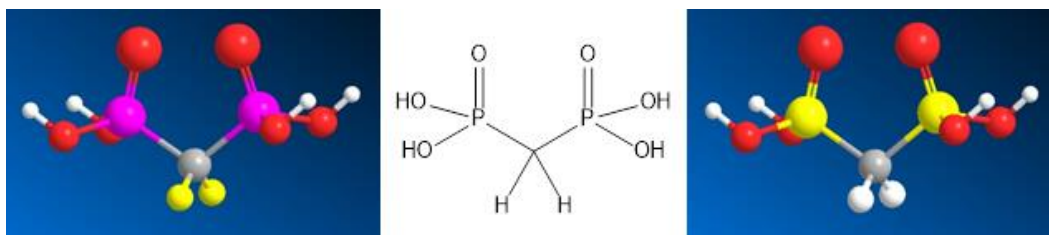


Figure 4.40: Graphical representation of the MBP: the methyl protons (on the left) and the phosphorus atoms (on the right) are highlighted in yellow

Following the elaboration of the experimental results and the study of the profiles obtained by expressing the chemical shift relative to the signals as a function of the pH (represented in Figure 3.41, Figure 4.42, Figure 4.43, Figure 3.44), the ^1H NMR analysis was found to be more sensitive in the determination of K_{a3} and K_{a4} while the ^{31}P NMR analysis for the constants K_{a1} and K_{a2} . Applying a first and second derivative study to the experimental results obtained, it was possible to determine the four acid dissociation constants of the MBP, characterized by the inflection points of the δ / pH curves [258] (Figure 4.45, Tab.23). These results can provide a better interpretation of the pH effect in the MBP loading process on inorganic nanoparticles.

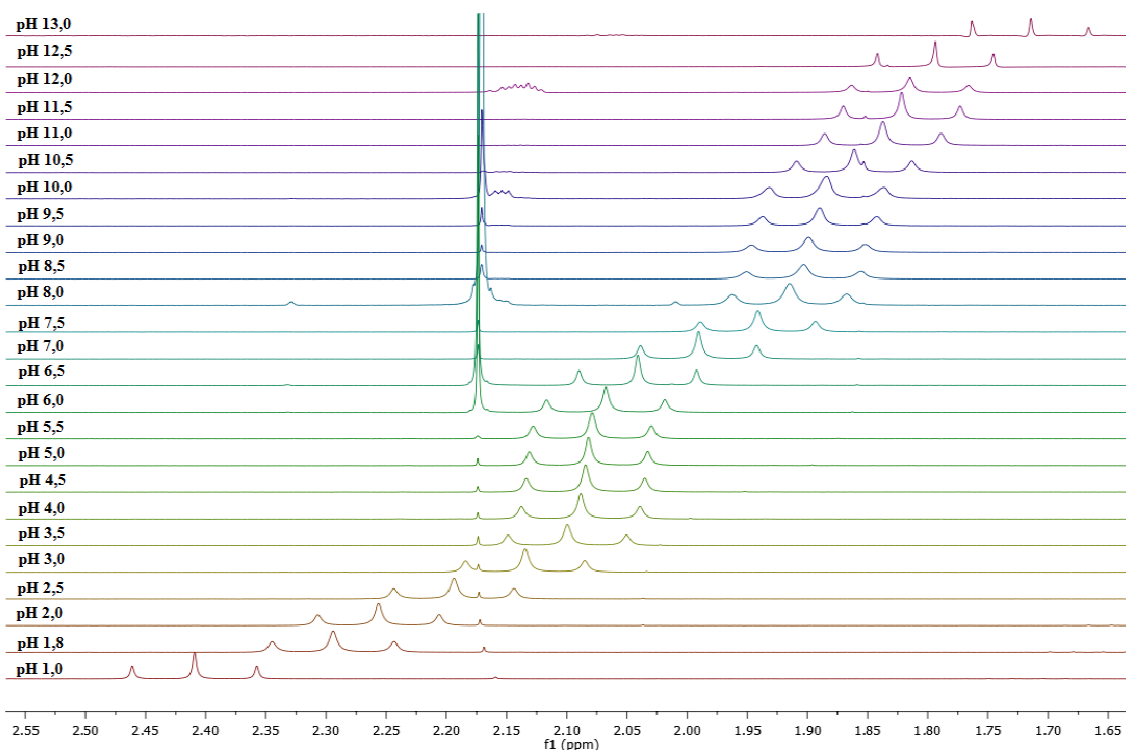


Figure 4.41: ^1H NMR spectra (400MHz, D_2O) of the MBP at different pH: triplet relative to the methylene protons present in the molecule; δ 2.17 (s) Acetone

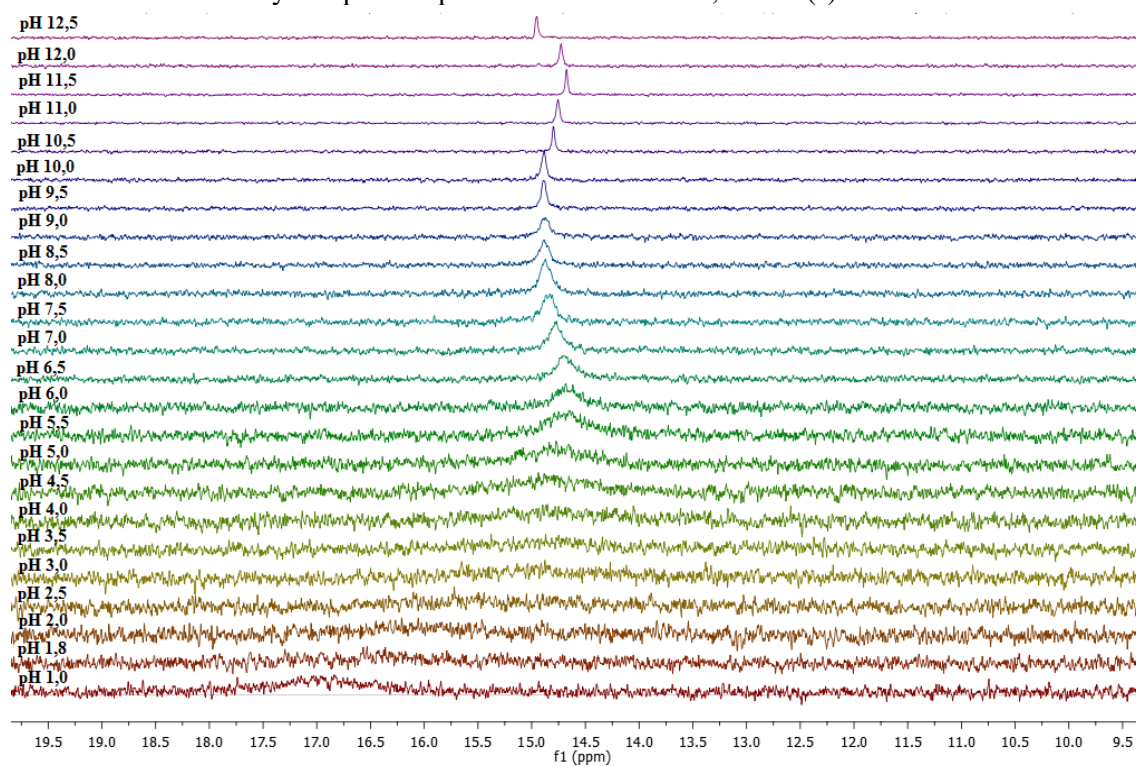


Figure 4.42: ^{31}P NMR spectra (162MHz, D_2O) of the MBP at different pH: singlet relative to the two equivalent phosphorus atoms present in the molecule

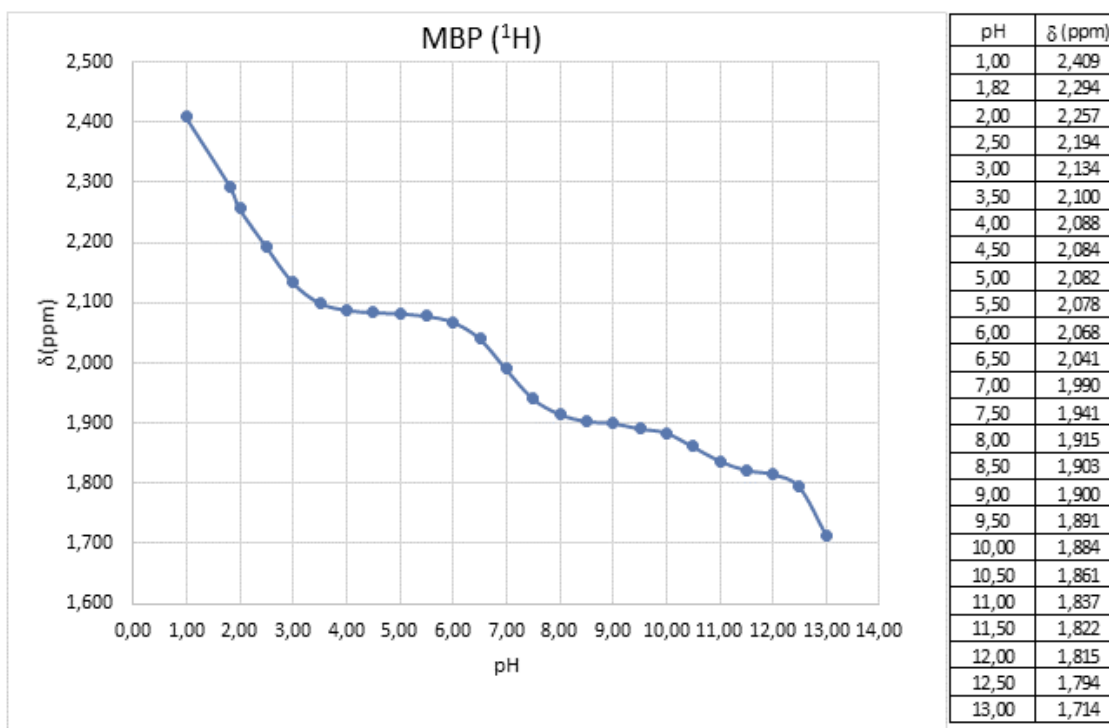


Figure 4.43: Graphical representation of the experimental results related to the MBP proton analysis

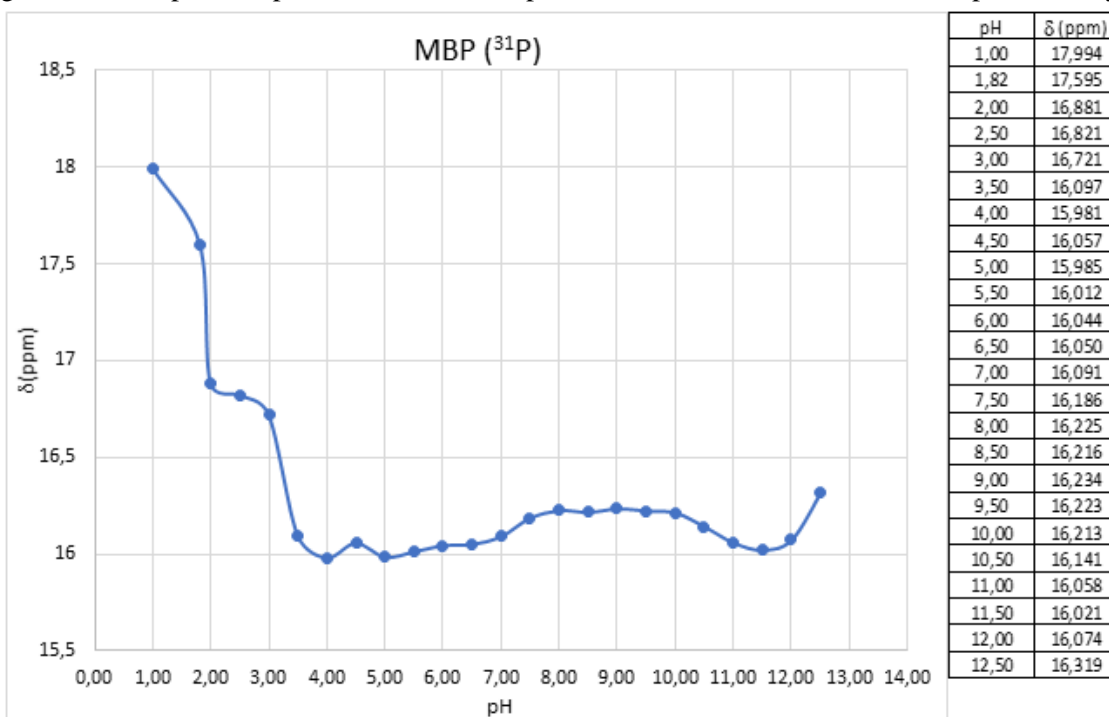


Figure 4.44: Graphical representation of the experimental results related to the phosphorus analysis of the MBP

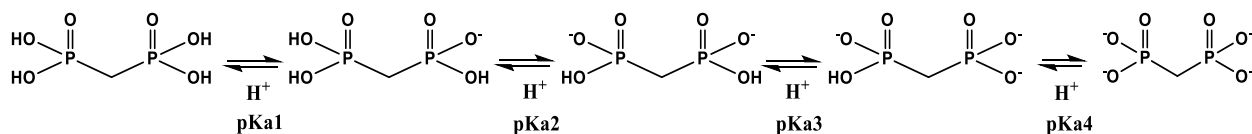


Figure 4.45: Graphical representation of the equilibrium related to the acid dissociation constants of the MBP

pKa 1	1,88
pKa2	3,24
pKa3	6,96
pKa4	10,55

Table 23 pKa of the MBP experimentally determined

Correlating the experimental results obtained in the study of the MBP-NPs system to the identified pKa, according to the information reported in the literature, the interaction between the different types of nanoparticles and the bis-phosphonic acid depends mainly on the chemical composition of the support and partly from the superficial charge possessed. The acidic zirconium oxide is characterized by a positive Z potential while at the basic pH the surface charge of the NPs is negative. Considering the pKa1 of the MBP, the latter is present in a solution at pH 4 as bis-ion, therefore the interaction between the two species can be determined by electrostatic attractive forces. By increasing the pH to 7.0, zirconia is almost neutral and MBP is characterized by a mixture of bis- and tris-anions, defining a lower efficacy interaction than the acid pH. At basic pH, as in the case of the TRIZMA buffer, zirconia is negatively charged and the methylene bis-phosphonic acid is in tris-anionic form: the link between the two species is hindered by electrostatic repulsion, resulting in a lower percentage of loading.

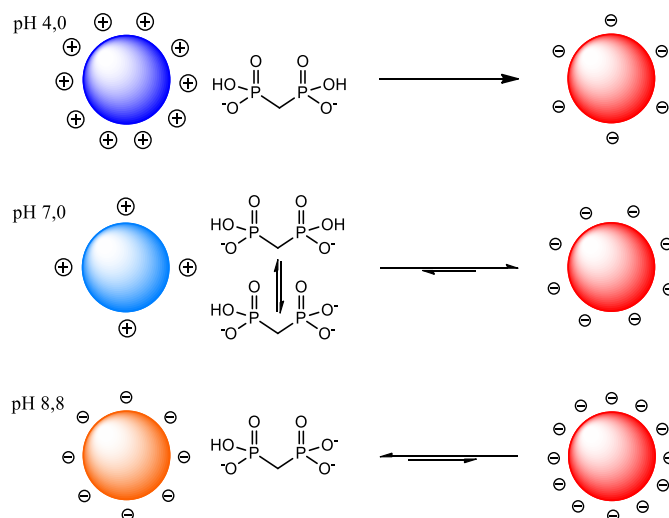


Figure 4.46: Graphical representation of the charge distribution on the NPs before and after the interaction with the MBP molecules

The greater the amount of MBP molecules that bind to the support, the greater will be the total surface negative charge that will take up the nanoparticles (Figure 4.46). From the interaction between MBP and zirconia, in all pH values in which the analyzes were carried out, the MBP-support species are characterized by an overall negative surface charge, as confirmed by the Z potential measurements carried out on the NPs following their functionalization (Figure 4.47). The high values of potential Z found define a greater stability of the dispersed systems as they originate electric type repulsions among the NPs that prevent the aggregation of the nanoparticles.

pH	Zeta P. ZrNPs (mV)	Zeta P. MBP@ ZrNPs (mV)
4.6	14.3	-15.6
5.9	10.7	-22.1
7.3	-7.9	-30.6
8.5	-25.4	-35.2
9.9	-31.4	-35.7

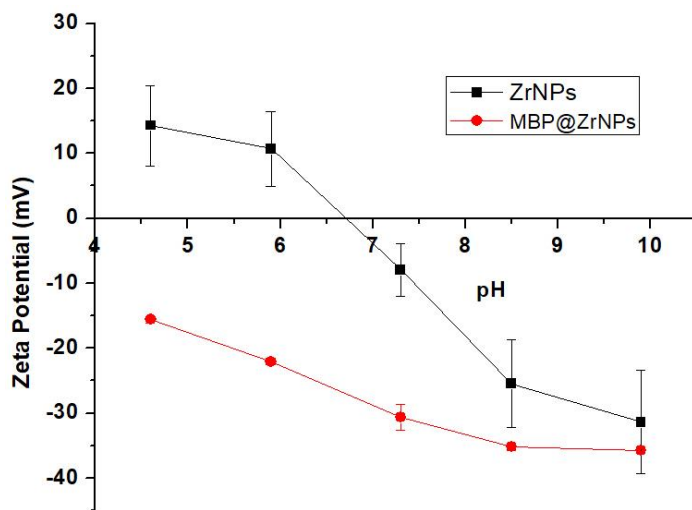
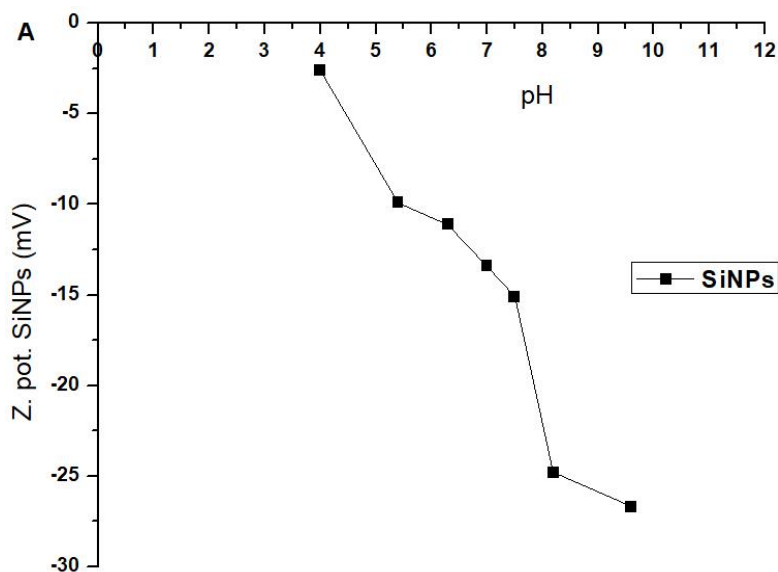


Figure 4.47: Z Potential Measures of the ZrNPs pre- and post-interaction with MBP

pH	Zeta P. SiNPs (mV)
4.0	-2.6
5.4	-9.9
6.3	-11.1
7.0	-13.4
7.5	-15.1
8.2	-24.8
9.6	-26.7



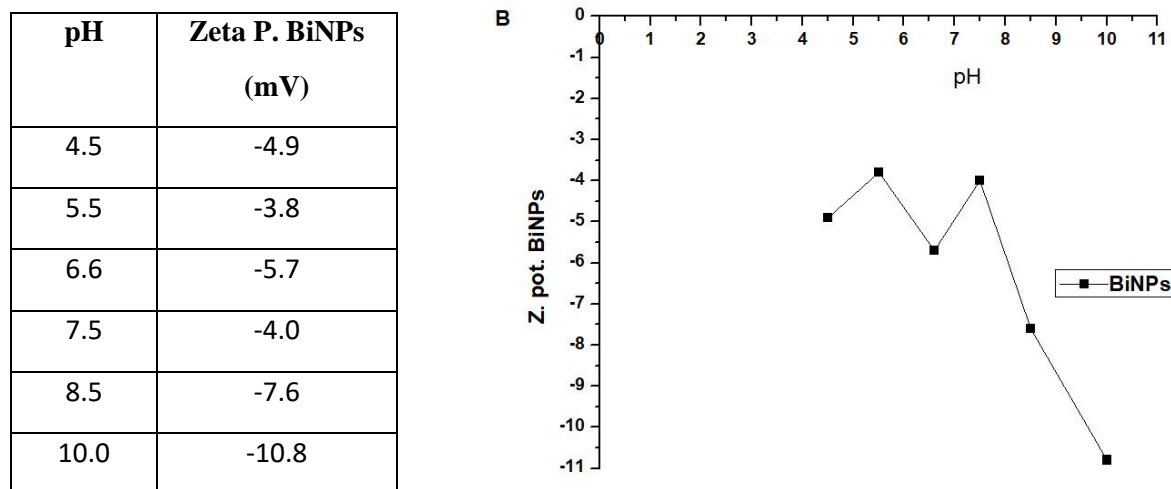


Figure 4.48: Z Potential Measures related to (A) SiNPs and (B) BiNPs

For the other tested media, the electrostatic hypothesis does not find any evidence: silica and bismuth nanoparticles, as shown in the graphs in Figure 3.48, both at acidic pH and at basic pH are characterized by negative surface charges (potential Z negative) and the electrostatic interaction between MBP and NPs is in principle hindered. The oxides analyzed, however, differ in their chemical composition: the metallic character of zirconium and bismuth has properties that are dissimilar to silicon, which being a non-metal can establish links and types of interactions that are certainly weaker such as hydrogen bonds and not as strong as those coordinated between the oxygenates of the BPs and ZrO_2 or Bi_2O_3 .

4.3.1 Zirconium oxide

The surface structure of zirconium oxide has multiple acid / base characteristics determined by the substituents binding the Zr atom (IV). This oxide possesses Lewis and Brønsted acid sites capable of coordinating the phosphonic groups of the organic molecules under examination forming stable structures. The Brønsted acid sites are defined by highly polarized surface hydroxyl groups capable of transferring H^+ while those of Lewis are co-ordinarily unsaturated cationic sites that can interact with other molecules in solution receiving a pair of electrons in unoccupied orbitals (in the case of zirconium the orbitals "D" are empty). The phosphonic functions present in the anionic form in the molecules under examination being strong Lewis bases can form covalent bonds with the zirconium atoms and hydrogen bonds with the surface hydroxyl groups (Figure 4.49).

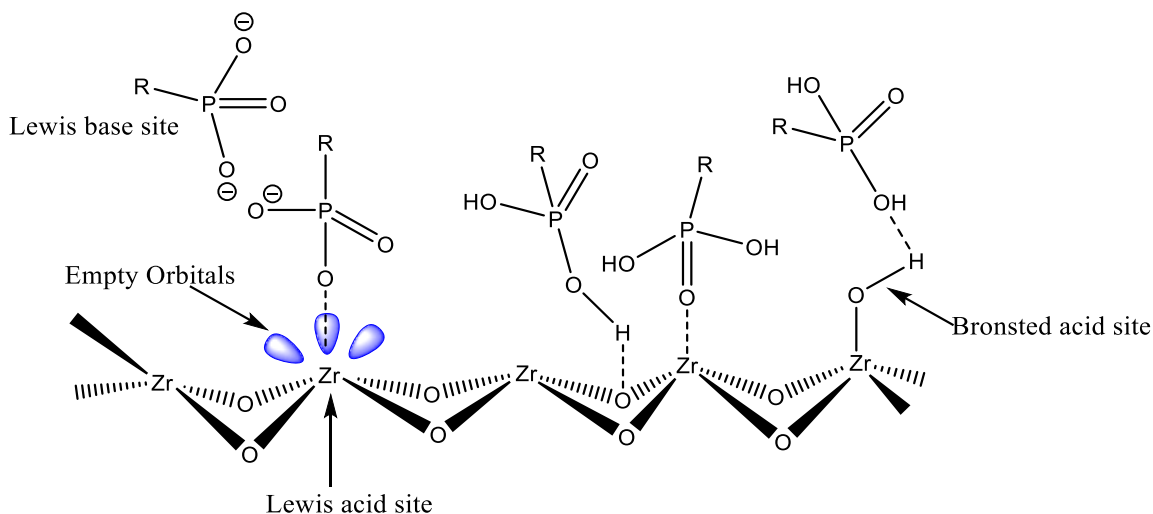


Figure 4.49: Graphical representation of the surface structure of the ZrNPs and of the possible bonds formed with the phosphonic functions

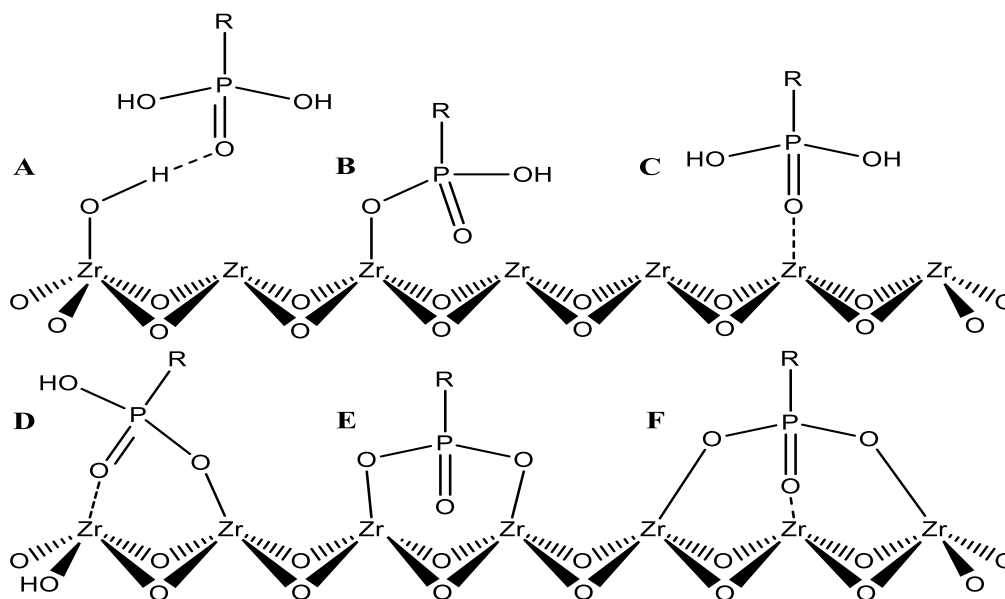


Figure 4.50: Graphical representation of the possible interactions between ZrNPs and phosphonic units: (A) physisorption; (B), (C) monodentate; (D), (E) Bidentate; (F) Tridentate

The extent of the interaction between the species depends on the type of coordination: in fact, the phosphonic group can adsorb on the surface as a monodentate bidentate, bidentate or tridentate or physisorption (weak bonds) (Figure 4.50). These structures are differentiated by adsorption energy (less for tridentate and greater coordination for monodentate) and geometry (length of the support lattice bonds). The tridentate adsorption carried out by a single phosphonic unit is energetically disadvantaged because the bonding distance between three coordinatively unsaturated zirconium atoms is very wide while the other two structures are both admissible

(results found in the literature [259]). The operating pH directly affects the number of functional groups that interact with the support: in agreement with the pKa found experimentally, in an acid environment two hydroxyl groups of the MBP can be de-protonated and coordinate two atoms of Zr (IV). However, as the pH increases, a competitive inhibition of the Lewis acid sites occurs due to the hydroxide ions present in the solution with the consequent decrease in the percentage of loading and formation of surface hydroxyl groups. Moreover, in basic conditions, hydrolysis of the ester bond between phosphonic function and support may occur. Together with these balances, hydrogen bonds can be established between the phosphonic groups and the functionalities present on the oxide surface through the coordination of the P=O oxo-group with the Brønsted acid sites of the surface support (OH) and with the hydroxyl groups of a vicinal phosphonic acid (intermolecular bond), thus stabilizing the formed system. The types of interaction and the involved hypothetical balances are summarized in Figure 4.51.

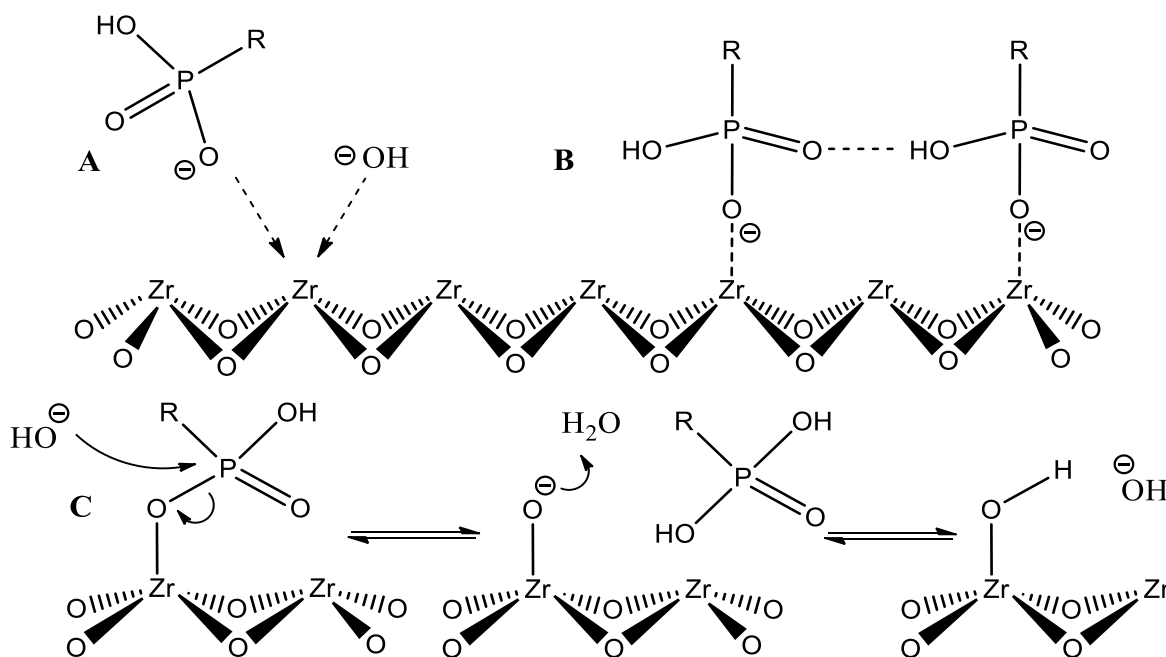


Figure 4.51: ZrNPs-phosphonic unit interaction: (A) competition with the OH⁻ in solution; (B) hydrogen bonds between neighborhood units; (C) basic hydrolysis of the ester bond.

4.3.2 Bismuth oxide

The Bi (III), despite expressing in some of its compounds a basic character, if linked to atoms or functional electronegative groups can show a weak Lewis acidity. The origin of this acidity can be justified based on the bonding models between metal and binder where there is the interaction between the σ^* bismuth orbital with the ligands [260]. This property gives oxide similar characteristics to zirconia such as the influence of pH on the types of coordination. The crystalline structure of bismuth oxide is not clearly defined, and many models have been proposed over the years. Sillén, following diffraction measurements, predicted two types of coordination of oxygen atoms around bismuth: one metallic atom is penta-coordinated while

follows a penta-coordinated intermediate transition state with the subsequent removal of a previously bound water molecule or organic acid. Such reactions are favored or not by the type of outgoing groups, their size (speed of hydrolysis increased by substituents that reduce the steric crowding around the silicon atom) and their ability to stabilize the charge of silicon in the transition state (electron-withdrawing character or donor). All the proposed mechanisms are of the SN2 type [263]. In aqueous solvents the phosphonic -P-O-Si- bond is more susceptible to hydrolysis than the same bond established with other oxides [264] and this characteristic has been found experimentally. The types of interaction between a phosphonic function and the surface silanol groups are like those described for zirconium oxide: the functional group can, in fact, operate from a monodentate binder, bidentate or physisorption on the surface of the support.

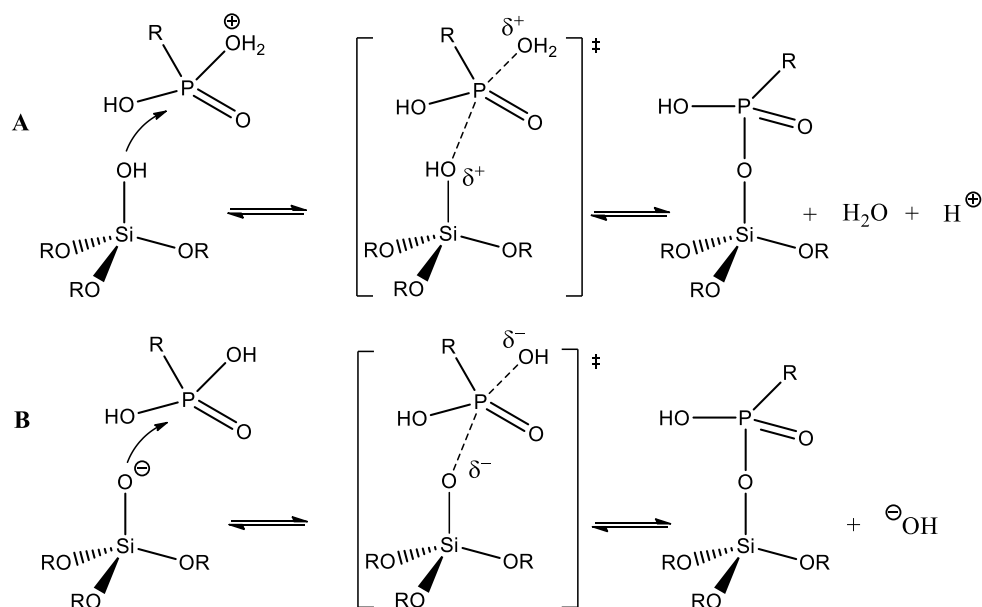


Figure 4.53: Condensing reactions between SiNPs and phosphonic units: (A) in an acid environment; (B) in a basic environment

From the experimental results obtained and described in the previous paragraphs it is possible to hypothesize that the formation of the ester bond by the silanolic hydroxyl unit against phosphonic functionality is less likely than the establishment of weak links, such as hydrogen bonds, between the species under consideration. In the stability tests, in fact, the MBP previously loaded on the nanoparticles has moved completely into solution following the preliminary wash with distilled water, indicating a weak interaction between support and MBP. To better understand the way in which acids and organic compounds in question interact with the supports, characterizing the bonds and the molecular organizations of multi-binder systems can be used by solid state NMR of atoms ^1H , ^{13}C , ^{31}P and ^{29}Si (cross-polarization (CP) and magic

angle spinning (MAS)), in conjunction with IR spectroscopy techniques. It was not possible to use this instrumentation as it was not present at the university where the experimental tests were carried out.

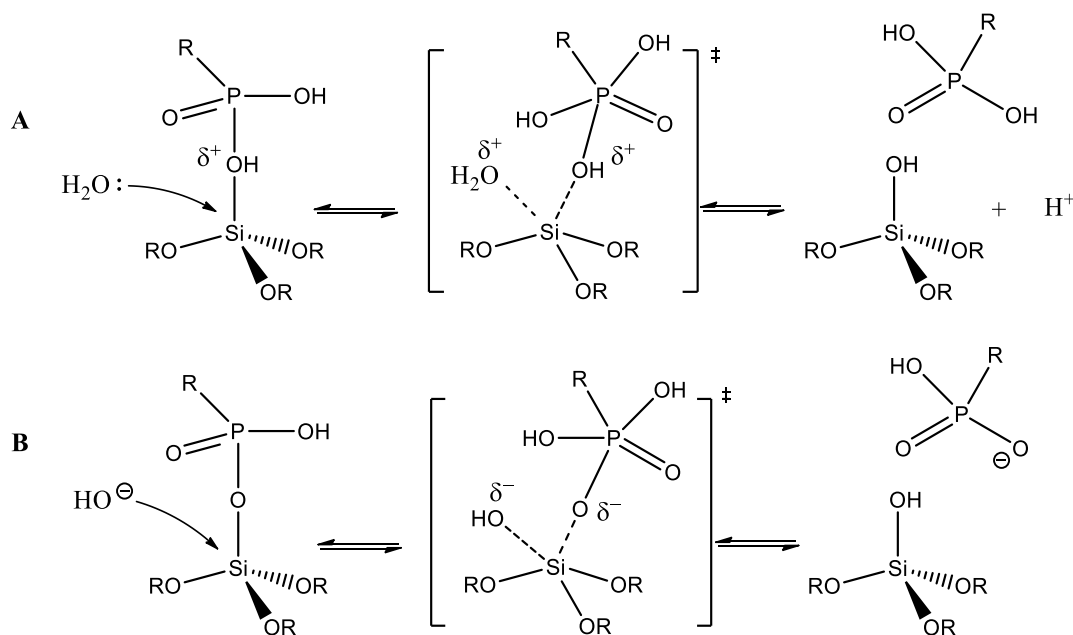


Figure 4.54: Hydrolysis reactions of the ester bond between SiNPs and phosphonic unit: (A) in acidic environment; (B) in a basic environment.

4.4 Study of the interaction between BPs and MPs with ZrNPs for applications in the biomedical field

In order to use in the future the oxides functionalized with bis- and monophosphonic acids in the biomedical field as a drug delivery system or as supports for biological systems, some stability tests have been performed in complex matrices. The experiments were carried out using PBS (Phosphate-buffered saline), a buffer solution with pH 7.2 used in the biological field to simulate an isotonic and blood plasma environment of human origin at the physiological pH. Both substances are characterized by the presence of phosphonic units in solution: the PBS consists of a mixture of saline phosphates such as potassium dihydrogen phosphate (KH_2PO_4) and disodium hydrogen phosphate (Na_2HPO_4) (Tab.24) while in the plasma there are phospholipids, peptides, proteins, salts and macromolecules such as DNA, RNA, which can bind to zirconia nanoparticles and compete with bis- and monophosphonates (Figure 4.55).

Phosphate Buffered Saline (PBS)

Reagents	Concentration (mM)	g / 1L of solution
NaCl	137,0	8,00
KCl	2,7	0,20
Na_2HPO_4	4,3	1,44
KH_2PO_4	1,4	0,25

Table 24 Reagents and composition of the Phosphate Buffered Saline (PBS)

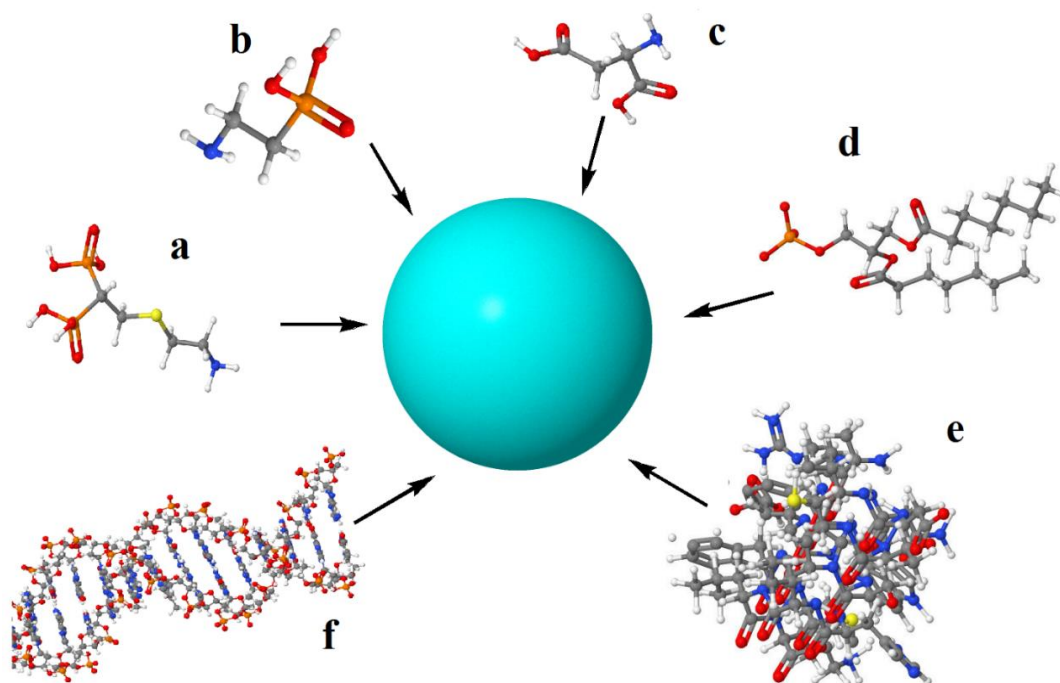


Figure 4.55: Graphical representation of the competition between the organic molecules present in the plasma and the bis- and monophosphonic acids against the ZrNPs (in blue): (a) Bisphosphonic acid, (b) Monophosphonic acid, (c) Amino acid, (d) Phospholipid, (e) Protein, (f) Nucleic acids

Tests have been carried out on BPSC and AFP molecules since the carboxylic functionality present in the side chain, through intermolecular esterification reactions, allows it to be used as a linker of biologically active macromolecules or of particular biological systems. In the same way as described for the determination of the percentage of release of the BPs and MPs in a basic environment for TRIZMA 25mM, four functionalized support rates (50mg) with 10mM BPSC and 10 mM AFP, previously isolated and washed with distilled water, were introduced into PBS and plasma solutions (5mL) respectively. The presence of the analyte in solution was monitored over time by taking 1 ml of solution at 15-30-60-1440-2880 minutes intervals, isolating the supernatant by centrifugation (10 minutes at 12000rcf) and analyzing the solution by quantitative ^1H NMR. with respect to the original solution of the analyte (BPSC 10mM + PBS, BPSC 10mM + plasma, AFP 10mM + PBS, AFP 10mM + plasma). The chemical and chemical-physical characteristics of the plasma, being a complex biological matrix, depend predominantly on the donor. The available plasma samples, identified by letters and numbers for privacy reasons, came from different donors. In order to make the comparison of the obtained experimental results of the respective molecules possible, a single plasma batch was constituted by combining the aliquots in a single solution. From this solution, previously centrifuged (10 minutes at 12000rcf) to eliminate the particulate due to the precipitation of the macro-proteins, the volumes necessary for the analyzes were taken. The presence in solution of organic molecules such as amino acids, carbohydrates, proteins, lipids and vitamins, makes the ^1H NMR spectrum of the plasma, represented in Figure 4.56, a very complex aspect. To determine and quantify the presence of the

molecules under examination, such as BPSC and AFP, it was necessary to resort to a functionality of the integration program of the "Bruker Advance 400" spectrometer to allow the subtraction of the plasma spectrum (white) from the following spectra obtained. The subtraction of the spectra allows the signals of the molecules of BPSC and of AFP to "emerge" with respect to all the other non-characteristic signals, allowing their integration.

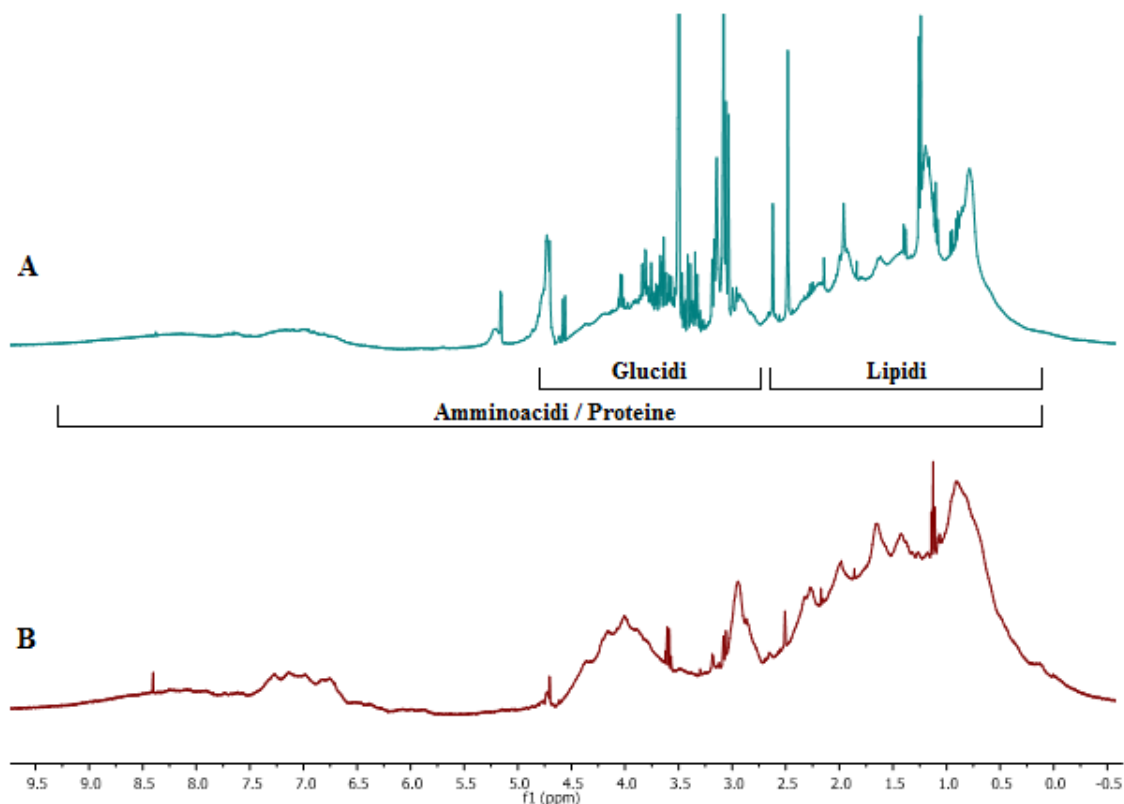


Figure 4.56: ^1H NMR spectra (400MHz, D_2O) of blood plasma in analysis (A) and of a BSA (Bovine Serum Albumine) 1mM (B) solution: the characteristic signals of the amino acids present in the plasma solution determine a greater complexity in the interpretation of the related spectrum. Albumin is the most abundant plasma protein (55%), as shown by the comparison between spectra (A) and (B). In the analytical field the standard derived from bovine serum (BSA) is used as standard

4.4.1 PBS (*Phosphate-buffered saline*)

Comparing the experimental results obtained from the ^1H quantitative NMR analysis of BPSC and AFP molecules in PBS, after a 48-hour time interval (2880 minutes), the release rates show a weak and reversible interaction between the zirconia nanoparticles and the AFP molecule (Figure 4.58, Figure 4.59, Tab.25). The phosphate ions present in the solution intervene in the equilibrium existing between the support and the mono and bis-phosphonic molecules determining the breakdown of the ester bond and the formation of a new phosphate-coordinated species, leading to an increase in the concentration of BP and MP in solution (bis and mono-

phosphonic acid good outgoing group, Figure 4.57). Compared to the results obtained by the analogue bis-phosphorus, the percentage of solution release of the AFP molecule results to be much higher (BPSC 5%, AFP 26%). The lower binding capacity of the AFP molecule in fact, characterized by the presence of only one phosphonic unit, has a significant influence on the equilibrium described above, thus defining a greater quantity of MPs in solution. Experimental tests carried out subsequently introducing the functionalized supports in a 150mM NaCl solution allowed to exclude the influence of the salts contained in the PBS in the equilibrium described above

Buffer	Molecule	Initial Conc. in sol. (mM)	Final Conc. in sol. (mM)	Release %
PBS pH 7.2	BPSC	0	0,53	5
	AFP	0	2,60	26

Table 25 Results related to stability tests for BPs and MPs 10mM-ZrNPs in PBS

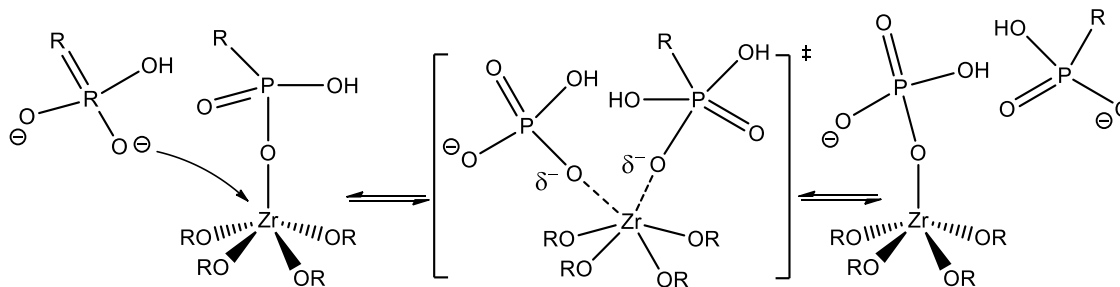


Figure 4.57: Representation of the equilibrium existing in solution between the coordinated phosphonic acid and a hydrogen phosphate molecule

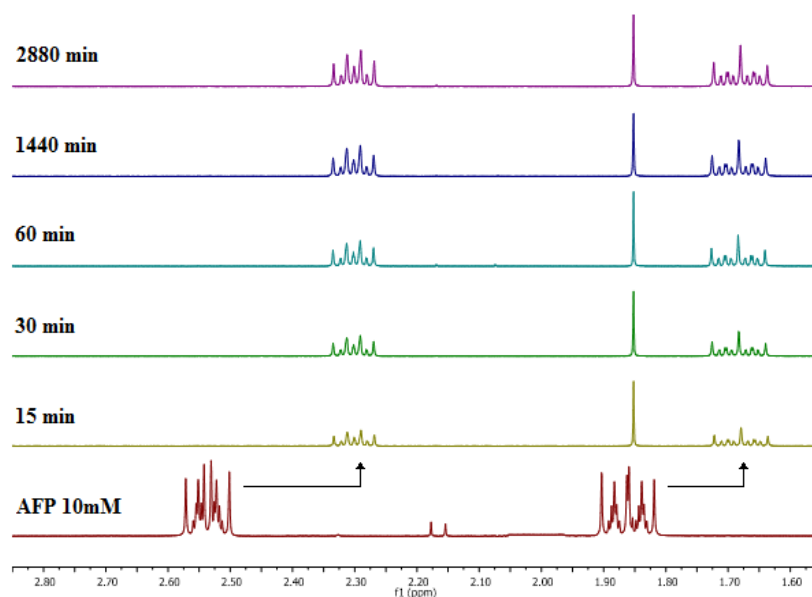


Figure 4.58: Release kinetics relative to the 10mM / ZrNPs AFP molecule in PBS (1H NMR spectra: 400MHz, D2O)

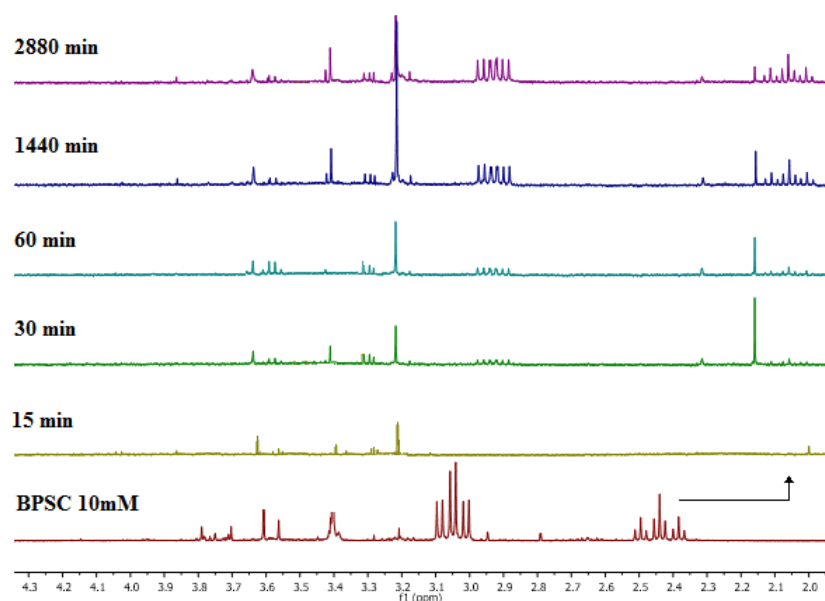


Figure 4.59: Release kinetics relative to the BPS 10mM / ZrNPs molecule in PBS (^1H NMR spectra: 400MHz, D_2O)

4.4.2 Plasma

From the results obtained following the integration of the ^1H NMR signals characteristic of the BPS and AFP molecules, it can be seen that, similarly to what was found in the PBS release tests, the monophosphonic acid in question exhibits a lower binding capacity towards the support correlable to the greater percentage of molecules released in solution in the time interval considered (Figure 4.60, Figure 4.61, Tab.26). In the plasma there are organic molecules such as proteins, nucleic acids and amino acids, which can bind to the zirconia nanoparticles and compete in the equilibrium described in the previous paragraph (Figure 4.57). The size of the organic molecules has a significant influence on this balance: the high steric size in fact, disadvantages the replacement of the molecules of AFP and of BPS from the support. The hydrophobic effect due to the greater length of the BPS carbon chain, compared to the AFP molecule, together with the double phosphonic functionality present, can determine a greater stability, a lower solubility of the molecule in the aqueous environment and a percentage of zero release, validating the results obtained in the release tests in TRIZMA and in PBS (Tab.26). The comparative experiments carried out confirm the greater affinity of bisphosphonic acids with respect to commercial monophosphate analogs in the functionalization and stabilization in biological environments of nanoparticulate supports consisting of inorganic oxides such as zirconia.

Solution	Molecule	Initial Conc. in sol. (mM)	Final Conc. in sol. (mM)	Release %
Blood plasma	BPS	0	0	0
	AFP	0	2,57	26

Table 26 Results related to stability tests for 10mM-ZrNPs BPs and MPs in Blood Plasma

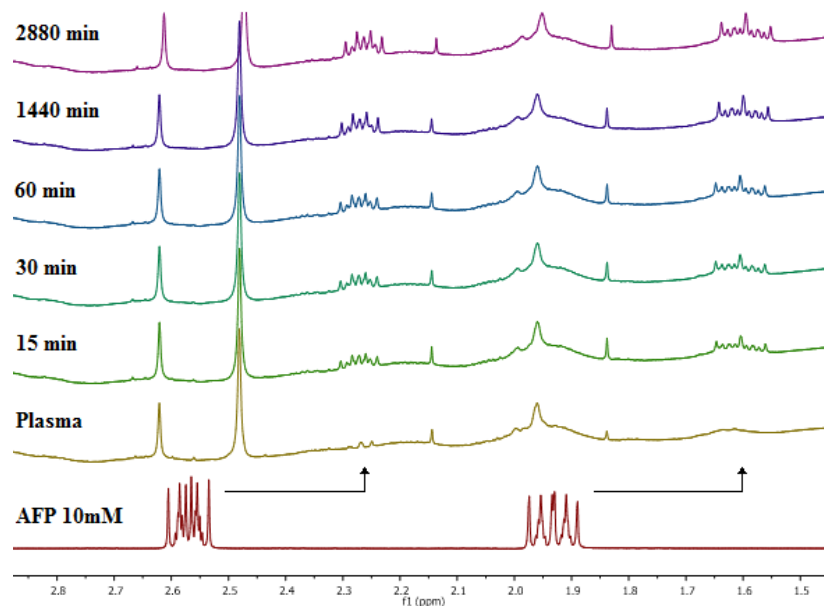


Figure 4.60: Release kinetics related to the AFP 10mM / ZrNPs molecule in plasma (1H NMR spectra: 400MHz, D2O)

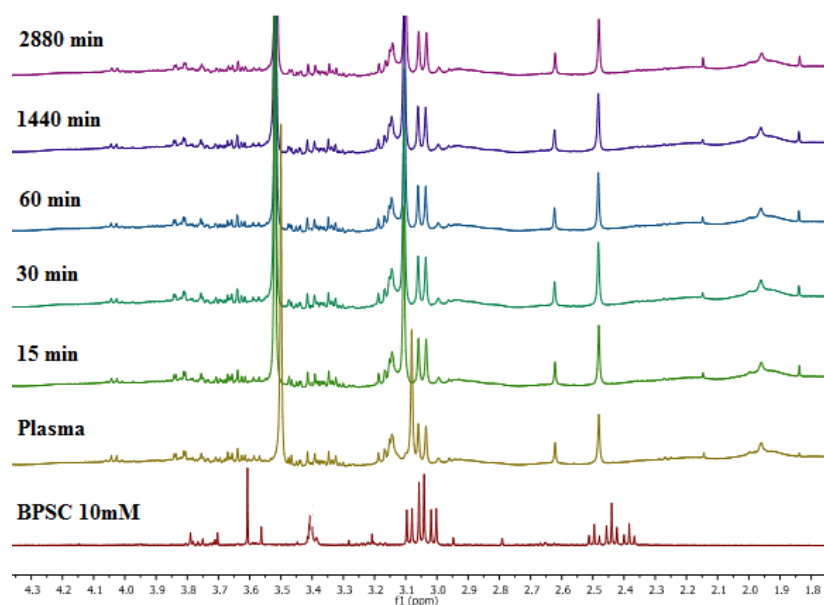


Figure 4.61: Release kinetics relative to the BPMC 10mM / ZrNPs molecule in plasma (1H NMR spectra: 400MHz, D2O)

Molecule	Release %		
	TRIZMA pH 8.8	PBS pH 7.2	Blood Plasma
BPSC	0	5	0
AFP	24	26	26

Table 27 Table comparing the BPSC and AFP molecules in the different solutions tested

4.5 Use of plasma components such as DDS

Blood plasma is a complex matrix consisting of 90% of water, 8% of proteins, 1.1% of organic components and 0.1% of inorganic salts. The protein component in turn sees albumin as the predominant macromolecule (~ 60%) followed by globulins and fibrinogen. Albumin is a multifunctional protein with an extraordinary binding capacity: this property makes it a vector of a wide range of metabolites, drugs, nutrients, metals and many other molecules with clinical, pharmaceutical and biochemical applications [265]. To this end, some experimental tests were carried out in order to ascertain the carrier properties of the main plasma protein component with respect to methyl bis-phosphonic acid and two biologically active molecules belonging to different pharmaceutical classes, in order to use this macromolecule as drug delivery systems. The tests performed saw the use of 0.1mM, 0.5mM and 1mM solutions of BSA (bovine serum albumin, Figure 4.62) to which 100mM of NaCl were added to maintain the osmolarity of a physiological solution. Non-quantitative determination of the interaction between the species was performed by ^1H NMR spectrometry.

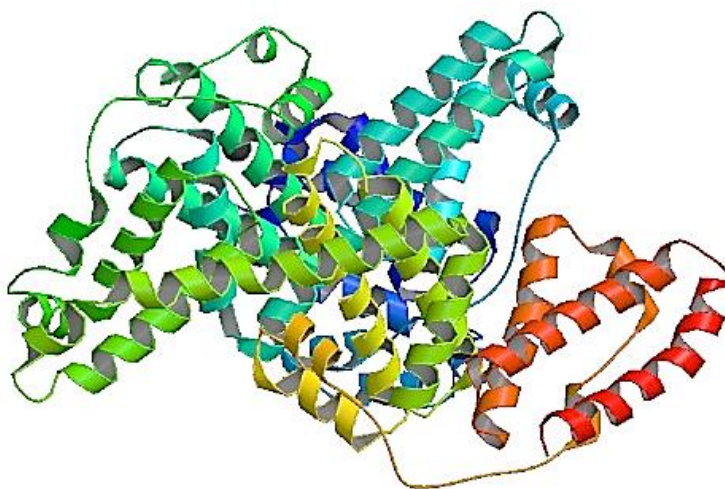


Figure 4.62: Tertiary structure of bovine serum albumin (BSA)

4.5.1 Methylene bis-phosphonic acid

The amount of MBP added to the BSA solutions analyzed is 1mmole / L. The experimental spectra shown in Figure 4.63 show that as the BSA concentration increases, the MBP signal decreases, defining a possible coordination between the bis-phosphonic acid and the biological macromolecule. Furthermore, the signal of the methylene bis-phosphonic acid undergoes a shorter ppm shift, confirming this hypothesis. The type of interaction can be of an electrostatic nature (through protein functional groups) through the formation of hydrogen and coordinate bonds, or mechanics (in the three-dimensional protein structure).

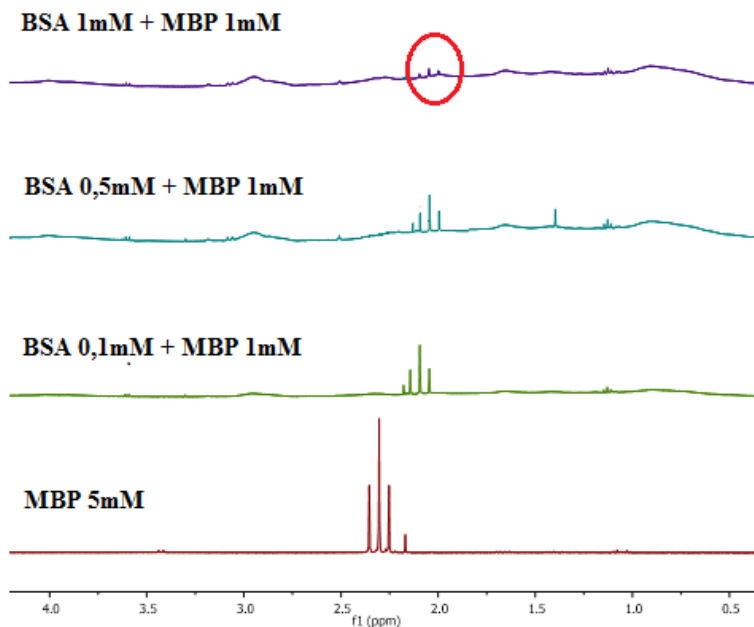


Figure 4.63: Analysis of the BSA-MBP 1mM interaction (1H NMR spectra: 400MHz, D2O)

4.5.2 *Indomethacin and Nitrofurantoin monohydrate*

The molecules with biological activity used in these experimental tests are indomethacin and nitrofurantoin monohydrate, active ingredients of two drugs belonging to different pharmacological categories. Indomethacin (Figure 4.64) is a non-steroidal anti-inflammatory agent (NSAID) with analgesic and antipyretic activity. The pharmacological effect is manifested through the inhibition of the enzyme cyclooxygenase, an enzyme responsible for the synthesis of prostaglandins responsible for inflammation and pain. Nitrofurantoin (Figure 4.65), on the other hand, has a bacterial or bacteriostatic antibiotic action in the body depending on the dose administered. Pharmacodynamics to date has not been clearly defined: the drug, activated within the bacterial cell by the reducing action of flavoproteins, intervenes by damaging ribosomal proteins, bacterial DNA and other macromolecules. The interaction of these molecules with albumin has been verified through the addition of 1mg of the respective drugs to solutions with increasing BSA concentration.

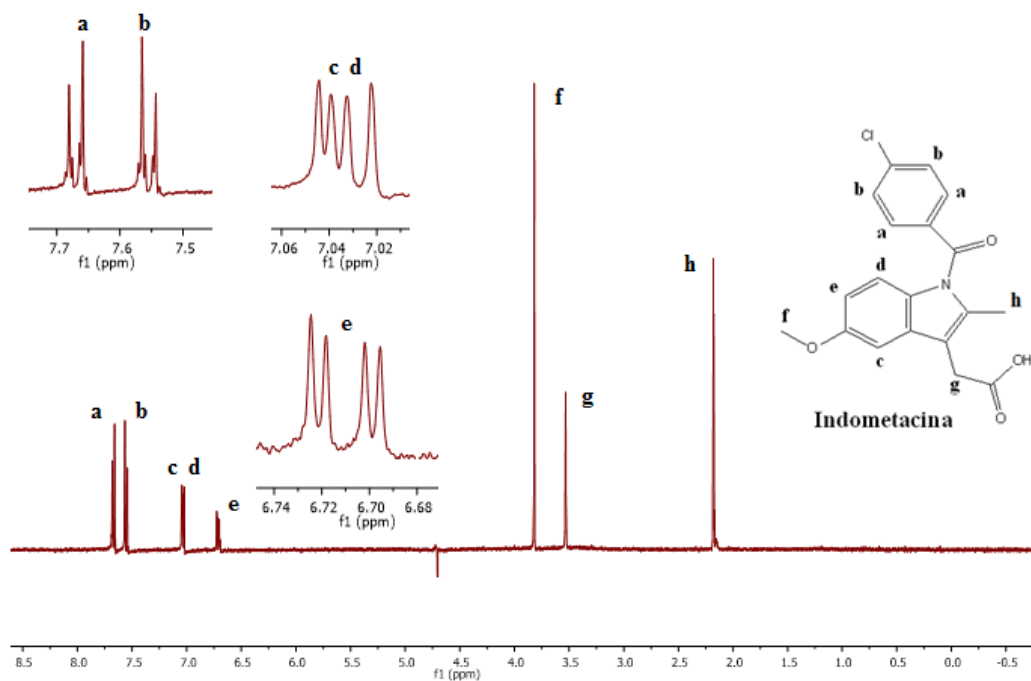


Figure 4.64: ^1H NMR spectrum Indometacin (400MHz, D_2O): multiple manifolds at 3.58ppm and 1.11ppm attributable to diethyl ether impurities

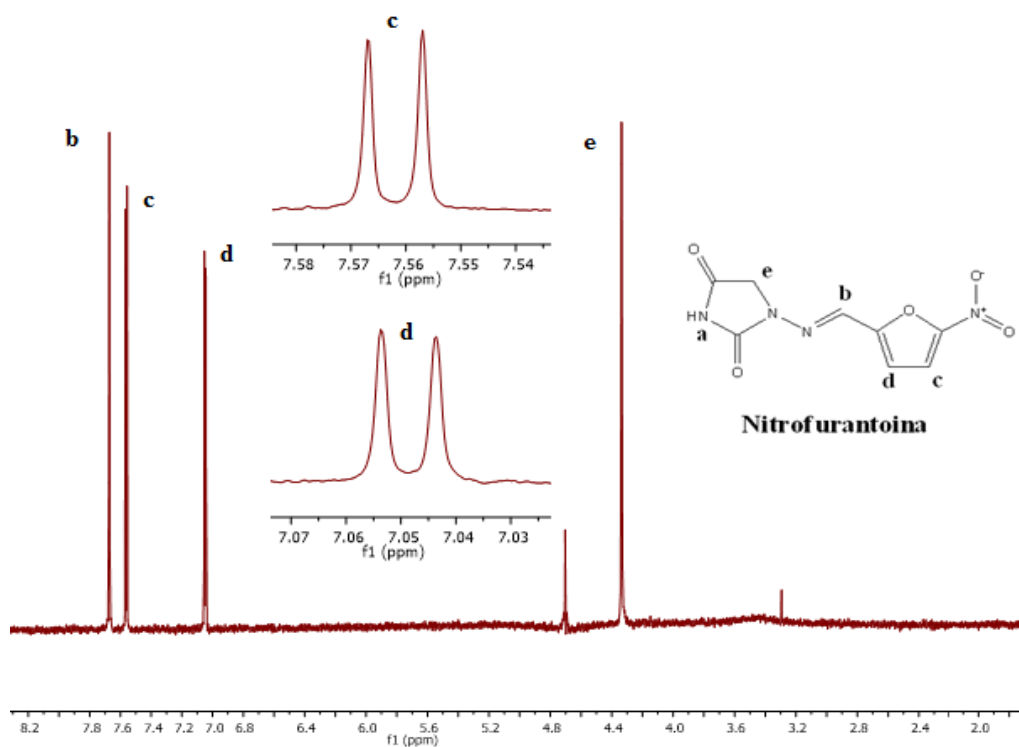


Figure 4.65: ^1H NMR spectrum Nitrofurantoin monohydrate (400MHz, D_2O): the proton (a) is not viewable due to the rapid exchange with the protons of the water present in solution

From the ^1H NMR spectra (Figure 4.67, Figure 4.68) it is possible to ascertain the extent of the coordinating force of the BSA in relation to the active ingredients under examination: a concentration of BSA equal to 0.1mM and 0.5mM is enough to not allow the identification of the characteristic NMR signals of indomethacin and of nitrofurantoin monohydrate in the ^1H NMR spectrum. Considering that the concentration range of this protein in humans is 35-55g / L, or 0.5-0.8mM, the molecule completely interacts with the pharmaceutical solutions used, effectively conveying the active ingredients within the body. To decrease the effect of first-pass in the case of enteral administration, the drugs can be conveyed using inorganic nanoparticulate supports and such structures, in turn, can interact with the biological components of the organism. In conjunction with the experimental tests described above, tests were carried out to highlight a possible interaction between zirconia, silica (most commonly used oxides in the clinical field as DDS) and BSA. In different vials, 10 mL of support were added to 1mL of a solution of BSA 1mM and NaCl 100mM and the whole was stirred for a time interval of 24h by magnetic stirrer (600rcf). At the end of this interval the suspensions were centrifuged at 12000rcf for ten minutes and the supernatant analyzed by ^1H NMR. From the spectra shown in Figure 3.69 it is possible to notice that the signal related to the protein macromolecule did not undergo any decrease in intensity or shift following the addition of the NPs, an indication of the non-interaction between BSA and support.

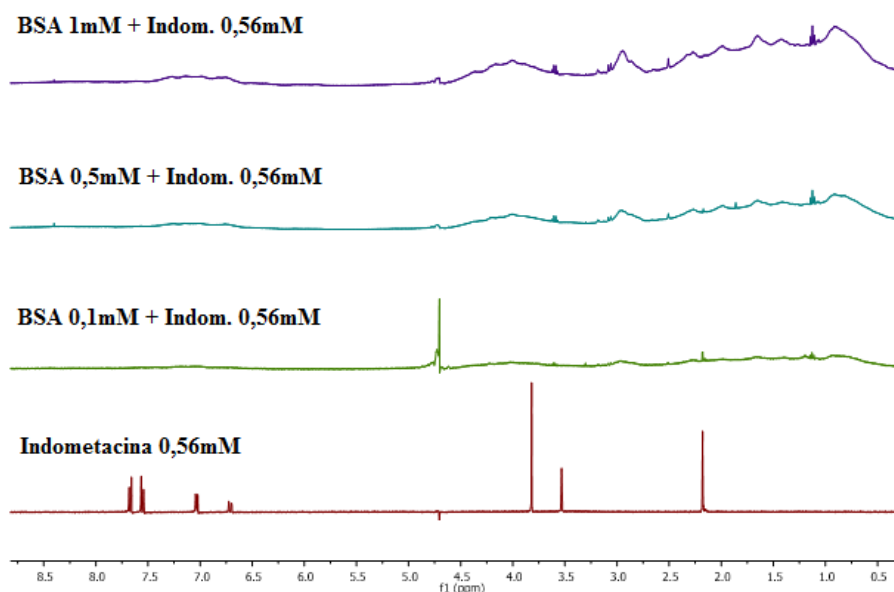


Figure 4.67: Analysis of the BSA-Indomethacin interaction (^1H NMR spectra: 400MHz, D2O)

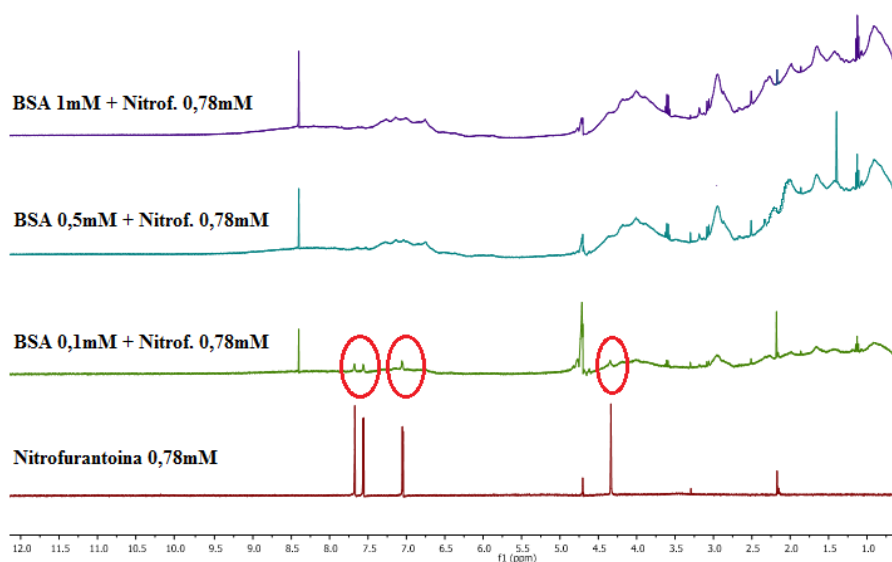


Figure 4.68: Analysis of the BSA-Nitrofurantoin interaction (^1H NMR spectra: 400MHz, D₂O)

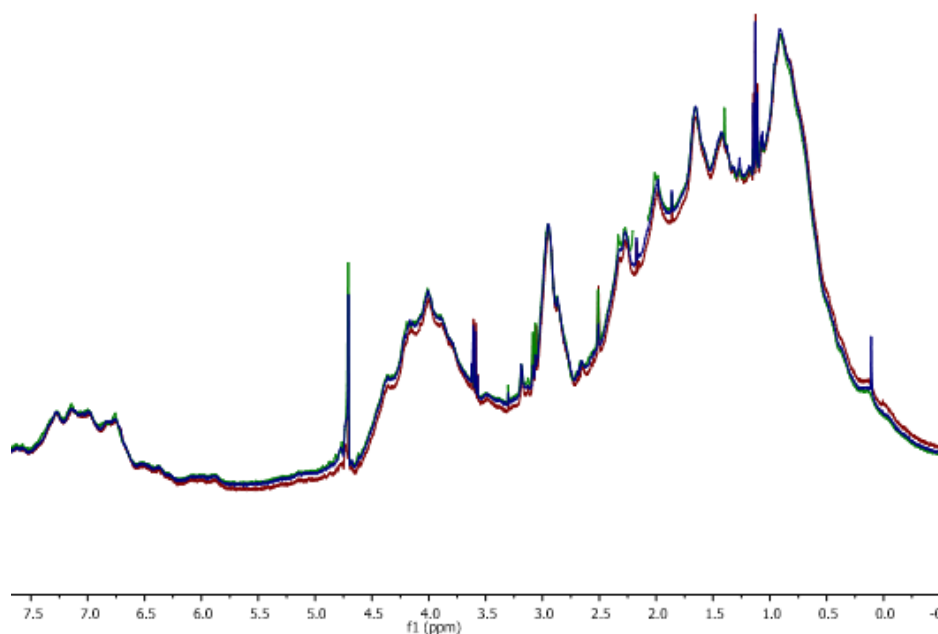


Figure 4.69: BSA-support interaction: (red) BSA 1 mM; (blue) ZeNOs-BSA 1mM; (green) SiNPs-BSA 1mM.

4.6 Study of the loading and release in aqueous solution of drugs from ZrNPs and SiNPs through quantitative ^1H NMR analysis

In order to use the nanoparticulate oxides previously studied as drug delivery systems of numerous categories of drugs, the mechanism of release in aqueous solution of indomethacin and of nitrofurantoin monohydrate previously loaded on NPs has been studied through different

processes: in supercritical CO₂ and in acetone deuterated (nitrofurantoin monohydrate only in deuterated acetone). The determination of the release percentage in solution was carried out by suspending 10 mg of support loaded in 10 ml of deuterated water maintaining the system under stirring (350rpm). To monitor the concentration of drug in solution, some aliquots were taken in an overall time interval of 1440 minutes (24h), isolating the supernatant by centrifugation (10 minutes at 12000 rcf) and analyzing it by quantitative ¹H NMR with respect to a solution of active substance at known concentration (2 mg of drug in 10 ml of D₂O). The type of loading and support used, as shown by the experimental results reported below, greatly influence the amount of drug loaded and released in solution.

4.6.1 Indomethacin

The supercritical CO₂ loading procedure of indomethacin on the supports under test was performed by introducing 100 mg of NPs and 2 mg of the drug into an autoclave. Subsequently, the carbon dioxide was added to the system until a pressure of 160 bar and a temperature of 34 °C were reached, to reach critical conditions. The drug and the NPs were stirred for a time interval of 12 hours and finally isolated by making carbon dioxide escape at the end of this interval. The samples related to the indomethacin loading in supercritical CO₂ were suspended in 10 ml of D₂O and tested following the procedure described in the previous paragraph. As can be seen from the spectra shown in Figure 4.70 and Figure 4.71 and from the experimental results (Tab.28), the release of indomethacin from SiNPs and from ZrNPs is a relatively fast process. About the quantity of drug loaded (25mg / 100mg support) equal to 2.5mg / 10mg of NPs tested, considering the experimental error, the silica is characterized by the complete release of the active substance while the zirconia, in the time interval of 60 minutes, reaches 92%. The tests conducted using the zirconia nanoparticles, however, show the partial decomposition of indomethacin in solution, confirmed by the splitting of all the characteristic ¹H NMR signals after 60 minutes from the suspension in solution. Following the GC-MS analysis (Figure 4.72, Figure 4.73) performed on the aliquot taken after 1440 minutes from the beginning of the test, extracting the sample in ethyl acetate, it was possible to attribute the new resonances to the acid molecule p-chlorobenzoic acid and the relative indole fragment deriving from the hydrolysis of the amide bond present in the molecule (Figure 4.76). The Lewis acid character of zirconium oxide (Lewis acid) is probably the cause of this decomposition which hydrolyzes the weaker site of the molecule on the amide group. These hypotheses are confirmed by the fact that the same molecule loaded on SiNPs, while showing a higher release rate, shows no decomposition (Figure.4.74, Figure.4.75).

Support	Time (min)	Indo. in solution (mM)	% release
ZrNPs	1440	0,15	21
SiNPs	1440	0,73	100

Table 28 Experimental results related to the release in CO₂ of Indomethacin / NPs in D₂O

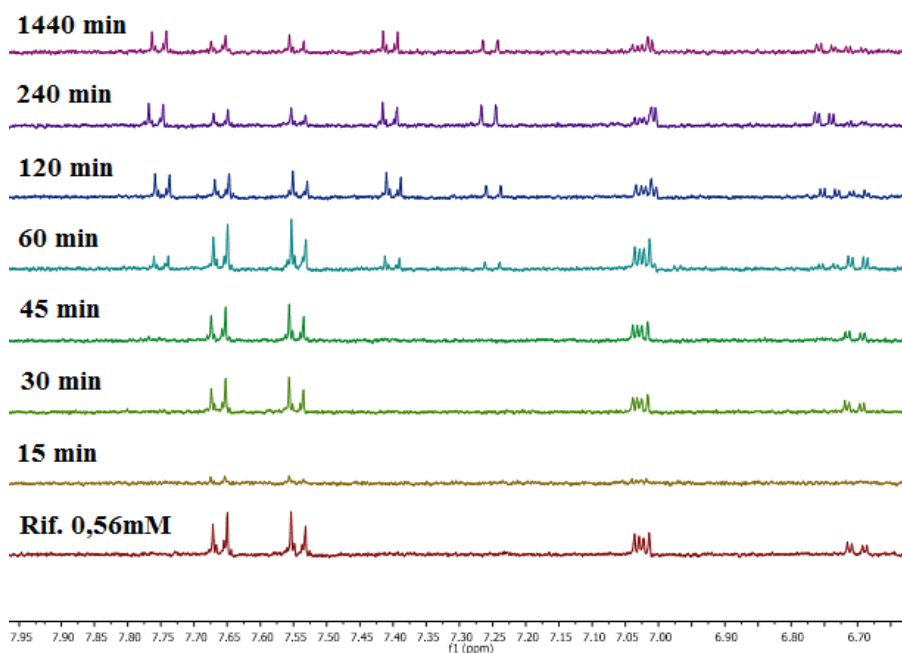


Figure 4.70: Kinetics of release in H_2O Indomethacin / ZrNPs loaded in supercritical CO_2 : ^1H NMR spectra (400MHz, D_2O) with reference to aromatic protons

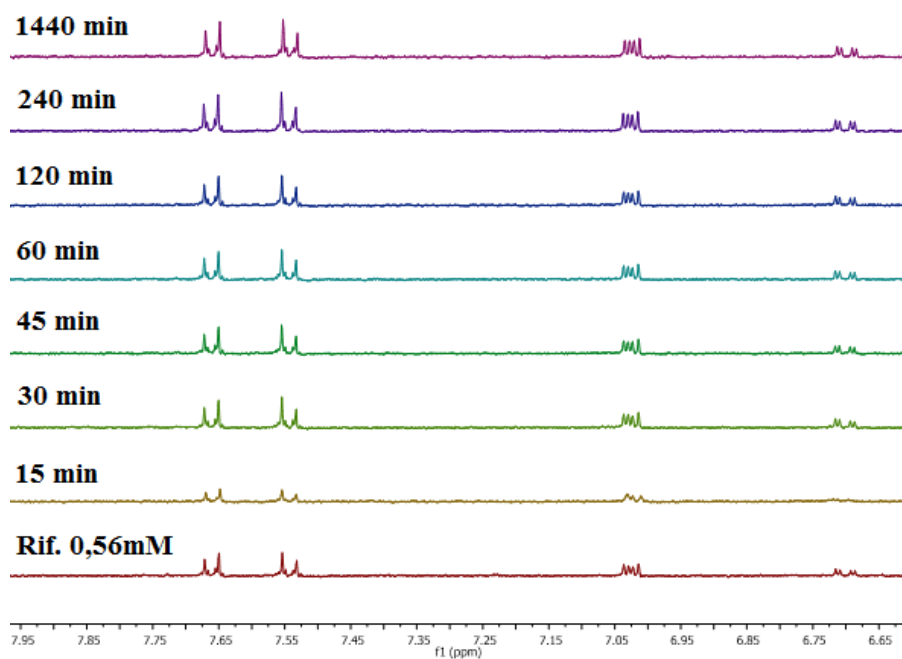


Figure 4.71: Release kinetics in H_2O Indomethacin / SiNPs loaded in supercritical CO_2 : ^1H NMR spectra (400MHz, D_2O) with reference to aromatic protons

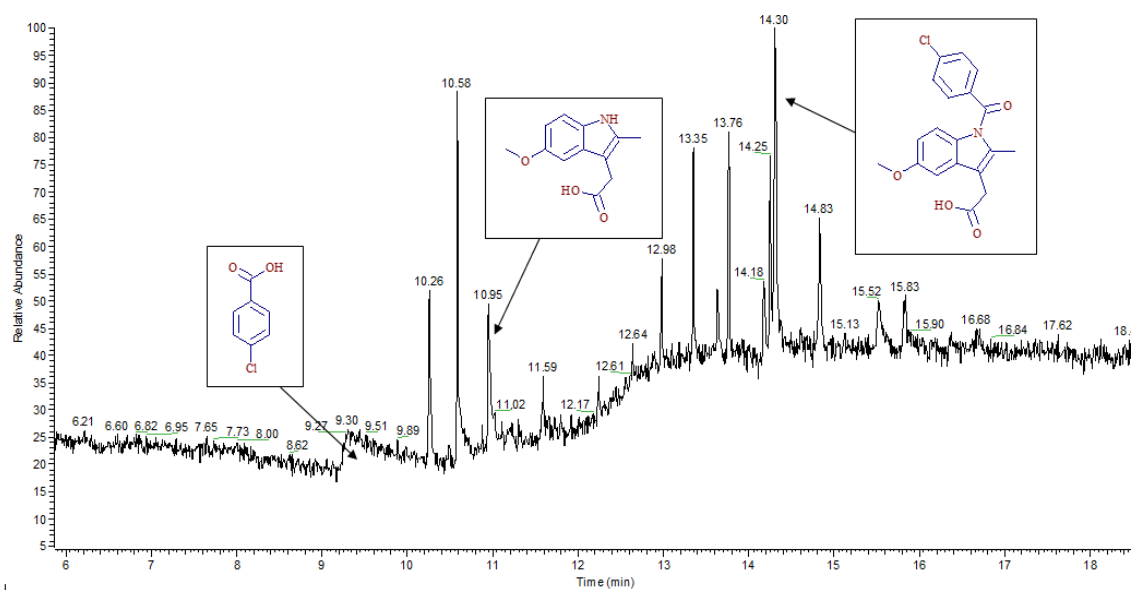


Figure 4.72: Chromatogram relating to the Indomethacin / ZrNPS sample in supercritical CO₂ 1440min

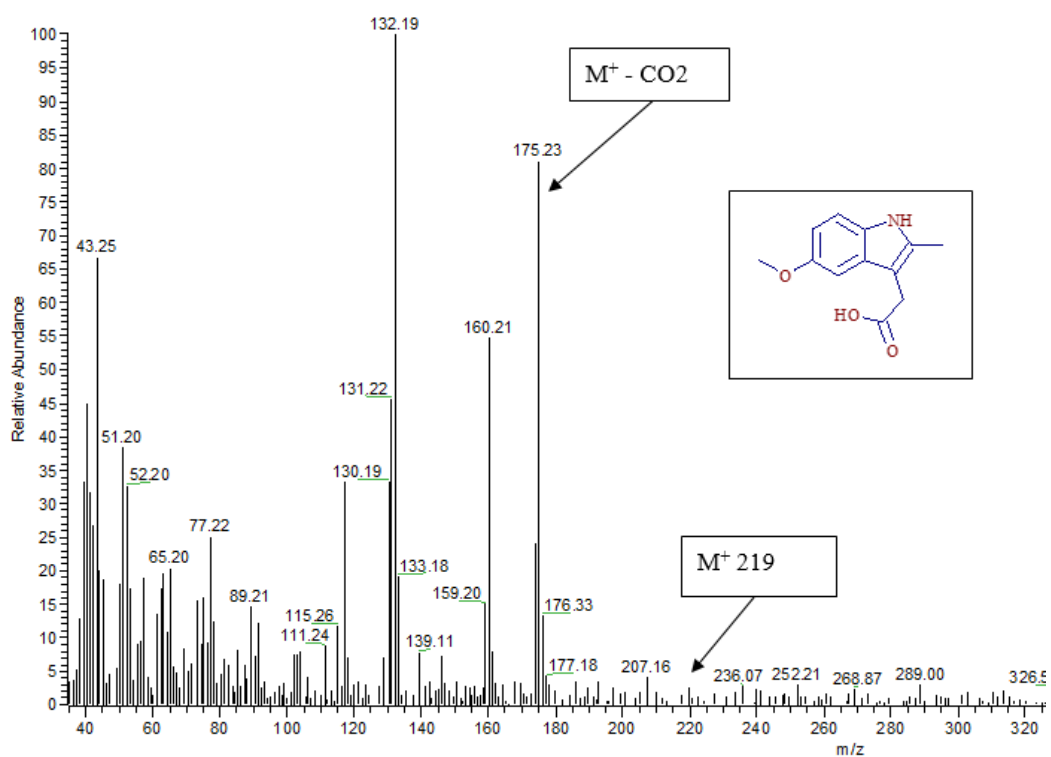


Figure 4.73: Mass spectrum relative to indole fragment deriving from the hydrolysis reaction of the drug (sample Indomethacin / ZrNPS in supercritical CO₂ 1440min)

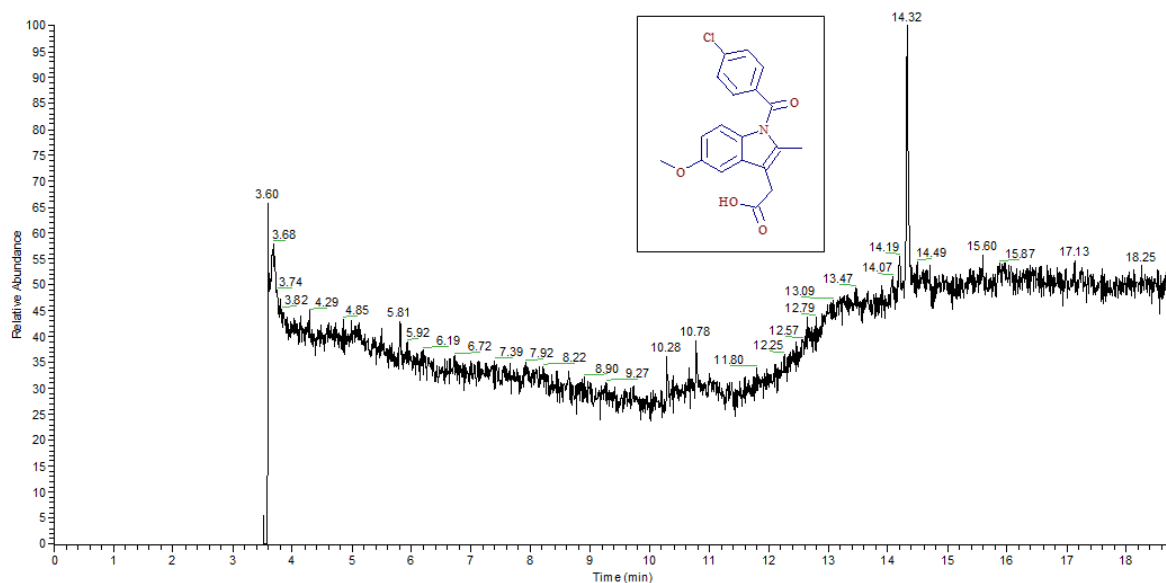


Figure 4.74: Sample chromatogram Indomethacin / SiNPS in supercritical CO₂ 1440min

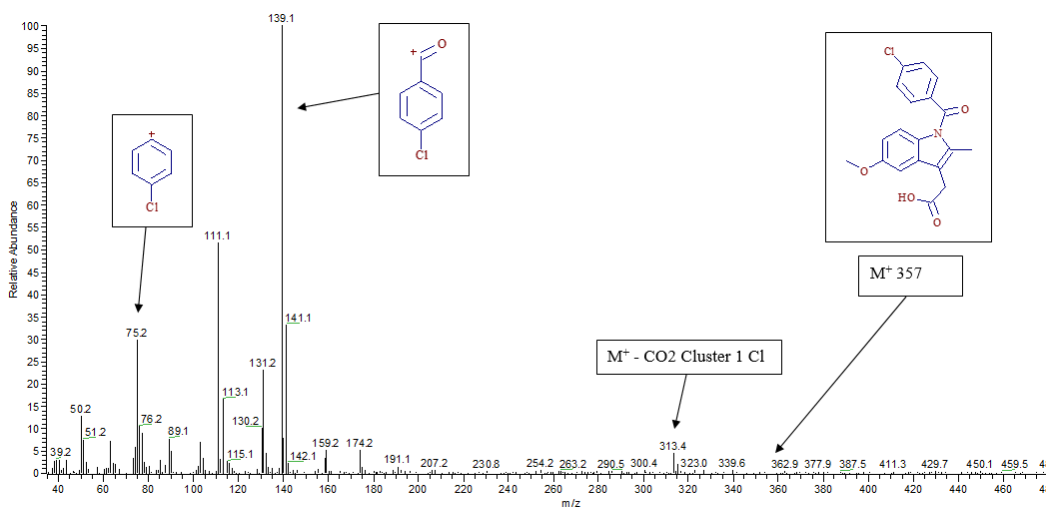


Figure 4.75: Mass spectrum relative to the Indomethacin / SiNPS sample in supercritical CO₂ 1440min

The same molecule, loaded on both supports under examination using deuterated acetone as solvent, has provided different results in terms of release percentages in solution. The loading phase of the active ingredient was carried out by adding a suspension consisting of 1ml of distilled water and 50mg of nanoparticles to a solution consisting of 100mg of indomethacin and 19ml deuterated acetone. After 12h of stirring, the NPs were isolated by filtration and an aliquot of 10mg of functionalized support was used in the tests. Zirconia, similarly to what is shown in the loading with supercritical CO₂, catalyzes the hydrolysis reaction of the amide bond. This

behavior can be seen from the first minutes of the suspension in solution of the ZrNPs, an index of a possible hydrolysis of the drug during the loading phases and a subsequent physisorption of the fragments on the surface of the NPs (Figure 4.77, Figure 4.81). In contact with the aqueous solvent the p-chlorobenzoic acid and indole molecules can transfer from the support into solution and the desorbed and not yet hydrolyzed drug can react with the active surface of the nanoparticles. The silica does not show any catalytic behavior but is characterized by a decrease in the percentage of release from 100% to 2% found in Figure 4.78. To verify if the loading of the drug on the supports has been quantitative, through analysis ^1H NMR the concentration of analyte was determined before and after the loading procedure in deuterated acetone. The analysis through the "ERETIC" functionality highlighted, within the errors on the measurements, a null load for both supports, that is a quantity of active principle that is minimal and can not be determined with accuracy (Figure 4.79, Figure 4.80). This result indicates a weak interaction between NPs and the drug. The percentages of release reported in Tab.29 were calculated assuming, for a 100% loading, a quantity of drug loaded equal to $5.3 \times 10^{-3} \text{ mmol} / \text{mg}$ of support ($1.9 \text{ mg} / \text{mgNPs}$).

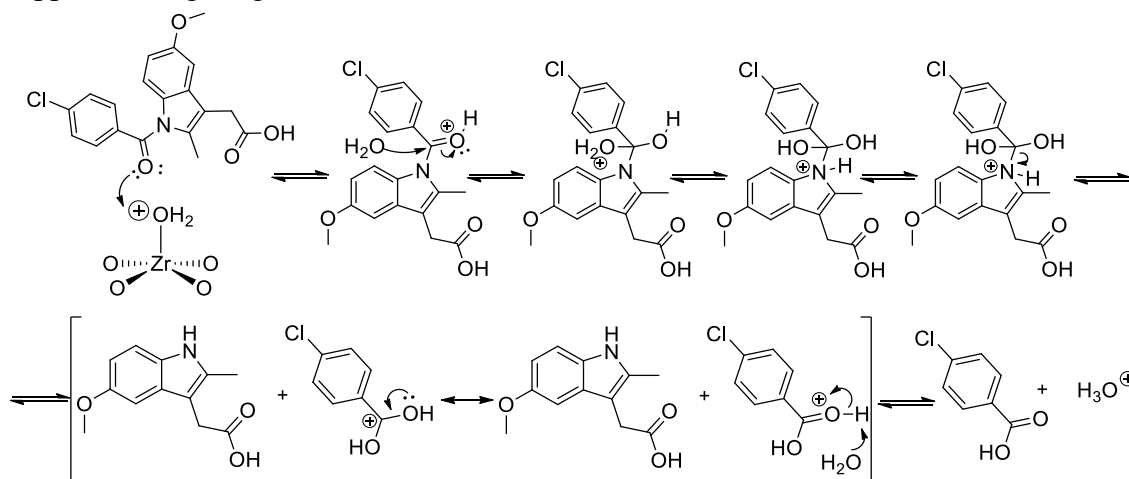


Figure 4.76: Reaction of acid hydrolysis of the amide bond of Indometacin following interaction with ZrNPs

Support	Time (min)	Indo. in solution (mM)	% release
ZrNPs	1440	0,52	10
SiNPs	1440	0,13	2

Table 29 Experimental results related to the release in D₂O of Indometacin / NPs loaded into deuterated acetone

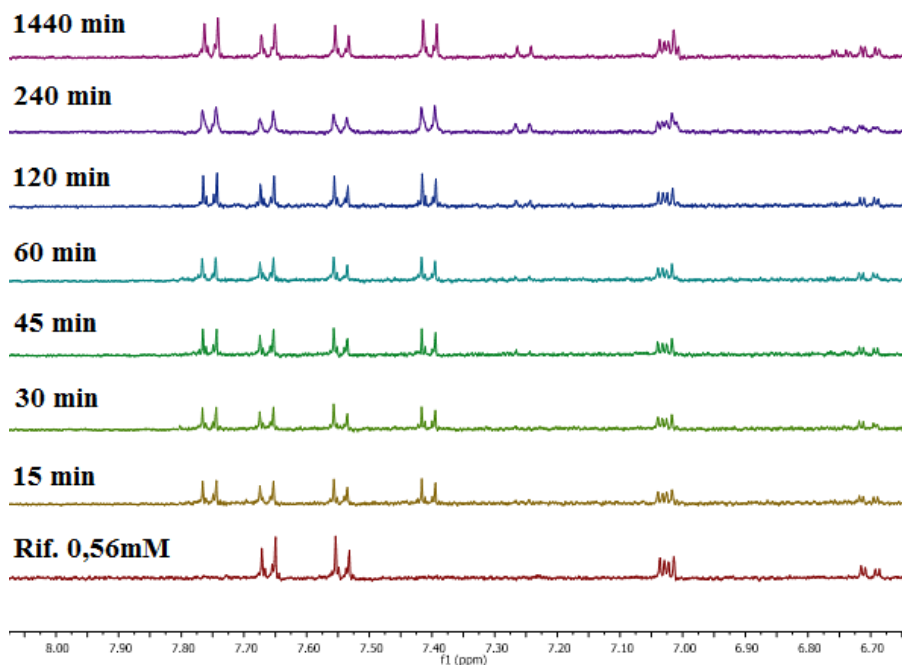


Figure 4.77: Kinetics of release in H₂O Indometacin / ZrNPs loaded in acetone: ^1H NMR spectra (400MHz, D₂O) with reference to aromatic protons

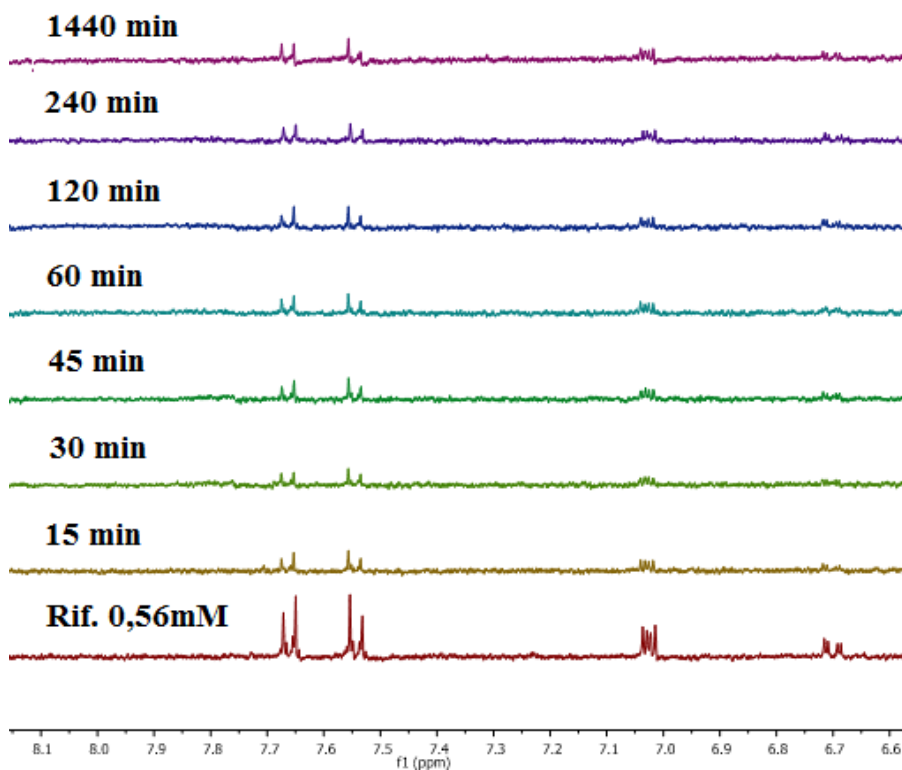


Figure 4.78: Kinetics of release in H₂O Indometacin / SiNPs loaded in acetone: ^1H NMR spectra (400MHz, D₂O) with reference to aromatic protons

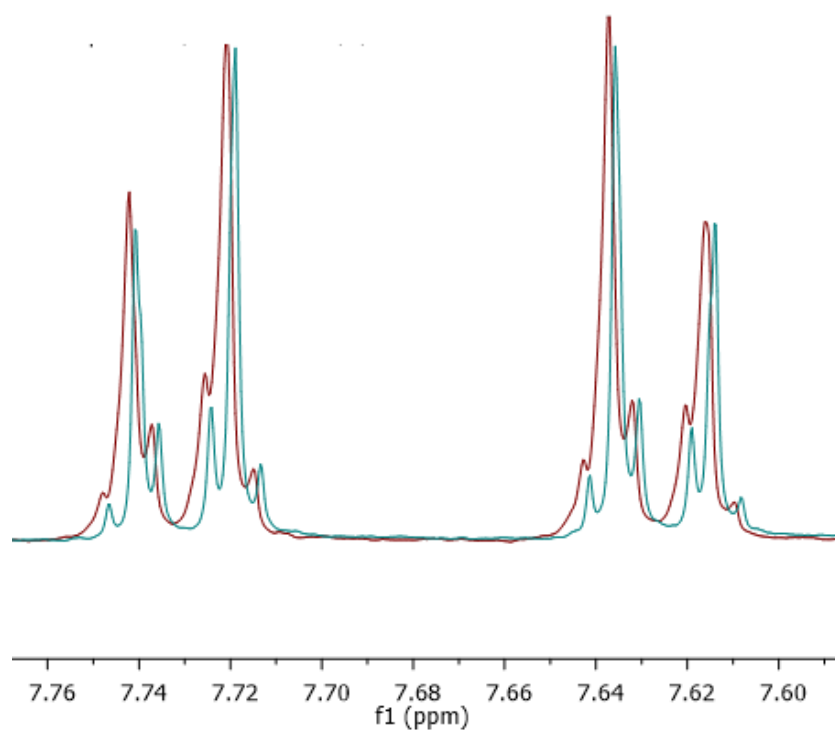


Figure 4.79: ¹H NMR spectra (400MHz, D₂O) related to the control solution (red) and supernatant (blue) following the functionalization of ZrNPs (reference to aromatic protons).

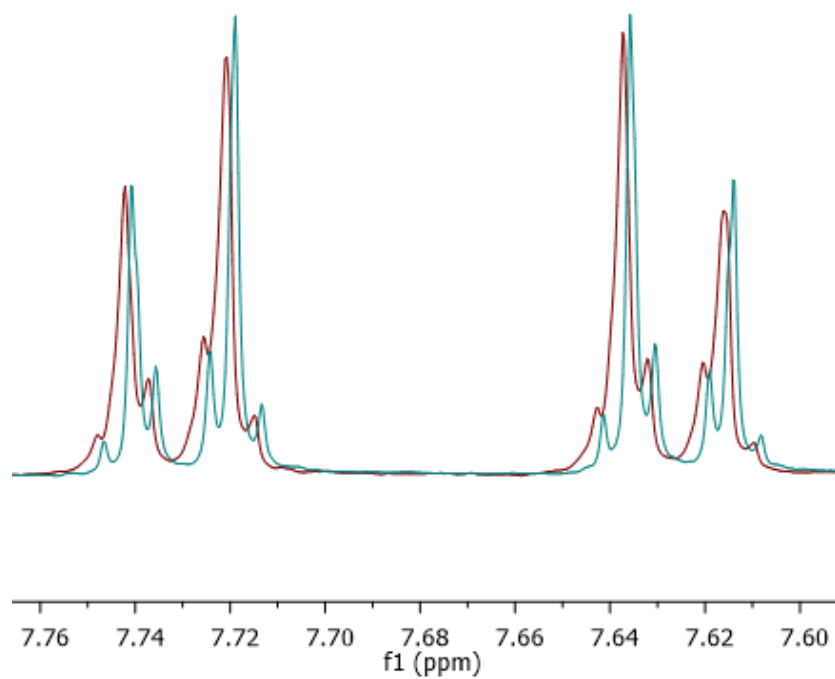


Figure 4.80: ¹H NMR spectra (400MHz, D₂O) related to the control solution (red) and supernatant (blue) following the functionalization of SiNPs (reference to aromatic protons).

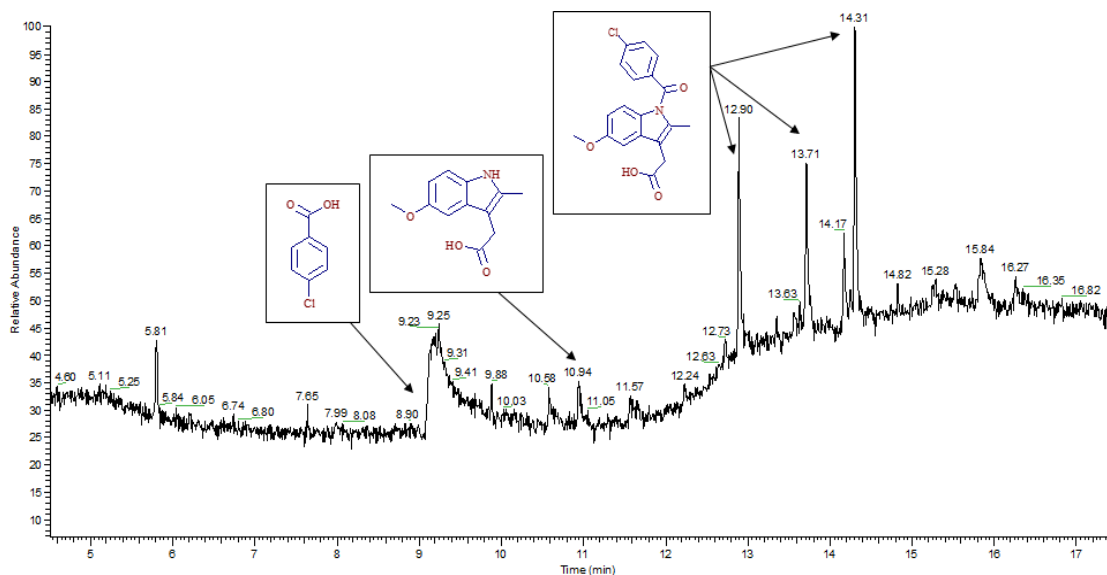


Figure 4.81 Chromatogram relating to the sample Indometacin / ZrNPS in acetone 1440min

4.6.2 Nitrofurantoin monohydrate

The determination of the nitrofurantoin release percentage in aqueous solution was carried out exclusively on the zirconia nanoparticles loaded in acetone, to confirm or not the catalytic character of the oxide with respect to the molecule under examination. The loading phase of the active ingredient was performed by adding to a suspension consisting of 1ml of distilled water and 50mg of nanoparticles, 2ml of a solution consisting of 250mg of nitrofurantoin and 5ml of N, N-dimethylformamide (DMF). Subsequently to the system 17 ml of deuterated acetone were added and after 12 hours of stirring, the support nanoparticles were isolated by filtration. Tests were conducted using an aliquot of 10mg of loaded ZrNPs. From the ^1H NMR spectra shown in Figure 4.82, it is possible to see, because of the dispersion in D_2O of the loaded support appear, after a time interval of 15 minutes, some signals not characterizing the molecule under examination. These signals are attributable to impurities deriving from sample preparation (DMF δ 7.87 (s, 1H), δ 2.95 (s, 3H), δ 2.79 (s, 3H)) and from the hydrolysis of the imino bond resulting in the formation of 5- nitro-2-furancarboxyaldehyde and 1-aminoino-numine (Figure 4.84). The presence of these products was confirmed by the characteristic ^1H NMR signals and by the GC-MS analysis (Figure 4.85) carried out on an aliquot of solution extracted in dichloromethane (solution at 1440 minutes from the suspension of NPs). Moreover, the ^1H NMR spectra show the presence at lower ppm of some resonances that could not be completely assigned. Following the integration of the nitrofurantoin signals, the release percentage determined in the time interval of 24h was found to be 2% (Tab.30). Similarly, to what was done for indomethacin, to verify if the loading of the drug on the supports was quantitative, through analysis ^1H NMR the analyte concentration was determined before and after the loading procedure in deuterated acetone. The analysis through the "ERETIC" functionality highlighted, within the errors on the measurements, a substantially zero loading for both supports, that is a quantity of active principle that is minimal and can not be determined with accuracy (Figure 4.85).

Support	Time (min)	Indo. in solution (mM)	% release
ZrNPs	1440	0,17	2

Table 30 Experimental results related to the release in D2O of Nitrofurantoin monohydrate / NPs loaded into deuterated acetone

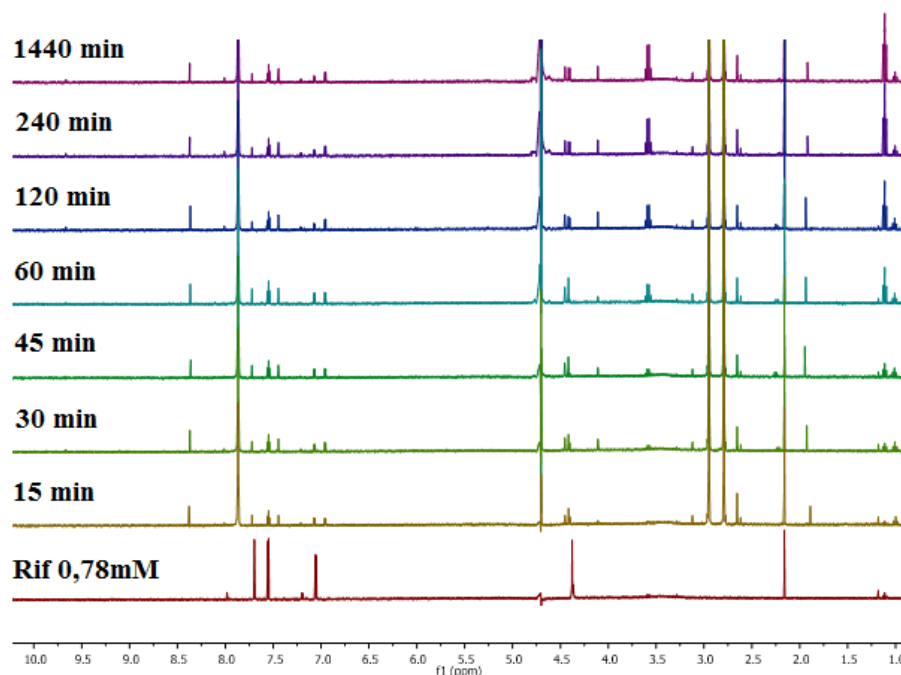


Figure 4.82: Release kinetics in H2O Nitrofurantoin / ZrNPs loaded in deuterated acetone / DMF (Spectrum 1H NMR: 400MHz, D2O)

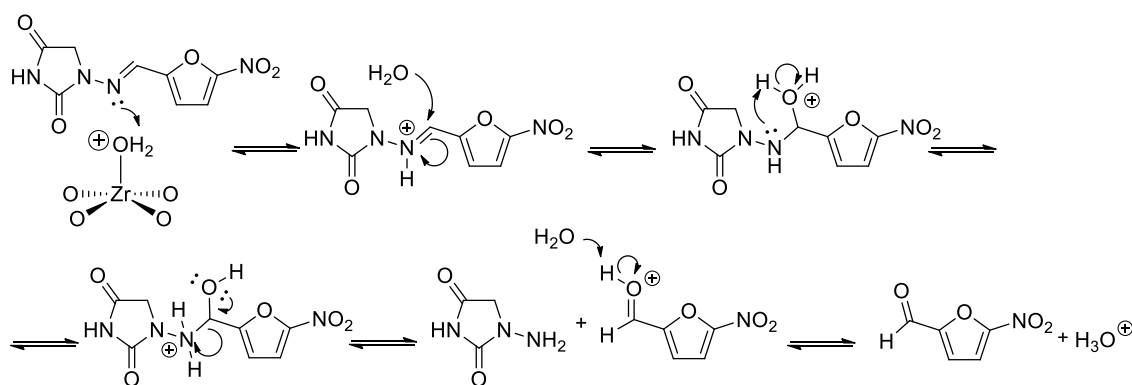


Figure 4.83: Acid hydrolysis reaction of the imine bond of Nitrofurantoin monohydrate following interaction with ZrNPs

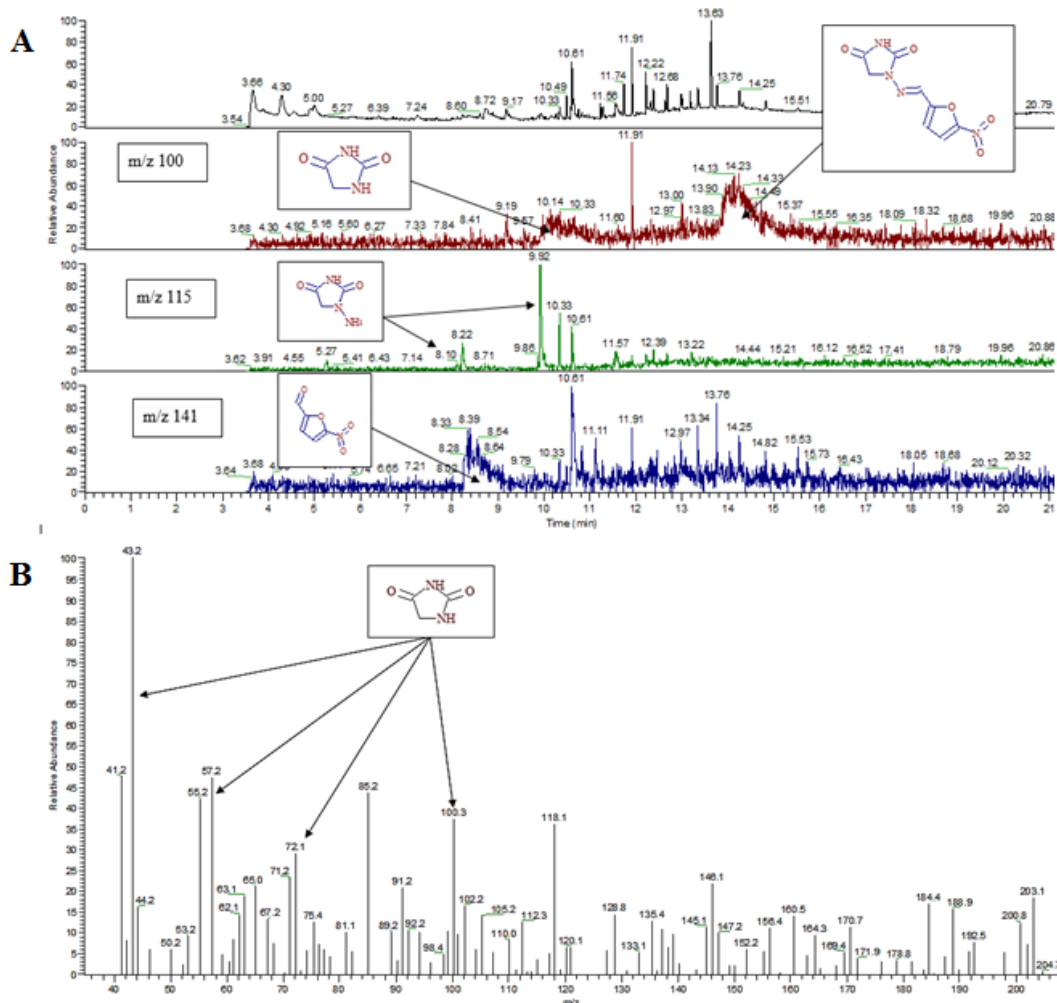


Figure 4.84: Chromatogram (A) and mass spectrum (B) for the sample Nitrofurantoin / ZrNPS in deuterated acetone / DMF 1440min

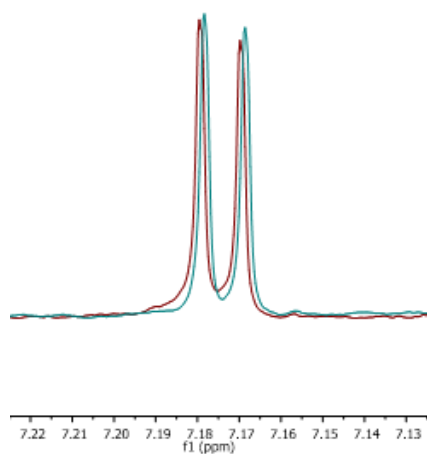


Figure 4.85: ^1H NMR spectra (400MHz, D_2O) related to the control solution (red) and supernatant (blue) following the functionalization of the ZrNPs (reference to the proton d Fig.78).

For both molecules analyzed, the Lewis acid character of zirconium oxide determines the hydrolysis and the subsequent possible inactivation of the active ingredient in solution. This phenomenon must be taken into consideration if you want to use zirconia nanoparticles as a support in the formulation of drug delivery systems of biologically active macromolecules characterized by hydrolysable bonds.

4.7 Experimental Part

4.7.1 Instrumentation

NMR spectroscopy:

The ^1H NMR and ^{31}P NMR spectra were conducted at 298K using a "Bruker Advance 400" spectrometer operating at 400MHz and 162MHz respectively and using deuterated water (D_2O) as solvent. To avoid the presence of the water signal, the ^1H NMR spectra were recorded in solvent suppression (solvent supp.). All spectra were recorded using the TMS for the proton and the phosphorus ones as internal reference., a solution of 85% phosphoric acid.

Gas chromatography-mass spectrometry:

The chromatographic analyzes were performed using a TRACE GC chromatograph coupled to a quadrupole mass spectrometer TRACE MS in Full Scan mode of Thermo Finnigan. The operating conditions adopted are shown in the table below:

Capillary Column:	HP5-MS 30 m, 0.25 mm x 0.25 μm
Initial Oven Temperature, $^{\circ}\text{C}$:	80 for 5 minutes
Ramp, $^{\circ}\text{C}$ /minute:	30
Final Temperature, $^{\circ}\text{C}$:	300 for 30 minutes
Injector Temperature (split), $^{\circ}\text{C}$:	280
Fluw, mL/minute:	00.08
Injected extract volume, μL :	1
Solvent delay, minutes:	03.00
Mass range, amu:	35-500
Detector voltage, V:	350
Interface Temperature, $^{\circ}\text{C}$:	300
Source Temperature, $^{\circ}\text{C}$:	200

Table 31 Gas chromatographic conditions / mass spectrometer TRACE GC / TRACE MS Thermo Finnigan

4.7.2 Experimental procedures

Buffer solutions:

The buffer solutions used in 25mM concentration were adjusted using a pH-meter with glass electrode and 100mM NaOH and 100mM HCl solutions.

Buffers-support affinity test:

In a vial introduce 1mL of 25mM buffer solution and 10mg of support. Agitating the system for a time interval of 24h (600rcf). Then centrifuge the sample at 12000rcf for 10 minutes (centrifuge HERMLE Z 383K, operating temperature 25 ° C) and analyze the supernatant by ¹H NMR spectroscopy.

Loading procedure BPs / MPs-support:

Formulate 6mL of a 5mM solution of BPs or MPs with a 25mM buffer solution. Withdraw 1ml of solution and analyze it by ¹H NMR spectroscopy (reference BPs / MPs 5mM). Introduce in the vial 50mg of support and place the system under stirring (600rcf). Take 1ml of solution at a time interval of 15-30-60-120 minutes. Centrifuge the sample (10 minutes at 12000rcf), isolate the supernatant and analyze it by ¹H NMR spectroscopy with respect to the previously prepared reference.

Stability testing BPs / MPs-support:

To 5ml of a 25mM buffer solution (TRIZMA, acetic acid / sodium acetate) add 50mg of support previously functionalized with phosphonic acids. Place the system under stirring (600rcf) and at regular intervals of 15-30-60-1440-2880 minutes, withdraw 1ml of solution. By centrifugation (10 minutes at 12000rcf) isolate the supernatant and analyze it by ¹H NMR spectroscopy.

Determination of the acid dissociation constants of the methylene bisphosphonate acid:

Split a 5mM MBP solution into 25 aliquots. Then add 100mM or 100mM NaOH to each sample to adjust the pH to the desired value to cover a pH range of 1-13 (use a pH meter). Analyze each solution by ¹H NMR and ³¹P NMR spectroscopy and graphically report the chemical shift of the characteristic signal of the molecule under examination as a function of pH. Perform a first and second derivative analysis in order to identify the inflection points of the previously obtained curves. The pKa of the molecule under examination correspond to the pH values at the inflection points [29].

Stability test BPs / MPs-support in a blood plasma of human origin:

The operating procedure used is similar to that described for stability tests in buffer solution. Basically, before proceeding with the creation of the single plasma batch, by combining the individual donor aliquots, the equipment to be used (vials, NMR tubes, pipettes, anchors) must be sterilized (VAPORMATIC 770, 121 ° C for 20min at 1atm) and UV radiation (1h). Conduct experimental tests under vertical laminar flow hood to avoid contamination by eliminating waste products such as "biological waste".

Procedure for the release of drugs from NPs:

To 10ml of a deuterated water solution add 10mg of support previously loaded with the test drug. Hold the system in agitation (350rpm) and at intervals of 15-30-45-60-120-240-1440 minutes withdraw 1ml of solution, isolate the supernatant by centrifugation (10 minutes at 12000rcf) and analyze it by ¹H NMR spectroscopy.

Physical Characterization of Metal Oxide Surface Modification

5. Experimental Section

5.1. Materials & Methods:

The reagents used for the sample's preparation, listed in Table 2.4, have been used as received without further purification.

Reagents	Abbreviation	Purity	M.W (g/mol)	Density (g/cm ³)	Supplier
Hexadecylamine	HDA	90%	241.46	0.81	Alfa Aesar
Zirconium Propoxide	ZP	70% in PrOH	327.58	1.04	Fluka
Titanium isopropoxide	TIP	97%	284.22	0.96	Fluka
Ethanol	EtOH	99.8%	46.07	0.79	Aldrich
Sodium Chloride	NaCl	99.5 %	58.44	2.16	Fluka
Sodium Fluoride	NaF	99%	41.99	2.56	Fluka
Milli Q	H ₂ O	99.99%	18.0	1	-

The nitrogen adsorption–desorption isotherms were obtained at the liquid nitrogen temperature (77 K) using a Micromeritics ASAP 2010 volumetric adsorption analyzer. From the adsorption data, the Brunauer–Emmett–Teller (BET) equation was used to calculate the specific surface area, while from the adsorption branches of the isotherms, the Barrett–Joyner–Halenda (BJH) model was used to estimate the pore size distribution and the pore volume was determined from the isotherm using the total adsorption value at relative pressure $p/p_0 = 0.26$.

The dimensions and the morphologies of the nanoparticles were investigated by electron microscopy using a Zeiss Sigma VP Field Emission Scanning Electron Microscope (FE-SEM). Mean and standard deviation of the FE-SEM micrographs were determined measuring at least 50 nanoparticles for each sample. The diameters were measured using the image analysis software ImageJ.

Also, morphological structure was studied using a JEOL JEM 3010 transmission electron microscope (TEM) operating at 300 kV. The powder specimens were suspended in isopropyl alcohol, and an aliquot of 5 μL was deposited on a copper grid (300 mesh) coated with holey carbon film. The copper grids were allowed to dry in air.

The surface chemistry of the functionalized mesoporous zirconia nanoparticles samples was characterized using several supplementing analysis methods. Fourier-transform infrared (FTIR) spectrometric measurements were carried out with a Spectrum BX (PerkinElmer Co.) spectrometer in both transmission mode and with horizontal ATR accessory equipped with a diamond crystal. The measurements were taken between 4000 and 500 cm^{-1} , averaging 32 scans. Grafting densities were calculated from mass losses in thermogravimetric analyses (TGA) of bare MZN and functionalized MZN performed in air from 30° C to 600° C with a heating rate of 10° C min^{-1} using a Netzsch STA 409 if complete decomposition of the organic part of the bisphosphonic acids occurred between 200 and 600° C.

X-ray photoelectron spectroscopy (XPS) was performed using a Perkin Elmer Φ 5600ci spectrometer using nonmonochromatic Al K_{α} radiation (1486.6 eV) in the 10^{-7} Pa pressure range. All the binding energy (BE) values are referred to the Fermi level. The correct calibration of the BE scale was verified during analysis by checking the position of both Au 4f_{7/2} and Cu2p_{3/2} bands (from pure metal targets), falling at 84.0 and 932.6 eV, respectively [266]. The raw XPS spectra were fitted using a non-linear least-square fitting program adopting a Shirley-type background and Gaussian–Lorentzian peak shapes for all the peaks (XPSPEAK41 software). Because of surface charging, samples presented a shift of the bands toward higher BEs: the charging effect was corrected by using an internal reference, depending on the considered nanoparticle system (Zr3d_{5/2} band centred at 182.4 eV for ZrO₂ system [266], Ti2p_{3/2} band at 458.6 eV for TiO₂ system [266], Fe2p_{3/2} band for 710.9 eV for Fe₂O₃ system [266],. The uncertainty of all the determined BEs was around 0.2 eV. The atomic composition was evaluated using sensitivity factors as provided by Θ V5.4A software. The relative uncertainty of the calculated atomic fraction of the different elements is around 5–10%.

The ζ -potential of the MZN nanoparticles and different bis-phosphonic acid modified MZN nanoparticles were calculated from electrophoretic mobility measurements done with a Zeta sizer Nano ZS (Malvern Instruments Ltd.). The measurements were performed after dilution of

colloidal solutions with ultra-pure water and buffer solution (pH range 4 to 10) to 1 wt%. About 2 mL of colloidal solutions were transferred into measuring cell. The measurements were run at E-field= 5.00 V/cm, T= 25 °C, with switch time at t = 33 s and averaging the obtained mobility data over six consecutive scans.

X-ray powder diffraction (XRPD) spectra were recorded with a Philips X'Pert powder diffractometer (Bragg–Brentano parafocusing geometry). A nickel-filtered Cu K α 1 radiation ($\lambda = 0.15406$ nm) and a step-by-step technique (step of 0.05° 2 θ) with collection times of 10 s/step were employed. From the XRPD patterns, the quantitative analysis and size distribution of the crystallites were carried out by means of the Rietveld refinement.

Grafting densities were calculated from mass losses in thermogravimetric analyses (TGA) of bare ZRNPS and functionalized ZRNPS performed in air from 30° C to 600° C with a heating rate of 10° C min⁻¹ using a Netzsch STA 409 assuming that complete decomposition of the organic part of the bisphosphonic acids occurred between 200 and 600° C.

For each of the BPs modified samples, the grafting density was calculated from the weight loss percentage (W_{BP}/W_{ZrO_2}) from the TGA measurements, SA=Surface area of the ZRNPS ZrO₂; N_A=Avogadro constant; MW=Molecular weight using the following equation.

$$\text{Grafting Density} = \left[\frac{\left(\frac{W_{BP}}{100 - W_{BP}} \right) 100 - W_{ZrO_2}}{M.W \times SA \times 100} \right] \times N_A$$

Solid State NMR spectra were recorded on a Varian Infinity Plus 400 spectrometer working at Larmor frequencies of 400.34 and 162.06 MHz for ¹H and ³¹P nuclei, respectively, using a CP-MAS probe-head accommodating rotors with outer diameters of 3.2 mm. Both ³¹P and ¹H spectra were recorded under Magic Angle Spinning (MAS) at a spinning frequency of 20 kHz, using a Direct Excitation (DE) pulse sequence, with high-power decoupling from ¹H nuclei in the case of ³¹P spectra. The duration of the excitation pulse was 2 μ s for both ³¹P and ¹H nuclei. ³¹P-MAS spectra were recorded with a relaxation delay of 5 s between consecutive transients and about 1000 scans were accumulated for each sample. The signal of H₃PO₄ (80%) at 0 ppm was used as reference for ³¹P chemical shift scale. ¹H-MAS spectra were recorded accumulating about 200

transients, with a recycle delay of 5 s, for each sample. ^1H - ^{31}P HETCOR spectra were recorded at a MAS frequency of 20 kHz, with frequency-switched Lee–Goldburg ^1H homonuclear decoupling, using a contact time of 300 μs in order to minimize ^1H spin-diffusion.

5.2 Surface Modification of Metal Oxides (ZrO₂, TiO₂, SiO₂, Bi₂O₃)

The Bis-phosphonic acids functionalized NPs were synthesis by dispersing 50 mg of Metal Oxide (ZrO₂, TiO₂, SiO₂, Bi₂O₃) nanoparticles into 5 mL MiliQ water using an ultrasonic finger. at room temperature. Then 5 mmol of respective mono-phosphonic & bis-phosphonic acid was added into the solution which was calculated to be the enough amount of necessary to give a complete monolayer, assuming a required area of 0.24 nm² per mono-phosphonic acid group. [269] Consequently, bis-phosphonic acids were assumed to require at least 0.48 nm²/molecule. Then the mixture was left overnight with continuous stirring. Day after, the particles were separated by centrifugation for 20 min at 12000 rpm. The supernatant was discarded, and the particles were dispersed in 20 mL of ethanol using a vortex shaker before being centrifuged again. This procedure was repeated in ethanol and in water. After the last washing cycle, the particles were dried at ambient temperature. Typical yields ranged from 90 to 95% because of losses in the washing procedure.

5.3 Result and Discussion

Nanoparticle Characterization after surface Modification:

5.3.1. Characterization of BPs@ZrNPs

The ZrNPs functionalized with **1a** were characterized by FE-SEM, Zeta potential, FTIR, TGA and XPS analysis. The surface functionalization of ZrNPs did not lead to structural modification with respect to the original naked ZrNPs, as visible from FE-SEM image reported in Figure 5.1. Moreover, no aggregation occurred after BP modification observing that the particles did not form clusters and remained well separated.

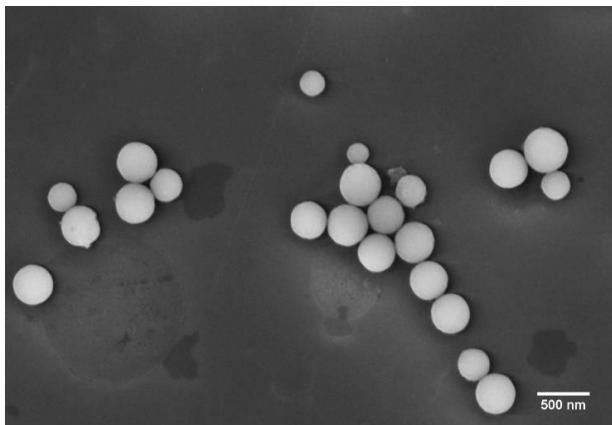


Figure 5.1. FE-SEM image of ZrNPs-1a.

A series of ζ -potential measurements were carried out on the NPs obtained before and after functionalization with **1a-f** in the range of pH between 4.0 and 10. The results reported in Figure 8 clearly shows that the original ZrNPs are characterized by the presence of surface positive charges at acidic pH and that moving to higher pH the surface ζ -potential of the NPs decreases becoming negatively charged at pH 10, displaying an isoelectric point (IEP) falling in the range between pH 6.5 and 7.0. Surface modified nanoparticles with **1a-f** display a different behaviour. In particular, it is worth to notice that for the ZrNPs-**1a** in all the pH range investigated the surface of the NPs turned out to be highly negatively charged due to the presence of several polyanionic **1a** molecules that modify the surface of the ZrNPs and, thanks to the high charge, prevent aggregation and ensure high colloidal stability for several days. Similarly, all the other BPs provided comparable effects on the ζ -potential of the NPs, except for the amino-BP **1d**. In the latter case at pH 4.0 the ζ -potential is highly positive due to the presence of protonated primary amino side chain of the BP that overall overcome the number of negative charges on the surface leading to positively charged NPs.

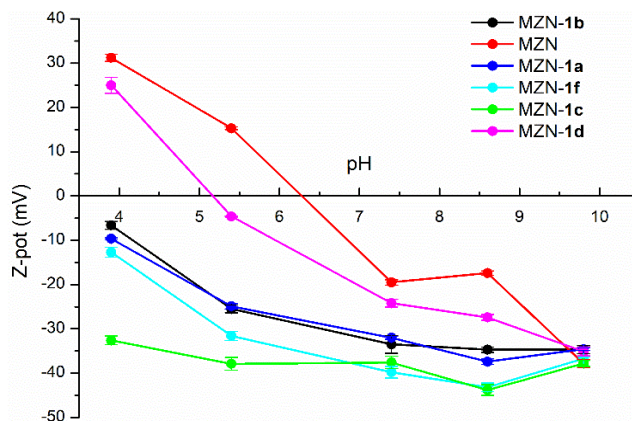


Figure 5.2: ζ -potential measurements of bare ZrNPs and ZrNPs functionalized with **1a-1f** as a function of the pH of the solution

Moving to higher pH values, the IEP at acidic pH is likely to be due to the terminal primary amino group that above pH 6 becomes neutral and the NPs become more and more negatively charged. It is worth to notice that between pH 6 and 9 all the BPs provide the nanoparticles with a superficial negative charge with overall potential below -20 mV that is highly responsible for the good colloidal stability. Moreover, repeated measurements on the same samples showed good reproducibility of the colloidal solutions, as clearly demonstrated by the rather small error scale-bar for each ζ -potential data.

DRIFT-FTIR spectra of bare ZrNPs and ZrNPs-**1a** and ATR-FTIR spectrum of pure **1a** are reported in Figure 5.3. Significant changes in the P-O region ($900-1250\text{ cm}^{-1}$) were observed

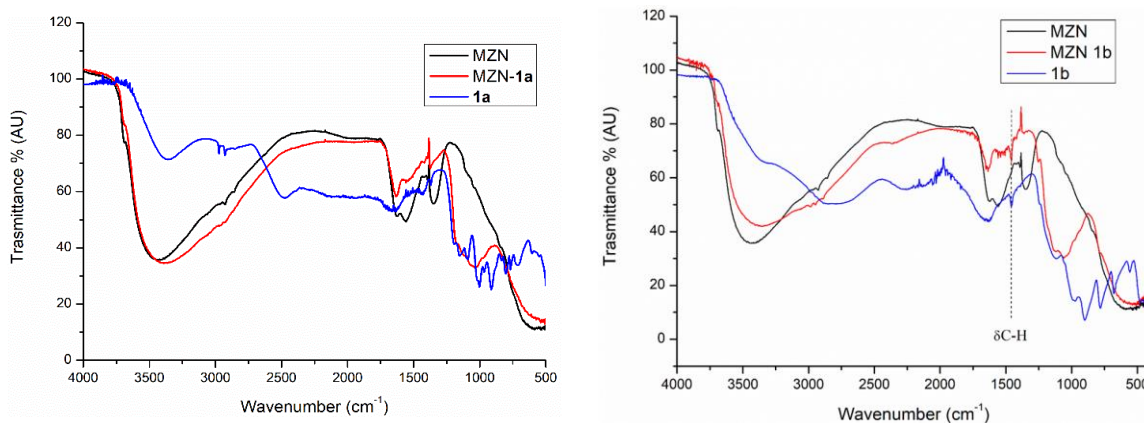


Figure 5.3: FTIR spectra of pure **1a** (blue), bare ZrNPs (black) and ZrNPs-**1a** (red) (left) & FTIR spectra of pure **1b** (blue) and spectra of ZRNPS (black) and ZRNPS **1b** (red).

comparing the free **1a** with the functionalized ZrNPs-**1a**. The stretching vibration of the P-OH at 906 cm^{-1} disappears in the infrared spectra of modified NPs, while other peaks typical of the free **1a** became a single broad band after conjugation.

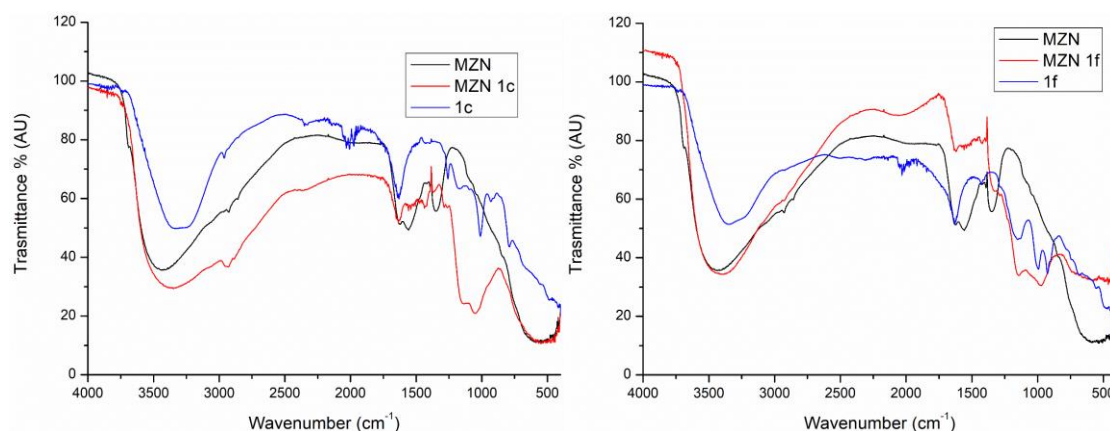


Figure 5.4. FTIR spectra of pure **1c** (blue) and spectra of ZRNPS (black) and ZRNPS **1c** (red) & FTIR spectra of pure **1f** (blue) and spectra of ZRNPS (black) and ZRNPS **1f** (red).

These modification on the IR spectrum are associated with the bonding of the BPs acid on the surface, probably via condensation reactions.[268, 269] The broadening and shifting of all peaks corresponding to the P-OH vibrations were observed for all the modified samples with BPs **1a-1f** and this common behavior further support the covalent modification of the ZrNPs. Accordingly, in the case of BPs like **1b** the presence of other peaks related to specific residues like the bending vibration of C-H bond were observed.

The quantification of the grafting of BPs on ZrNPs was determined also by thermogravimetric analysis (TGA, see supporting information) and differential thermal analysis for **1a** (DTA, Figure 5.5).

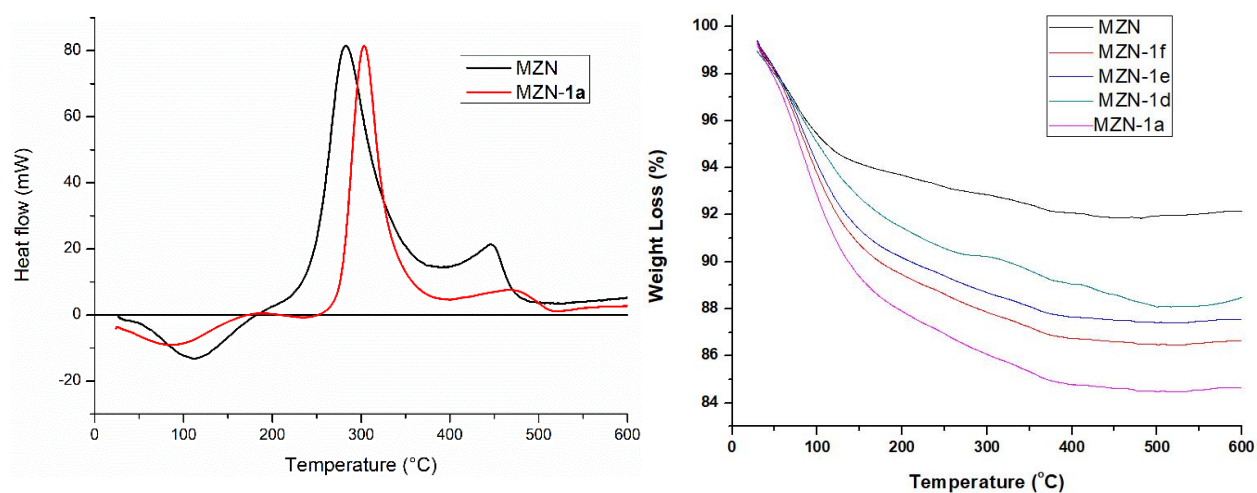


Figure 5.5. DTA curve for bare ZrNPs and ZrNPs-**1a** (left) & TGA profile for ZrNPs as reference and for functionalized with different BPs (right)

The DTA profile shows an initial small endothermic peak at around 100 °C corresponding to the evaporation of the residual water and residual possible organic solvents. Other weight loss stages above 150 °C characterized by an exothermic peak at around 300 °C were observed and attributed to the decomposition of the organic BP molecules chemisorbed on the surface of ZrNPs. Moreover, the shifting of the exothermic peak at higher temperature in modified ZrNPs, compared to bare ZrNPs could be ascribable to the thermal stabilization imparted by the presence of the BP. Indeed, phosphonate molecules are usually used as flame retardant additives in polymers [270] to improve their thermal stability.

For the BPs **1a** and **1b** the grafting density (GD) was calculated from the TGA measurements using weight loss percentage (W_{BP}/W_{ZrO_2}). In table 1 are reported the GD determined by both the data from the TGA and from quantitative 1H NMR. The two techniques provide information on the same measurement from two different points of view: the TGA measures the loss of the BP from the surface of the ZrNPs and the NMR measures by difference in solution the BP that is taken up by the ZrNPs. It is worth to notice that the two techniques for the ZrNPs provided a good agreement. The GD from TGA are a bit higher for **1a** compared to **1b**, 2.0 molecules/nm² and 1.5 molecules/nm², respectively. The lower GD values obtained from TGA data compared to NMR data is likely to be related to the formation of zirconium phosphate species during the TGA experiments which are non-volatile species, thus decreasing the total mass losses calculated.

BPs	MW (g/mol)	TGA Mass Loss Wt (%)	GD TGA (molecules/nm ²)	GD NMR (molecules/ nm ²)
1a	176.0	15.0	2.0	3.2
1b	190.0	13.5	1.5	3.1

Table 1: Grafting density of BPs on ZrNPs determined both the uptake of BP from the solution by NMR and by TGA analysis on the modified ZRNPs.

To further validate the presence of BPs on the surface of the functionalized ZrNPs, XPS spectra were performed on different samples. Being the XPS sampling depth typically around 5-10 nm, this technique evidences the presence on the surface of different chemical elements belonging to the molecules of interest. Figure 5.6 shows a wide-range survey XPS spectrum for ZrNPs-**1a** sample, evidencing the presence of bands related to Zr, O, C, and P. By detail spectra recorded in

higher resolution condition and after correction for the sample charging using a Zr internal reference (see supporting information), the binding energy (BE) was determined for Zr3p_{3/2} (332.8 eV), Zr3p_{1/2} (345.8 eV) and O1s (530.2 eV) bands: the detected BE values are characteristic for ZrNPs. P2p and C1s bands were centred at 133.1 eV and 284.3 eV, respectively.

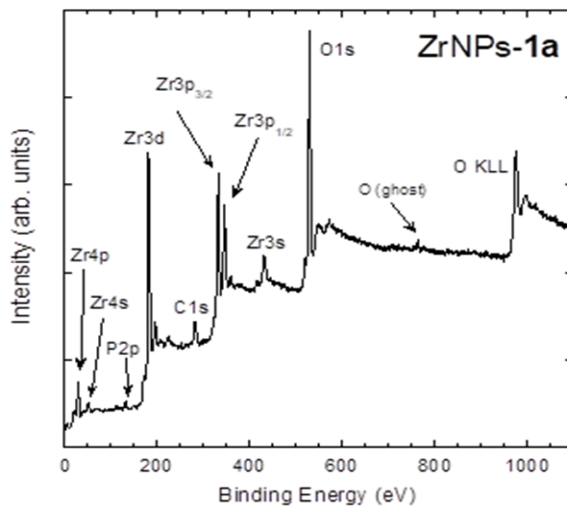


Figure 5.6. The XPS survey spectrum of ZrNPs-**1a** showing a dominant signal attributed to the ZrNPs and weak signals attributed to P and C, related to the presence of **1a** on the nanoparticles surface.

C, O, Zr, P, S, and N atomic fraction for the samples ZrNPs-**1b-f** are summarized in Table 2 as detected by XPS. For all the functionalized ZrNPs samples the presence of the specific elements, in particular P arising from the bisphosphonate moiety, was confirmed. Moreover, the comparison of the atomic fraction of P, S, and N shows a good agreement with the nominal amount ratio of these elements in the corresponding BPs. The binding energy values of the P2p, S2p, and N1s bands was determined by detail spectra and the results are reported in Table 3.

Samples	C	O	Zr	P	S	N
	(%)	(%)	(%)	(%)	(%)	(%)
ZrNPs	27	54	19	-	-	-
ZrNPs- 1a	17	62	19	~ 2.8	-	-
ZrNPs- 1b	17	61	19	~ 2.4	-	-
ZrNPs- 1c	16	61	16	~ 4.0	~ 1.7	-
ZrNPs- 1d	15	60	19	~ 3.4	~ 1.3	~ 1.3

ZrNPs-**1f** 18 60 18 - 2.5 - 1.0 -

Table 2: C, O, Zr, P, S, and N atomic fraction as obtained by XPS data for ZrNPs, ZrNPs-**1a**, ZrNPs-**1b**, ZrNPs-**1c**, ZrNPs-**1d** and ZrNPs-**1f** samples

Modified ZrNPs	P2p (eV)	S2p (eV)	N1s (eV)
ZrNPs- 1a	133.4	-	-
ZrNPs - 1c	133.2	163.4	-
ZrNPs - 1d	133.2	163.6	400.7
ZrNPs - 1f	133.3	163.4	-

Table 3: Binding energy values of P2p, S2p, and N1s bands as detected in the functionalized ZrNPs.

The detected values are compatible with the chemical environment of the elements considered in the different functional groups. In particular, the P2p BE values detected for all the P-containing samples (falling in the range 133.2-133.4 eV) are slightly lower than those reported for the single BP molecule [271] This is ascribable to the coordination of the phosphonate moieties on the superficial Zr atoms as observed also for similar systems [271, 272] These experimental findings once more attest the desired functionalization of the ZrNPs. In Figure 5.7 the detail XPS spectrum of P2p band for ZrNPs-**1a** sample is reported. As far as the S2p and N1s bands are concerned, their BE values are consistent with the presence of S atoms in the thioether side chains of the BPs [273] and with N atoms in amine functionalized ZrNPs with **1d**, [274] respectively.

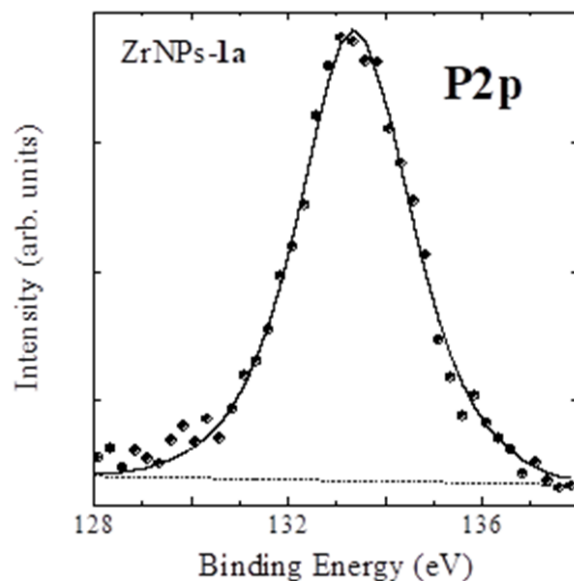


Figure 5.7. XPS detail spectrum of P2p band, recorded for ZrNPs-1a sample

Solid state NMR experiments on functionalized ZrNPs

The functionalization of ZrNPs with **1a** and **1b** was also investigated by means of solid-state NMR spectroscopy. ^{31}P -MAS spectra (Figure 5.8) provide useful information on the local environment of ^{31}P nuclei: the spectra of both ZrNPs-**1a** and ZrNPs-**1b** show a single broad peak centered at about 14 and 19 ppm, respectively. These peaks are shifted by about -10 ppm with respect to the signals of the corresponding pure bisphosphonic acids [275]. Based on the literature, in which the interaction of mono- and, only in few cases, BPs with zirconia has been investigated exploiting ^{31}P Solid State NMR spectroscopy [276-282], a ≈ 10 ppm decrease in the ^{31}P chemical shift can be attributed to the formation of a multi-dentate anchoring of **1a** and **1b** to the zirconia surface by reaction of P-OH to form P-O-Zr bonds. The broadness of the peaks is indicative of the presence of a distribution of geometries around ^{31}P nuclei and, on the whole, of the amorphous nature of the organic layer. Additional information arises from ^1H -MAS spectra (see below): for both ZrNPs-**1a** and ZrNPs-**1b** no signals ascribable to P-OH hydrogen nuclei, expected at about 10-11 ppm [278, 283-286] were observed, thus suggesting that most of them reacted with zirconia. Moreover, ^1H - ^{31}P HETCOR experiments, in which spatially close ^1H and ^{31}P nuclei give rise to cross-peaks, highlighted for both ZrNPs-**1a** and ZrNPs-**1b** an expected strong correlation between phosphorus nuclei of **1a** and **1b** and ^1H nuclei of directly bonded -CH₂- groups (at about 2 ppm), and a weaker correlation with protons resonating at about 6 ppm

(see supporting information). These protons give rise to a broad signal in the corresponding ^1H -MAS spectra, which can be ascribed to water firmly adsorbed on ZrNPs and/or possible residual Zr-OH groups [287], both strongly hydrogen-bonded. It is possible that these protons establish hydrogen-bonds also with P=O oxygens of phosphonates. Moreover, in one case [288], also P-OH protons in functionalized mesoporous silica have been reported to resonate at 6.5 ppm, thus it cannot be ruled out that also some residual P-OH groups contribute to this signal.

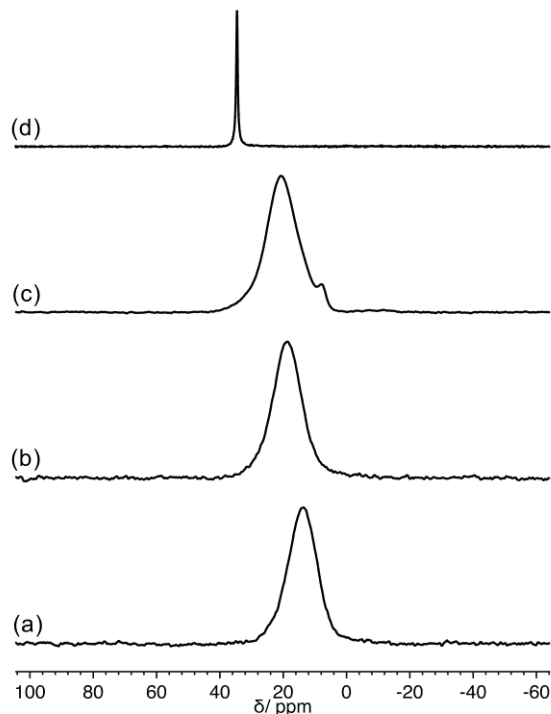


Figure 5.8. ^{31}P DE-MAS spectra of: (a) ZrNPs-**1a** (b) ZrNPs-**1b** (c) ZrNPs-**6e** (d) **6e**.

For comparison we also looked at ZrNPs functionalized with 3-phosphonopropionic acid **6e**. In Figure 4.11 the ^{31}P -MAS spectra of ZrNPs-**6e** and of pristine **6e** are reported. While pristine **6e** shows a single narrow peak resonating at about 35 ppm, characteristic of a crystalline solid, ZrNPs-**6e** gives rise to a very broad signal centered at a chemical shift of 20 ppm, with a minor component at about 8 ppm. Similarly to BPs, the 15 ppm decrease of the chemical shift in passing from the pure acid to the zirconia hybrid can be ascribed to a bi-dentate anchoring of **6e** on the zirconia surface, involving the reaction of most P-OH groups. The small signal at 8 ppm can be tentatively ascribed to a minor fraction of molecules forming a tri-dentate anchoring also

involving the P=O group or to a small amount of bulk metal phosphonate [277]. ^1H -MAS spectra (see below) confirmed these results: in the spectrum of ZrNPs-**6e** a signal at about 11 ppm, due to P-OH, observed in the spectrum of pristine **6e**, is not recognized, suggesting that most of P-OH groups reacted. Moreover, while in the ^1H - ^{31}P HETCOR spectrum of pristine **6e** (see below) cross-peaks were observed between phosphorus nuclei and methylene (at about 2 ppm) and P-OH (at about 11 ppm) hydrogen nuclei, the HETCOR spectrum of ZrNPs -**6e** appeared completely similar to that of ZrNPs-**1a** and ZrNPs-**1b**.

^1H -MAS and ^1H - ^{31}P HETCOR Solid State NMR spectra of BP functionalized ZrNPs

In the ^1H -MAS spectra of all samples (Figure 5.9), apart 3-phosphonopropanoic acid **6e**, intense signals of hexadecylamine and ethanol used in the synthesis, are present between 0 and 4 ppm. In the spectrum of ZrNPs it is possible to recognize (also with the support of a spectral fitting) an intense signal at about 5 ppm, ascribable to physisorbed water and Zr-OH and a broad one centered at about 6.5 ppm, likely due to water and Zr-OH strongly hydrogen-bonded. Indeed, after heating in oven, the intensity of the former peak strongly decreases, while the latter remains approximately the same. In all functionalized ZrNPs samples (spectra c, d, f) the region at high chemical shifts is still dominated by the peak at about 6 ppm. The spectrum of pristine **6e** shows an intrinsic worse signal resolution, due to the strongly rigid character of the crystalline solid and the consequently strong homonuclear dipolar couplings. The signal at lowest chemical shift can be ascribed to CH_2 protons, that at about 7 ppm is likely due to tightly bound water, while the broad signal above 10 ppm could be fitted with one peak at about 11 ppm, ascribable to P-OH protons and one at about 14 ppm due to COOH protons.

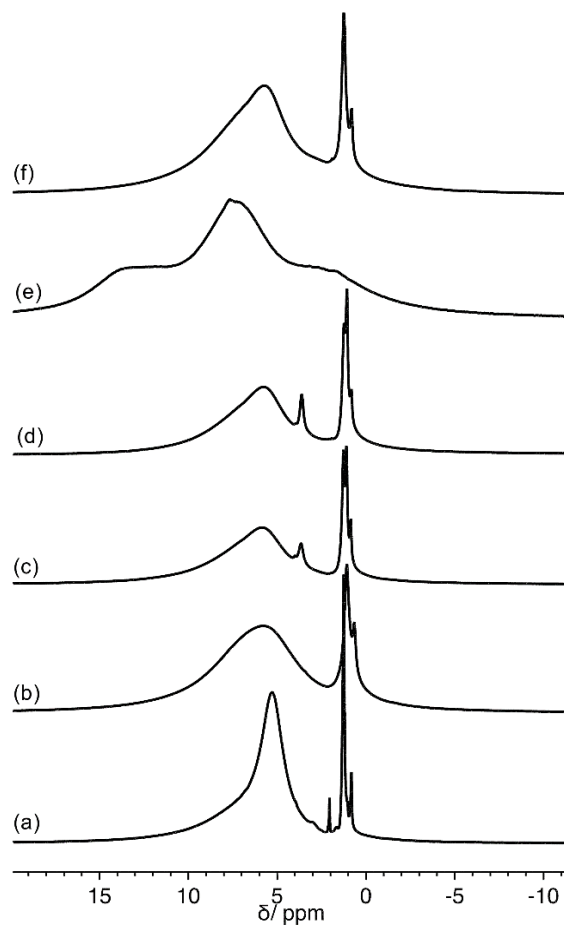


Figure 5.9. ^1H -MAS spectra of (a) ZrNPs (b) ZrNPs after heating at 80°C for 4 hours (c) ZrNPs -**1a** (d) ZrNPs -**1b** (e) **6e** (f) ZrNPs -**6e**.

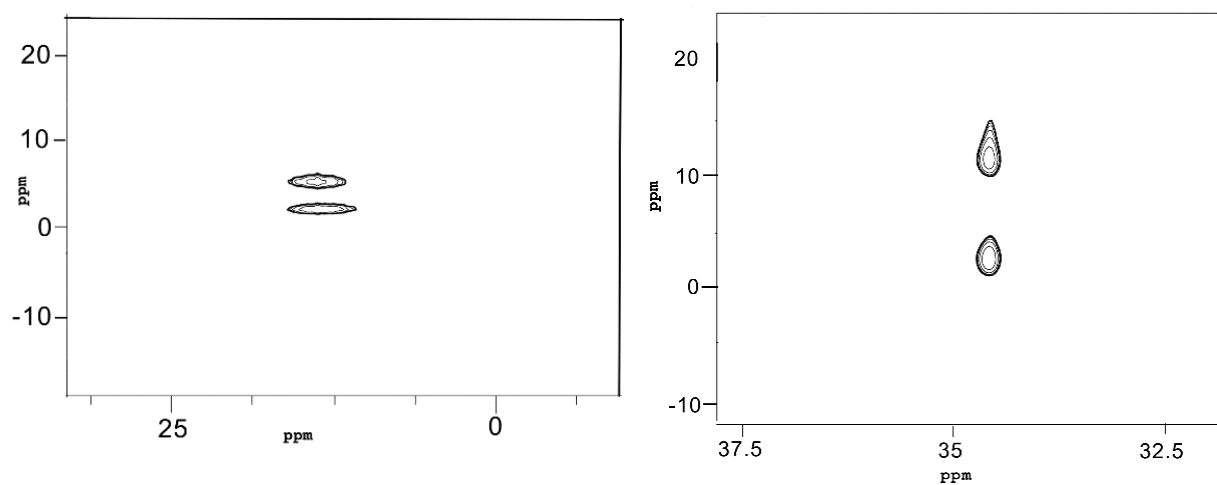


Figure 5.10. ^1H - ^{31}P HETCOR spectrum of ZrNPs -**1a** (left) & ^1H - ^{31}P HETCOR spectrum of **6e** (right)

5.3.2 Characterization of MBP@ BiNPs

The uptake of **1a** was rapid since after 10 min the loading was achieved 78% and after 1h it did not grow above with 82%. The saturation of the surface of the Bi₂O₃ NPs was rapid due to the very small surface area. In fact, a GD of more than 80 molecules per nm² which means a multilayer coverage of the non-porous material, probably due to initial coordination on the superficial metal centers followed by H-bonding interactions between molecules of BPs. Release test showed that at pH 4 no release was observed after 2h and at pH 8.8 only 10% release was present after 2h.

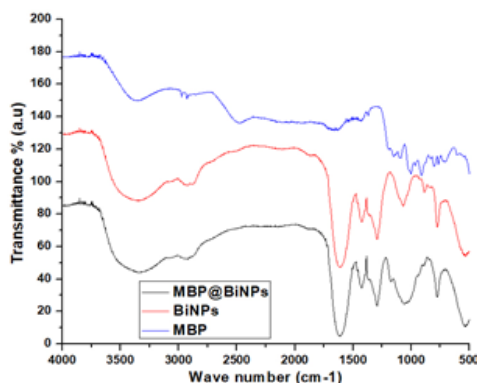


Figure 5.11: FTIR spectra of **1a**@BiNPs with comparison of BiNPs and pure molecules MBP

The FTIR spectra for MBP and MBP@BiNPs are compared. The broadness and complexity of the peaks in this region make it difficult to interpret, but the large changes observed show that a strong interaction of the phosphonate headgroup with the BiNPs surface is present. Band at 3500 ~ 3400 cm⁻¹ is a characteristic group frequency from the stretch vibration of O-H. The broad band at 2800~3200 cm⁻¹ comes from C-H stretch vibration and the stretch -CH₂ of located at 2880 cm⁻¹. The broad band around 700 ~ 400 cm⁻¹ originates from the metal-oxygen (Bi-O) vibration. Moreover, the asymmetric and the symmetric stretching vibrations of the P-OH at 906 and 962 cm⁻¹ disappear in the infrared spectra, which are associated with covalent bonding of phosphonic acid to the surface of BiNPs.

5.3.3. Characterization of MBP@ TiNPs

The bonding of MBP towards TiNPs was evidenced using FTIR using the 400–1400 cm⁻¹ range. At all the pH range zeta potential value all negative due to the presence of several polyanionic MBP molecules that modify the surface of the TiNPs as like ZrNPs.

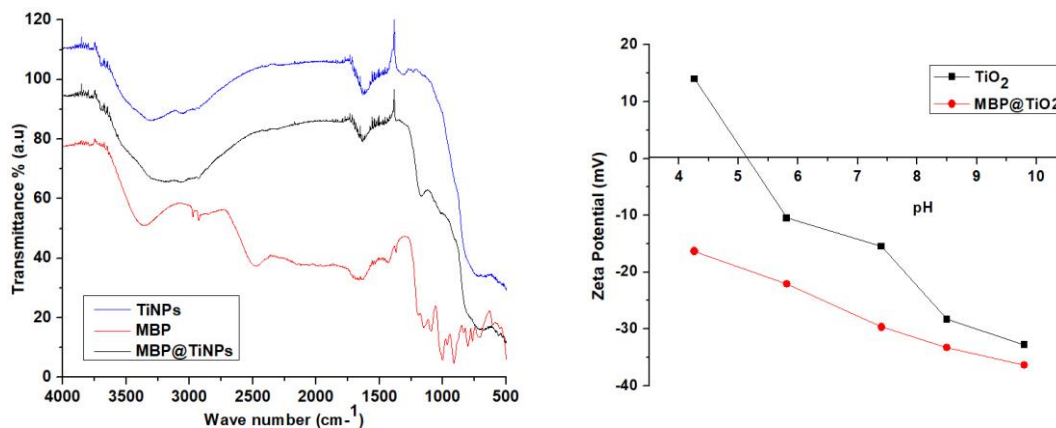


Figure 5.12: FTIR spectra of MBP@TiNPs with comparison of TiNPs and pure molecules MBP (left) & ζ -potential measurements of bare ZrNPs and ZrNPs functionalized with **MBP** as a function of the pH of

The affinity tests with **1a** showed a quantitative uptake just after 10 minutes as predicted by the affinity of monophosphonates for iron magnetic nanoparticles [291]

	Surface Area	Average Size	Loading	GD
NPs	(m ² /g)	(nm)	(%)	NMR (molecules/ nm ²)
SiO ₂	950	160	55	1-2
TiO ₂	17	100	93	7.2
Bi ₂ O ₃	15	123	82	8.2
Fe ₃ O ₄	176	5.4	>98	8.5

Table 4: Binding efficiency of **MBP** 25 mM on 50 mg of different NP oxides at pH 4.0 determined by ¹H quantitative NMR after 1h.

To further analyze the oxides that showed affinity for **MBP**, XPS analyses were performed on functionalized TiO₂, Bi₂O₃ and Fe₃O₄ NPs. In Table 6 the atomic fractions of the main elements are reported (as obtained by XPS data), evidencing the effectiveness of the functionalization with **MBP** by the detection of P on the surface of the NPs

Samples	Ti	Bi	Fe	O	C	P
	(%)	(%)	(%)	(%)	(%)	(%)
TiO ₂ NPs-MBP	18	-	-	63	15	~ 4.0

Bi ₂ O ₃ NPs-MBP	-	6	-	37	53	- 3.7
Fe ₃ O ₄ NPs-MBP	-	-	40	43	16	- 0.8

Table 5: Ti, Bi, Fe, O, C, and P atomic fraction as obtained by XPS data for TiO₂, Bi₂O₃ and Fe₂O₃ nanoparticles after **MBP** functionalization

Calculating the atomic fraction ratio P/metal from data reported in Tables 2 and 6, a marked efficiency of the **MBP** functionalization is evidenced in the case of Bi and Ti oxide NPs. This is likely due, as observed before, to the possible formation of multilayers of **MBP** on the Bi₂O₃ and TiO₂ NPs that are both characterized by rather low surface area and that showed high values of GD.

5.4 Application of thiol bearing BPs as linker of mMZN and AuNPs

For nanomedical applications, a system that could exploit different properties may represent the right answer to the urgent demand of a complete theranostic system and excellent biosensor. Coupling together magnetic and plasmonic properties is an interesting approach to achieve this goal. Furthermore, SERS signals associated to magnetic nanoparticles are useful for the identification of different analytes, also separated with a magnetic sorting [292-295]. SERS signals show intensities similar to those of fluorescence, but with some advantages, such as narrow peaks with characteristic fingerprints and absence of bleaching. To do this, other member of my research group prepared a nanotool exploiting both magnetic and plasmonic properties using free thiol end group bearing bisphosphonic acid (BPODE, **1h**) (see section 2.4.18) to modify the magnetic zirconia nanoparticles (mMZN) and then to attach the gold nanoparticles. This was obtained through the synthesis and characterization of cobalt-ferrites/zirconia nanocomposites, showing magnetic properties comparable to the ones of bulk cobalt iron oxides. The spherical nanoparticles (mMZN) were modified with a thiol functionalized bisphosphonic acid **1h**, which was used to link gold nanoparticles and obtaining nanostructures with magnetic and plasmonic properties.

The sample mMZN has been successfully functionalized with bis-phosphonic as proved by EDX, IR, ζ-potential analysis. In EDX measurements the mMZN-1h spectrum shows the sulfur peak at 2.30 keV that is evident when compared with the pattern of the unmodified MZN.

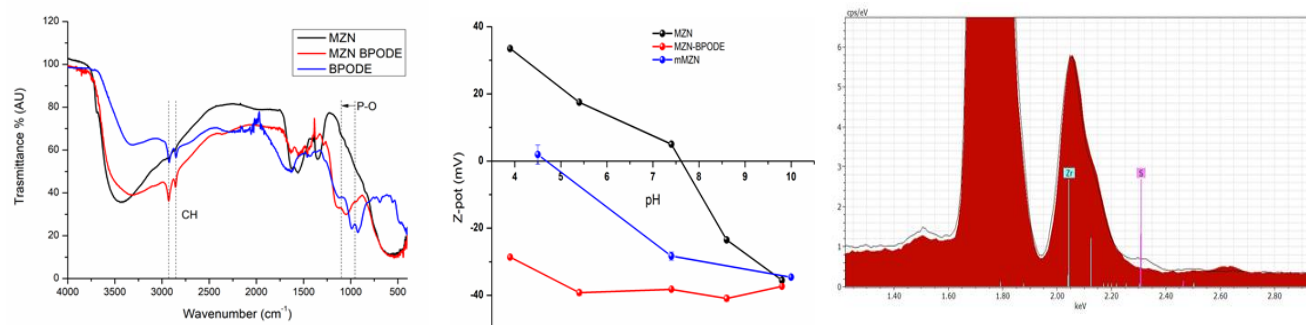


Figure 5.13: DRIFT- IR spectra of MZN (black line), pure 1h (blue line) and MZN-1h (red line); ζ -potential measurements of bare MZN, mMZN and MZN functionalized with **1h** as a function of the pH of the solution (middle) and EDX spectra of MZN-1h, red spectra for unmodified MZN, black line for MZN modified with 1h.

For plasmonic applications, the mMZN functionalized with 1h were coupled with gold nanoparticles obtained by laser ablation. TEM and FEG-SEM images, reported in 4.18, clearly show the presence of the AuNP on the surface of the mMZN nanoparticles.

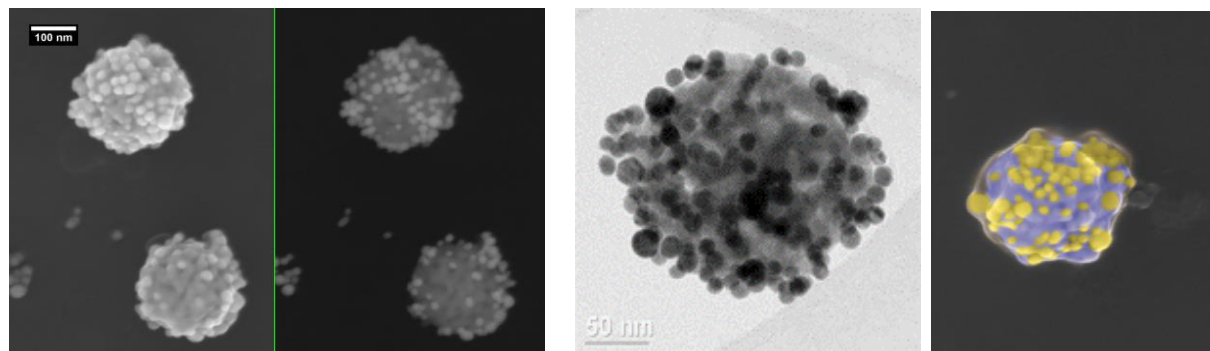


Figure 5.14. 1:FEG-SEM and TEM images of mMZN-@Au.

Magnetic and plasmonic properties of all nanostructures were performed but these are not included in this thesis.

Optical properties of Neodymium doped Zirconia NPs

The Ln^{3+} ions embedded in inorganic nanomaterials, such as the oxides and fluorides, are considered as a new generation of optically active bioprobes. Compared to fluoride NPs, Ln^{3+} doped inorganic oxide NPs are attractive luminophores because of their unique spectral characteristics: long luminescence lifetime, resistance to photobleaching, sharp luminescence bands that are spaced across the entire visible and near-infrared (NIR) spectral region depending on the choice of the Ln^{3+} , and minimal intra- and inter- Ln^{3+} emission spectral band overlap [296–301]. Zirconia (ZrO_2), possessing low phonon energy (470 cm^{-1}) and high host absorption coefficient, [303] is considered as an ideal oxide host for Ln^{3+} doping to achieve intense long-lived luminescence of Ln^{3+} , [304] which is the prerequisite for its bioapplications. Moreover, neodymium ions (Nd^{3+}) present emission bands in the first and second biological windows (890, 1060, and 1300 nm), all of which can be used for in vivo imaging purposes [302]. However, it remains a challenge to synthesize biocompatible bioprobes based on sub-5 nm oxide NPs. Usually oxide NPs were prepared via coprecipitation followed by calcination or post annealing procedures, which unfortunately often result in large, aggregated, and hydrophobic NPs. [305] The synthesis of Nd^{3+} doped ZrNPs with controlled size, structure and surface properties is thus of technological and fundamental importance. So far, multistep synthetic routes involving wet chemical synthesis such as sol–gel, precipitation and microemulsion-based methods followed by high temperature annealing have been reported for the preparation of zirconia nanoparticles doped with other Ln^{3+} .

Here we present a study of non-aqueous synthesis of metal of ZrNPs doped with Neodymium at different concentrations and then non-aqueous NPs convert into water soluble NPs. The investigation of the optical properties combined with the information obtained from the structural and chemical characterization.

6.1 Materials and methods

6.1.1 Chemicals

Zirconium (IV) isopropoxide isopropanol (99.9%), neodymium (III) acetate hydrate (99.9%) and benzyl alcohol (99%), oleic acid (90%), hexane (99%), ethanol (100%, Commercial Alcohols) were used as received from Aldrich Inc.

6.1.2 Synthesis of Nd^{3+} -doped ZrNPs

Monodisperse Nd^{3+} doped ZrNPs were synthesized according to a modified solvothermal procedure reported in the literature [306]. Briefly, the assembly of precursors was done in a glove box ($<0.1\text{ ppm H}_2\text{O}$) to ensure highest purity. A Teflon cup with an inner volume of 45 mL was charged with benzyl alcohol (20 mL), zirconium (IV) isopropoxide isopropanol complex (5.72 mmol) and the appropriate amount of neodymium acetate hydrate corresponding to 1, 3, 5, 7, 9, 11 mol% as to the zirconia. After sliding the Teflon cup into a steel autoclave, the autoclave was sealed and removed from the glove box. The particle synthesis was conducted by placing the autoclave in a preheated oven at $230\text{ }^\circ\text{C}$ for 2 days. A milky suspension resulted, which was

centrifuged, and the white precipitate washed three times with ethanol. For the post-functionalization treatments, the obtained powders were not dried after washing but a chloroform solution of oleic acid (50 mg in 5 mL CHCl_3) was added immediately after the decantation of ethanol. Upon sonication for 5 min, a transparent dispersion was formed.

6.1.3 Synthesis of water soluble Nd^{3+} -doped ZrNPs

To obtain water dispersible NPs, procedure was adapted from the procedure the literature [307] with some modification. 250 mg of oleate-capped Nd^{3+} -doped ZrNPs obtained from the previous step were dispersed in 25 mL of hexane and mixed with 25 mL of a HCl solution (adjusted to pH 4). The mixture was kept on a shaker for 3 h, and subsequently transferred into a separation funnel, from which the aqueous phase containing the Nd^{3+} -doped ZrNPs was collected. The NPs were precipitated with acetone (1:5 aqueous: organic ratio), collected by centrifugation and re-dispersed in 25 mL of HCl (adjusted to pH 7). The dispersion was placed on the shaker for an additional 2 h. Finally, the NPs were precipitated with acetone, washed three times with acetone and water, collected by centrifugation and dispersed in water for further experiments.

6.1.4 Characterization techniques

The crystalline phase of all nanostructures under investigation was analyzed by X-ray diffraction (XRD, Bruker D8 Advanced Diffractometer, $\text{Cu K}\alpha$ radiation). The morphology was analyzed by means of TEM using a JEOL JEM 3010 microscope (1.7 Å point to point resolution at Scherzer defocus). Before TEM measurements, each sample was further diluted in water to an approximate concentration of 0.1 mg/mL and sonicated for 2 min. Luminescent measurements were carried out under 980 nm excitation using a laser diode (Thorlabs fiber-coupled laser 305 diode). The laser beam was focused on the sample using a lens to obtain a spot with a Gaussian intensity distribution with a 0.4 mm diameter. The emitted light was collected by a lens in a 90° configuration, and then transferred to a spectrophotometer (Avaspec-2048L-USB2) using an optical fiber.

6.2 Results and discussion

XRD patterns of the as prepared ZrNPs with varying Neodymium concentration are shown in Figure 6.1 and compared with undoped ZrNPs. Due to the nanocrystalline nature of the ZrO_2 , a significant broadening of the reflections is observed; however, it is clearly visible that the relative intensity and position of the peaks match well with the cubic fluorite crystal structure of zirconia (JCPDS 27-991). From our XRD data, it is visible that the crystallinity of the doped samples is as high as for the undoped sample, with no phase change or any additional phases appearing even for the sample with doping concentration of 11 mol%, indicating that the europium ions are homogeneously distributed within the zirconia.

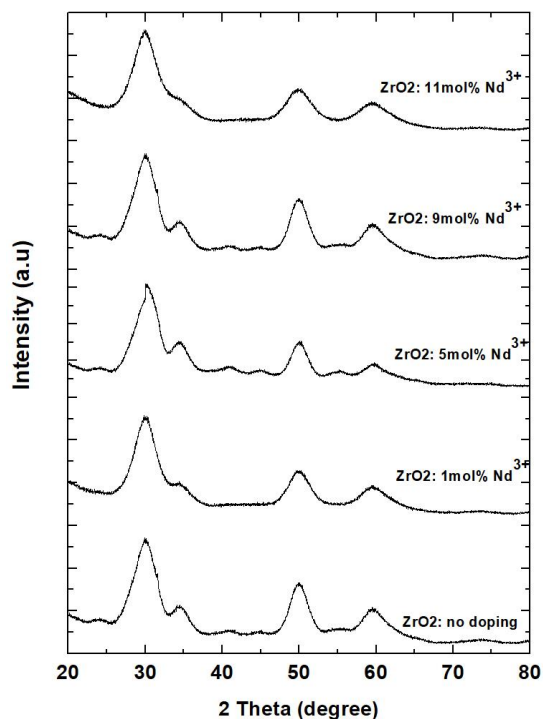


Figure 6.1. XRD patterns of undoped and Nd³⁺-doped ZrNP with varying dopant concentration.

In Figure 6.2, TEM images of the 1 mol%, 5 mol% and 9 mol% Nd³⁺-doped ZrNPs are presented, with the overview images showing the presence of spherical nanoparticles with a mean diameter of 4 nm, which is in good agreement with the results from XRD analysis. For all samples, the nanoparticles possess a rather narrow particle size distribution.

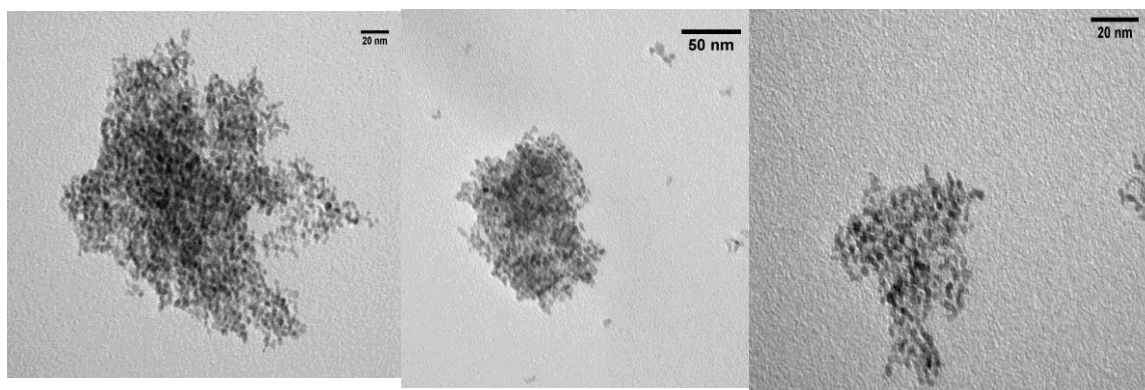


Figure 6.2. TEM images of the 1 mol% (eft), 5 mol% (middle) and 9 mol% Nd³⁺ doped ZrNPs

The materials will be used for infrared fluorescence bioimaging. These data require additional time for acquisition and are not included in this thesis.

7. Conclusions

In conclusion we successfully developed a straightforward method for ZrNPs surface modification based on the interaction with aqueous solutions of bisphosphonic acids. The latter class of organic molecules can be easily prepared bearing different substituents in the side chain that can be tailored in terms of length of C atoms, presence of functional groups and polarity. The use of BPs enabled the functionalization of the ZrNPs leading to new highly charged materials characterized by very low aggregation properties and high colloidal stability. The interaction between the BPs and the ZrNPs has been thoroughly investigated by quantitative ^1H NMR in solution to ascertain the effects of the structures and charges of the organic BPs, and by TEM, SEM, ζ -potential measurements, IR, TGA, solid state NMR and XPS to investigate the surface properties of the NPs before and after functionalization. Overall, the BPs ensure higher affinity compared to commercially available monophosphonates thanks to both better chelating properties and higher charge content. BPs turned out to be suitable for the modification of the surface properties of ZrNPs with a straightforward method that resembles the use of trichloro or *tris*-alkoxysilanes with silica NPs but based on much simpler, faster covalent process with no by-product formation. The possibility to use BPs bearing other functional groups in the side chain like amino, carboxylic acid and alkene paves the way for further covalent functionalization, in particular for biomedical applications. Moreover, thanks to preliminary experiments here reported, the functionalization method could be extended to other nanostructured metal oxides such as TiO_2 , Bi_2O_3 and Fe_3O_4 for which the traditional *tris*-alkoxysilane method is commonly employed.

8. Reference

- [1]. Arzt, E., Size effects in materials due to microstructural and dimensional constraints: A comparative review. *Acta Mater.* **1998**, *46* (16), 5611-5626.
- [2]. Forrest, J.; Dalnoki-Veress, K.; Stevens, J.; Dutcher, J., Effect of free surfaces on the glass transition temperature of thin polymer films. *Physical review letters* **1996**, *77* (10), 2002.
- [3]. Pankhurst, Q. A.; Connolly, J.; Jones, S.; Dobson, J., Applications of magnetic nanoparticles in biomedicine. *Journal of physics D: Applied physics* **2003**, *36* (13), R167.
- [4]. Steinhögl, W.; Schindler, G.; Steinlesberger, G.; Engelhardt, M., Size-dependent resistivity of metallic wires in the mesoscopic range. *Physical Review B* **2002**, *66* (7), 075414.
- [5]. Kelly, K. L.; Coronado, E.; Zhao, L. L.; Schatz, G. C., The optical properties of metal nanoparticles: the influence of size, shape, and dielectric environment. *The Journal of Physical Chemistry B* **2003**, *107* (3), 668-677.
- [6] (a). Buchmeister, M. R. J. *Chromatogr.*, A **2001**, *918*, 233. (b) Leonard, M. J. *Chromatogr.*, B: Biomed. Sci. Appl. **1997**, *699*, 3.
- [7]. Xie, Y. B.; Zhou, L. M.; Huang, H. A. T. *Biosens. Bioelectron.* **2007**, *22*, 2812.
- [8]. Popat, K. C.; Eltgroth, M.; La Tempa, T. J. *Biomaterials* **2007**, *28*, 4880.
- [9]. Shrestha, N. K.; Macak, J. M.; Schmidt-Stein, F. *Angew. Chem., Int. Ed.* **2009**, *48*, 969.
- [11]. Huang, F.; Chen, D.; Zhang, X. L.; Caruso, R. A.; Cheng, Y. B. *Adv. Funct. Mater.* **2010**, *20*, 1301
- [12]. Adamson, A. W.; Gast, A. P. *Physical Chemistry of Surfaces*, 6th ed.; Wiley-Interscience: New York, **1997**.
- [13]. N.T.K. Thanh, L.A.W. Green, *Nano Today*; **2010**, *5*, 213—230
- [14]. B. Basu and K. Balani, *Advanced Structural Ceramics*, Wiley, **2011**.
- [15]. R. B. Heimann, *Classic and Advanced Ceramics: From Fundamentals to Applications*, Wiley-VCH, **2010**.
- [16]. Chang, J.P.; Lin, Y.S.; Chu, K. *J. Vac. Sci. Technol. B*, **2001**, *19*, 1782.
- [17]. J. Gao, Y. He and W. Gao, *High Temp. Mater. Processes*, **2011**, *30*, 289.
- [18]. J. R. Kelly and I. Denry, *Dent. Mater.*, **2008**, *24*, 289.
- [19]. E. Tsalouchou, M. J. Cattell, J. C. Knowles and P. Pittayachawan, *Dent. Mater.*, **2008**, *24*, 308.
- [20]. T. Chartier, D. Merle and J. L. Besson, *J. Eur. Ceram. Soc.*, **1995**, *15*, 101.
- [21]. A. Tsoga, A. Gupta, A. Naoumidis and P. Nikolopoulos, *Acta Mater.*, **2000**, *48*, 4709.
- [22]. K. Wincewicz and J. Cooper, *J. Power Sources*, **2005**, *140*, 280.
- [23]. J. H. Lee, *J. Mater. Sci.*, **2003**, *38*, 4247.
- [24]. G. Lu, N. Miura and N. Yamazoe, *Sens. Actuators, B*, **1996**, (35-36), 130.
- [25]. R. Reisfeld, M. Zelner and A. Patra, *J. Alloys Compd.*, **2000**, *300–301*, 147.
- [26]. S. H. Yang, S. B. Kim, B. A. Kang, Y. H. Yun, Y. Kim and K. S. Hwang, *J. Mater. Synth. Process.*, **2001**, *9*, 275.

- [27]. P. D. L. Mercera, J. G. van Ommen, E. B. M. Doesburg, A. J. Burggraaf and J. R. H. Ross, *Appl. Catal.*, **1991**, 78, 79.
- [28]. P. C. Guess, W. Att and J. R. Sturb, *Clin. Implant Dent. Relat. Res.*, **2012**, 14, 663.
- [29]. Sang, L.; Zhao, Y.; Burda, C., TiO₂ Nanoparticles as Functional Building Blocks. *Chem. Rev.* **2014**, 114 (19), 9283-9318.135
- [30]. Diebold, U. *Surf. Sci. Rep.* **2003**, 48, 53.
- [31]. Roy, P.; Berger, S.; Schmuki, P. *Angew. Chem. Int. Ed.* **2011**, 50, 2904
- [32]. Howe, R. F.; Gratzel, M., EPR study of hydrated anatase under UV irradiation. *Journal of Physical Chemistry* **1987**, 91 (14), 3906-3909.
- [33]. Bachinger, A.; Kickelbick, G., Photocatalytic stability of organic phosphonates and phosphates on TiO₂ nanoparticles. *Appl. Catal., A* **2011**, 409-410, 122-132.
- [34]. Ulrich, G. D., Theory of particle formation and growth in oxide synthesis flames. *Combust. Sci. Technol.* **1971**, 4 (2), 47-57.
- [35]. Burns, A.; Ow, H.; Wiesner, U., Fluorescent core-shell silica nanoparticles: towards "Lab on a Particle" architectures for nanobiotechnology. *Chemical Society Reviews* **2006**, 35 (11), 1028-1042.
- [36]. Stöber, W.; Fink, A.; Bohn, E., Controlled growth of monodisperse silica spheres in the micron size range. *Journal of Colloid and Interface Science* **1968**, 26 (1), 62-69.
- [37]. Kresge, C. T.; Leonowicz, M. E.; Roth, W. J.; Vartuli, J. C.; Beck, J. S. *Nature* **1992**, 359, 710-712 (alkyltrimethylammonium).
- [38]. Huo, Q. S.; Leon, R.; Petroff, P. M.; Stucky, G. D. *Science* **1995**, 268, 1324-1327 (gemini surfactant).
- [39]. Bagshaw, S. A.; Prouzet, E.; Pinnavaia, T. J. *Science* **1995**, 269, 1242-1244 (ethylene oxide).
- [40]. Zhao, D. Y.; Feng, J. L.; Huo, Q. S.; Melosh, N.; Fredrickson, G. H.; Chmelka, B. F.; Stucky, G. D. *Science* **1998**, 279, 548-552 (block copolymer).
- [41]. Zhao, D. Y.; Huo, Q. S.; Feng, J. L.; Chmelka, B. F.; Stucky, G. D. *J. Am. Chem. Soc.* **1998**, 120, 6024-6036 (block copolymer).
- [42]. Tanev, P. T.; Pinnavaia, T. J. *Science* **1995**, 267, 865-867 (amine).
- [43]]. Oudghiri-Hassani H, Rakass S, Al Wadaani FT, Al-ghamdi KJ, Omer A, et al. (2015) Synthesis, characterization and photocatalytic activity of α -Bi₂O₃ nanoparticles. *J Taibah Univ, Sci* 9: 508-512.
- [44]. P. Patnaik, Handbook of Inorganic Chemical Compounds, McGraw-Hill (2003).
- [45]. P. Shuk, H. D. Wiemhofer, U. Guth, W. Gopel, and M. Greenblatt, *Solid State Ionics* 89, 179, **1996**
- [46]. N. M. Sammes, G. A. Tompsett, H. Nafe, and F. Aldinger, *J. Eur. Cer. Soc.* 19, 1801, **1999**
- [47]. N. X. Jiang, E. D. Wachsman, and S.-H. Jung, *Solid State Ionics* 150, 347, **2002**.
- [48]. S. Hull, *Rep. Prog. Phys.* 67, 1233, **2004**.
- [49]. A. Orera and P. R. Slater, *Chem. Mat.* 22, 675 (2010).
- [50]. F. H. Elbatal, *Nucl. Instr. and Meth. in Phys. Res. B* 254, 243 (2007).

- [51]. A. Bajaj, A. Khanna, B. G. Chen, J. G. Longstaffe, U.-W. Zwanziger, J. W. Zwanziger, Y. Gómez, and F. González, *J. Non-Cryst. Solids* 355, 45 (2009).
- [52]. N. Chanthima, J. Kaewkhao, C. Kedkaew, W. Chewpraditkul, A. Pokaipist, and P. Limsuwan, *Prog. Nucl. Sci. Tech.* 1, 106 (2011).
- [53]. K. Won-in, S. Pongkrapan, and P. Dararutana, *Mat. Sci. Forum* 695, 223 (2011).
- [54]. S. Ghedia, T. Locherer, R. Dinnebier, D. L. V. K. Prasad, U. Wedig, M. Jansen, and A. Senyshyn, *Phys. Rev. B* 82, 024106 (2010).
- [55]. T. Locherer, Dasari L. V. K. Prasad, R. Dinnebier, U. Wedig, M. Jansen, G. Garbarino, and T. Hansen, *Phys. Rev. B* 83, 214102 (2011).
- [56]. Wells, A.F. (1984) *Structural Inorganic Chemistry*. 5th. London, England: Oxford University Press. p.890 [ISBN 0-19-855370-6](#)
- [57]. Radaev, S. F.; Simonov, V. I.; Kargin, Yu. F. (1992). "Structural features of γ -phase Bi_2O_3 and its place in the sillenite family". *Acta Crystallographica Section B*. **48** (5): 604–9.
- [58]. Harwig, H. A. (1978). "On the Structure of Bismuthsesquioxide: The α , β , γ , and δ -phase". *Zeitschrift für anorganische und allgemeine Chemie*. **444**: 151–66
- [59]. Meyyappan, S.; Shadnam, M. R.; Amirfazli, A., Fabrication of surface energy/chemical gradients using self-assembled monolayer surfaces. *Langmuir* **2008**, 24, (6), 2892-2899.
- [60]. Arima, Y.; Iwata, H., Effect of wettability and surface functional groups on protein adsorption and cell adhesion using well-defined mixed self-assembled monolayers. *Biomaterials* **2007**, 28, (20), 3074-3082.
- [61]. Feng, X. J.; Jiang, L., Design and creation of superwetting/antiwetting surfaces. *Advanced Materials* **2006**, 18, (23), 3063-3078.
- [62]. Balss, K. M.; Avedisian, C. T.; Cavicchi, R. E.; Tarlov, M. J., Nanosecond imaging of microboiling behavior on pulsed-heated Au films modified with hydrophilic and hydrophobic self-assembled monolayers. *Langmuir* **2005**, 21, (23), 10459-10467.
- [63]. Critchley, K.; Jeyadevan, J. P.; Fukushima, H.; Ishida, M.; Shimoda, T.; Bushby, R. J.; Evans, S. D., A mild photoactivated hydrophilic/hydrophobic switch. *Langmuir* **2005**, 21, (10), 4554-4561.
- [64]. Yang, Y.; Wang, W.; Li, J. R.; Mu, J.; Rong, H. L., Manipulating the solubility of gold nanoparticles reversibly and preparation of water-soluble sphere nanostructure through micellar-like solubilization. *Journal of Physical Chemistry B* **2006**, 110, (34), 16867-16873.
- [65]. Love, J. C.; Estroff, L. A.; Kriebel, J. K.; Nuzzo, R. G.; Whitesides, G. M., Selfassembled monolayers of thiolates on metals as a form of nanotechnology. *Chemical Reviews* **2005**, 105, (4), 1103-1169.
- [66]. Klauk, H.; Zschieschang, U.; Halik, M., Low-voltage organic thin-film transistors with large transconductance. *Journal of Applied Physics* **2007**, 102, (7), 074514.
- [67]. Klauk, H.; Zschieschang, U.; Pflaum, J.; Halik, M., Ultralow-power organic complementary circuits. *Nature* **2007**, 445, (7129), 745-748.36

- [68]. Byrne, P. D.; Facchetti, A.; Marks, T. J., High-performance thin-film transistors from solution-processed cadmium selenide and a self-assembled multilayer gate dielectric. *Advanced Materials* **2008**, 20, (12), 2319-2324.
- [69]. DiBenedetto, S. A.; Frattarelli, D.; Ratner, M. A.; Facchetti, A.; Marks, T. J., Vapor phase self-assembly of molecular gate dielectrics for thin film transistors. *Journal of the American Chemical Society* **2008**, 130, (24), 7528-7529.
- [70]. Facchetti, A.; Yoon, M. H.; Marks, T. J., Gate dielectrics for organic field-effect transistors: New opportunities for organic electronics. *Advanced Materials* **2005**, 17, (14), 1705-1725.
- [71]. Gawalt, E. S.; Avaltroni, M. J.; Danahy, M. P.; Silverman, B. M.; Hanson, E. L.; Midwood, K. S.; Schwarzbauer, J. E.; Schwartz, J., Bonding organics to Ti alloys: Facilitating human osteoblast attachment and spreading on surgical implant materials corrections (vol 19, pg 200, 2003). *Langmuir* **2003**, 19, (17), 7147-7147.
- [72]. Wang, L.; Yoon, M. H.; Facchetti, A.; Marks, T. J., Flexible inorganic/organic hybrid thin-film transistors using all-transparent component materials. *Advanced Materials* **2007**, 19, (20), 3252-3256.
- [73]. Felhosi, I.; Telegdi, J.; Palinkas, G.; Kalman, E., Kinetics of self-assembled layer formation on iron. *Electrochimica Acta* **2002**, 47, (13-14), 2335-2340.
- [74]. Yip, H. L.; Hau, S. K.; Baek, N. S.; Ma, H.; Jen, A. K. Y., Polymer solar cells that use self-assembled-monolayer-modified ZnO/metals as cathodes. *Advanced Materials* **2008**, 20, (12), 2376-2382.
- [75]. Paniagua, S. A.; Hotchkiss, P. J.; Jones, S. C.; Marder, S. R.; Mudalige, A.; Marrikar, F. S.; Pemberton, J. E.; Armstrong, N. R., Phosphonic acid modification of indium-tin oxide electrodes: Combined XPS/UPS/contact angle studies. *Journal of Physical Chemistry C* **2008**, 112, (21), 7809-7817.
- [76]. Koh, S. E.; McDonald, K. D.; Holt, D. H.; Dulcey, C. S.; Chaney, J. A.; Pehrsson, P. E., Phenylphosphonic acid functionalization of indium tin oxide: Surface chemistry and work functions. *Langmuir* **2006**, 22, (14), 6249-6255.
- [77]. Ashkenasy, G.; Cahen, D.; Cohen, R.; Shanzer, A.; Vilan, A., Molecular engineering of semiconductor surfaces and devices. *Accounts of Chemical Research* **2002**, 35, (2), 121-128.
- [78]. (a) Ribot, F.; Sanchez, C. *Comments Inorg. Chem.* **1999**, 20, 327. (b) Schubert, U.; Husing, N.; Lorenz, A. *Chem. Mater.* **1995**, 7, 2010.
- [79]. Pesek, J. J.; Tang, V. H. *Chromatographia* 1994, 39, 649.
- [80]. Brinker, C. J.; Scherer, G. W. In *Sol-Gel Science: The Physics and Chemistry of Sol-Gel Processing*; Academic Press: New York, **1990**.
- [81]. Schubert, U.; Husing, N.; Lorenz, A. *Chem. Mater.* **1995**, 7, 2010-2027
- [82]. Delattre, L.; Dupuy, C.; Babonneau, F. *J. Sol-Gel Sci. Technol.* **1994**, 2, 185-188.
- [83]. Marcinko, S.; Fadeev, A. Y. *Langmuir* **2004**, 20, 2270-2273.
- [84]. Silberzan, P.; Leger, L.; Ausserre, D.; Benattar, J., Silanation of silica surfaces. A new method of constructing pure or mixed monolayers. *Langmuir* **1991**, 7 (8), 1647-1651.

- [85]. Glaser, A.; Foisner, J.; Hoffmann, H.; Friedbacher, G., Investigation of the Role of the Interplay between Water and Temperature on the Growth of Alkylsiloxane Submonolayers on Silicon. *Langmuir* **2004**, *20* (13), 5599-5604.
- [86]. Fadeev, A. Y.; McCarthy, T. J., Self-Assembly Is Not the Only Reaction Possible between Alkyltrichlorosilanes and Surfaces: Monomolecular and Oligomeric Covalently Attached Layers of Dichloro- and Trichloroalkylsilanes on Silicon. *Langmuir* **2000**, *16* (18), 7268-7274.
- [87]. Sugahara, Y.; Okada, S.; Sato, S.; Kuroda, K.; Kato, C., ²⁹Si-NMR study of hydrolysis and initial polycondensation processes of organoalkoxysilanes. II. Methyltriethoxysilane. *J. Non-Cryst. Solids* **1994**, *167* (1-2), 21-8.
- [88]. Mutin, P. H.; Guerrero, G.; Vioux, A., Hybrid materials from organophosphorus coupling molecules. *Journal of Materials Chemistry* **2005**, *15*, 3761 - 3768.
- [89]. Julian, B.; Gervais, C.; Rager, M.-N.; Maquet, J.; Cordoncillo, E.; Escribano, P.; Babonneau, F.; Sanchez, C. *Chem. Mater.* **2004**, *16*, 521-529.
- [90]. Nawrocki, J.; Dunlap, C.; Li, J.; Zhao, J.; McNeff, C. V.; McCormick, A.; Carr, P. W. *J. Chromatogr., A* **2004**, 1028, 31.
- [91]. Tosatti, S.; De Paul, S. M.; Askendal, A.; VandeVondele, S.; Hubbell, J. A.; Tengvall, P.; Textor, M. *Biomaterials* **2003**, *24*, 4949-4958.
- [92]. Prucker, O.; Rühhe, J. *Macromolecules* **1998**, *31*, 592-601.
- [93]. Böttcher, H.; Hallensleben, M. L.; Nuss, S.; Wurm, H. *Polym. Bull.* **2000**, *44*, 223-229.
- [94]. Jordan, R.; Ulman, A.; Kang, J. F.; Rafailovich, M. H.; Sokolov, J. *J. Am. Chem. Soc.* **1999**, *121*, 1016-1022.
- [95]. Jordan, R.; Ulman, A. *J. Am. Chem. Soc.* **1998**, *120*, 243-247.
- [96]. Witte, P.; Menzel, H. *Macromol. Chem. Phys.* **2004**, *205*, 1735-1743.
- [97]. Kickelbick, G., Concepts for the incorporation of inorganic building blocks into organic polymers on a nanoscale. *Progress in Polymer Science* **2003**, *28* (1), 83-114.
- [98]. Queffelec, C.; Petit, M.; Janvier, P.; Knight, D. A.; Bujoli, B., Surface Modification Using Phosphonic Acids and Esters. *Chem. Rev.* **2012**, *112* (7), 3777-3807
- [99]. Gao, W.; Dickinson, L.; Grozinger, C.; Morin, F. G.; Reven, L. *Langmuir* **1996**, *12*, 6429-6435.
- [100]. Guerrero, G.; Mutin, P. H.; Vioux, A. *Chem. Mater.* **2001**, *13*, 4367-4373.
- [101]. Brovelli, D.; Haehner, G.; Ruiz, L.; Hofer, R.; Kraus, G.; Waldner, A.; Schloesser, J.; Oroszlan, P.; Ehrat, M.; Spencer, N. D. *Langmuir* **1999**, *15*, 4324-4327.
102. Traina, C. A.; Schwartz, J. *Langmuir* **2007**, *23*, 9158-9161.
103. Daou, T. J.; Greneche, J. M.; Pourroy, G.; Buathong, S.; Derory, A.; Ulhaq-Bouillet, C.; Donnio, B.; Guillon, D.; Begin-Colin, S. *Chem. Mater.* **2008**, *20*, 5869-5875.
104. Rill, C.; Ivanovici, S.; Kickelbick, G. *Mater. Res. Soc. Symp. Proc.* **2007**, paper no. 1007-S1012-1002.
- [105]. Schulmeyer, T.; Paniagua, S. A.; Veneman, P. A.; Jones, S. C.; Hotchkiss, P. J.; Mudalige, A.; Pemberton, J. E.; Marder, S. R.; Armstrong, N. R. *J. Mater. Chem.* **2007**, *17*, 4563-4570.
- [106]. P. H. Mutin, G. Guerrero and A. Vioux, *J. Mater. Chem.*, **2005**, *15*, 3761-3768.

- [107]. C. Queffelec, M. Petit, P. Janvier, D. A. Knight and B. Bujoli, *Chem. Rev.*, **2012**, 112, 3777–3807.
- [108]. H. Ma, O. Acton, D. O. Hutchins, N. Cernetic and A. K. Y. Jen, *Phys. Chem. Chem. Phys.*, **2012**, 14, 14110–14126.
- [109]. P. J. Hotchkiss, S. C. Jones, S. A. Paniagua, A. Sharma, B. Kippelen, N. R. Armstrong and S. R. Marder, *Acc. Chem. Res.*, **2012**, 45, 337–346.
- [110]. J. C. Love, L. A. Estroff, J. K. Kriebel, R. G. Nuzzo and G. M. Whitesides, *Chem. Rev.*, **2005**, 105, 1103–1170.
- [111]. S. Onclin, B. J. Ravoo and D. N. Reinhoudt, *Angew. Chem., Int. Ed.*, **2005**, 44, 6282–6304.
- [112]. A. Ulman, *Chem. Rev.*, **1996**, 96, 1533–1554.
- [113]. G. Guerrero, P. H. Mutin and A. Vioux, *Chem. Mater.*, **2001**, 13, 4367–4373.
- [114]. G. Guerrero, P. Mutin and A. Vioux, *J. Mater. Chem.*, **2001**, 11, 3161–3165.
- [115]. I. L. Liakos, R. C. Newman, E. McAlpine and M. R. Alexander, *Langmuir*, **2007**, 23, 995–999.
- [116]. K.-C. Liao, H. Anwar, I. G. Hill, G. K. Vertelov and J. Schwartz, *ACS Appl. Mater. Interfaces*, **2012**, 4, 6735–6746.
- [117]. Angelom_e, P. C.; Aldabe-Bilmes, S. *New J. Chem.* **2005**, 29, 59.
- [118]. Corbridge, D. E. C. Phosphorus—An Outline of its Chemistry, Biochemistry and Technology; Elsevier Science: Amsterdam, **1990**.
- [119]. He, H. B.; Feng, Y.-Q.; Da, S.-L.; Wang, Z.-H. *Anal. Chim. Acta* **2005**, 551, 213.
- [120]. Sizgek, G. D.; Griffith, C. S.; Sizgek, E.; Luca, V. *Langmuir* **2009**, 25, 11874.
- [121]. Lafond, V.; Gervais, C.; Maquet, *J. Chem. Mater.* **2003**, 15, 4098.
- [122]. S. Marcinko and A. Y. Fadeev, *Langmuir*, **2004**, 20, 2270–2273.
- [123]. Helmy, R.; Fadeev, A. Y. *Langmuir* **2002**, 18, 8924.
- [124]. Fujishima, A.; Zhang, X.; Tryk, D. A. *Surf. Sci. Rep.* **2008**, 63, 515.
- [125]. [G. Guerrero, P. H. Mutin and A. Vioux, *Chem. Mater.*, **2001**, 13, 4367–4373.
- [126]. G. Guerrero, P. Mutin and A. Vioux, *J. Mater. Chem.*, **2001**, 11, 3161–3165.
- [127]. G. Mani, D. M. Johnson, D. Marton, V. L. Dougherty, M. D. Feldman, D. Patel, A. A. Ayon and C. M. Agrawal, *Langmuir*, **2008**, 24, 6774–6784103
- [128]. K.-M. Jo, H.-Z. Yu and H.-S. Yang, *Electrochim. Acta*, **2011**, 56, 4828–4833
- [129]. G. Lecollinet, N. Delorme, M. Edely, A. Gibaud, J. F. Bardeau, F. Hindré, F. Boury and D. Portet, *Langmuir*, **2009**, 25, 7828–7835.
- [130]. C. S. Griffith, M. D. L. Reyes, N. Scales, J. V. Hanna and V. Luca, *ACS Appl. Mater. Interfaces*, **2010**, 2, 3436–3446.
- [131]. P. Cao, L. Tong, Y. Hou, G. Zhao, G. Guerin, M. A. Winnik and M. Nitz, *Langmuir*, **2012**, 28, 12861–12870.
- [132]. A. Ide, G. L. Drisko, N. Scales, V. Luca, C. H. Schiesser and R. A. Caruso, *Langmuir*, **2011**, 27, 12985–12995.

- [133]. I. Rehor, V. Kubicek, J. Kotek, P. Hermann, J. Szakova and I. Lukes, *Eur. J. Inorg. Chem.*, **2011**, 1981–1989
- [134]. Denizot, B.; Tanguy, G.; Hindre, F.; Rump, E.; Jacques Le Jeune, J.; Jallet, P. Phosphorylcholine Coating of Iron Oxide Nanoparticles. *J. Colloid Interface Sci.* **1999**, 209(1), 66-71.
- [135]. Portet, D.; Denizot, B.; Rump, E.; Lejeune, J. J.; Jallet, P. Nonpolymeric Coatings of Iron Oxide Colloids for Biological Use as Magnetic Resonance Imaging Contrast Agents. *J. Colloid Interface Sci.* **2001**, 238(1), 37-42.
- [136]. Mani, G.; Johnson, D. M.; Marton, D.; Dougherty, V. L.; Feldman, M. D.; Patel, D.; Ayon, A. A.; Agrawal, C. M. Stability of Self-Assembled Monolayers on Titanium and Gold. *Langmuir* **2008**, 24(13), 6774-6784.
- [137]. Hofer, R.; Textor, M.; Spencer, N. D., Alkyl Phosphate Monolayers, Self- Assembled from Aqueous Solution onto Metal Oxide Surfaces. *Langmuir* **2001**, 17, 4014-4020.
- [138]. Portet, D.; Lecollinet, G.; Hindre, F.; Bejanin, S.; Chappard, D.; Denizot, B. Procédure de recouvrement de surfaces métalliques et minérales par des monocouches autoassemblées de composés bisphosphoniques et leurs utilisations. EP2007/058320, 2008-02-15, **2006**.
- [139]. Gawalt, E. S.; Avaltroni, M. J.; Koch, N.; Schwartz, J. Self-Assembly and Bonding of Alkanephosphonic Acids on the Native Oxide Surface of Titanium. *Langmuir* **2001**, 17, 5736-5738.
- [140]. Gouzman, I.; Dubey, M.; Carolus, M. D.; Schwartz, J.; Bernasek, S. L. Monolayer vs Multilayer Self-Assembled Alkylphosphonate Films: X-ray Photoelectron Spectroscopy Studies. *Surf. Sci.* **2006**, 600(4), 773-781.
- [141]. Ito, T.; Forman, S. M.; Cao, C.; Li, F.; Eddy, C. R.; Mastro, M. A.; Holm, R. T.; Henry, R. L.; Hohn, K. L.; Edga, J. H. Self-Assembled Monolayers of Alkylphosphonic Acid on GaN Substrates. *Langmuir* **2008**, 24, 6630-6635.
- [142]. T.A. Einhorn, R. Marcus, D. Feldman, J. Kelsey, “*Osteoporosis*”, Elsevier Academic Press, San Diego, **2008**, pp. 3-22.
- [143]. J. O. Hollinger, T. A. Einhorn, B. Doll, and C. Sfeir, *Bone Tissue Engineering*. Taylor & Francis, **2004**.
- [144]. N. A. Sims and J. H. Gooi, “Bone remodeling: Multiple cellular interactions required for coupling of bone formation and resorption,” *Seminars in Cell and Developmental Biology*, vol. 19, no. 5, pp. 444–451, **2008**.
- [145]. K. Matsuo and N. Irie, “Osteoclast-osteoblast communication,” *Archives of Biochemistry and Biophysics*, vol. 473, no. 2, pp. 201–209, **2008**.
- [146]. H. M. Frost, “Tetracycline-based histological analysis of bone remodeling,” *Calcified Tissue Research*, vol. 3, no. 1, pp. 211–237, **1969**.
- [147]. E. M. Hauge, D. Qvesel, E. F. Eriksen, L. Mosekilde, and F. Melsen, “Cancellous bone remodeling occurs in specialized compartments lined by cells expressing osteoblastic markers,” *Journal of Bone and Mineral Research*, vol. 16, no. 9, pp. 1575–1582, **2001**.

- [148]. T. L. Andersen, T. E. Sondergaard, K. E. Skorzynska et al., “A physical mechanism for coupling bone resorption and formation in adult human bone,” *American Journal of Pathology*, vol. 174, no. 1, pp. 239–247, **2009**
- [149]. M. Capulli, R. Paone, and N. Rucci, “Osteoblast and osteocyte: games without frontiers,” *Archives of Biochemistry and Biophysics*, vol. 561, pp. 3–12, **2014**.
- [150]. H. C. Anderson, “Matrix vesicles and calcification,” *Current Rheumatology Reports*, vol. 5, no. 3, pp. 222–226, **2003**.
- [151]. Y. Yoshiko, G. A. Candeliere, N. Maeda, and J. E. Aubin, “Osteoblast autonomous Pi regulation via Pit1 plays a role in bone mineralization,” *Molecular and Cellular Biology*, vol. 27, no. 12, pp. 4465–4474, **2007**.
- [152]. R. Florencio-Silva, G. R. D. S. Sasso, E. Sasso-Cerri, M. J. Simões, and P. S. Cerri, “Biology of Bone Tissue: Structure, Function, and Factors That Influence Bone Cells,” *Biomed Res. Int.*, vol. 2015, **2015**.
- [153]. U. H. Lerner, “Osteoblasts, Osteoclasts, and Osteocytes: Unveiling Their Intimate-Associated Responses to Applied Orthodontic Forces,” *Semin. Orthod.*, vol. 18, no. 4, pp. 237–248, **2012**.
- [154]. Florencio-Silva, R., et al., 2015. Biology of bone tissue: structure, function, and factors that influence bone cells. *Biomed. Res. Int.* **2015**.
- [155]. NIH consensus statement, *J.Am.Med.Ass.*, **2001**, 285, 785–795
- [156]. B.L. Riggs, H.W. Wahner, E. Seeman, K.P. Offord, W.L. Dunn, L.J. Melton, *J. Clin. Invest.*, **1982**, 70, 716–723.
- [157]. M. T. Drake, B. L. Clarke, and E. M. Lewiecki, “The Pathophysiology and Treatment of Osteoporosis,” *Clin. Ther.*, vol. 37, no. 8, pp. 1837–1850, **2015**
- [158]. J. E. Rossouw, G. L. Anderson, R. L. Prentice, A. Z. LaCroix, C. Kooperberg, M. L. Stefanick, R. D. Jackson, S. A. Beresford, B. V. Howard, K. C. Johnson, J. M. Kotchen, and J. Ockene, “Risks and Benefits of Estrogen Plus Progestin in Healthy Postmenopausal Women,” *Jama*, vol. 288, no. 3, pp. 321–333, **2002**.
- [159]. Morris, C.D.; Einhorn, T.A. Bisphosphonates in orthopaedic surgery. *J. Bone Jt. Surg. Am.* **2005**, 87, 1609–1618.
- [160]. Patel, S. Current and potential future drug treatments for osteoporosis. *Ann. Rheum Dis.* **1996**, 55, 700–714. [CrossRef] [PubMed]
- [161]. Weinstein, R.S.; Roberson, P.K.; Manolagas, S.C. Giant osteoclast formation and long-term oral bisphosphonate therapy. *N. Engl. J. Med.* **2009**, 360, 53–62. [CrossRef] [PubMed]
- [162]. Perugini, P.; Genta, I.; Conti, B.; Modena, T.; Pavanetto, F. Long-term release of clodronate from biodegradable microspheres. *AAPS Pharm. Sci. Tech.* **2001**, 2, 6–14. [CrossRef] [PubMed]
- [163]. Ismail, N.; Tahri, A.; Belbaraka, R. Bisphosphonates and innovative drugs in the prevention of skeletal complications secondary to metastatic prostate cancer. *Clin. Cancer Investig. J.* **2013**, 2, 294–297.
- [164]. European Medicines agency, <http://www.ema.europa.eu/ema/>

- [165]. F.H. Ebetino, M.D. Francis, M.J. Rogers, *Rev. Contemp. Pharmacother.*, **1999**, 9, 233–243.
- [166]. S.P. Luckman, F.P. Coxon, F.H. Ebetino, *J. Bone Miner. Res.*, **1998**, 13, 1668–1678.
- [167]. Bigi, A.; Gyorgi, E.; Oner, E.T. *Lasers in Materials Science*; Castillejo, M., Ossi, P.M., Zhigilei, L., Eds.; Springer: Cham, Switzerland, **2011**
- [168]. Drake, M.T.; Clarke, B.L.; Khosla, S. Bisphosphonates: Mechanism of action and role in clinical practice. *Mayo Clin. Proc.* **2008**, 83, 1032–1045.
- [169]. M. J. Rogers, J. C. Crockett, F. P. Coxon, and J. Mönkkönen, “Biochemical and molecular mechanisms of action of bisphosphonates,” *Bone*, vol. 49, no. 1, pp. 34–41, **2011**.
- [170]. F. H. Ebetino, A. M. L. Hogan, S. Sun, M. K. Tsoumpra, X. Duan, J. T. Triffitt, A. A. Kwaasi, J. E. Dunford, B. L. Barnett, U. Oppermann, M. W. Lundy, A. Boyde, B. A. Kashemirov, C. E. McKenna, and R. G. G. Russell, “The relationship between the chemistry and biological activity of the bisphosphonates,” *Bone*, vol. 49, no. 1, pp. 20–33, **2011**.
- [171]. Y. Zhang, R. Cao, F. Yin, F. Lin, H. Wang, K. Krysiak, J. No, D. Mukkamala, K. Houlihan, J. Li, C.T. Morita, E. Oldfield, *Angew. Chem. Int. Ed.*, **2010**, 49, 1136–1138.
- [172]. Fleisch, H. Bisphosphonates: Mechanisms of action. *Endocr. Rev.* **1998**, 19, 80–100. [CrossRef] [PubMed]
- [173]. Von Knoch, F.; Jaquier, C.; Kowalsky, M.; Schaeren, S.; Alabre, C.; Martin, I.; Rubash, H.E.; Shanbhag, A.S. Effects of bisphosphonates on proliferation and osteoblast differentiation of human bone marrow stromal cells. *Biomaterials* **2005**, 26, 6941–6949. [CrossRef] [PubMed]
- [174]. Im, G.I.; Qureshi, S.A.; Kenney, J.; Rubash, H.E.; Shanbhag, A.S. Osteoblast proliferation and maturation by bisphosphonates. *Biomaterials* **2004**, 18, 4105–4115. [CrossRef] [PubMed]
- [175]. Reinholz, G.G.; Getz, B.; Pederson, L.; Sanders, E.S.; Subramaniam, M.; Ingle, J.N.; Spelsberg, T.C. Bisphosphonates directly regulate cell proliferation, differentiation, and gene expression in human osteoblasts. *Cancer Res.* **2000**, 60, 6001–6007. [PubMed]
- [176]. Delmas, P.D.; Meunier, P.J. The management of Paget’s disease of bone. *N. Engl. J. Med.* **1997**, 336, 558–566. [PubMed]
- [177]. Kanis, J.A. Rationale for the use of bisphosphonates in breast cancer. *Acta Oncol.* **1996**, 35, 61–67. [CrossRef] [PubMed]
- [178]. Fleisch, H. Bisphosphonates: Preclinical aspects and use in osteoporosis. *Ann. Med.* **1997**, 29, 55–62.
- [179]. Seton, M.; Krane, S.M. Use of zoledronic acid in the treatment of Paget’s disease. *Ther. Clin. Risk Manag.* **2007**, 3, 913–918. [PubMed]
- [180]. Pazianas, M.; Abrahamsen, B.; Ferrari, S.; Russell, R.G.G. Eliminating the need for fasting with oral administration of bisphosphonates. *Ther. Clin. Risk Manag.* **2013**, 9, 395–402. [CrossRef] [PubMed]
- [181]. Johansen, A.; Stone, M.; Rawlinson, F. Bisphosphonates and the treatment of bone disease in the elderly. *Drugs Aging* **1996**, 8, 113–126. [CrossRef] [PubMed]
- [182]. Lin, J.H. Bisphosphonates: A review of their pharmacokinetic properties. *Bone* **1996**, 18, 75–85.

- [183]. Gómez, V.; Xiao, S.Y. Alendronate-induced esophagitis in an elderly woman. *Int. J. Clin. Exp. Pathol.* **2009**, *2*, 200–203. [PubMed]
- [184]. Niemi, R.; Vepsäläinen, J.; Taipale, H.; Jarvinen, T. Bisphosphonates prodrugs: Synthesis and an in vitro evaluation of novel acyloxyated esters of clodronic acid. *J. Med. Chem.* **1999**, *42*, 5053–5085. [CrossRef] [PubMed]
- [185]. Niemi, R.; Vepsäläinen, J.; Taipale, H.; Jarvinen, T. Bisphosphonates prodrugs: Synthesis and in vitro evaluation of alkyl and acyloxy esters of etidronic acid as bioreversible prodrugs of etidronate. *Eur. J. Pharm. Sci.* **2000**, *11*, 173–180.
- [186]. Boulenc, X.; Breul, T.; Gautier, J.C.; Saudemon, P.; Joyeux, H.; Roques, C.; Berger, Y.; Fabre, G. Sodium lauryl sulphate increases tiludronate paracellular transport using epithelial Caco-2 monolayers. *Int. J. Pharm.* **1995**, *123*, 71–83.
- [187]. Lindmark, T.; Kimura, Y.; Artursson, P. Absorption enhancement through intracellular regulation of tight junction permeability by medium chain fatty acids in Caco-2 cells. *J. Pharmacol. Exp. Ther.* **1998**, *284*, 362–369. [PubMed]
- [188]. Raiman, J.; Törmälehto, S.; Yrity, K.; Junginger, H.E.; Mönkkönen, J. Effect of various absorption enhancer on transport of clodronate through Caco-2 cells. *Int. J. Pharm.* **2003**, *261*, 129–136.
- [189]. Low, S.A.; Kopeček, J. Targeting polymer therapeutics to bone. *Adv. Drug Deliv. Rev.* **2012**, *64*, 1189–1204. [CrossRef] [PubMed]
- [190]. Wysowski, D.K.; Chang, J.T. Alendronate and risedronate: Reports of severe bone, joint, and muscle pain. *Arch. Intern. Med.* **2005**, *165*, 346–347. [PubMed]
- [191]. Penning-Van Beest, F.J.; Goettsch, W.G.; Erkens, J.A.; Herings, R.M. Determinants of persistence with bisphosphonates: A study in women with postmenopausal osteoporosis. *Clin. Ther.* **2006**, *28*, 236–242. [CrossRef] [PubMed]
- [192]. Ideguchi, H.; Ohno, S.; Hattori, H.; Ishigatsubo, Y. Persistence with bisphosphonate therapy including treatment courses with multiple sequential bisphosphonates in the real world. *Osteoporos. Int.* **2007**, *18*, 1421–1427. [CrossRef] [PubMed]
- [193]. S. Zhang, G. Gangal, and H. Uludağ, “‘Magic bullets’ for bone diseases: progress in rational design of bone-seeking medicinal agents,” *Chem. Soc. Rev.*, vol. 36, no. 3, pp. 507–531, **2007**
- [194]. Giger, E.V.; Castagner, B.; Leroux, J.C. Biomedical applications of bisphosphonates. *J. Control. Release* **2013**, *167*, 175–188. [CrossRef] [PubMed]
- [195]. Cartmell, S. Controlled release scaffolds for bone tissue engineering. *J. Pharm. Sci.* **2009**. [CrossRef] [PubMed]
- [196]. Roussière, H.; Fayon, F.; Alonso, B.; Rouillon, T.; Schnitzler, V.; Verron, E.; Guicheux, J.; Petit, M.; Massiot, D.; Janvier, P.; et al. Reaction of zoledronate with α -tricalcium phosphate for the design of potential drug device combined systems. *Chem. Mater.* **2008**, *20*, 182–191.
- [197]. Zhang, Y.; Dusad, A.; Ren, K. Drug delivery strategies for treating osteoporosis. *Orthop. Muscular. Syst.* **2014**, *3*, 1–4.

- [198]. Ezra, A.; Golomb, G. Administration routes and delivery systems of bisphosphonates for the treatment of bone resorption. *Adv. Drug Deliv. Rev.* **2000**, 42, 175–195.
- [199]. Seshima, H.; Yoshinari, M.; Takemoto, S.; Hattori, M.; Kawada, E.; Inoue, T.; Oda, Y. Control of bisphosphonate release using hydroxyapatite granules. *J. Biomed. Mater. Res. B* **2006**, 78, 215–221. [CrossRef] [PubMed]
- [200]. Su, K.; Shi, X.; Varshney, R.; Wang, D. Transplantable delivery systems for in situ-controlled release of bisphosphonate in orthopedic therapy. *Expert Opin. Drug Deliv.* **2011**, 8, 113–126. [CrossRef] [PubMed]
- [201]. Josse, S.; Faucheux, C.; Soueidan, A.; Grimandi, G.; Massiot, D.; Alonso, B.; Janvier, P.; Laib, S.; Pilet, P.; Gauthier, O.D.G.; et al. Novel biomaterials for bisphosphonate delivery. *Biomaterials* **2005**, 26, 2073–2080. [CrossRef] [PubMed]
- [202]. Karrholm, J.; Borssen, B.; Lowenhielm, G.; Snorrason, F. Does early micromotion of femoral stem prostheses matter? 4–7-Year stereoradiographic follow-up of 84 cemented prostheses. *J. Bone Jt. Surg. Br.* **1994**, 76, 912–917.
- [203]. Cremers, S.; Papapoulos, S. Pharmacology of bisphosphonates. *Bone* **2011**, 49, 42–49. [CrossRef] [PubMed]
- [204]. Sousa, S.; Auriola, S.; Mönkkönen, J.; Määttä, J. Liposome encapsulated zoledronate favours M1-like behaviour in murine macrophages cultured with soluble factors from breast cancer cells. *BMC Cancer* **2015**, 15, 1–11. [CrossRef] [PubMed]
- [205]. Bellido, T.; Plotkin, L.I. Novel actions of bisphosphonates in bone: Preservation of osteoblast and osteocyte viability. *Bone*. **2011**, 49, 50–55. [CrossRef] [PubMed]
- [206]. Gutman, D.; Golomb, G. Liposomal alendronate for the treatment of restenosis. *J. Control. Release*. **2012**, 161, 619–627. [CrossRef] [PubMed]
- [207]. Zeisberger, S.M.; Odermatt, B.; Marty, C.; Zehnder-Fjallman, A.H.M.; Ballmer-Hofer, K.; Schwendener, R.A. Clodronate-liposome-mediated depletion of tumour associated macrophages: A new and highly effective antiangiogenic therapy approach. *Br. J. Cancer* **2006**, 95, 272–281. [CrossRef] [PubMed]
- [208]. Salzano, G.; Marra, M.; Porru, M.; Zappavigna, S.; Abbruzzese, A.; la Rotonda, M.I.; Leonetti, C.; Caraglia, M.; de Rosa, G. Self-assembly nanoparticles for the delivery of bisphosphonates into tumors. *Int. J. Pharm.* **2011**, 403, 292–297. [CrossRef] [PubMed]
- [209]. Shmeeda, H.; Amitay, Y.; Gorin, J.; Tzemach, D.; Mak, L.; Ogorka, J.; Kumar, S.; Zhang, J.A.; Gabizon, A. Delivery of zoledronic acid encapsulated in folate-targeted liposome results in potent in vitro cytotoxic activity on tumor cells. *J. Control. Release* **2010**, 146, 76–83. [CrossRef] [PubMed]
- [210]. Kristen B. Farrell, Alexander Karpeisky, Douglas H. Thamm, Shawn Zinnen; *Bone Reports* **2018**, 9, 47–60
- [211]. Hochdorffer, K.; Abu, A.K.; Schafer-Obodozie, C.; Kratz, F. Development of novel bisphosphonate prodrugs of doxorubicin for targeting bone metastases that are cleaved pH dependently or by cathepsin B: Synthesis, cleavage properties, and binding properties to

hydroxyapatite as well as bone matrix. *J. Med. Chem.* **2012**, 55, 7502–7515. [CrossRef] [PubMed]

[212]. Klenner, T.; Wingen, F.; Kepper, B.K.; Krempien, B.; Schmahl, D. Anticancer-agent-linked phosphonates with antiosteolytic and antineoplastic properties: A promising perspective in the treatment of bone-related malignancies? *J. Cancer Res. Clin. Oncol.* **1990**, 116, 341–350. [CrossRef] [PubMed]

[213]. Sanchis, J.; Canal, F.; Lucas, R.; Vicent, M.J. Polymer-drug conjugates for novel molecular targets. *Nanomedicine* **2010**, 5, 915–935. [CrossRef] [PubMed]

[214]. Baabur-Cohen, H.; Omer, L.; Satchi-Fainaro, R. Recent progress in polymer therapeutics as nanomedicines. In *Handbook of Harnessing Biomaterials in Nanomedicine: Preparation, Toxicity and Applications*; Peer, D., Ed.; CRC Press: Boca Raton, FL, USA, **2012**.

[215]. B. Aderibigbe, I. Aderibigbe, and P. Popoola, “Design and biological evaluation of delivery systems containing bisphosphonates,” *Pharmaceutics*, vol. 9, no. 1, pp. 1–24, **2017**.

[216]. Parveen S, Sahoo SK. Nanomedicine: clinical applications of polyethylene glycol conjugated proteins and drugs. *Clin Pharmacokinet* **2006**; 45:965-88.

[217]. Lee HJ. Protein drug oral delivery: the recent progress. *Arch Pharm Res* **2002**; 25:572-84.

[218]. Kayser O, Lemke A, Hernandez-Trejo N. The impact of nanobiotechnology on the development of new drug delivery systems. *Curr Pharm Biotechnol* **2005**; 6:3-5.

[219]. S. Parveen, R. Misra, and S. K. Sahoo, “Nanoparticles: A boon to drug delivery, therapeutics, diagnostics and imaging,” *Nanomedicine Nanotechnology, Biol. Med.*, vol. 8, no. 2, pp. 147–166, **2012**.

[220]. W. H. De Jong and P. J. A. Borm, “Drug delivery and nanoparticles: applications and hazards,” *Int. J. Nanomedicine*, vol. 3, no. 2, pp. 133–149, **2008**.

[221]. F. H. Ebetino, A. M. L. Hogan, S. Sun, M. K. Tsoumpra, X. Duan, J. T. Triffitt, A. A. Kwaasi, J. E. Dunford, B. L. Barnett, U. Oppermann, M. W. Lundy, A. Boyde, B. A. Kashemirov, C. E. McKenna, and R. G. G. Russell, “The relationship between the chemistry and biological activity of the bisphosphonates,” *Bone*, vol. 49, no. 1, pp. 20–33, **2011**.

[222]. A. Z. Wilczewska, K. Niemirowicz, K. H. Markiewicz, and H. Car, “Nanoparticles as drug delivery systems,” *Pharmacol. Reports*, vol. 64, no. 5, pp. 1020–1037, **2012**.

[223] M. Petit and J. Monot, “Functionalization of Zirconium Oxide Surfaces,” *Chem. Organo-Hybrids*, pp. 168–199, **2015**

[224]. Garvie, R. C.; Nicholson, P. S. *J. Am. Ceram. Soc.* **1972**, 55, 152.

[225]. Garvie, R. C.; Hannink, R. H.; Pascoe, R. T. *Nature*, **1975**, 258, 703.

[226] C. Piconi and G. Maccauro, “Zirconia as a ceramic biomaterial,” *Biomaterials*, vol. 20, no. 1, pp. 1–25, Jan. **1999**.

[227] S. Nagarajan, M. Mohana, P. Sudhagar, and V. Raman, “ACS App Mat Nag **2012** Nanocomposite Coatings on Biomedical Grade Stainless Steel for Improved Corrosion Resistance and Biocompatibility,” no. October 2014

[228] S. Biz and M.L. Occelli. “Synthesis and Characterization of Mesostructured Materials”. In: *Catalysis Reviews* 40 (**1998**), pp. 329–407.

- [229] B. Basu and K. Balani. *Advanced Structural Ceramics*. Ed. by The American Ceramic Society. Wiley, **2011**. isbn: 978-0-470-49711-1.
- [230] R.B. Heimann. *Classic and Advanced Ceramics: From Fundamentals to Applications*. Wiley-VCH, **2010**. isbn: 978-3-527-32517-7.
- [231] P.D.L. Mercera et al. "Influence of ethanol washing of the hydrous precursor on the textural and structural properties of zirconia". In: *Journal of Materials Science* **27** (1992), pp. 4890–4898.
- [232] a) S. Zhang, G. Gangal, H. Uludağ, *Chem. Soc. Rev.* **2007**, *36*, 507; b) R. G. G. Russell, *Bone* **2011**, *49*, 2; c) F.H. Ebetino, A.-M.L. Hogan, S. Sun, M.K. Tsoumpra, X. Duan, J.T. Triffitt, A.A. Kwaasi, J.E. Dunford, B.L. Barnett, U. Oppermann, M.W. Lundy, A. Boyde, B.A. Kashemirov, C.E. McKenna, R.G.G. Russell, *Bone* **2011**, *49*, 20; d) M.J. Rogers, J.C. Crockett, F.P. Coxon, J. Mönkkönen, *Bone* **2011**, *49*, 34.
- [233] B. Heuzé, M. Lemarié, M. Vazeux, M. Gulea, S. Masson, Phosphorus, Sulfur, Silicon and Rel. El., **2009**, *184*, 820-829
- [234] J. J. Brophy, M. J. Gallagher, *Australian Journal of Chemistry*, **1967**, *20*, 503-513.
- [235] O.E.O. Hormi, E.O. Pajinen, A.C. Avall, P. Pennanen, *Synth. Comm.*, **1990**, *20*, 1865-1867.
- [236] D. Meziane, J. Hardouin, A. Elias, E. Gu'enin, M. Lecouvey, *Heteroatom Chemistry*, **2009**, *20*, 369-377.
- [237] J.B. Rodriguez, *Synthesis*, **2014**, *46*, 1129–1142.
- [238] C.R. Degenhardt, D.C. Burdsall, *J. Org. Chem.*, **1986**, *51*, 3488-3490
- [239] L. Kamm, W. McIlwraith, C. Kawcak, *J. Equine Vet. Sci.*, **2008**, *28*, 209-214.
- [240] Seto, H.; Takara, M.; Yamashita, C.; Murakami, T.; Hasegawa, T.; Hoshino, Y.; Miura, Y. *ACS Appl. Mater. Interfaces* **2012**, *4* (10), 5125–5133.
- [241] Khire, V. S.; Benoit, D. S. W.; Anseth, K. S.; Bowman, C. N. *J. Polym. Sci., Part A: Polym. Chem.* **2006**, *44* (24), 7027–7039.
- [242] Khire, V. S.; Kloxin, A. M.; Couch, C. L.; Anseth, K. S.; Bowman, C. N. *J. Polym. Sci., Part A: Polym. Chem.* **2008**, *46* (20), 6896–6906.
- [243] Khire, V. S.; Lee, T. Y.; Bowman, C. N. *Macromolecules* **2007**, *40* (16), 5669–5677.
- [244] Wang C, Qi C. Mechanistic insights into N- or P-centered nucleophile promoted thiol-vinylsulfone Michael addition. *Tetrahedron*. **2013**; *69*(26):5348–5354.

- [245]. Xi W, Wang C, Kloxin CJ, Bowman CN. Nitrogen-centered nucleophile catalyzed thiol-vinylsulfone addition, another thiol-ene “click” reaction. *ACS Macro Lett.* **2012**; 1:811–814. [Google Scholar]
- [246]. Chan JW, Hoyle CE, Lowe AB, Bowman M. Nucleophile-initiated thiol-Michael reactions: effect of organocatalyst, thiol and ene. *Macromolecules.* **2010**;43(15):6381–6388. [Google Scholar]
- [247] R. Lenin,R.M. Raju, D.V.N. Srinivasa Rao,U.K. Ray, *Med. Chem. Res.*, **2013**, 22, 1624-1629.
- [248]. C. Leung, A.M. Langille, J. Mancuso, Y.S. Tsantrizos, *Bioorganic & Medicinal Chemistry*, **2013**, 21, 2229–2240.
- [249]. D. Granchi, A. Scarso, G. Bianchini, A. Chiminazzo, G. Di Pompo, S. Avnet, G. Strukul, *Eur. J. Med. Chem.*, **2013**, 65, 448-455.
- [250] Alleti, R.; Oh, W. S.; Perambuduru, M.; Ramana, C. V.; Reddy, V. P. *Tetrahedron Lett.* **2008**, 49 (21), 3466–3470.
- [251] Moghaddam, F. M.; Bardajee, G. R.; Veranlou, R. O. C. *Synth. Commun.* **2005**, 35 (18), 2427–2433.
- [252] Movassagh, B.; Shokri, B. *Int. J. Org. Chem.* **2012**, 2, 248–253.
- [253] W. L. F. Armarego, C. Chai in *Purification of Laboratory Chemicals (Seventh Edition)*, Butterworth-Heinemann, Boston, **2013**.
- [254] W. C. Still, M. Kahn, A. Mitra, *J. Org. Chem.*, **1978**, 14, 2923-2925.
- [255] O.E.O. Hormi, E.O. Pajinen, A.C. Avall, P. Pennanen, *Synth. Comm.*, **1990**, 20, 1865-1867.
- [256] W. Gao, L. Dickinson, C. Grozinger, F. G. Morin, and L. Reven, “Self-Assembled Monolayers of Alkylphosphonic Acids on Metal Oxides,” *Langmuir*, vol. 12, no. 26, pp. 6429–6435, **1996**.
- [257] W. Xiong, J. Tong, Z. Yang, G. Zeng, Y. Zhou, D. Wang, P. Song, R. Xu, C. Zhang, and M. Cheng, “Adsorption of phosphate from aqueous solution using iron-zirconium modified activated carbon nanofiber: Performance and mechanism,” *J. Colloid Interface Sci.*, vol. 493, pp. 17–23, **2017**.
- [258] J. Bezençon, M. B. Wittwer, B. Cutting, M. Smieško, B. Wagner, M. Kansy, and B. Ernst, “pKadetermination by ¹H NMR spectroscopy - An old methodology revisited,” *J. Pharm. Biomed. Anal.*, vol. 93, pp. 147–155, **2014**.
- [259] M. Nilsing, S. Lunell, P. Persson, and L. Ojamäe, “Phosphonic acid adsorption at the TiO₂anatase (1 0 1) surface investigated by periodic hybrid HF-DFT computations,” *Surf. Sci.*, vol. 582, no. 1–3, pp. 49–60, **2005**.
- [260] N. C. Norman, *Chemistry of arsenic, antimony, and bismuth*, 1st ed. London, GB: Blackie Academic & Professional, **1998**.

- [261] M. Gunnar.” The Crystal Structure of alpha-Bi₂O₃.” *Acta Chemica Scandinavica*, vol. 24, pp. 384-396, **1970**.
- [262] K. Maruoka and T. Akiyama. *Brønsted base and acid catalysts, and additional topics*. vol. 2. Stuttgart, D: Thieme, **2012**.
- [263] C. J. Brinker, “Hydrolysis and condensation of silicates: Effects on structure,” *J. Non. Cryst. Solids*, vol. 100, no. 1–3, pp. 31–50, Mar. **1988**.
- [264] S. K. Davidowski and G. P. Holland, “Solid-State NMR Characterization of Mixed Phosphonic Acid Ligand Binding and Organization on Silica Nanoparticles,” *Langmuir*, vol. 32, no. 13, pp. 3253–3261, **2016**.
- [265] K. A. Majorek, P. J. Porebski, A. Dayal, M. D. Zimmerman, K. Jablonska, A. J. Stewart, M. Chruszcz, and W. Minor, “NIH Public Access,” vol. 52, pp. 174–182, **2013**.
- [266]. Naumkin, A. V. NIST X-Ray Photoelectron Spectroscopy Database, Version 4.1; Kraut-Vass, A., Powell, C. J., Gaarenstroom, S. W., Eds
- [267]. G. Sponchia, E. Ambrosi, F. Rizzolio, M. Hadla, A. D. Tedesco, C. R. Spena, G. Toffoli, P. Riello and A. Benedetti, *J. Mater. Chem. B*, **2015**, 3, 7300–7306
- [268] S. Marcinko, A.Y. Fadeev, *Langmuir* **2004**, 20, 2270-2273.
- [269] G. Guerrero, P.H. Mutin, A. Vioux, *Chem Mater* **2001**, 13, 4367-4373.
- [270] D. Price, L.K. Cunliffe, K.J. Bullett, T.R. Hull, G.J. Milnes, J.R. Ebdon, B.J. Hunt, P. Joseph, *Polymer Deg. Stab.* **2007**, 92, 1101-1114.
- [271] B. Basly, G. Popa, S. Fleutot, B.P. Pichon, A. Garofalo, C. Ghobril, C. Billotey, A. Berniard, P. Bonazza, H. Martinez, D. Felder-Flesch, S. Begin-Colin, *Dalton Trans.* **2013**, 42, 2146-2157.
- [272] P. Canepa, I. Solano, S. Uttiya, G. Gemme, R. Rolandi, M. Canepa, O. Cavalleri, *MATEC Web Conf.* **2017**, 98, 03001.
- [273] U. Glebe, J.E. Baio, L. Árnadóttir, U. Siemeling, T. Weidner, *ChemPhysChem* **2013**, 14, 1155-1160.
- [274] G. Zorn, L.-H. Liu, L. Árnadóttir, H. Wang, L.J. Gamble, D.G. Castner, M. Yan, *J. Physical Chem. C* **2014**, 118, 376-383
- [275] N. Zhao, L. Yan, X. Zhao, X. Chen, A. Li, D. Zheng, X. Zhou, X. Dai, F.-J. Xu, *Chem. Rev.* **2019**, 119, 1666-1762.
- [276] A. Heuer-Jungemann, N. Feliu, I. Bakaimi, M. Hamaly, A. Alkilany, I. Chakraborty, A. Masood, M.F. Casula, A. Kostopoulou, E. Oh, K. Susumu, M.H. Stewart, I.L. Medintz, E. Stratakis, W.J. Parak, A.G. Kanaras, *Chem. Rev.* **2019**, 119, 4819-4880.
- [277]. Birkby, R. Stevens, Applications of zirconia ceramics. In *Key Engineering Materials*, Vol. 122, pp. 527–552, Trans Tech Publications, **1996**.
- [278] S. Tang, X. Huang, X. Chen, N. Zheng, *Adv. Funct. Mater.*, **2010**, 20, 2442-2447.
- [279] a) S.H. Gong, H. Lee, A. Pae, K. Noh, Y.M. Shin, J.H. Lee, Y.H. Woo, *J. Adv. Prosthodont.* **2013**, 5, 416–422; b) C. Piconi, G. Maccauro, *Biomaterials*, **1999**, 20, 1–25

- [280] E.W. Leib, U.Vainio, R. M. Pasquarelli, J.Kus, C. Czaschke, N. Walter, R. Janssen, M. Müller, A. Schreyer, H. Weller, T.Vossmeyer, *J. Coll. Int. Sci.* **2015**, *448*, 582-592.
- [281] L. Renuka, K.S. Anantharaju, S.C. Sharma, H. Nagabhushana, Y.S. Vidya, H.P. Nagaswarupa, S.C. Prashan, *J. Alloys Compd.* **2017**, *695*, 382-395.
- [282] G. Sponchia, E. Ambrosi, F. Rizzolio, M. Hadla, A. Del Tedesco, C. Russo Spina, G. Toffoli, P. Riello, A. Benedetti, *J Mater Chem B* **2015**, *3*, 7300-7306
- [283] G. Pacchioni, *Eur. J. Inorg. Chem.* **2019**, 751–761.
- [284] J. Nawrocki, C. Dunlap, J. Li, J. Zhao, C.V. McNeff, A. McCormick, P.W. Carr, *J. Chromatogr. A* **2004**, *1028*, 31-62.
- [285] A. Bai, H. Song, G. He, Q. Lin, C. Yang, L. Tang, Y. Yu, *Ceramics Int.* **2016**, *42*, 7583–7592.
- [286] a) A. Liberman, N. Mendez, W. C. Trogler, and a. C. Kummel, *Surf. Sci. Rep.* **2014**, *69*, 132–158; b) S. Čampelj, D. Makovec, M. Drogenik, *J. Magn. Mater.* **2009**, *321*, 1346–1350; c) A. R. M. Dalod, L. Henriksen, T. Grande, M.-A. Einarsrud, *Beilstein J. Nanotechnol.* **2017**, *8*, 304–312
- [287] S. Kouva, K. Honkala, L. Lefferts, J. Kanervo, *Catal. Sci. Technol.* **2015**, *5*, 3473-3490.
- [288] H. Liu, X. Sun, C. Yin, C. Hu, *J. Haz. Mat.* **2008**, *151*, 616–622.
- [289] C.-C. Lin, Y.-S. Lin, J.-M. Ho, *J. Alloys Comp.* , **2016**, *666*, 153-158.
- [290] C.-C. Lin, J.-M. Ho, H.-L. Hsieh, *Chem. Eng. J.*, **2012**, *203*, 88–94.
- [291] a) J. Chen, Y. Ju, H. Chen, *Nano*, **2019**, *14*, 1950019; b) A.K. Tucker-Schwartz, R.L. Garrell, *Chem. Eur. J.* **2010**, *16*, 12718 – 12726
- [292] Bertorelle, F.; Pinto, M.; Zappone, R.; Pilot, R.; Litt, L.; Fiameni, S.; Conti, G.; Gobbo, M.; Toffoli, G.; Colombatti, M.; Fracasso, G.; Meneghetti, M., Safe core-satellite magneto-plasmonic nanostructures for efficient targeting and photothermal treatment of tumor cells. *Nanoscale* **2018**, *10* (3), 976-984
- [293] Leung, K. C.-F.; Xuan, S.; Zhu, X.; Wang, D.; Chak, C.-P.; Lee, S.-F.; Ho, W. K. W.; Chung, B. C. T., Gold and iron oxide hybrid nanocomposite materials. *Chemical Society Reviews* **2012**, *41* (5), 1911-1928.
- [294] Fan, Z.; Shelton, M.; Singh, A. K.; Senapati, D.; Khan, S. A.; Ray, P. C., Multifunctional Plasmonic Shell–Magnetic Core Nanoparticles for Targeted Diagnostics, Isolation, and Photothermal Destruction of Tumor Cells. *ACS Nano* **2012**, *6* (2), 1065-1073.
- [295] Bertorelle, F.; Ceccarello, M.; Pinto, M.; Fracasso, G.; Badocco, D.; Amendola, V.; Pastore, P.; Colombatti, M.; Meneghetti, M., Efficient AuFeOx Nanoclusters of Laser-Ablated Nanoparticles in Water for Cells Guiding and Surface-Enhanced Resonance Raman Scattering Imaging. *The Journal of Physical Chemistry C* **2014**, *118* (26), 14534-14541.
- [296] Bünzli, J.-C. G.; Piguet, C. Taking Advantage of Luminescent Lanthanide Ions. *Chem. Soc. Rev.* **2005**, *34*, 1048–1077.
- [297] Moore, E. G.; Samuel, A. P. S.; Raymond, K. N. From Antenna to Assay: Lessons Learned in Lanthanide Luminescence. *Acc. Chem. Res.* **2009**, *42*, 542–552.

- [298] Eliseeva, S. V.; Bünzli, J.-C. G. Lanthanide Luminescence for Functional Materials and Bio-Sciences. *Chem. Soc. Rev.* **2010**, 39, 189–227.
- [299] Bünzli, J.-C. G. Lanthanide Luminescence for Biomedical Analyses and Imaging. *Chem. Rev.* **2010**, 110, 2729–2755.
- [300] Binnemans, K. Lanthanide-Based Luminescent Hybrid Materials. *Chem. Rev.* **2009**, 109, 4283–4374.
- [301] Montgomery, C. P.; Murray, B. S.; New, E. J.; Pal, R.; Parker, D. Cell-Penetrating Metal Complex Optical Probes: Targeted and Responsive Systems Based on Lanthanide Luminescence. *Acc. Chem. Res.* **2009**, 42, 925–937.
- [302] G. H. Dieke, H. M. Crosswhite, and H. Crosswhite, *Spectra and Energy Levels of Rare Earth Ions in Crystals* (Interscience Publishers, New York, **1968**).
- [303] (a) Kang, Y. S. *J. Phys. Chem. C* **2009**, 113, 16652. (b) Liu, H. Q.; Wang, L. L.; Chen, S. G.; Zhou, B. S.; Peng, Z. W. *Appl. Surf. Sci.* **2007**, 253, 3872. (c) Ye, X. C.; Collins, J. E.; Kang, Y. J.; Chen, J.; Chen, D. T. N.; Yodh, A. G.; Murray, C. B. *Proc. Natl. Acad. Sci. U.S.A.* **2010**, 107, 22430.
- [304] (a) Sato, K.; Abe, H.; Ohara, S. *J. Am. Chem. Soc.* **2010**, 132, 2538. (b) Joo, J.; Yu, T.; Kim, Y. W.; Park, H. M.; Wu, F. X.; Zhang, J. Z.; Hyeon, T. *J. Am. Chem. Soc.* **2003**, 125, 6553.
- [305] (a) Jiang, C. L.; Wang, F.; Wu, N. Q.; Liu, X. G. *Adv. Mater.* **2008**, 20, 4826. (b) Ninjbadgar, T.; Garnweitner, G.; Börger, A.; Goldenberg, L. M.; Sakhno, O. V.; Stumpe, J. *Adv. Funct. Mater.* **2009**, 19, 1819. (c) Qu, X.; Song, H.; Pan, G.; Bai, X.; Dong, B.; Zhao, H.; Dai, Q.; Zhang, H.; Qin, R.; Lu, S. *J. Phys. Chem. C* **2009**, 113, 5906.
- [306] Tsedev Ninjbadgar, Georg Garnweitner,* Alexander Boßrger, Leonid M. Goldenberg, Oksana V. Sakhno, and Joachim Stumpe, *Adv. Funct. Mater.* **2009**, 19, 1819–1825
- [307] Y. Huang, E. Hemmer, F. Rosei and F. Vetrone, *J. Phys. Chem. B*, **2016**, 120, 4992–5001.